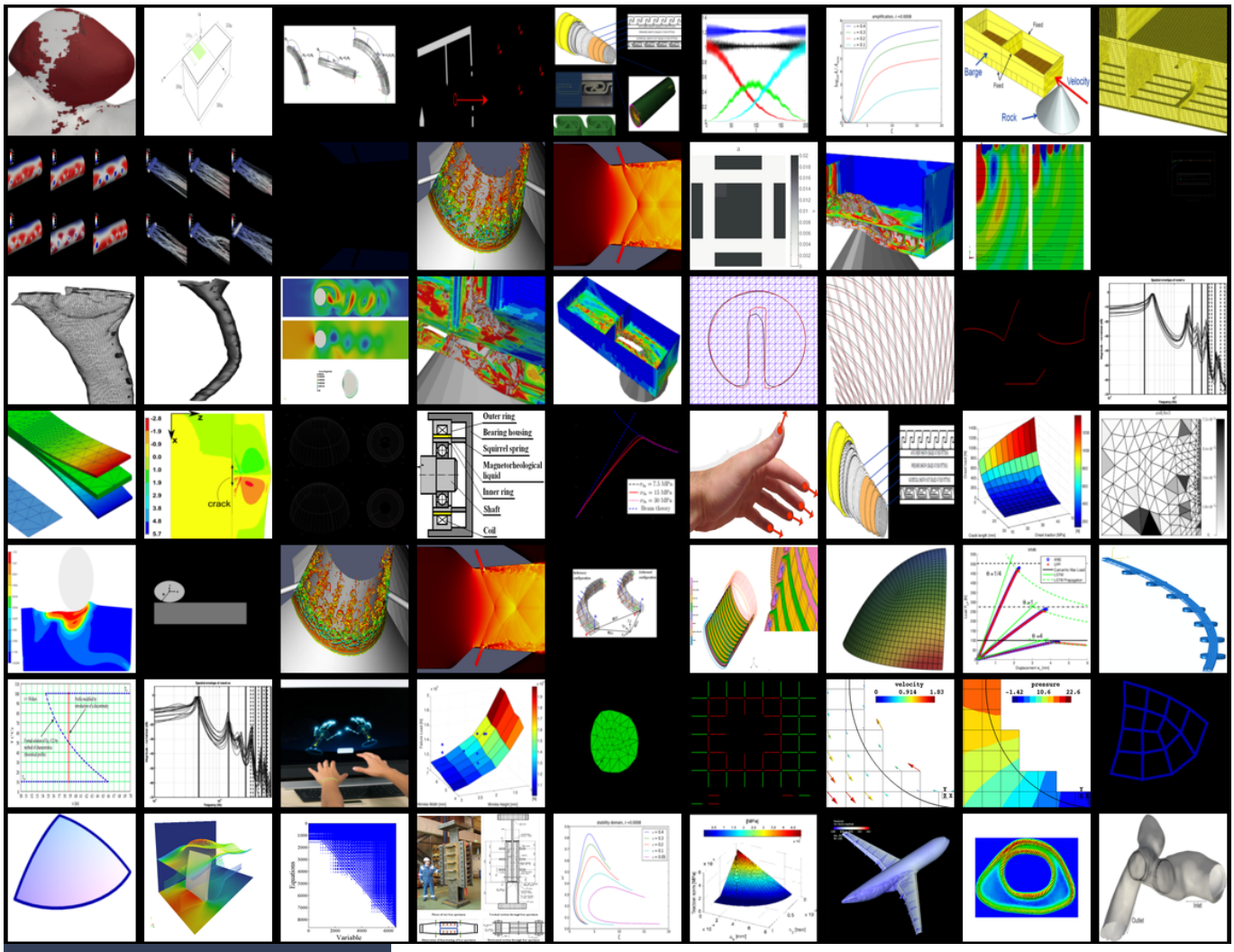

PROCEEDINGS OF THE 26th NORDIC SEMINAR ON COMPUTATIONAL MECHANICS

Oslo, 23–25 October 2013

A. Logg, K.-A. Mardal, and A. Massing (editors)

Center for Biomedical Computing
Simula Research Laboratory

Anders Logg · Kent-Andre Mardal · André Massing

Editors

Proceedings of the 26th Nordic Seminar on Computational Mechanics

Center for Biomedical Computing
Simula Research Laboratory

Editors

Anders Logg
Mathematical Sciences
Chalmers University of Technology
SE-412 96 Gothenburg
Sweden
logg@chalmers.se

André Massing
Simula Research Laboratory
PO Box 134
1325 Lysaker
Norway
massing@simula.no

Kent-Andre Mardal
Simula Research Laboratory
PO Box 134
1325 Lysaker
Norway
kent-and@simula.no

ISBN 978-82-92593-12-7

Preface

These proceedings contain the papers presented at the 26th Nordic Seminar on Computational Mechanics, held at the Center for Biomedical Computing hosted by Simula Research Laboratory in Oslo, Norway, October 23-25 2013.

The Nordic Seminars on Computational Mechanics represent the major activity of the Nordic Association for Computational Mechanics (NoACM). The NoACM was founded in 1988 with the objective to stimulate and promote research and practice in computational mechanics, to foster the interchange of ideas among the various fields contributing to computational mechanics, and to provide forums and meetings for dissemination of knowledge in computational mechanics. Younger researchers, in particular doctorate students, are especially encouraged to take part at these seminars. The member countries of NoACM are the Nordic countries (Denmark, Finland, Iceland, Norway and Sweden) and the Baltic countries (Estonia, Latvia and Lithuania). NoACM is a subchapter of the International Association for Computational Mechanics (IACM) and the European Community on Computational Methods in Applied Sciences (ECCOMAS).

This year's seminar features plenary talks from Professor Erik Burman (University College London), Professor Elena Celledoni (Norwegian University of Science and Technology NTNU), Associate Professor Jakob S. Jensen (Technical University of Denmark DTU), Dr. Juho Könnö (Wärtsilä), and Dr. Garth N. Wells (Hibbit Reader in Solid Mechanics at the University of Cambridge). This year's seminar also includes two honorary sessions: a session in honor of Professor Pål Bergan, and two sessions in honor of the 65th birthday of Professor Juhani Pitkäranta and the 60th birthday of Professor Rolf Stenberg.

On behalf of the organizing committee, we express our great appreciation to all contributors to the 26th Nordic Seminar on Computational Mechanics, including plenary speakers, session organizers, the authors of these proceedings, speakers, participants, and staff and students at Simula Research Laboratory.

Anders Logg, Kent-Andre Mardal and André Massing
Oslo, October 2013

Contents

Proceedings of the 26th Nordic Seminar on Computational Mechanics
A. Logg, K.A. Mardal, A. Massing (Eds.)

A stabilized Nitsche fictitious domain formulation for the three-field Stokes problem

S. Claus[1], E. Burman[1] and A. Massing[2]

(1) Department of Mathematics, University College London, Gower Street, London WC1E 6BT, susanne.claus@ucl.ac.uk, e.burman@ucl.ac.uk
(2) Center for Biomedical Computing at Simula Research Laboratory, P.O. Box 134, 1325 Lysaker, massing@simula.no

Summary. We propose a Nitsche fictitious domain method for the three-field Stokes problem where the dependent variables of velocity, pressure and extra-stress tensor are discretised with linear finite elements. To stabilise the equal order approximation, we employ a continuous interior penalty (CIP) method involving the normal gradient jumps of the velocity and pressure. On the unfitted boundary, Dirichlet boundary conditions are weakly enforced using Nitsche's method. Adding CIP-like ghost-penalties in the vicinity of the boundary allows us to prove the inf-sup stability and optimal convergence of our method and to bound the condition number independent of the location of the boundary with respect to the computational mesh. Numerical examples corroborate the theoretical findings.

Key words: Three-field Stokes, continuous interior penalty, fictitious domain, ghost penalty, Nitsche's method

Introduction

The aim of our work is to develop a robust and efficient scheme for the simulation of viscoelastic free surface flows in which the fluid surface undergoes large deformations. The free surface flow of viscoelastic liquids plays a key role in a wide range of industrial applications such as surface coating for molten plastics, filtration operations of engine oils or inkjet printing. In all these applications, the surface of the liquid undergoes large deformations and drop detachments may occur. The use of interface tracking techniques such as the arbitrary Lagrangian Eulerian methods in which the mesh is fitted and moved with the interface involve frequent re-meshing and sophisticated mesh moving algorithms that can be prohibitively expensive for these challenging free surface flows. To circumvent this problem, we propose an unfitted finite element method (e.g. [5], [6]) where the surface motion is tracked independently of the mesh. Consequently, the fluid surface can intersect elements in the computational mesh in an arbitrary manner. A major challenge for such an unfitted scheme is to achieve robustness and optimal approximation properties independent of the interface location. In this contribution, we develop a stabilised unfitted Nitsche method for a simple viscoelastic flow model problem augmented with so-called ghost-penalties to ensure these properties.

A continuous interior penalty method for three-field Stokes problem

The flow of a viscoelastic fluid is characterised by the conservation of mass, momentum and a constitutive equation which relates the stress tensor to the rate of deformation. Here, we assume the simplest constitutive relation of the stress tensor to the rate of deformation tensor which is simply characterised by a constant viscosity η:

$$\boldsymbol{\sigma} - 2\eta\boldsymbol{\epsilon}(\mathbf{u}) = 0 \text{ in } \Omega. \tag{1}$$

Together with the conservation of mass and momentum

$$\begin{cases} -\nabla\cdot\boldsymbol{\sigma} + \nabla p &= \mathbf{f} \text{ in } \Omega, \\ \nabla\cdot\mathbf{u} &= 0 \text{ in } \Omega, \\ \mathbf{u} &= \mathbf{g} \text{ on } \Gamma, \end{cases} \tag{2}$$

this system of equations forms the so-called **three-field Stokes** equations. Here, $\mathbf{u}$ is the velocity, p is the pressure, $\boldsymbol{\sigma}$ is the extra-stress tensor, $\boldsymbol{\epsilon}(\mathbf{u}) = \frac{1}{2}\left(\nabla\mathbf{u} + \nabla\mathbf{u}^T\right)$ is the rate of deformation tensor, $\mathbf{f} : \Omega \to \mathbb{R}^d$ is the body force and $\mathbf{g}$ is a prescribed velocity on the fluid surface Γ. In our scheme, we approximate the extra-stress tensor, the velocity and the pressure in the finite element space of continuous, piecewise linears

$$\mathcal{V}_h := \left\{v_h \in C^0(\Omega) : v_h|_K \in \mathcal{P}_1(K)\,\forall K \in \mathcal{T}_h\right\}, \tag{3}$$

$$\mathcal{V}_h^d := \left\{\mathbf{v}_h \in C^0(\Omega) : \mathbf{v}_h|_K \in [\mathcal{P}_1(K)]^d\,\forall K \in \mathcal{T}_h\right\}, \tag{4}$$

$$\mathcal{V}_h^{d\times d} := \left\{\mathbf{S}_h \in C^0(\Omega) : \mathbf{S}_h|_K \in [\mathcal{P}_1(K)]^{d\times d}\,\forall K \in \mathcal{T}_h\right\}, \tag{5}$$

where $\{\mathcal{T}_h\}_{0<h\leq 1}$ denotes a shape-regular family of triangulations of the domain Ω.

We employ the continuous interior penalty method ([3]) to avoid inf-sup related instabilities. Denoting the set of interior faces in $\mathcal{T}_h$ by $\mathcal{F}_h^i$, we can introduce the interior penalty operators of the form

$$s_k(x,y) = \sum_{F\in\mathcal{F}_h^i} h^k \int_F [\![\nabla x]\!]_n [\![\nabla y]\!]_n \, dS. \tag{6}$$

These terms involve the normal gradient jumps $[\![\partial_n x]\!]$ across the set of interior faces $\mathcal{F}_h^i$ depicted in Figure 1b. To ensure the stability of our numerical scheme, two modified inf-sup compatibility conditions need to be satisfied for the three-field Stokes problem: one arising from the pressure-velocity coupling and one arising from the extra-stress-velocity coupling. Consequently, we define two corresponding stabilisation operators

$$s_u(\mathbf{u}_h, \mathbf{v}_h) = 2\eta\gamma_u s_1(\mathbf{u}_h, \mathbf{v}_h), \tag{7}$$

$$s_p(p_h, q_h) = \frac{\gamma_p}{2\eta} s_3(p_h, q_h). \tag{8}$$

Moreover, we employ Nitsche's method to enforce the Dirichlet boundary condition (12) in a weak manner. Introducing the notation

$$a_h\left(\boldsymbol{\sigma}_h.\mathbf{v}_h\right) = \left(\boldsymbol{\sigma}_h,\, \boldsymbol{\epsilon}(\mathbf{v}_h)\right)_\Omega - \langle\boldsymbol{\sigma}_h\cdot\boldsymbol{n},\, \mathbf{v}_h\rangle_{\partial\Omega},$$
$$b_h\left(p_h.\mathbf{v}_h\right) = -\left(p_h,\, \nabla\cdot\mathbf{v}_h\right)_\Omega + \langle p_h\cdot\boldsymbol{n},\, \mathbf{v}_h\rangle_{\partial\Omega},$$

the complete formulation of the three-field Stokes problem reads: find $U_h := (\boldsymbol{\sigma}_h, \mathbf{u}_h, p_h) \in \mathcal{V}_h^{d\times d} \times \mathcal{V}_h^d \times \mathcal{V}_h$ with $\mathcal{V}_h = \left\{v_h \in C^0(\Omega) : v_h|_K \in \mathcal{P}_1(K)\, \forall K \in \mathcal{T}_h\right\}$ such that for all $V_h := (\boldsymbol{\tau}_h, \mathbf{v}_h, q_h) \in \mathcal{V}_h^{d\times d} \times \mathcal{V}_h^d \times \mathcal{V}_h$

$$A_h(U_h, V_h) + S_h(U_h, V_h) = L(V_h), \tag{9}$$

where

$$A_h(U_h, V_h) := a_h(\boldsymbol{\sigma}_h, \mathbf{v}_h) - a_h(\boldsymbol{\tau}_h, \mathbf{u}_h) + b_h(p_h, \mathbf{v}_h) - b_h(q_h, \mathbf{u}_h) + \left(\frac{1}{2\eta}\boldsymbol{\sigma}_h, \boldsymbol{\tau}_h\right), \tag{10}$$

$$S_h(U_h, V_h) := s_u(\mathbf{u}_h, \mathbf{v}_h) + s_p(p_h, q_h) + \frac{\gamma_b \eta}{h}\langle u_h, v_h\rangle_{\partial\Omega}, \tag{11}$$

$$L_h(V_h) := (\mathbf{f}, \mathbf{v}_h) + \langle \boldsymbol{\tau}_h \cdot \boldsymbol{n}, \mathbf{g}\rangle_{\partial\Omega} - \langle q_h \cdot \boldsymbol{n}, \mathbf{g}\rangle_{\partial\Omega} + \frac{\gamma_b \eta}{h}\langle \mathbf{g}, v_h\rangle_{\partial\Omega}. \tag{12}$$

For sufficiently large penalty parameters γ_u, γ_p and γ_b, the discretisation scheme (10)-(12) satisfy an inf-sup condition ([2], [1]).

A stabilized Nitsche fictitious domain formulation for the three-field Stokes problem

In fictitious domain methods, the boundary surface Γ of a domain Ω is represented independently of the underlying computational mesh $\mathcal{T}^*$, see Figure 1. In [7, 4] it has been shown, that the use of the classical Nitsche method to weakly enforce Dirichlet boundary conditions may result in a unstable numerical scheme in the fictitious domain setting. More specifically, the convergence rate of the method and the conditioning of the resulting discrete system are highly dependent of the boundary location with respect to the computational mesh. To achieve optimal approximation properties and well-behaved condition numbers irrespective of the boundary location, Nitsche-type methods can be augmented with so-called ghost penalties [7]. A prominent example are face-based jump penalty operators similar to continuous interior penalty. To this end, we can define suitable ghost penalty operators for the pressure p_h and velocity $\mathbf{u}_h$ by requiring that the CIP face integrals in (7) and (8) are always evaluated on the entire face, even if they are intersected by the boundary Γ. For the extra stress tensor $\boldsymbol{\sigma}_h$, we add a ghost-penalty of the form

$$s_\sigma(\boldsymbol{\sigma}_h, \boldsymbol{\tau}_h) = \gamma_\sigma \sum_{F\in\mathcal{F}_h^g} h^3 \int_F [\![\nabla\boldsymbol{\sigma}_h]\!]_n [\![\nabla\boldsymbol{\tau}_h]\!]_n \, dS, \tag{13}$$

acting only on faces F in the vicinity of the boundary, see Figure 1. The precise definition of $\mathcal{F}_h^g$ is given by

$$\mathcal{F}_h^g = \{F \in \mathcal{F}_h^i : T_F^+ \cap \Gamma \neq \emptyset \vee T_F^- \cap \Gamma \neq \emptyset\}, \tag{14}$$

where the two elements shared by an interior face are denoted by T_F^+ and T_F^-.

In summary, the stabilised Nitsche fictitious domain formulation for the three-field Stokes equation reads: find $U_h \in \mathcal{V}_h^{d\times d} \times \mathcal{V}_h^d \times \mathcal{V}_h$ such that for all $V_h \in \mathcal{V}_h^{d\times d} \times \mathcal{V}_h^d \times \mathcal{V}_h$

$$A_h(U_h, V_h) + S_h(U_h, V_h) = L_h(V_h), \tag{15}$$

where the stabilisation form $S_h(U_h, V_h)$ is now defined by

$$S_h(U_h, V_h) := \underbrace{s_u(\mathbf{u}_h, \mathbf{v}_h) + s_p(p_h, q_h)}_{\text{Interior/ghost penalty}} + \underbrace{s_\sigma(\boldsymbol{\sigma}_h, \boldsymbol{\tau}_h)}_{\text{Ghost penalty}} + \underbrace{\frac{\gamma_b \eta}{h}\langle u_h, v_h\rangle_{\partial\Omega}}_{\text{Boundary penalty}}. \tag{16}$$

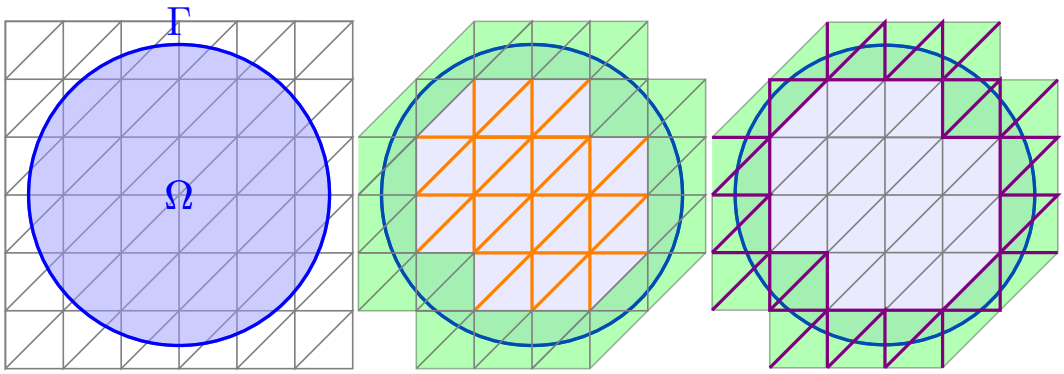

(a) (b) (c)

Figure 1: (a) Fluid domain Ω with interface Γ intersecting the background mesh, (b) set of interior edges, $\mathcal{F}^i$, where the interior penalty terms are employed and (c) set of ghost penalty edges, $\mathcal{F}^g$, where the ghost penalty terms are employed.

Stability and a priori estimates

For the proposed scheme, we prove that a suitable inf-sup conditions is satisfied and that our scheme has optimal convergence properties independent of the interface location. Introducing the energy norm

$$|||(\boldsymbol{\sigma}, \mathbf{u}, p)|||^2 = \frac{1}{2\eta} \|\boldsymbol{\sigma}\|^2_{0,\Omega} + 2\eta \|\boldsymbol{\epsilon}(\mathbf{u})\|^2_{0,\Omega} + \frac{1}{2\eta} \|p\|^2_{0,\Omega} \tag{17}$$

and its discrete counterpart

$$|||(\boldsymbol{\sigma}_h, \boldsymbol{u}_h, p_h)|||^2_h = \frac{1}{2\eta} \|\boldsymbol{\sigma}_h\|^2_{0,\Omega} + 2\eta \|\boldsymbol{\epsilon}(\mathbf{u}_h)\|^2_{0,\Omega} + \frac{1}{2\eta} \|p_h\|^2_{0,\Omega} + S_h(U_h, V_h), \tag{18}$$

we can prove the following theorems:

Theorem 1. *For all* $(\boldsymbol{\sigma}_h, \boldsymbol{u}_h, p_h) \in \mathcal{V}_h^{d\times d} \times \mathcal{V}_h^d \times \mathcal{V}_h$ *there holds*

$$c_s \, |||\, (\boldsymbol{\sigma}_h, \boldsymbol{u}_h, p_h)|||_h \leq \sup_{(\boldsymbol{\tau}_h, \boldsymbol{v}_h, q_h) \in \mathcal{V}_h^{d\times d} \times \mathcal{V}_h^d \times \mathcal{V}_h} \frac{A_h[(\boldsymbol{\sigma}_h, \boldsymbol{u}_h, p_h), (\boldsymbol{\tau}_h, \boldsymbol{v}_h, q_h)] + S_h(U_h, V_h)}{|||(\boldsymbol{\sigma}_h, \boldsymbol{v}_h, q_h)|||_h},$$

where the constant c_s *is independent of how the boundary cuts the mesh.*

Theorem 2. *Assuming that the solution* $U := (\boldsymbol{\sigma}, \mathbf{u}, p) \in H^1(\Omega)^{d\times d} \times H^2(\Omega)^d \times H^1(\Omega)$*, we have the error estimates*

$$|||U - U_h||| \leq ch \left(\eta^{1/2} \|\boldsymbol{u}\|_{2,\Omega} + \frac{1}{\eta^{1/2}} \|p\|_{1,\Omega} + \frac{1}{\eta^{1/2}} \|\boldsymbol{\sigma}\|_{1,\Omega} \right),$$

The constant c *is independent of how the boundary cuts the mesh.*

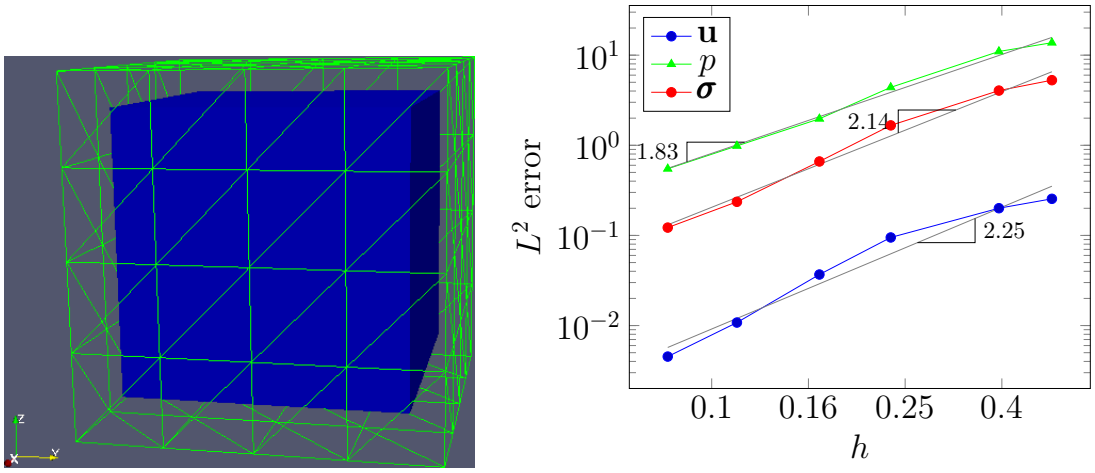

(a) (b)

Figure 2: Convergence rates for reference solution on unit cube.

Numerical results

Numerically, we investigate the quality of our numerical solution for the analytical reference solution

$$(u, v, w) = (\cos(\pi y)\cos(\pi z), \cos(\pi x)\cos(\pi z), \cos(\pi x)\cos(\pi y))$$

$$p = -\pi^2 \cos(\pi x)\cos(\pi y)$$

on the unit cube. Here, we embed a unit cube in a dilated background mesh as shown in Figure 2a. Figure 2b shows the convergence of the variables with mesh refinement in the L^2 norm. For the velocity and the extra stress tensor, the sum of the error of the components is evaluated. We obtain a convergence order of 2.25 for the velocity in the L^2 norm which is what we expect from our error analysis and a convergence order of 2.14 and 1.83 for the stress and pressure which is slightly better than expected. However, this can be explained by the smoothness of the solution. More numerical evidence for the stability and convergence properties of the scheme independent of the interface location will be given in the presentation and details of the scheme and the solutions can be found in [8], which is in preparation.

References

[1] A. Bonito and E. Burman. A Continuous Interior Penalty Method for Viscoelastic Flows. *SIAM Journal on Scientific Computing*, 30(3): 1156–1177, 2008.

[2] A. Bonito and E. Burman. A face penalty method for the three fields Stokes equation arising from Oldroyd-B viscoelastic flows. *Numerical mathematics and advanced applications*, Springer Berlin Heidelberg, 487–494, 2006.

[3] E. Burman and P. Hansbo. Edge stabilization for Galerkin approximations of convection–diffusion–reaction problems. *Computer Methods in Mechanics and Engineering*, 193(15-16): 1437–2566, 2004.

[4] E. Burman and P. Hansbo. Fictitious domain finite element methods using cut elements: II. A stabilized Nitsche method. *Applied Numerical Mathematics*, 62(4): 328–341, 2012.

[5] A. Hansbo and P. Hansbo. An unfitted finite element method, based on Nitsche's method, for elliptic interface problems. *Computer methods in applied mechanics and engineering*, 191(47): 5537–5552, 2002.

[6] P. Hansbo. Nitsche's method for interface problems in computational mechanics. *GAMM-Mitteilungen*, 28(2): 183-206, 2005.

[7] E. Burman. Ghost penalty. *Comptes Rendus Mathematique*, 348(21): 1217–1220, 2010.

[8] S.Claus, E. Burman, A. Massing. A stabilized Nitsche fictitious domain formulation for the three-field Stokes problem. in preparation.

Proceedings of the 26th Nordic Seminar on Computational Mechanics
A. Logg, K.A. Mardal, A. Massing (Eds.)

An iterative penalisation method for fluid/solid interfaces in vortex methods

Mads M. Hejlesen[1], Petros Koumoutsakos[2], Anthony Leonard[3] and Jens H. Walther[1,2]

(1)Department of Mechanical Engineering, Technical University of Denmark, Building 403, DK-2800 Kgs. Lyngby, Denmark, mmhej@mek.dtu.dk, jhw@mek.dtu.dk
(2)Computational Science and Engineering Laboratory, ETH Zürich, Clasiusstrasse 33, CH-8092 Zürich, Switzerland, walther@mavt.ethz.ch
(3)Division of Engineering and Applied Science, California Institute of Technology, 1200 E California Blvd., CA 91125 Pasadena, USA

Summary. We present a novel iterative implementation of the Brinkman penalisation method for the enforcement of solid boundaries in a fluid domain. This is done by utilising the conventional split step algorithm of vortex method where the velocity field is first calculated by kinematic relations after which the vorticity equation is solved in its Lagrangian form by evolving vortex particles. Hence the penalisation of the velocity field can be performed through the kinematic relations by simply correcting the velocity in the penalised region. In the present work we show that an iterative implementation of the penalisation method is generally needed in order to impose the correct no-slip boundary condition in the fluid/solid interface.

Key words: Immersed boundary methods, Brinkman penalisation, vortex methods.

Introduction

The idea of Brinkman penalisation in fluid mechanics is to emulate a solid as a porous media by locally penalising the governing flow equation. In the context of enforcing solid boundary conditions in an incompressible flow, the Brinkman penalisation was first proposed by Angot et al. [1] in the context of an immersed boundary method. Here the penalisation term was included as an additional expression in the Navier-Stokes equation to absorb the momentum of the flow within a specified penalisation region i.e. the solid body.

The vorticity formulation of the penalisation term was implemented in a split step algorithm by Coquerelle and Cottet [2]. Here the penalisation term was excluded from the governing equation and simply handled as a correction of the velocity field from which the the vorticity can be recalculated. The split step algorithm has been implemented in the vortex-in-cell method by Coquerelle and Cottet [2], Rossinelli et al. [3], Rasmussen et al. [4], and Gazzola et al. [5] where it has been validated for the flow past different geometries, both fixed and moving. These implementations clearly demonstrated that the penalisation method is capable of producing results in good agreement with benchmark cases however at the cost of using a very small time step.

In the present work we will show that the necessity of the small time step is not related to the accuracy of the penalisation method rather than the incapability of producing the correct boundary conditions within a single time step. The penalisation of the velocity field does not inherently posses the same global characteristic as the elliptic governing equations, as it simply enforces a given local velocity condition within the penalised region without modifying the surrounding flow. This will create divergence in the velocity field at the interface of the non-penalised and penalised regions when the non-penalised flow has a non-zero velocity component normal to the interface. Creating a velocity divergence is evidently incorrect as it violates the criteria of mass conservation. Therefore the no-slip boundary condition must be enforced exclusively by creating rotation in the velocity field i.e. vorticity.

In this work we follow the idea of the semi-implicit penalisation method of Rasmussen et al. [4], where the vorticity of the flow is updated rather than recalculated from the penalised velocity field. We propose an extended algorithm where the penalisation is performed in an iterative fashion. This gradually eliminates the velocity divergence created by penalising the velocity field to achieve a boundary condition that is entirely enforced by the surface vorticity.

The iterative penalisation method for incompressible viscous flow

In vortex methods, an incompressible flow field is described solely by evolving the distribution of vorticity $\boldsymbol{\omega}$ by the vorticity equation

$$\frac{D\boldsymbol{\omega}}{Dt} = \nu\nabla^2\boldsymbol{\omega}, \tag{1}$$

where the vorticity is defined from the velocity $\boldsymbol{\omega} = \boldsymbol{\nabla}\times\boldsymbol{u}$ which is inversely coupled through the Poisson equation $\nabla^2\boldsymbol{u} = -\boldsymbol{\nabla}\times\boldsymbol{\omega}$. By ensuring that the velocity field $\boldsymbol{u}$ is sufficiently smooth it may be represented as a linear superposition of several equally smooth velocity fields. Thus the velocity field may be decomposed into three components $\boldsymbol{u} = \boldsymbol{u}_{\tilde{\omega}} + \boldsymbol{u}_\gamma + \boldsymbol{U}_\infty$ which represents the velocity induced by the non-penalised vorticity field $\tilde{\boldsymbol{\omega}}$, the velocity induced by the penalisation vorticity $\boldsymbol{\gamma}$, and the free stream velocity. Thus the penalisation vorticity is generated such that the resulting penalisation velocity $\boldsymbol{u}_\gamma$ counteracts the non-penalised velocity field $\tilde{\boldsymbol{u}} = \boldsymbol{u}_{\tilde{\omega}} + \boldsymbol{U}_\infty$ leaving only the given velocity of the solid $\mathbf{v}$ in the penalisation region. Hence, in the penalised region where we wish to enforce $\boldsymbol{u} = \mathbf{v}$ we now obtain

$$\chi\,\mathbf{v} = \chi(\tilde{\boldsymbol{u}} + \boldsymbol{u}_\gamma) \qquad \rightarrow \qquad \chi\,\boldsymbol{u}_\gamma = \chi(\mathbf{v} - \tilde{\boldsymbol{u}}) = \chi\,\mathbf{v}_o \qquad \text{where} \quad \chi = \begin{cases} 1 & \boldsymbol{x} \in S, \\ 0 & \boldsymbol{x} \in F. \end{cases} \tag{2}$$

Here χ is the characteristic function which defines the region of active penalisation where S denotes the mesh cells occupied by the solid and F the mesh cells occupied by the fluid cf. Fig. 1a.

From Eq. (2) it is seen that $\mathbf{v}_o = \mathbf{v} - \tilde{\boldsymbol{u}}$ is the velocity that needs to be penalised in order to enforce the given velocity $\mathbf{v}$ within the penalised region. Thus an effective penalisation is obtained when $\chi(\mathbf{v}_o - \boldsymbol{u}_\gamma) = \mathbf{0}$. In order to achieve this within a certain tolerance ϵ an iterative

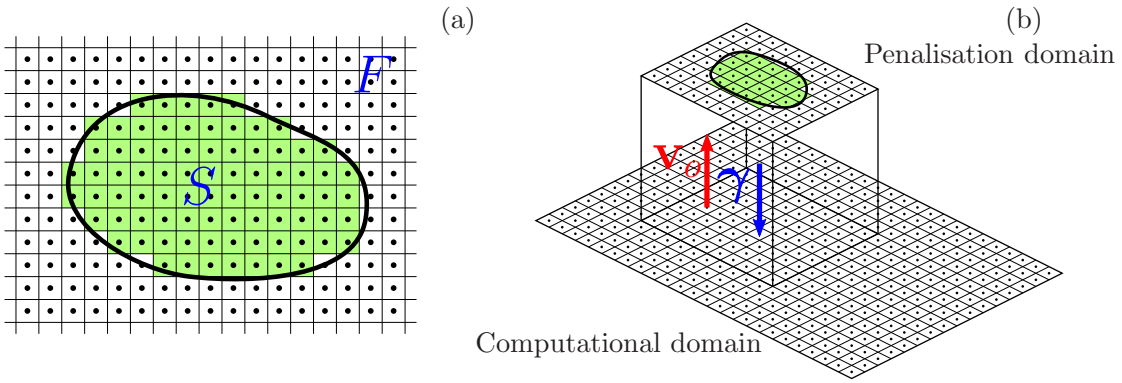

Figure 1. Schematic of the computational domain. (a) The solid is discretized onto the Cartesian grid by penalising the mesh cells (S) that fall inside the solid surface (black curve). F denotes the fluid region. The • mark the center of the mesh cells. (b) The iterative penalisation annihilates the residual velocity ($\mathbf{v}_0$) through the creating of image vorticity $\boldsymbol{\gamma}$. The iteration requires solution of the Poisson equation and is performed on the minimal "penalisation domain" surrounding the solid.

penalisation algorithm is proposed which is summarised by:

1. Set the initial penalisation vorticity $\boldsymbol{\gamma} = \mathbf{0}$ and penalisation velocity $\boldsymbol{u}_\gamma = \mathbf{0}$.
2. While $\int \chi(\mathbf{v}_o - \boldsymbol{u}_\gamma) d\boldsymbol{x} > \epsilon$:
   - Update the penalisation vorticity by: $\boldsymbol{\gamma} \leftarrow \boldsymbol{\gamma} + \boldsymbol{\nabla} \times \chi(\mathbf{v}_o - \boldsymbol{u}_\gamma)$.
   - Solve the Poisson equation: $\nabla^2 \boldsymbol{u}_\gamma = -\boldsymbol{\nabla} \times \boldsymbol{\gamma}$.
3. $\boldsymbol{\omega} = \tilde{\boldsymbol{\omega}} + \boldsymbol{\gamma}$ and recalculate the velocity field on the full domain by solving: $\nabla^2 \boldsymbol{u} = -\boldsymbol{\nabla} \times \boldsymbol{\omega}$.

It is noticed that $\mathbf{v}_o$ can be calculated outside the iterative loop whereas it suffices to solve the Poisson equation in a small domain bounding the geometry cf. Fig. 1b. In this way the computational work of the iterative penalisation is significantly reduced as it becomes independent of the extend of the total vorticity field.

An illustrative example of a uniformly accelerated flow normal to a flat plate

The shortcomings of the conventional penalisation method and the improved result obtained by using the iterative penalisation method is briefly illustrated in Fig. 2. Here, the obtained flow fields are shown of a uniformly accelerated flow normal to a flat plate of finite thickness. This case is particularly challenging in that the acceleration of the flow continuously creates an additional flow momentum which is normal to the plate surface. It is seen that even at late times the conventional penalisation method is unable to deflect the flow around the plate and the flow is seen to penetrate the plate. The insufficient penalisation creates a distorted separation region and a large difference is noticed in the flow field compared to the results obtained using the iterative penalisation. The results obtained by the iterative penalisation method is found to be in excellent agreement with similar flow simulations using boundary element based methods [6] (not shown).

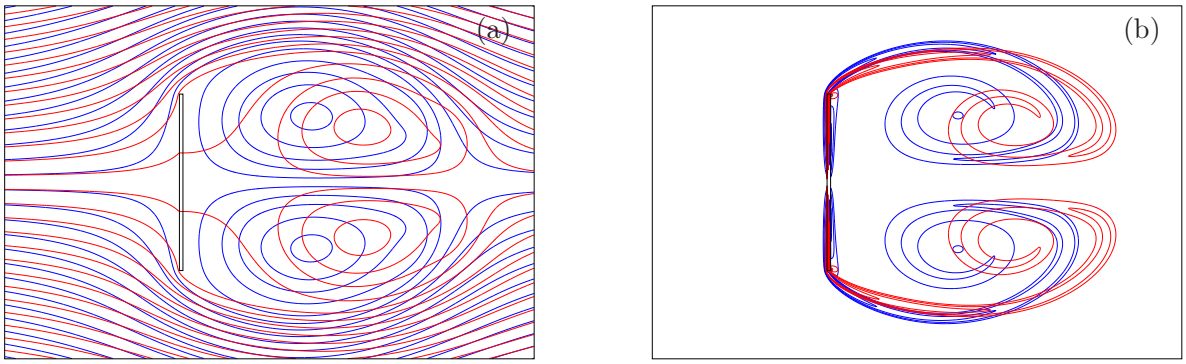

Figure 2. Comparison of the streamlines (a) and vorticity contours (b) obtained by conventional, non-iterative penalisation (red), and iterative penalisation (blue) for an accelerated flow normal to a flat plate of thickness-to-length ratio 1:50 at a non-dimensional time $at^2/L = 3.36$. The acceleration formulated Reynolds number $aL^3/\nu^2 = 1.68 \times 10^6$, where a is the acceleration of the flow, ν the kinematic viscosity and L the height of the plate. Vorticity contours are $\pm 2^i$ where $i = \{4, 5, 6, 7\}$.

Conclusion

In the work which we will present at the seminar we intent to illustrate by a number of benchmark cases how using the conventional Brinkman penalisation method to introduce a solid interface in a numerical flow simulation can result in an insufficient enforcement of solid boundaries. Furthermore we show that by extending the conventional Brinkman penalisation method to an iterative algorithm, the method is able to obtain results in good agreement with those obtained by simulations using boundary element based methods. Here the calculated flow induced forces are generally in excellent agreement with results found in the literature. Furthermore, the resulting flow fields are significantly improved for the iterative algorithm compared to that obtained by the conventional, non-iterative penalisation method.

References

[1] P. Angot, C.-H. Bruneau, P. Fabrie, A penalization method to take into account obstacles in incompressible viscous flows, Numer. Math. 81 (1999) 497–520.

[2] M. Coquerelle, G.-H. Cottet, A vortex level set method for the two-way coupling of an incompressible fluid with colliding rigid bodies, J. Comput. Phys. 227 (21) (2008) 9121–9137.

[3] D. Rossinelli, M. Bergdorf, G.-H. Cottet, P. Koumoutsakos, GPU accelerated simulations of bluff body flows using vortex particle methods, J. Comput. Phys. 229 (89) (2010) 3316–3333.

[4] J. T. Rasmussen, G.-H. Cottet, J. H. Walther, A multiresolution remeshed vortex-in-cell algorithm using patches, J. Comput. Phys. 230 (17) (2011) 6742–6755.

[5] M. Gazzola, P. Chatelain, W. M. van Rees, P. Koumoutsakos, Simulations of single and multiple swimmers with non-divergence free deforming geometries, J. Comput. Phys. 230 (2011) 7093–7114.

[6] P. Koumoutsakos, D. Shiels, Simulations of the viscous flow normal to an impulsively started and uniformly accelerated flat plate, J. Fluid Mech. 328 (1996) 177–227.

Proceedings of the 26th Nordic Seminar on Computational Mechanics
A. Logg, K.A. Mardal, A. Massing (Eds.)

Swirling flow in a two-stroke marine diesel engine

Casper S. Hemmingsen[1], Kristian M. Ingvorsen[1], Jens H. Walther[1,2], and Stefan Mayer[3]

(1)Department of Mechanical Engineering, Technical University of Denmark, Denmark, jhw@mek.dtu.dk
(2) Computational Science and Engineering Laboratory, ETH Zürich, Switzerland, Walther@mavt.ethz.ch
(3)MAN Diesel & Turbo, Denmark, Stefan.mayer@man.eu

Summary. Computational fluid dynamic simulations are performed for the turbulent swirling flow in a scale model of a low-speed two-stroke diesel engine with a moving piston. The purpose of the work is to investigate the accuracy of different turbulence models including two-equation Reynolds-Averaged Navier-Stokes models and large eddy simulations. The numerical model represent the full three-dimensional geometry and the piston motion is modeled by compressing cells in the axial direction. The CFD predictions are compared to experimental results and a reasonable agreement is found.

Key words: CFD, RANS, LES, swirl, turbulence, two-stroke, marine diesel

Introduction

Low-speed two-stroke (LSTS) diesel engines are used to power the worlds largest marine vessels, such as tankers and container ships. When the piston approaches the bottom dead center (BDC) of the cylinder, it uncovers a series of angled scavenge ports in the cylinder wall. Fresh air is blown into the cylinder through the scavenge ports, thereby flushing the old combustion gas out through the exhaust valve located in the cylinder head. This gas exchange process is known as uniflow-scavenging. The angled ports induce a rotational motion to the incoming scavenge air, thereby creating a swirling flow.

Accurate computational fluid dynamics (CFD) simulations of the in-cylinder swirling flow is important for engine optimization and emission reduction. Recently, a database for CFD validation was established based on an experimental investigation of the flow in a dynamic scale model of a LSTS diesel engine [1]. The model has a moving piston but compression and combustion are neglected.

The purpose of the present work is to evaluate the accuracy of different turbulence models

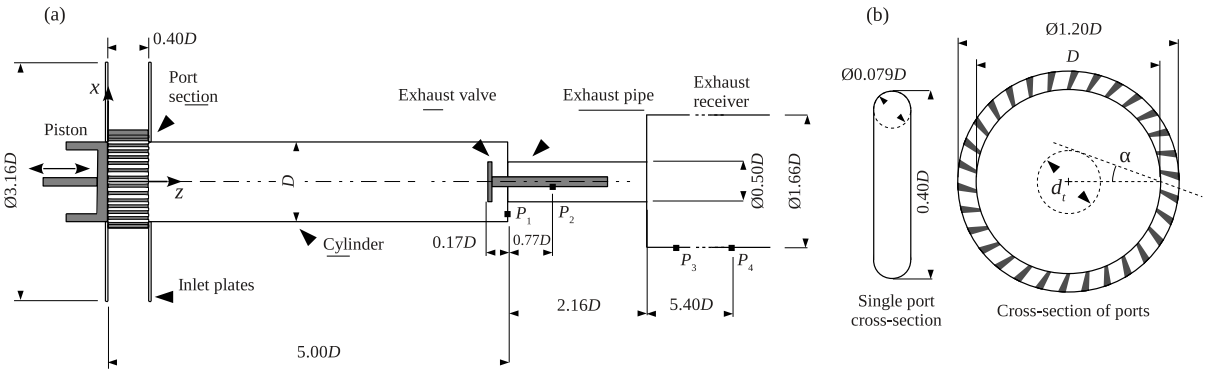

Figure 1. (a) Geometric of the main model, (b) details on the scavenge port geometry.

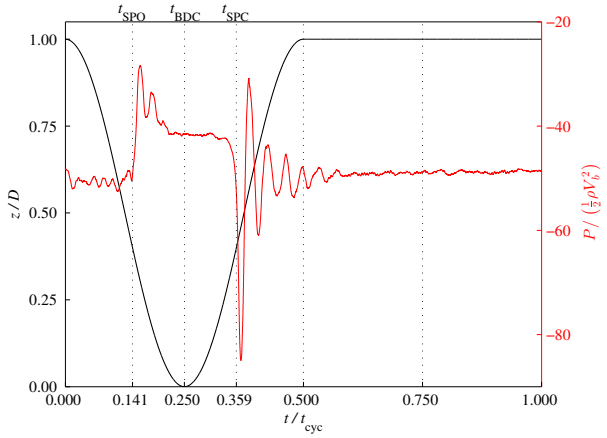

Figure 2. Piston motion (*black curve*) and outlet pressure (*red curve*).

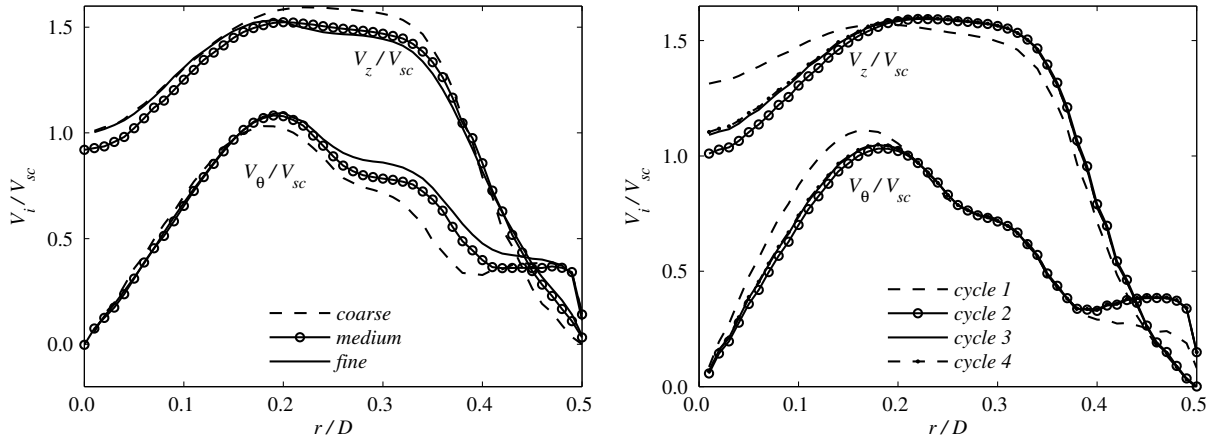

Figure 3. Numerical sensitivity study showing radial velocity profiles. (*left*) Spatial convergence, (*right*) cyclic convergence.

and to investigate the dynamics of the turbulent swirling flow. This is achieved by simulating the flow in the model using CFD and comparing the obtained predictions with the experimental results.

Methodology

The model geometry is shown in Figure 1 and described in detail in [1, 2]. The internal cylinder diameter is $D = 190\,\text{mm}$ and the Reynolds number of the flow is $\text{Re} = V_{sc}D/\nu = 50{,}000$, where ν is the kinematic viscosity and V_{sc} is the characteristic scavenge velocity. In the present work, a port section is used with 30 equally spaced ports and a port angle of $\alpha = 20°$. The piston motion is presented in Figure 2 together with the pressure measured at the model outlet (P_4 in Figure 1). The time is normalized with the total cycle time which is $t_{cyc} = 1.20\,\text{s}$.

The simulations are performed with the commercial CFD code STAR-CCM+ version 8.02.008. A hybrid mesh is used with polyhedral cells in the main volume and prismatic cells on the wall. The mesh used for the simulations, referred to as the '*fine*' mesh, has approximately 5.2 million cells. A second order linear upwind scheme is used for the spatial derivatives and a second order implicit scheme is used for the temporal derivatives. Both Reynolds-Averaged Navier-Stokes turbulence models and large eddy simulations are investigated.

A sensitivity study is carried out in order to investigate the effect of the numerical parameters. Figure 3 shows the radial velocity profiles of tangential velocity V_θ and axial velocity V_z for

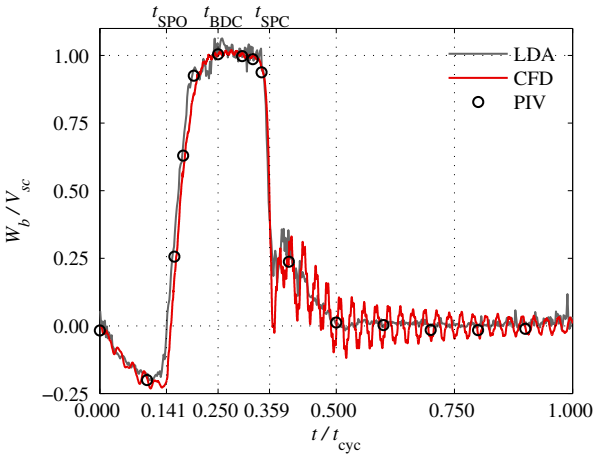

Figure 4. Comparison of predicted and experimental bulk velocity.

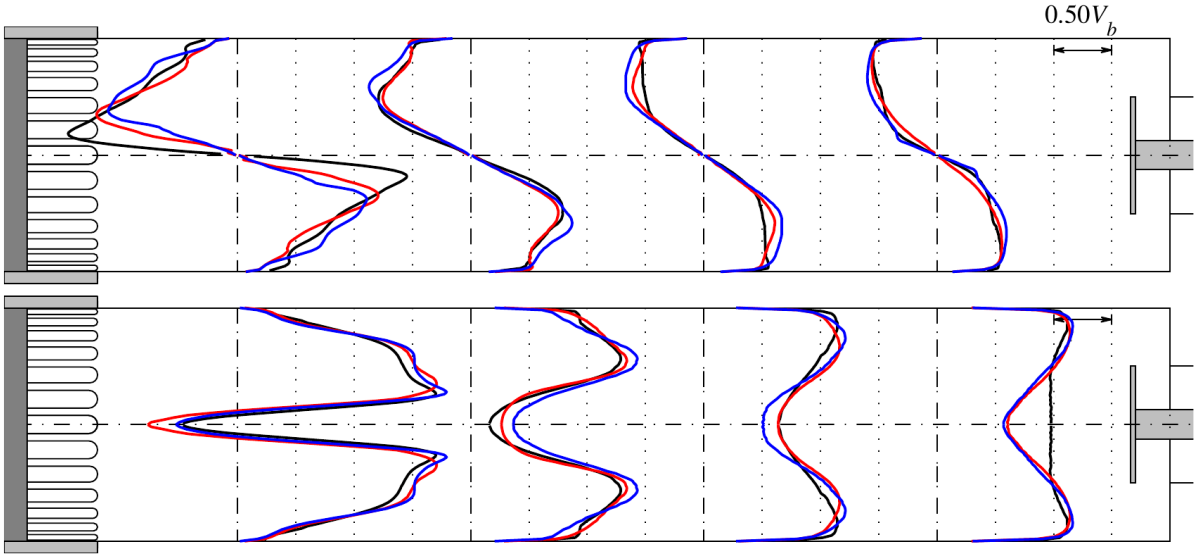

Figure 5. Comparison of radial velocity profiles. (*top*) tangential velocity V_θ, (*bottom*) axial velocity V_z. (*blue curves*) Spalart-Allmaras, (*red curves*) K-ω SST, (*black curves*) experiments.

different mesh sizes and cycles after simulation start. It is seen that the results obtained on the '*fine*' mesh can be considered mesh independent as no significant changes occur from the '*medium*' to '*fine*' mesh. Furthermore, it is seen that the flow becomes approximately periodic already after the second cycle.

Results

A comparison between the predicted and experiential bulk velocity W_b is presented in Figure 4. The numerical results are obtained with the Spalart-Allmaras turbulence model [4] and the experimental results are measured with particle image velocimetry (PIV) and laser Doppler anemometry (LDA). After the scavenge port closing, the CFD predicts large amplitude oscillations which do not exist in the experimental data. This is, however, a result of the experimental phase-averaging and therefore not a 'true' discrepancy. In general, it is concluded that the predicted bulk velocity is in good agreement with the experiments.

Figure 5 shows a comparison of the radial velocity profiles at $t/t_{cyc} = 0.30$ which is shortly after the piston reaches BDC and corresponds to 25% port closure. Profiles are presented

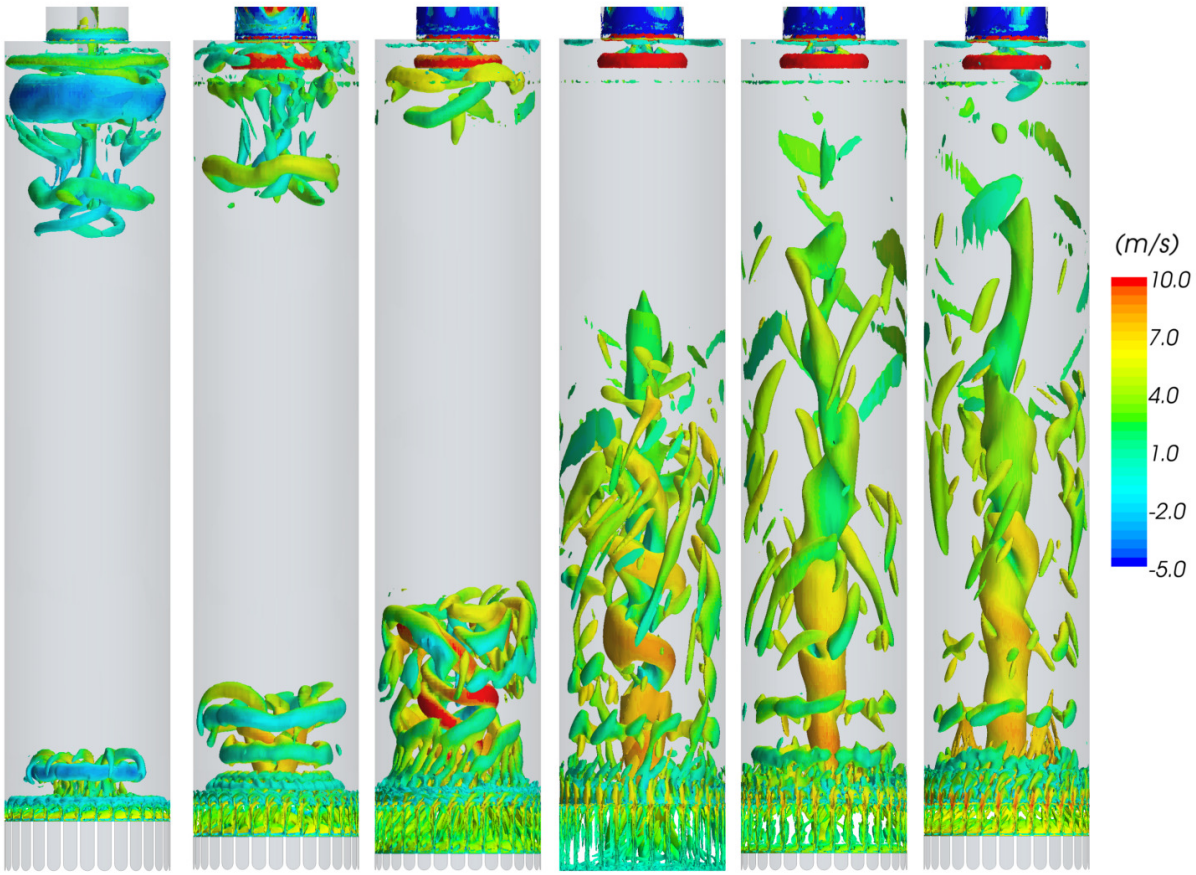

Figure 6. Visualization of flow structures during the scavenging period using iso-surfaces of the λ^2-criterion colored by the axial velocity.

for simulations using both the Spalart-Allmaras and the k-ω SST [3] turbulence model. The predictions obtained with the two turbulence models are in general similar and in reasonable agreement with the experimental data. The tangential velocity is underestimated near the ports and the axial velocity deficit is overpredicted in the top of the cylinder. Both models do, however, correctly predict the reversed axial flow at the centerline near the ports, which shows the occurrence of a vortex breakdown.

The numerical results are also used to investigate the complex flow dynamics of the turbulent swirling flow. In Figure 6 the unsteady flow structures are visualized using iso-surfaces of the λ^2-criterion colored by the axial velocity. In the start of the scavenging process, multiple vortex rings are formed, and later in the process, a coherent vortex core is established. When the ports are fully open, the vortex core has a pronounced helical shape.

References

[1] K. M. Ingvorsen, K. E. Meyer, J. H. Walther, and S. Mayer. Turbulent swirling flow in a dynamic model of a uniflow-scavenged two-stroke engine. *Exp. Fluids*, under review, 2013.

[2] K. M. Ingvorsen, K. E. Meyer, J. H. Walther, and S. Mayer. Turbulent swirling flow in a model of a uniflow-scavenged two-stroke engine. *Exp. Fluids*, 54:1494, 2013.

[3] Florian R. Menter. Zonal two equation k-ω turbulence models for aerodynamic flows. *AIAA J.*, 1993. Paper 93-2906.

[4] P. R. Spalart and S. R. Allmaras. A one-equation turbulence model for aerodynamic flows. *Rech. Aerospatiale*, 1:5–21, 1994.

Proceedings of the 26th Nordic Seminar on Computational Mechanics
A. Logg, K.A. Mardal, A. Massing (Eds.)

A face-oriented stabilized fictitious domain approach for 3D incompressible Navier-Stokes equations applied to fluid-structure interaction

Benedikt Schott[1] and Wolfgang A. Wall[1]

(1)Institute for Computational Mechanics, Boltzmannstraße 15, 85747 Garching b. München, Germany

Summary. A new stabilized XFEM based fixed-grid approach for the transient incompressible Navier-Stokes equations using cut elements is proposed. Boundary conditions on embedded boundaries are imposed weakly using a Nitsche type approach. Ghost-penalty terms for velocity and pressure are added for stability reasons and to improve the conditioning of the system matrix. The idea of ghost-penalties, previously developed for Stokes problems, is extended to the incompressible Navier-Stokes equations by the usage of face-oriented fluid stabilizations also in the interface zone. We obtain optimal error convergence and a good system conditioning in the viscous and the convective dominated cases. Further, the results are much more accurate and less sensitive to the location of the interface compared to methods without additional face-oriented stabilizations in the interface zone. Numerical results of a convergence analysis and results for fluid-structure interaction problems are shown.

Key words: Navier-Stokes equations, face-oriented stabilization, ghost-penalty, Nitsche's method, extended finite element method, fictitious domain method, fluid-structure interaction

Introduction

XFEM based fixed-grid methods represent very promising approaches when dealing with moving boundaries or more complex fluid-structure interaction (FSI) applications involving large deformations of the structure. Classical ALE-based FSI schemes are limited when the structure undergoes too large displacements or even topological changes. In contrast, describing the entire fluid domain by a fixed-grid Eulerian formulation using cut elements allows for large and complex changes of the physical fluid domain without fluid mesh distortion and, eventually, remeshing of the fluid domain.

Recently, hybrid fixed-grid fluid-structure interaction methods using an additional moving boundary layer mesh around the structure have been developed. Despite their advantages with respect to accuracy at the fluid-structure interface, a direct coupling of the structure described in a Lagrangean frame of reference with the flow field formulated in a pure fixed-grid Eulerian setting using cut elements is still more flexible regarding the motion of the structure. Moreover, such techniques allow for more advanced couplings of fluid-structure interaction problems involving for example multiple contacting submersed bodies.

For the robustness and, hence the applicability of such fixed-grid FSI-approaches it is essential to satisfy the highest demands on approximation quality, stability and accuracy of the fixed-grid fluid formulation, particularly with regard to moving boundaries or interfaces in time. And most if not all existing approaches show severe weaknesses in one or all of these aspects.

In this talk we propose a novel robust fixed-grid FSI approach based on a stabilized fictitious domain fluid formulation for the 3D Navier-Stokes equations on moving fluid domains.

Methodology

Stabilized fluid formulation including weak enforcement of boundary conditions

Our stabilized fictitious domain fluid formulation for the Navier-Stokes equations reads as

$$\begin{aligned}\Big(\boldsymbol{v}^h, \rho\dot{\boldsymbol{u}}^h\Big) + \Big(\boldsymbol{v}^h, \rho\boldsymbol{u}^h \cdot \nabla\boldsymbol{u}^h\Big) + \Big(q^h, \operatorname{div}\boldsymbol{u}^h\Big) - \Big(\operatorname{div}\boldsymbol{v}^h, p^h\Big) + \Big(\boldsymbol{\epsilon}(\boldsymbol{v}^h), 2\mu\boldsymbol{\epsilon}(\boldsymbol{u}^h)\Big) \\ + \Big\langle \boldsymbol{v}^h, p^h\cdot\boldsymbol{n}\Big\rangle_\Gamma - \Big\langle \boldsymbol{v}^h, 2\mu\boldsymbol{\epsilon}(\boldsymbol{u}^h)\cdot\boldsymbol{n}\Big\rangle_\Gamma - \Big\langle q^h\cdot\boldsymbol{n}, \boldsymbol{u}^h - \bar{\boldsymbol{u}}\Big\rangle_\Gamma - \Big\langle 2\mu\boldsymbol{\epsilon}(\boldsymbol{v}^h)\cdot\boldsymbol{n}, \boldsymbol{u}^h - \bar{\boldsymbol{u}}\Big\rangle_\Gamma \\ + \sum_{K\in G_h}\sum_{V\in\Omega_K^f}\Big\langle \gamma_u\cdot\boldsymbol{v}^h, \rho(\boldsymbol{u}^h - \bar{\boldsymbol{u}})\Big\rangle_{\Gamma_K\cap\bar{V}} + S_h\Big[(\boldsymbol{v}^h, q^h), (\boldsymbol{u}^h, p^h)\Big] = \Big(\boldsymbol{v}^h, \rho\boldsymbol{b}\Big) + \Big\langle \boldsymbol{v}^h, \bar{\boldsymbol{h}}\Big\rangle_{\partial\Omega_N^f}\end{aligned} \tag{1}$$

where $\bar{\boldsymbol{u}}$ is the prescribed interface velocity and S_h is a symmetric stabilization operator

$$S_h\Big[(\boldsymbol{v}^h, q^h), (\boldsymbol{u}^h, p^h)\Big] = j_{GP}(\boldsymbol{v}^h, \boldsymbol{u}^h) + j_p(q^h, p^h) + j_{stream}(\boldsymbol{v}^h, \boldsymbol{u}^h) + j_{div}(\boldsymbol{v}^h, \boldsymbol{u}^h). \tag{2}$$

The different terms of S_h are discussed below. For the penalty term in line three of (1), the stabilization parameter is given as

$$\gamma_u = \max\left(\gamma_\nu, \gamma_{conv}, 1.0\right) = \max\left(\alpha_\nu\frac{\nu}{h_K}, |\boldsymbol{u}^h\cdot\boldsymbol{n}^f|, 1.0\right). \tag{3}$$

Weak imposition of boundary conditions and viscous ghost penalties

Since the mesh is not fitted to the domain, boundary and coupling conditions are imposed weakly using a stabilized Nitsche-type approach [3]. In case of arbitrary cut fluid elements stability and the control of non-physical degrees of freedom outside the physical fluid domain are crucial. To retain accuracy in imposing boundary conditions a recently developed viscous Ghost Penalty stabilization operator $j_{GP}(\boldsymbol{v}^h, \boldsymbol{u}^h)$ is used, see [3]. This operator, evaluated along faces in the interface zone, balances missing coercivity on cut elements when using a uniform scaling $\gamma_\nu = \alpha_\nu\frac{\nu}{h_K}$ for the penalty term in the symmetric Nitsche method independent of the interface location.

In order to account for instabilites at the interface Γ due to the nonlinear convective term in case of inflow boundaries, we add the second part in γ_u with $\gamma_{conv} = |\boldsymbol{u}^h\cdot\boldsymbol{n}^f|$ and an additional penalty factor for a uniform enforcement of the boundary condition $(\boldsymbol{u}^h - \bar{\boldsymbol{u}})$, see results.

Face-oriented fluid stabilizations for viscous and convection dominated flows

In order to account for the inf-sup-instability when using equal order ansatz function for velocity and pressure, we apply a symmetric pressure-stabilizing term from [4]

$$j_p(q^h, p^h) = \sum_{f\in\mathcal{F}}\int\limits_{\substack{F\supseteq f\\ F\in\mathcal{F}_\mathcal{T}}} \alpha_p h_F^2\cdot\left(1 + \frac{\nu}{h_F}\right)^{-1}\rho^{-1}\cdot\Big[\!\Big[\operatorname{Grad} q^h\Big]\!\Big]\Big[\!\Big[\operatorname{Grad} p^h\Big]\!\Big]\,\mathrm{ds}. \tag{4}$$

In contrast to [3], we account for viscous and convection dominated flows like in [4].
Convective instabilities are stabilized using a velocity-gradient-jump based operator from [4]

$$j_{stream}(\boldsymbol{v}^h, \boldsymbol{u}^h) = \sum_{f\in\mathcal{F}}\int\limits_{\substack{F\supseteq f\\ F\in\mathcal{F}_\mathcal{T}}} \alpha_{stream} h_F^2\rho\cdot|\boldsymbol{u}^h\cdot\boldsymbol{n}^F|\Big[\!\Big[\operatorname{Grad}\boldsymbol{v}^h\Big]\!\Big] : \Big[\!\Big[\operatorname{Grad}\boldsymbol{u}^h\Big]\!\Big]\,\mathrm{ds}. \tag{5}$$

In a similar way as for the viscous ghost penalty operator $j_{GP}(\boldsymbol{v}^h, \boldsymbol{u}^h)$, we evaluate the proposed pressure and streamline stabilization operators in a classical way as interior penalties along all inner edges, but also as ghost penalties in the interface zone which is done by intergrating these terms along the cut faces entirely. Evaluating these terms along the cut faces gives control over the pressure and velocity ghost degrees of freedom in the viscous and the convection dominated regime. Moreover, these terms improve the system conditioning in all flow regimes.

Numerical Results

Optimal convergence properties for viscous and convection dominated flows

A 2D-Kim-Moin flow shows optimal error convergence for domain and interface errors. For viscous dominated flows with $\nu = 0.1$, a clear improvement of the viscous and pressure fluxes is obtained. As can be seen in Figure 1a and 1b, due to the viscous ghost penalty operator and the pressure ghost penalties the sensitivity of the interface errors with respect to the interface position is clearly reduced, whereas optimal convergence is retained for the discrete interface and bulk norms. For convection dominated flows with $\nu = 0.0001$, the importance of the different contributions in the penalty term for γ_u, especially for the enforcement of the boundary condition, is highlighted in Figure 1c. A more detailed discussion of the results is given in [1].

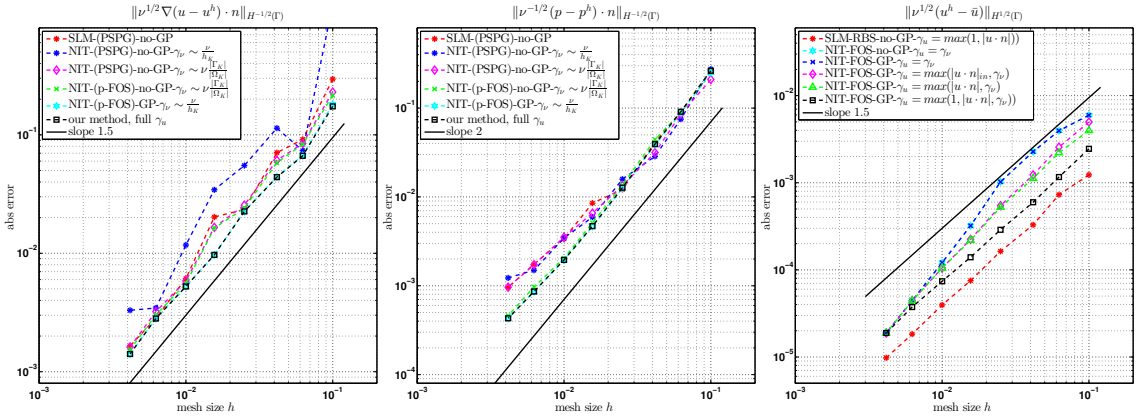

Figure 1: Kim-Moin-flow: spatial error convergence versus element length h, viscous and pressure flux error with $\nu = 0.1$ and boundary condition error with $\nu = 0.0001$ at time $T = 0.1\,s$ with $\Delta t = 0.01\,s$, our method (dashed black line with square markers).

Stability and control over ghost values

In Figure 2, the effect of the different $\boldsymbol{u}$ and p fluid stabilizations in the interface zone is depicted. A comparison of the proposed method with methods using residual-based fluid stabilizations without ghost-penalty terms in the interface zone shows the lack of stability and the loss of control over the ghost values.

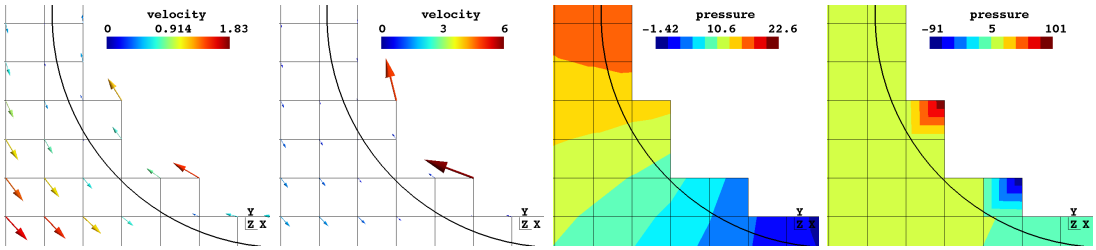

Figure 2: Flow around a cylinder: $\boldsymbol{u}$ and p values around a cylinder. From left to right: $\boldsymbol{u}$ with and without ghost-penalty stabilizations, p with and without ghost-penalty stabilizations.

Moving interfaces and fixed-grid partitioned fluid-structure interaction

In Figure 3, the large movement of a rigid cylinder in a channel at a Reynold's number of $RE = 300$ is shown. This example shows the capability of a semi-Lagrangean time-integration

scheme [2] and the robustness of the proposed fluid-formulation over time for problems involving moving domains.

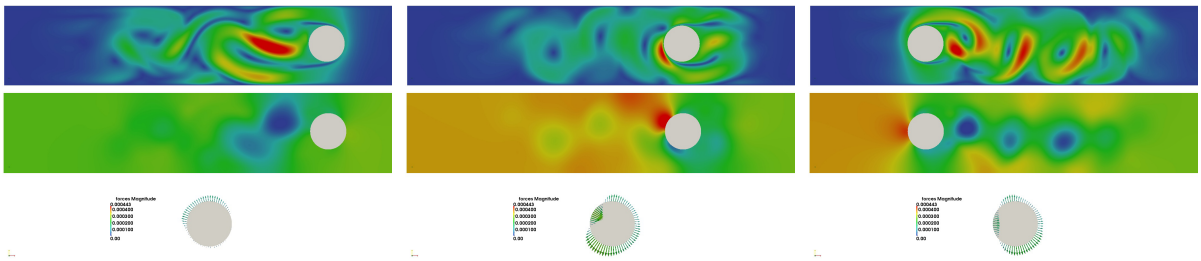

Figure 3: Moving interfaces: moving cylinder at $RE = 300$, velocity, pressure and interface forces at different t.

In Figure 4, the results of a partitioned fluid-structure interaction simulation for the flow over a bending flexible wall are shown.

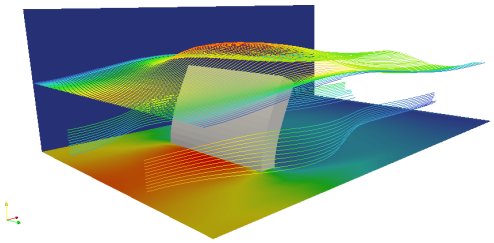

Figure 4: Fluid-structure interaction: flow over a bending flexible wall.

Conclusion

The proposed fictitious domain method for 3D incompressible Navier-Stokes equations using cut elements is stable and shows optimal convergence results in bulk and at the interface for all considered discrete norms. The system conditioning is improved due to the different ghost-penalty stabilizations for viscous and convection dominated flows. Results obtained with a partitioned fluid-structure interaction approach using the stabilized fixed-grid fluid formulation shows the applicability of our method to complex large deformation fluid-structure interaction problems.

References

[1] B. Schott and W.A. Wall. A new face-oriented stabilized XFEM approach for 3D incompressible Navier-Stokes equations. *Submitted for publication in Comp. Meth. Appl. Mech. Engng.*, 2013.

[2] F. Henke, M. Winklmaier, W.A. Wall and V. Gravemeier. A semi-Lagrangean time-integration approach for extended finite element methods. *Submitted for publication in Int. J. Numer. Meth. Engng.*, 2013.

[3] E. Burman and P. Hansbo. Fictitious domain methods using cut elements: III. A stabilized Nitsche method for Stokes problem. *School of Engineering, Jönköping University, JTH, Mechanical Engineering*, 2011.

[4] E. Burman, M.A. Fernández and P. Hansbo. Continuous Interior Penalty finite element method for Oseen's equations. *SIAM J. Numer. Anal.*, 44(3):1248–1274, 2006.

Proceedings of the 26th Nordic Seminar on Computational Mechanics
A. Logg, K.A. Mardal, A. Massing (Eds.)

Influence of the jet location in supersonic crossflow disposed in a C-D duct

Bernhard Semlitsch[1], Mihai Mihaescu[1], and Laszlo Fuchs[1]

(1) *Linné FLOW Center*, Department of Mechanics, Osquars Backe 18, 10044 Stockholm, Sweden, bernhard@mech.kth.se, mihai@mech.kth.se, lf@mech.kth.se

Summary. The influence of shear-layer jet interaction on the flow structure generation with multiple jets in supersonic crossflow is investigated by Large Eddy Simulations (LES). A duct geometry is investigated, where the supersonic crossflow evolves in a rather sharp transition between the straight convergent and divergent section and therefore shocks establish. The jet origin location in the divergent section of the duct relative to the narrowest cross-section is significant for the shock pattern structure and the interaction point between the established separation bubble and the jets. The interaction of the separation bubble and the jets plays an important role for the flow structure generation by the jets.

Key words: multiple jets in crossflow, performance optimization, shock-pattern, compressible flow

Introduction

Jet in crossflow occurs in many engineering applications and thus, the phenomenon has been investigated by many researchers. Predominantly, a single jet in crossflow was considered and the generation of coherent flow structures, the stability of the jet, the heat transport with the jet, and mixing process were investigated. Also, the shock pattern formation and the mixing with jet in supersonic crossflow has been analyzed [1]. The occurrence of certain flow structures is described most commonly by the ratio $\mathcal{R}$ of the jet momentum to the crossflow momentum quantifying the operation regime of the jet in crossflow,

$$\mathcal{R}^2 = \left(\frac{\rho_j U_j^2}{\rho_{cf} U_{cf}^2} \right) , \tag{1}$$

where ρ is the density of the fluid and U the velocity. The subscript j refers to the jet quantities, where the subscript cf refers to the crossflow quantities.

However, only a small number of investigators address the effect to the flow structures with two or more jets in crossflow, as e.g. [2]. In this work, the flow structure generation with multiple jets in supersonic crossflow is investigated, where the jets are closely placed such that a slight interaction between the jets is possible. LES simulations have been performed to analyze the impact of shifting the jet location in the divergent section of a convergent-divergent duct.

Case setup and numerical simulation approach

Figure 1 shows the considered geometry, which consists of a cylindrical duct with a convergent-divergent section and guides the flow into a stationary environment at ambient conditions. At the duct inlet, the flow is pressurized to a total pressure of four times the ambient pressure and

the incoming stream has been heated up to a total temperature T_0 of 367 K. The convergent-divergent section can be characterized by the duct exit diameter D_e of 57.5 mm and the area ratio of 1.23.

In the divergent duct section, twelve cylindrical pipes with the diameter D_j of 2.67 mm are disposed equidistantly on the circumference, which are 60° inclined towards the flow direction. The total temperature applied at the pipe inlets is the ambient temperature. The exit of the jet pipes are placed at $-0.857D_e$ (*Case 1*) and $-0.768D_e$ (*Case 2*) duct exit diameters (D_e) upstream from the duct exit. The flow momentum in the pipe has been varied as investigation parameter.

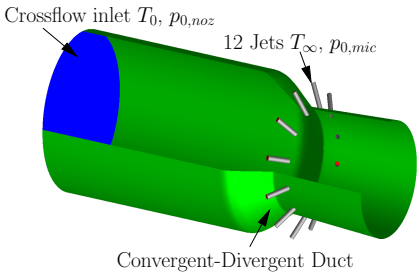

parameter	symbol	value	unit
duct exit diameter	D_e	57.5	mm
injectors diameter	D_j	2.67	mm
area ratio	$A_e/A^\star$	1.23	(-)
duct design Mach-number	$\overline{M_e}$	1.56	(-)
duct pressure ratio	$p_{0,noz}/p_\infty$	4	(-)
duct inlet temperature	T_0	367	K
ambient pressure	p_∞	101,325	Pa
ambient temperature	T_∞	288.15	K

Figure 1. The geometry of the C-D duct with the disposed pipes is shown and the characteristic parameters are listed.

The three-dimensional Navier-Stokes equations together with the conservation equations for continuity and energy are simulated using a finite-volume based solver. The flowing media is air and therefore the ideal gas law has been chosen as the equation of state, where the ratio of the specific heats is 1.4. The temperature dependence of viscosity was modeled using the Sutherland's formula.

For time integration, a low-storage four-stage Runge-Kutta scheme has been applied with a constant time-step of $1 \cdot 10^{-8}$ s. A second order central difference scheme was used for discretization of the convective terms and a Jameson-type artificial dissipation was added to prevent from spurious numerical oscillations near sharp gradients in the flow, such as e.g. shocks.

Adiabatic no-slip boundary conditions have been employed at the walls. Characteristic boundary conditions at the inlets and the outlets have been implemented. Block-structured grids with 44 million hexahedral cells have been used for this investigation. Mesh refinement towards the walls has been applied to resolve the wall-boundary as accurate as possible. Despite the large Reynolds-number flow, a substantial range of the turbulent energy decay is captured by the numerical grid. Only a small proportion of the dissipative flow scales has not been resolved. These flow scales can be modeled by a sub-grid scale model. Thus, Large Eddy Simulation is performed.

Results

At the narrowest cross-section of the duct an expansion fan manifests, which leads to the development of a separation bubble right downstream of the expansion fan, see also Fig. 2. The shape formation of the separation bubble shape is highly influenced by the position of the pipes guiding the jets into the crossflow. Figure 2 illustrates a rather short separation bubble for Case 1, where the induced shear-layer impinges the exhausting jet. With the downstream shift of the jet exit the separation bubble is elongated until it interacts with the jet pipes or the jets coming from the pipes. High vorticity is induced with the expansion fan and with the formation of the separation bubble at the narrowest cross-section. As visible in Fig. 3(a), the vortical structures shading from the separation bubble interact closely with Case 1, while for the Case 2 (Fig. 3(b))

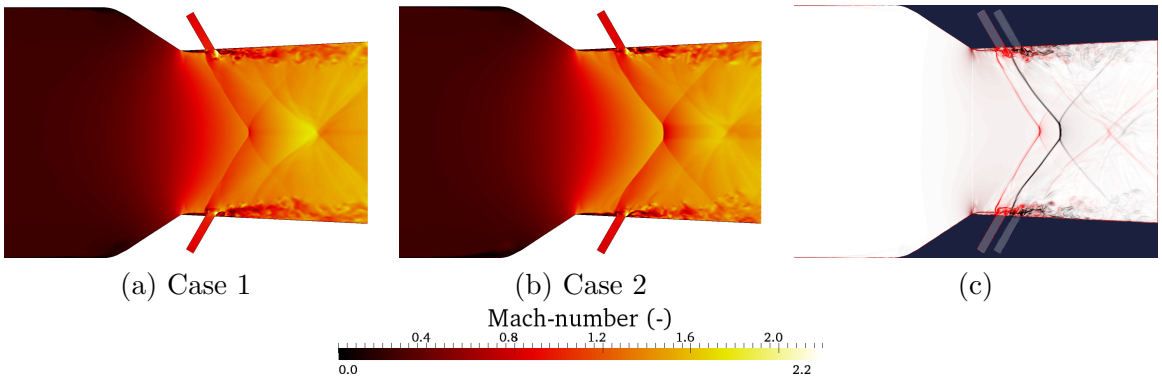

(a) Case 1 (b) Case 2 (c)

Figure 2. The contours of the Mach-number are shown in a mid-plane view for an $\mathcal{R}^2$ of 1.18, with the jets at the upstream location (a) and with jets at the downstream location (b). At rightmost (c), overlapping numerical Schlieren of the two cases is shown, where the red contours correspond to Case 1 and the black contours to Case 2.

the strength of the vortical structures decays and rather longitudinal structures are generated before interaction with the jet. It can also be seen that with Case 2 spatial high vortical structures are shade downstream and cause shock root movement in the immediate region to the jet.

For all simulated cases of $\mathcal{R}^2$, a shock root establishes of the separation bubble and the resulting oblique shock arises. For $\mathcal{R}^2 < 1.5$, the oblique shocks merge in the center of the duct, in form of a regular or irregular (Mach) shock reflection, as shown in Fig. 2(a-b). The Mach-disk provokes a slip-line, which is appeared far downstream in the flow field. With increasing $\mathcal{R}^2$, the initial oblique shock $\mathcal{R}^2 = 0$ originating from the separation bubble begins to steepen. Figure 2(a-b) illustrates that after a certain achieved steepness of the upstream shock pattern, the shock reflection is not reflected back from the nozzle walls or the jets and thus, this shock pattern is not apparent in the downstream shock train.

Generally, the occurring shock train exhibits similarities for equal $\mathcal{R}^2$ at the two jet locations, as visible in Fig. 2(c). However, the shock-patters is slightly shifted with the jet location and Case 1 is more sensitive and faster in responding to changes of $\mathcal{R}^2$. Furthermore, the strength of the shocks is distinguished. The upstream located shock is significantly stronger when the jet location is placed downstream and the downstream located shock pattern becomes weaker.

For Case 1, the upstream shock merges either in a regular reflection or a Mach reflection

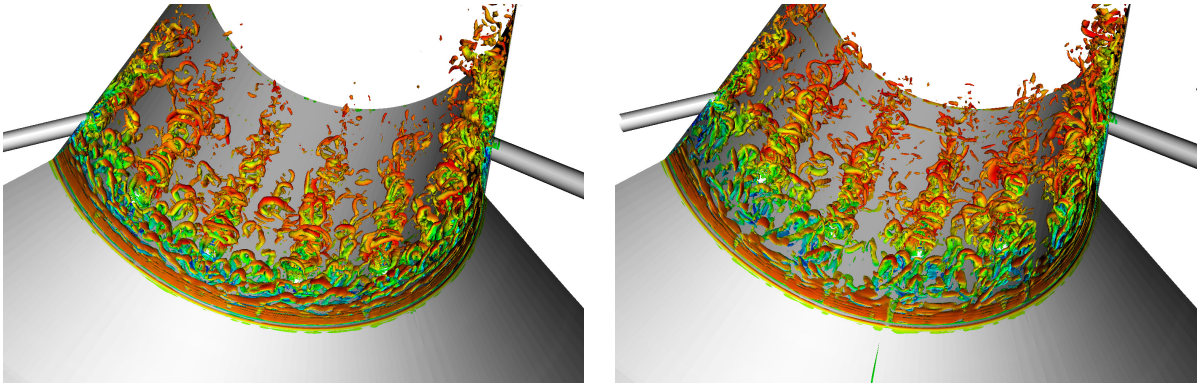

(a) Case 1 (b) Case 2

Figure 3. Looking from inside of the nozzle towards the nozzle exit: the vortical structures are visualized by the λ_2 criteria for an $\mathcal{R}^2$ of 1.18 and colored by the stream-wise velocity for the cases of the jets placed close to the nearest cross-section of the duct (a) and further downstream (b).

provoking a rather small Mach-disk. Contrary, with Case 2, a rather wide Mach-disk from the upstream shock pattern could be observed for all simulated cases and an apparent slip line is visible. As visible in Fig. 2(b), the generated slip line causes a decrease in the shock-strength for the downstream shock pattern by reflecting the incident shocks partially. Moreover, a rather diffuse wave pattern is visible and no clear shocks are discernible.

The increased shock strength of the upstream shock with Case 2 increases the losses in the duct. However, the diffusivity of the second downstream shock pattern is likely to be indicated in the further shock train, since the following downstream shocks are as well diffuse and do not form a clear shock diamond pattern.

Conclusions

The effect of displacing the jet location in the divergent section of a supersonic convergent-divergent duct has been investigated by simulating the governing equations for compressible flow. The ratio of jet momentum to crossflow momentum has been varied to explore the influence ability of the evolving shock-pattern in the divergent duct. The obtained flow-fields for the two jet locations have been compared to each other.

It has been shown that delaying the jet locations further downstream has a significant impact onto the shape of the separation bubble. The location of the jet pipes for Case 1 was placed such that the strong shear-layer induced at the sharp transition between the C-D duct sections interacts closely with the jets. Case 2 permits the shading of the generated vortices in the shear-layer before the interactions. This influences the dynamics and the generated flow frequencies in the flow.

The original shock pattern at $\mathcal{R}^2 = 0$ starts steepening with increasing $\mathcal{R}^2$, while a second downstream located shock pattern occurs. For high values of $\mathcal{R}^2 > 1.5$, the steepened shock reduces to a bow shock in front of the jet and the downstream located shock pattern preserves. The shock train generated with Case 1 reacts more sensitive to changes of $\mathcal{R}^2$ and the upstream shock exhibits only a very narrow Mach-disk or a regular reflection.

With jets emerging at Case 2, the shock train is also shifted downstream and the upstream shock is stronger than for Case 1. Furthermore, the shock pattern provoked with Case 1 causes in all investigated cases a Mach-disk, which induces a slip-line. Due to the stronger shock the slip line is stronger and causes in several cases partial shock reflections, such that the second downstream shock-pattern is very diffuse or does not clearly arise. Thus, the clear shock train does not develop with Case 2 at certain $\mathcal{R}^2$.

Acknowledgment

This work was supported by the Swedish National Infrastructure for Computing (SNIC 2013-11-19) via PDC.

References

[1] Kawai S., and Lele K. S., Large-Eddy Simulation of Jet Mixing in Supersonic Crossflows. *AIAA Journal*, 48(9): 2063-2083, 2010.

[2] Gutmark J. E., Ibrahim M. I., and Murugappan S., Dynamics of single and twin circular jets in cross flow. *Experiments in Fluids*, 50(3): 653-663, 2011.

Proceedings of the 26th Nordic Seminar on Computational Mechanics
A. Logg, K.A. Mardal, A. Massing (Eds.)

Transitions in the boundary layer under a solitary wave: Avoiding wrong conclusions by direct numerical simulation

Joris C.G. Verschaeve[1], Geir K. Pedersen[2]

(1)Norwegian Geotechnical Institute, Po.Box 3930, Ullevål Stadion, 0806 Oslo, Norway
(2)University of Oslo, Po.Box 1072 Blindern, 0316 Oslo, Norway

Summary. In the present discussion we focus on the prediction of transitions in the boundary layer under a solitary wave. In particular we compare results obtained by model equations of linear stability to results obtained by direct numerical simulation. These are then related to results published in literature.

Key words: Orr-Sommerfeld, Parabolic Stability Equation, Spectral Element Navier Stokes solver, NEK5000, critical Reynolds number, boundary layer flow, solitary wave, amplification, perturbation, Tollmien-Schlichting waves

Introduction

The boundary layer flow under a solitary wave has received considerable attention since Liu *et al.* [6] published approximate formulae for this problem in 2007. In the following the transition of this flow has been investigated by multiple methods. Vittori and Blondeaux investigated the transitions to turbulence numerically by direct numerical simulation in 2008 [9, 10] and by RANS simulation in 2011 [3]. Later on, a linear stability analysis of this flow was published in 2012 [2]. An experimental investigation on the transitions in this flow was performed in 2010 by Sumer *et al.* [7]. A common denominator of the above investigations is the determination of a critical Reynolds number beyond which the flow undergoes transition. This Reynolds number has been determined by Vittori and Blondeaux to be 5×10^5 [9, 10], whereas Sumer *et al.* found 2×10^5 for their experiments. A value in between these figures has been found for the RANS simulations [3].
In the present discussion we solve the non-linear boundary layer equations numerically and performe a linear stability analysis by means of the Orr-Sommerfeld equation and the parabolic stability equation [1]. A direct numerical simulation using the spectral element Navier-Stokes solver `NEK5000` [5] was used to verify the present findings. The major result is that the concept of a critical Reynolds number does not apply to this type of flow, instead the flow is always unstable in the sense of linear stability [4]. The stability properties of the flow are characterized by the growth rate of the perturbations, which can be measured by the amplification of the perturbations.

Description of the problem

The inviscid free stream flow of a solitary wave can accurately be computed by the method of Tanaka [8]. We use a Chebyshev colocation method to solve the boundary layer equations which gives us the base flow used for a linear stability analysis. An example of the boundary layer flow under a solitary wave is given in figure 1. Since the flow is steady in the frame of reference of

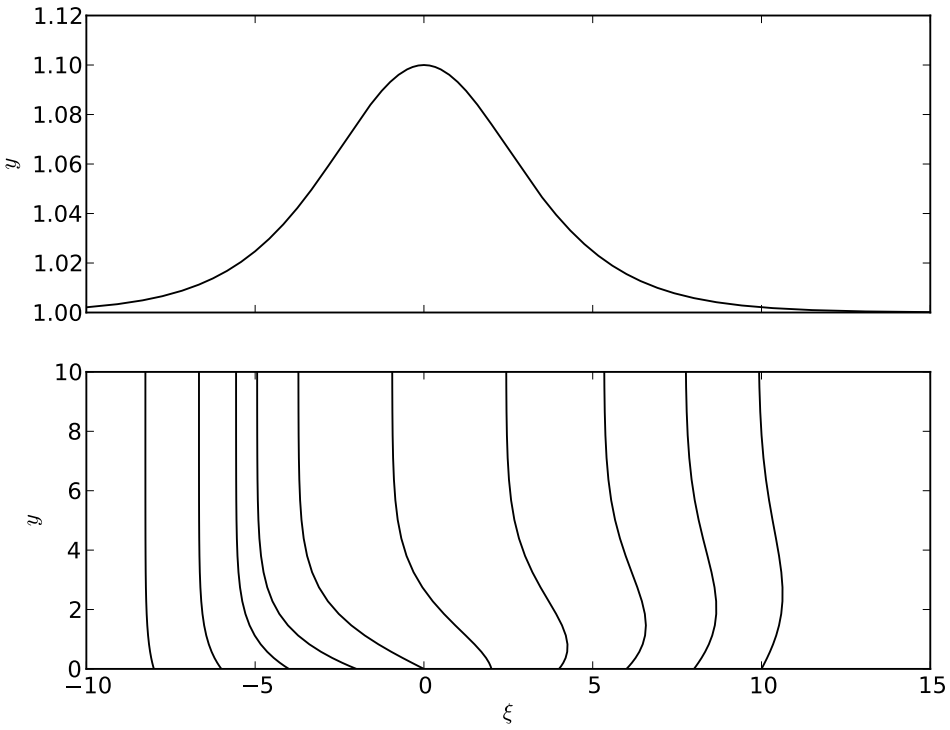

Figure 1. Top: Elevation of a solitary wave. Bottom: Profiles of the horizontal velocity in the boundary layer under a solitary wave.

the moving solitary wave, a classical stability analysis by means of the Orr-Sommerfeld equation and the parabolic stability equation [1] can be performed.

Results

Using the model equations we computed stability domains for this type of flow, cf. figure 2. The size of the unstable regions depends on the amplitude ϵ of the solitary wave and the viscosity which can be characterized by a dimensionless parameter δ corresponding to the inverse of the Reynolds number, cf. definition in [9]. The bigger the amplitude ϵ of the wave and the smaller δ, the bigger the unstable region. Once a Tollmien-Schlichting wave reaches the neutral curve it starts to grow and may destabilize the flow. The growth of the Tollmien-Schlichting wave can be characterized by its amplification. In figure 3, we plotted the amplification of the critical Tollmien-Schlichting waves for $\delta = 8 \times 10^{-4}$. As can be observed from this figure, the amplification is bigger for increasing ϵ. The question when instabilities are observable is thus linked to the initial amplitude of the perturbation. If the initial amplitude is too small a perturbation might not grow sufficiently to have a visible effect on the flow.
Direct numerical simulation of the growth of these Tollmien-Schlichting waves reproduced these amplifications remarkebly well.

Conclusions

If the initial perturbation as in the references above is uncontrolled, the flow might appear unstable at different Reynolds numbers. Strict control of the initial perturbation is necessary for repeatability of the problem for both numerical simulations and experiments.

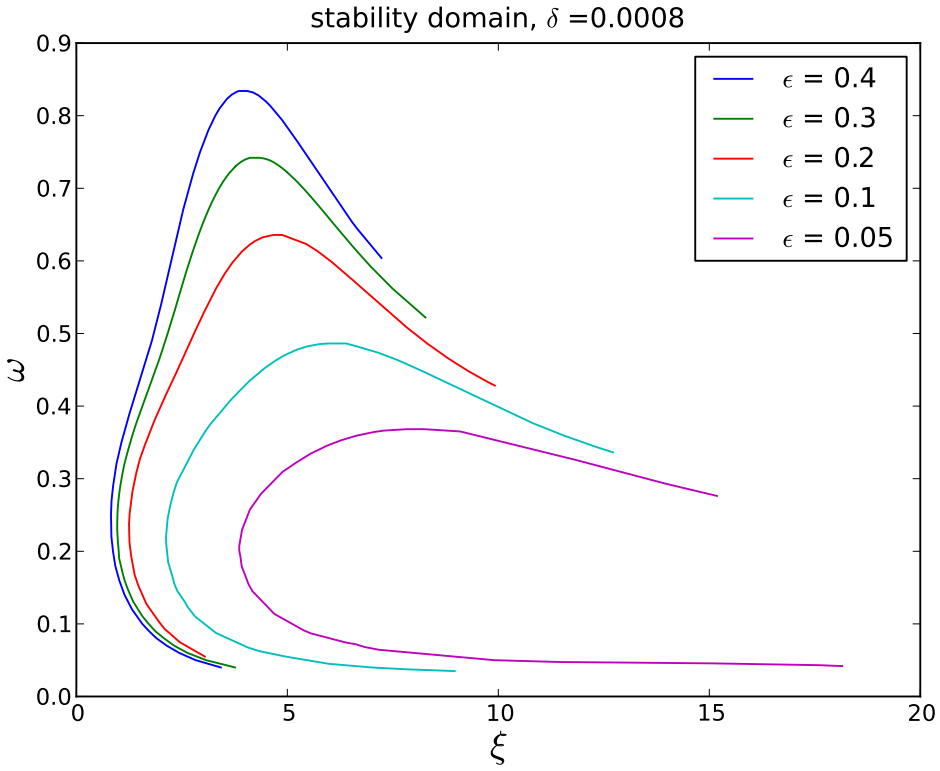

Figure 2. Stability domain for the boundary layer flow under a solitary wave for different amplitudes ϵ and $\delta = 8 \times 10^{-4}$.

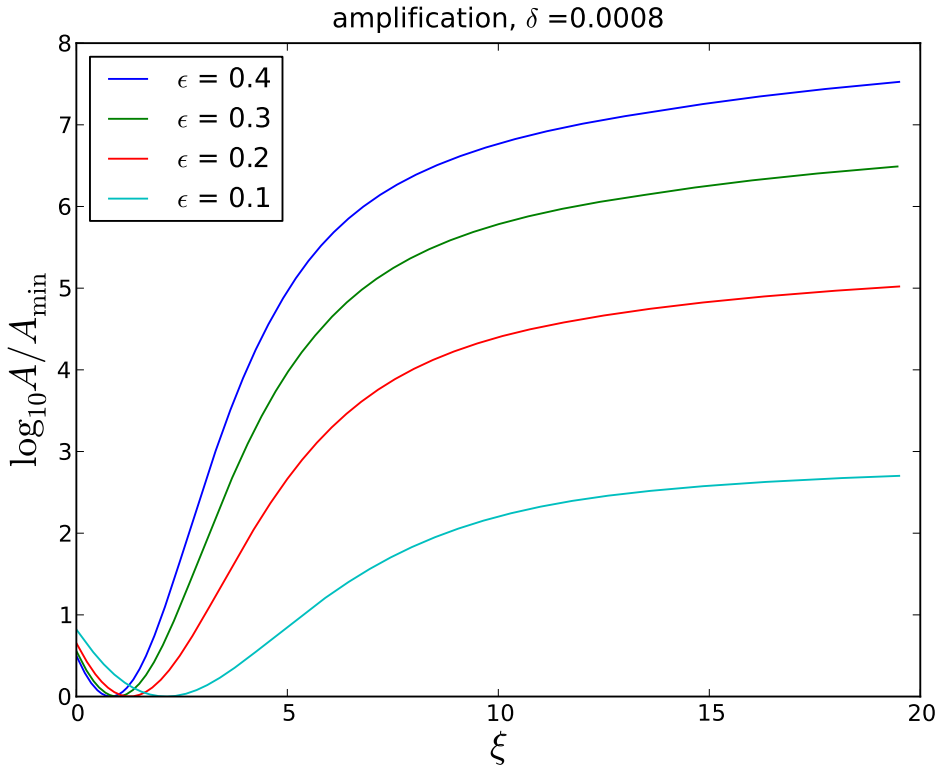

Figure 3. Amplification of the critical Tollmien-Schlichting wave for different amplitudes ϵ and $\delta = 8 \times 10^{-4}$.

References

[1] F. Bertolotti, T. Herbert, and P. Spalart. Linear and nonlinear stability of the Blasius boundary layer. *Journal of Fluid Mechanics*, 242:441–474, 1992.

[2] P. Blondeaux, J. Pralits, and G. Vittori. Transition to turbulence at the bottom of a solitary wave. *Journal of Fluid Mechanics*, 709:396–407, 2012.

[3] P. Blondeaux and G. Vittori. Rans modelling of the turbulent boundary layer under a solitary wave. *Coastal Engineering*, 60:1–10, 2012.

[4] P. G. Drazin and W. H. Reid. *Hydrodynamic Stability*. Cambridge University Press, 1981.

[5] P. F. Fischer, J. W. Lottes, and S. G. Kerkemeier. Nek5000 Web page, 2008. http://nek5000.mcs.anl.gov.

[6] P. L.-F. Liu, Y. S. Park, and E. A. Cowen. Boundary layer flow and bed shear stress under a solitary wave. *Journal of Fluid Mechanics*, 574:449–463, 2007.

[7] B. M. Sumer, P. M. Jensen, L. B. Sørensen, J. Fredsøe, P. L.-F. Liu, and S. Carstensen. Coherent structures in wave boundary layers. part 2. solitary motion. *Journal of Fluid Mechanics*, 646:207–231, 2010.

[8] M. Tanaka. The stability of solitary waves. *Physics of Fluids*, 29:650–655, 1986.

[9] G. Vittori and P. Blondeaux. Turbulent boundary layer under a solitary wave. *Journal of Fluid Mechanics*, 615:433–443, 2008.

[10] G. Vittori and P. Blondeaux. Characteristics of the boundary layer at the bottom of a solitary wave. *Coastal Engineering*, 58:206–213, 2011.

Proceedings of the 26th Nordic Seminar on Computational Mechanics
A. Logg, K.A. Mardal, A. Massing (Eds.)

Vibration reduction in soil by addition of surface masses

Vedad Alic[1] and Kent Persson[1]

[(1)]Division of Structural Mechanics, Lund University, Box 118, 221 00 Lund, Sweden,
vedad.alic@construction.lth.se

Summary. The possibilites of vibration mitigation by placing masses in between an external source (road) and a very sensitive high tech facility are investigated. FE models of the soil are developed and guyan reduction is employed to all degrees of freedom below the surface in order to increase efficiency. Steady-state analyses are performed in the frequency range 5-30Hz. Results from the two-dimensional studies showed that masses can be used as a method of mitigating vibrations, although they have to be very heavy. Three-dimensional simulations showed that by varying the organization of the masses great vibration reduction as well as amplification was obtained, however, by using discrete masses improvements were always obtained.

Key words: vibration reduction, surface masses, guyan reduction, soil dynamics

Introduction

MAX-lab (Mictrotron Accelerator for X-rays) is a national laboratory in Lund, which is operated jointly by the Swedish Research Council (VR) and Lund University. Currently the project consists of three storage rings, MAX I-III, and a fourth being built, MAX-IV. [1]

MAX-IV will be a new facility, consisting of an electron pre-accelerator, a 250 meter long linac, and two storage rings with 96 and 528 meters circumference. The larger storage ring will be able of a 3-GeV energy level with low emittance for the production of soft and hard x-rays as well as an expansion into the free electron laser field. The facility will be located northeast of Lund, at the outskirt of a new area, Lund North-East roughly 100 meters south-east of the highway E-22. The instruments that are operating on nano-level scale at MAX-IV are extremely sensitive to vibrations (vertical displacements limit of 26nm RMS during one second for frequencies above 5Hz and below 100Hz). With the facility located closely to the highway and on top of very soft soil measures have been taken to ensure good operation of the facility. The measures include stabilization of the soil underneath the facility (stiffening), and the shaping of the ground around the facility in a way that will reduce vibrations.

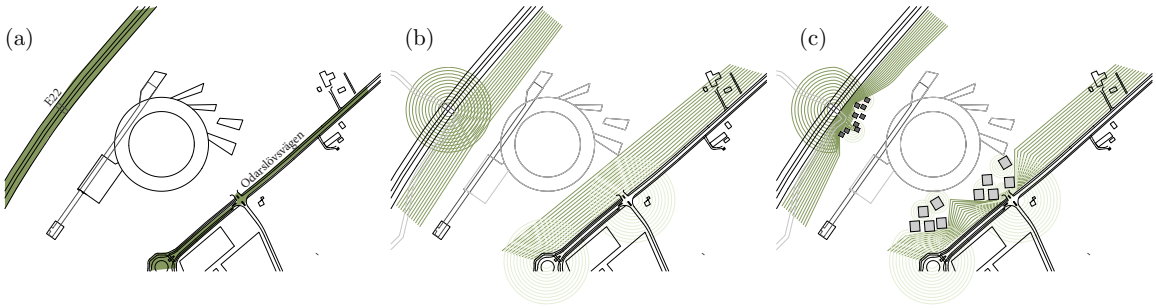

Figure 1. Research idea: (a) roads close to facility (b) vibrations from roads (c) reduced by masses?

This research investigates another method for vibration reduction: placing out heavy masses on the soil surface between the external sources and the facility, see Figure 1(c). The method could be seen as a cost effective and maintenance free solution. As such, it is of interest to find out if it is a possible method of vibration mitigation, and which configurations are most effective. The masses could be parts of buildings, or if smaller, they could be artificial concrete blocks or natural stones. If care is taken with the design they would not only serve as vibration reducers but could also enhance the aesthetic qualities of the site.

Resonant mass scatterers

Most energy from traffic vibrations is normally in the frequency range of 5-50Hz. The principle of operation for resonant mass scatterers (heavy masses on the ground) is based on the fact that any topographic irregularities on the surface cause scattering of incident Rayleigh waves. For masses on the ground the scattering is particularly strong around the natural frequencies of the masses resting on the ground, and as such they have been considered as a viable method of vibration mitigation both theoretically [2], and numerically [3] [4]. Petyt and Jones [4] consider an evaluation point 25 meters from the load, in between which they place different sets of heavy masses and come to the conclusion that in general a heavy mass close to the load works best for their situation. Krylov [2] shows (for a 2D model) analytically that only 10% of the incoming wave energy is transmitted past a lumped mass around its resonant frequency, the rest of it is either reflected back or propagated as body waves trough the half-space medium. The solution should be taken as a very rough estimate as it does not take into account the mass moment of inertia, and models a *mass - elastic half-space medium* interaction, while for the ground at MAX-IV several sub-surface layers need to be accounted for.

Numerical model and mass topology

The work has been carried out using finite element analysis in two (axisymmetric), and three dimensions. Steady state models in the frequency range 5-30Hz have been established with main evaluation points along a line 100 meters from the load application point, with masses placed in between (green area in Figure 2).

Soil as a material is generally treated as highly non-linear and inhomogeneous, however, with the present low magnitude loading and large wavelengths in comparison to grain size the soil is modelled as a homogeneous linear visco-elastic material, as is the bedrock. Table 1 lists the material properties of the upper and lower soil layers and of the bedrock layer. Loss factor includes all attenuation effects (e.g. varying topology of the soil and bedrock).

The finite element software ABAQUS was used for the axisymmetric simulations, while for the 3D simulations stiffness, mass, and damping matrices were exported from ABAQUS

Table 1. Soil and bedrock viscoelastic properties by loss factor.

-	Upper clay	Lower clay	Bedrock
Depth [m]	2	12	-
E [MPa]	215	1136	8800
ν	0.48	0.48	0.40
ρ [Kg/m^3]	2125	2125	2600
loss factor [%]	14	14	4
c_S [m/s]	185	425	1100
c_P [m/s]	943	2167	2694

into MATLAB in order to perform model reductions. The axisymmetric model consisted of 135000 degrees of freedom, of which most belonged to axisymmetryic elements with quadratic approximation and reduced integration, and a lesser part that belonged to infinite elements that were applied to the boundaries in order to avoid reflections. The 3D model used brick elements with quadratic approximation and reduced integration, and infinite elements along the boundary. In order for the 3D model to give accurate results for a steady state analysis in the frequency range of 5-30Hz, a rather fine mesh was used which resulted in 2 620 860 complex-number degrees of freedom.

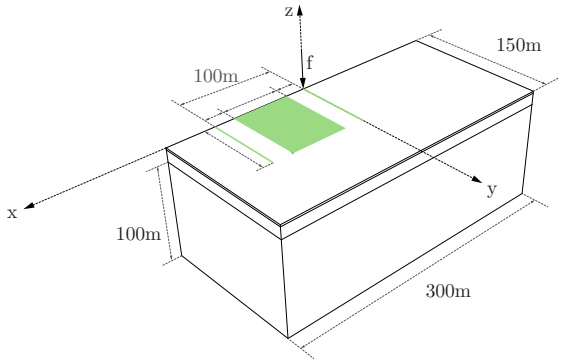

Figure 2. 3D model with the parts that were kept in the reduced model marked in green.

Most of the degrees of freedom in the model, see Figure 2, were below surface level and of little interest. In order to reduce computational costs Guyan reduction together with domain decomposition was applied and all degrees of freedom which are not part of the green areas in Figure 2 were removed by static condensation. The reduction method is exact at ω (apart from the approximation in the original dynamic matrices). Performing the reduction for each frequency studied allows for a reduced system with no loss of accuracy. The reduced system is no longer sparse and a large reduction in degrees of freedom is necessary in order for the method to be efficient. The 3D model was reduced to 11 646 degrees of freedom. The reduced 3D model allowed for simulations with a great number of configurations of masses (see Figure 3, where each pixel represents a mass with the size 2x2x2 m^3, and the gray-scale represents the density of each mass).

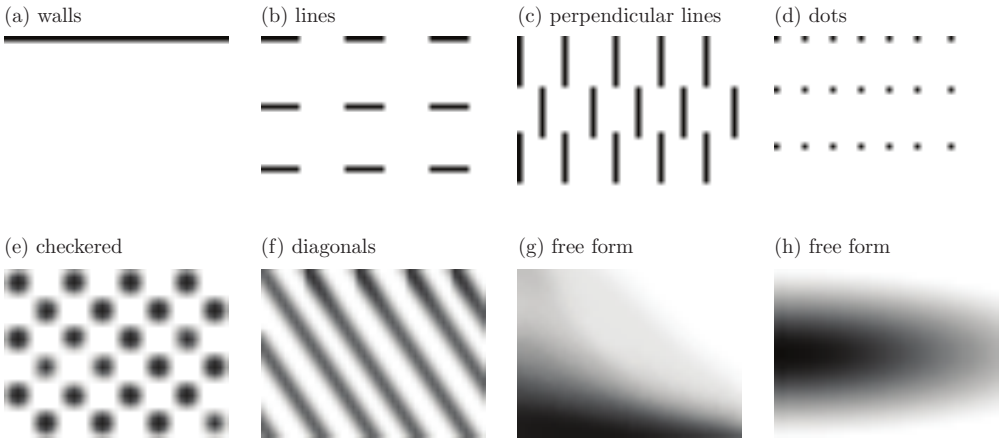

Figure 3. Examples of patterns used in 3D simulations, applied on top of the green area in Figure 2.

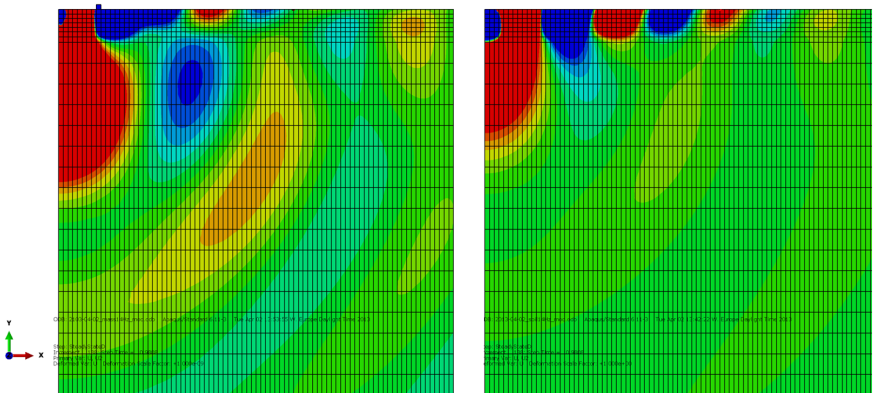

Figure 4. Vertical displacement amplitude of (left) soil model with mass $\rho = 8271\text{kg/m}^3$ and (right) model with no mass, for a prescribed harmonic load with excitation frequency 14Hz and unit amplitude.

Results and conclusions

Two-dimensional results indicate that masses on the ground can be used as a means to mitigate ground vibration, but in order for them to be effective they need to be very heavy. However, due to the nature of being effective around the mass-soil systems resonance frequency they can instead lead to larger vibrations in the soil, if they are excited at frequencies close to their resonant frequencies. Figure 4 shows an increase in vertical displacement amplitudes caused by scattering of incoming waves due to the mass on top of the surface.

With insight from the 2D simulations the 3D simulations attempt to find spatial organizations for masses between vibration source and the facility. Different organizations of masses were assembled on top of the reduced ground model and steady state analysis was performed in the frequency range between 5-29Hz. Three-dimensional results show that locating masses in a careful manner can be effective for vibration mitigation, and by combining masses of different densities reduction in a wider frequency range can be reached. Some conclusions from the research were:

- Masses applied continuously over the whole area can lead to amplification due to lensing (Figure 3 (g), (h)) or acting as wave guides (Figure 3 (f)), however, all *discrete* masses show reductions in vibrations.
- Small masses applied with large spacing are ineffective (Figure 3 (d)).
- Density variation for the different masses is more important than their position.

References

[1] Maxlab, 2013. *MAX-lab* [online] Available at:<https://www.maxlab.lu.se/>[Accessed March 2013]

[2] V. Krylov. Control of traffic-induced ground civrations by placing heavy masses on the ground surface. *Low Frequency Noise, Vibration and Active Control*, 26(4):311-320, 2007.

[3] R. Ford. Inhibiting the transmission of ground-borne vibrations by placing masses on the surface of the ground. *Australian Vibration and Noise Conference 1990: Vibration and Noise-measurement Prediction and Control; Preprints of Papers.* Institution of Engineers, Australia. p. 227, 1990.

[4] D. Jones and M. Petyt. Ground borne vibrations from passing trains: the effect of masses placed on the ground's surface. *ISVR Technical Memorandum*, 1986.

Proceedings of the 26th Nordic Seminar on Computational Mechanics
A. Logg, K.A. Mardal, A. Massing (Eds.)

Model order reduction for dynamic analysis of lightweight building structures

Ola Flodén[1], Kent Persson[1], and Göran Sandberg[1]

[(1)]Department of Construction Sciences, Lund University, Box 118, SE-221 00 Lund, Sweden, ola.floden@construction.lth.se

Summary. This paper presents an investigation of different model order reduction methods applied to models of lightweight building structures, intended to be used in substructure models for vibration analysis of multi-storey buildings. A wide range of methods are implemented and tested for a wooden floor structure by performing both eigenvalue analyses and steady-state analyses.

Key words: model order reduction, finite element modelling, vibration analysis, lightweight building structures

Introduction

In 1994, a century-old ban on the construction of wooden buildings more than two storeys in height in Sweden was lifted, leading to the reintroduction of such buildings. Compared to conventional concrete buildings, it is more difficult to build lightweight structures of wood in such a way that noise and disturbing vibrations in the different storeys and rooms are avoided. Vibrations can be caused by, for example, footsteps, airborne sound, vibrating machines and external sources such as railway and road traffic.

To produce buildings of high performance regarding the hindrance of disturbing vibrations and structure-borne sound, it is desirable to have tools for predicting the effects of structural modifications prior to construction. The objective of this project is to develop numerical prediction tools making use of finite element (FE) models that are valid for general load-cases. Accurately assessing the dynamic behaviour of lightweight structures when rather high vibration frequencies are involved requires use of FE models representing the geometry in considerable detail, resulting in large models, the number of degrees of freedom (dofs) of which easily exceeds the limits of computer capacity. The question arises then of how such models can be reduced in size while at the same time being able to represent the dynamic characteristics of the buildings in question with sufficient accuracy. The method of dividing a large model into components and creating a global model through coupling models of reduced size of each component is referred to as substructuring. In the present study, low-frequency vibrations in multi-storey lightweight buildings are modelled by adopting a substructuring approach.

There are many methods for model order reduction available in the literature, some being implemented in commercial FE software, which enables the methods to be applied to large-scale problems directly. In the analyses presented in this paper, the efficiency of different model order reduction methods, when applied to models of lightweight building structures, were investigated by exporting a model of a wooden floor structure from the FE software Abaqus to the numerical computing environment Matlab, where model order reduction was employed by implementing a wide range of methods. The studies are restricted to frequencies below 200 Hz.

Model order reduction

The dofs in a reduced model can be divided into two categories: physical dofs and generalised coordinates. The physical ones are dofs of the full system that are retained in the reduction process, whereas the generalised coordinates are included to improve the accuracy of the reduced models and has no physical interpretation. The reduction methods can be categorised according to the type of dofs generated in the reduction process, where *condensation methods* involve only physical dofs, *generalised coordinate methods* are based solely on generalised coordinates, and *hybrid reduction methods* employ a combination of dofs of both types. The most frequently employed methods within each category are listed below.

- Condensation methods
  - Guyan reduction [1]
  - Dynamic reduction [2]
  - Improved reduction system (IRS) [3, 4]
  - System equivalent expansion reduction process (SEREP) [5]
- Generalised coordinate methods
  - Modal truncation [6]
  - Component mode synthesis (CMS): Craig–Chang [6, 7]
  - Krylov subspace methods [8, 9]
  - Balanced truncation [8, 10]
- Hybrid methods
  - Component mode synthesis (CMS): Craig–Bampton [6, 11]

When employing substructure modelling, where the reduction is performed for each of the substructures, it is beneficial to retain the physical dofs at the interfaces since this greatly simplifies the coupling of substructures. The generalised coordinate methods are therefore excluded from the analyses. The Krylov subspace method is, however, employed in a modified version, which is similar to CMS by Craig and Bampton and referred to as KCMS. CMS involves the eigenmodes of the model, while KCMS exchanges the eigenmodes for vectors calculated by Krylov subspace iterations. Moreover, modified versions of CMS and KCMS, referred to as improved CMS (ICMS) and improved KCMS (IKCMS) [12], are included in the analyses.

Numerical example

A wide range of reduction methods were compared for a numerical example consisting of a model of a wooden floor structure, the FE mesh being shown in Figure 1. The 2445×4090×242 mm^3 large floor structure consisted primarily of five load-bearing wooden beams, supporting a particle board surface. At the two shorter sides of the floor, beams where placed perpendicular to the load-bearing beams, creating a box-like structure. The mesh of the full model contained 30,807 dofs, while the reduced models contained between 576-626 dofs. The reduced models of the floor structure were investigated in terms of eigenfrequencies and eigenmodes in a free-free state and transmitted vibrations in a steady-state analysis. The reduced models were, in the steady-state analysis, coupled to two wall panels, one on each short side of the floor. A load was applied at one of the panels, the vibration amplitudes being evaluated at the other panel in terms of RMS-values of the displacement amplitudes in all mesh nodes of the panel for each

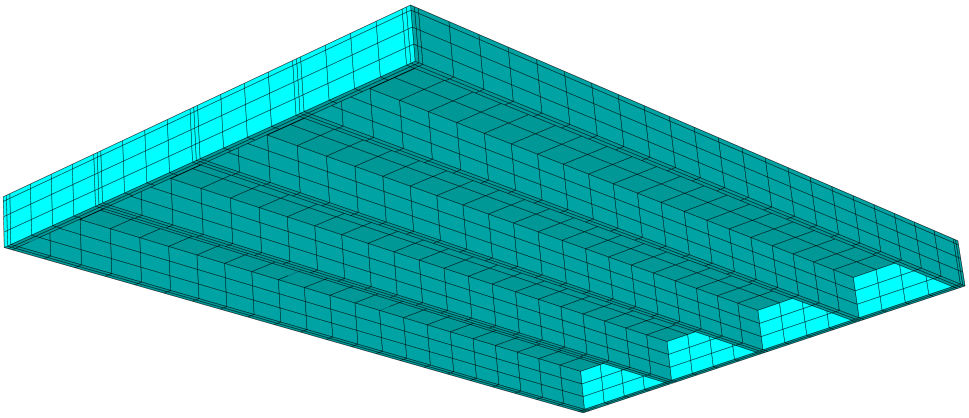

Figure 1. The mesh of the floor structure in the numerical example.

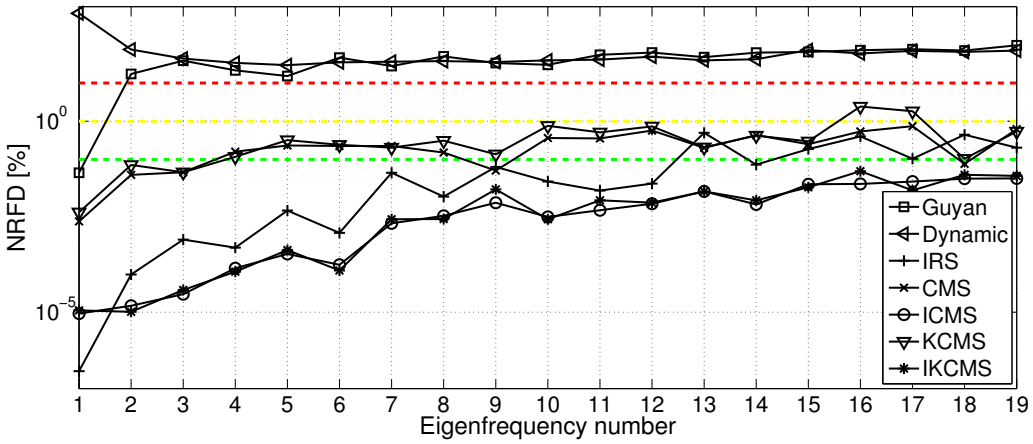

Figure 2. Normalised error in eigenfrequencies obtained for the model order reduction methods applied to the numerical example.

frequency. The normalised errors in eigenfrequencies are shown in Figure 2 and the errors of the RMS-values are shown in Figure 3. The errors in the steady-state analysis has been averaged by sweeping a 20 Hz wide window over the frequency range.

The results show a large difference in accuracy between the different model order reduction methods. Selecting the most appropriate method in a certain situation requires knowledge concerning both the properties of the different methods and specific details of the problem in question. In the numerical example, CMS and KCMS provide reliable results regarding both eigenfrequencies and vibration transmission in the steady-state analysis, CMS being the most frequently employed reduction method among civil and mechanical engineers. KCMS is less common, but offers a comparable accuracy while it is less costly to construct the reduced models, since it does not require an eigenvalue analysis of the full model, as is the case for CMS. An important observation when studying the results in Figure 2 and Figure 3 is that there is no direct correlation between the accuracy in eigenfrequencies and in the steady-state analysis when comparing the different reduction methods. This shows the importance of applying realistic boundary conditions and loads when comparing the reduced models, as is the case in the steady-state analysis, and not only comparing free-free eigenmodes.

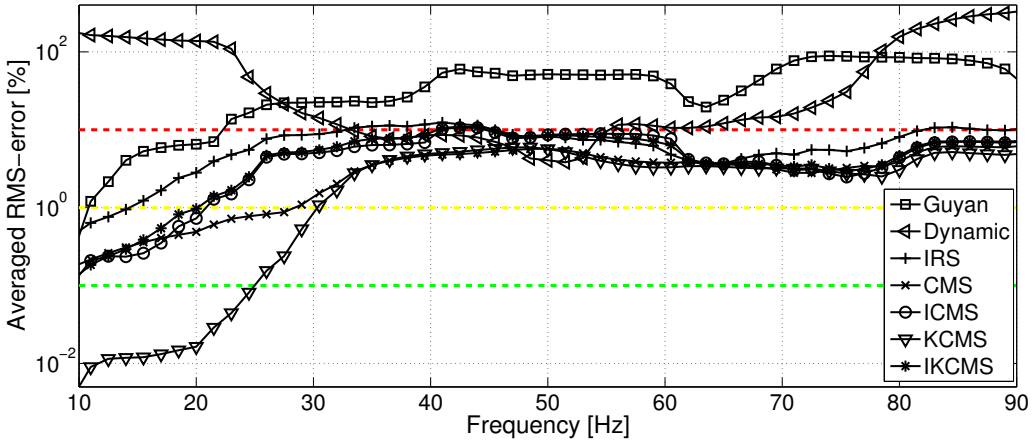

Figure 3. Averaged errors of the RMS-values obtained from the steady-state analysis, when applying the model order reduction methods to the numerical example.

References

[1] R.J. Guyan. Reduction of Stiffness and Mass Matrices. *AIAA J*, 3:380, 1965.

[2] A.Y.T. Leung. An Accurate Method of Dynamic Condensation in Structural Analysis. *Int J Numer Methods Eng*, 12:1705–1715,1 978.

[3] J. O'Callahan. A procedure for an improved reduced system (IRS) model. *Proc 7th Int Modal Anal Conf*, 17–21, 1989.

[4] M.I. Friswell, S.D. Garvey and J.E.T. Penny. Model reduction using dynamic and iterated IRS techniques. *J Sound Vib*, 186:311–323, 1995.

[5] J. O'Callahan, P. Avitabile and R. Riemer. System equivalent reduction expansion process (SEREP). *Proc 7th Int Modal Anal Conf*, 29–37, 1989.

[6] R.R. Craig. *Structural Dynamics; An Introduction to Computer Methods*. John Wiley & sons Inc., New York, 1981.

[7] R.R. Craig and C.J. Chang. A review of substructure coupling methods for dynamic analysis. *Adv Eng Sci*, 2:393–408, 1976.

[8] P. Benner. Numerical Linear Algebra for Model Reduction in Control and Simulation. *GAMM Mitt*, 29(2):275–296, 2006.

[9] B. Lohmann and B. Salimbahrami. Introduction to Krylov Subspace Methods in Model Order Reduction. *Methods Appl Autom*, 1–13, 2003.

[10] T. Reis and T. Stykel. Balanced truncation model reduction of second-order systems. *Math Comput Model Dyn Syst*, 14(5):391–406, 2008.

[11] R.R. Craig and M. Bampton. Coupling of substructures in dynamic analysis. *AIAA J* 6:1313–1319, 1968.

[12] P. Koutsovasilis and M. Beitelschmidt. Model order reduction of finite element models: improved component mode synthesis. *Math Comput Model Dyn Syst*, 16(1):57-73, 2010.

Proceedings of the 26th Nordic Seminar on Computational Mechanics
A. Logg, K.A. Mardal, A. Massing (Eds.)

Molecular dynamic simulation of mechanical properties of polymer particles

Jianying He[1], Jianyang Wu[1] and Zhiliang Zhang[1]

(1)Department of Structural Engineering, Norwegian University of Science and Technology (NTNU), Trondheim 7491, Norway

Summary. Polymeric particles with controlled microstructure play an important role as constituents in many composite materials for a number of emerging applications. The mechanical properties of composite polymer particles have been investigated by classical molecular dynamic simulation with a combination of united-atom force fields. The effect of particle size, chain architecture and temperature on the mechanical response of polymer particles has been explored and compared with experimental results to guide the design and control of particles.

Key words: molecular dynamic simulation, polymer particles, chain structure, nanoindentation

Introduction

Ugelstad monodisperse polymer particles have been widely used in chemical industries and biotechnology. Recently there is a growing interest in polymer particles with potential application in new electronic packaging technologies, such as Anisotropic Conductive Adhesives (ACA) in Flat Panel Displays. The particles are conductive through deposition of nano-scale metal coating on the particle surface. The metallized particles usually consist of a micron sized polymer core for improving contact compliance, a nanoscale nickel inner layer for bonding to polymer core and obtaining electrical conductivity, and a nanoscale gold outer layer for protecting inner layer from oxidation and improving the reliability of electrical performance. The use of metallized polymer particles in ACA technology possesses many advantages in terms of being lead-free, reducing package size and achieving high-density interconnections. The electrical characteristics as well as the reliability of the interconnection are mainly determined by the mechanical performance of the conductive polymer particles. Therefore, the mechanical performance of particles is of crucial importance to a reliable connection. This motivates us to study the mechanical properties of composite polymer particles and explore the structure-properties relationship to better design polymer particles for specific applications.

Methods

Molecular dynamic simulation

A combination of united-atom force fields was used for the molecular dynamic (MD) models of polyethylene nanoparticles in which carbon contained unit groups CH, CH2 and CH3 groups were considered to be single spherical beads interacting with each other, resulting in great saving in terms of the total number of atoms in the simulated systems. The total potential energy can be expressed as:

$$E_{total} = E_{nb} + E_{bond} = E_{nb} + E_b + E_\theta + E_\phi, \tag{1}$$

where the total potential energy (E_{total}) includes two components: non-bonded (E_{nb}) and bonded (E_{bond}) interaction terms. MD models of polyethylene nanoparticles were constructed with different sizes and different molecular architecture for bulk MD models. The prepared polyethylene particles were compressed by rigid plates placed at the top and bottom of particles, similar as nanoindentation-based flat punch test in experiment. During compression the real time force and displacement on particles were monitored and the contact force-displacement curves were obtained. To compare the particle behaviour, the stress-strain relationship was calculated as follows:

$$\sigma_N = \frac{P}{\pi R^2} \tag{2}$$

$$\epsilon_N = \frac{D}{R} \tag{3}$$

where P was the applied force, D was the half displacement during compression and R was the radius of undeformed particle.

Experiment

The mechanical test of single micron-sized polystyrene particles was performed by using a nanoindentation-based flat punch methodology. A diamond flat punch of $100\mu m$ in diameter was specially designed to compress individual particles. The results were compared with MD simulation.

Results

Molecular dynamic simulation has been utilized to understand the mechanical properties of polymeric particles. In agreement with experimental results, a strong size effect has been observed which states that the smaller particle sizes the stronger it behaves. It is attributed to the increase in surface to total energy ratio in smaller particles. The increasing crosslinking density significantly strengthens mechanical properties of particles. Based on the results, the polymeric particles can be tailor-made to realize the required mechanical properties in different applications.

References

[1] J Y He, H Kristiansen, K Redford, G Fonnum, G I Modahl and Z L Zhang. Crosslinking effect on mechanical properties of monodisperse PS-DVB particles. *Express Polymer Letters*, 7 (2013) 365-374.

[2] J Y He, Z L Zhang, M Midttun, G Fonnum, G I Modahl, H Kristiansen and K Redford. Size effect on mechanical properties of micron-sized PS-DVB polymer particles. *Polymer*, 49 (2008) 3993-3999.

[3] J Y Wu, J Y He, G Odegard and Z Zhang. Effect of chain architecture on the compression behavior of nanoscale polyethylene particles. *Nanoscale Research Letters*. 8 (2013) 322.

Proceedings of the 26th Nordic Seminar on Computational Mechanics
A. Logg, K.A. Mardal, A. Massing (Eds.)

Multi-material and thickness optimization utilizing casting filters for laminated composite structures

René Sørensen[1], Erik Lund[2]

[(1,2)]Aalborg University Department of Mechanical and Manufacturing Engineering, Fibigerstraede 16 Aalborg-DK, [(1)]rso@m-tech.aau.dk

Summary. This extended abstract presents a new parameterization for performing discrete material and thickness optimization of laminated composite structures. The parameterization is based on the work by [4], where we present a reformulation of the original parameterization. The reformulation eliminates the need for having explicit constraint for ensuring that intermediate void does not appear in between layers of the laminate. This is achieved by utilizing a filtering technique known as a casting constraint from traditional topology optimization with isotropic materials.

Key words: Laminated Composite Structures, Discrete Material Optimization, Topology Optimization, Casting Filter

Introduction

In a recent paper [4], the authors presented a gradient based optimization methodology for determining an appropriate material and thickness variation for laminated composite structures. The methodology utilizes the so-called Discrete Material Optimization (DMO) [3, 2] method for determining an optimum material from a list of candidates. The thickness variation is achieved by adding a topology variable to each layer, in order to effectively terminate individual plies. Furthermore, in order to increase manufacturability the authors also developed a series of common design rules also known as manufacturing constraints. One of the presented manufacturing constraints prevents intermediate void from appearing in between layers; ensuring that the laminate can be manufactured using vacuum infusing techniques. The focus of this work is to effectively remove the need for this type of constraint by utilizing casting constraints or filters applied in standard topology optimization of isotropic materials [1]. Effectively, all the layerwise density variables are replaced by a continuous through-the-thickness design variable; removing the need for having constraints preventing intermediate void.

The remaining paper is organized as follows; first the problem formulation is presented; secondly, the numerical examples are presented together with results. Finally, the overall conclusions are presented.

Problem formulation

In the original parameterization by [4] the material selection is performed on the basis of a discrete set of candidates. These candidates may represent orthotropic lamina with different orientations, Non Crimp Fabrics (NCF)'s, or isotropic materials such as foam or wood. The material selection is performed using DMO, where each material candidate is represented by a design variable or density; specifying how much of each candidate that is present for the given design domain. The thickness variation is achieved by introducing a so-called topology variable. Effectively, the topology variable scales the material properties between full and no presence.

Consequently, the constitutive properties for a given layer, l, in a given element, e, are governed by

$$\mathbf{E}_{el} = \mathbf{E}_0 + \frac{\tilde{\rho}_i}{1+p(1-\tilde{\rho}_i)} \sum_{c=1}^{n^c} \frac{x_{jc}}{1+p(1-x_{jc})} (\mathbf{E}_c - \mathbf{E}_0); \quad \tilde{\rho}_i, x_{jc} \in [0,1] \quad \forall (i,j,c), \tag{1a}$$

$$\sum_{c=1}^{n^c} x_{jc} = 1; \quad \forall\, j. \tag{1b}$$

In (1a), $\mathbf{E}_c$ is the constitutive properties of candidate c, and x_{jc} is the associated design variable covering the j'th candidate design domain. Because both the candidate and topology design variables are treated as continuous variables, penalization of intermediate valued design variables is needed in order to drive them to their respective bounds. In (1a) the RAMP (Rational Approximation of Material Properties) scheme by [5] is applied.

Preventing intermediate void

With the formulation in (1), nothing prevents the optimizer from converging to structures with void in between layers of the laminate. In [4], the authors presented a set of linear inequality constraints for the topology variables to overcome this phenomenon.

$$\tilde{\rho}_{e(l+1)} \leq f(\tilde{\rho}_{el}, T); \quad \forall e, \quad l = 1, 2, \ldots, n^l - 1. \tag{2}$$

Here, f is a function prescribing the upper bound for the topology variables in all n^l layers. This bound is a function of the topology variable in the layer below, and the threshold parameter T. Because of the function dependency of the topology variables in (2), the bounds on the individual topology variables have to be updated for each design iteration. In this work, we pursue to eliminate the need for such constraints by replacing the layerwise topology variables with a single continuous through-the-thickness design variable.

Casting filters

In [1], the authors presented a filtering technique for achieving castable designs using standard topology optimization with isotropic materials. The casting filter ensures that void does not appear inside the optimized topology, without the need for explicit constraints, making it possible to cast the final design. This principle is directly applicable for the problem of preventing intermediate void in between layers of laminated composite structures. For laminated composites, the basic idea is illustrated in figure 1.

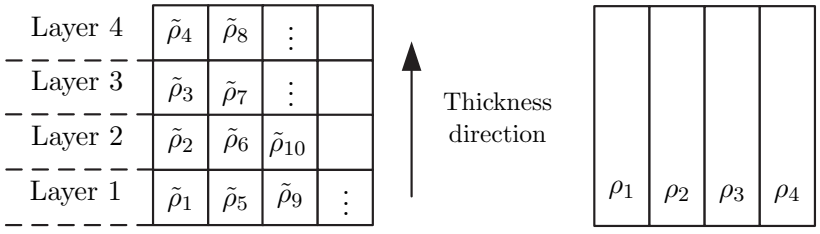

Figure 1. Four layered laminate, with four columns representing individual design domains. Left, design domain with the filtered layerwise densities $\tilde{\rho}_i$. Right, design domain with the continuous through-the-thickness design variables ρ_j

In figure 1, $\tilde{\rho}_i$ is the filtered density associated with each layer, and ρ_j is the design variable for the j'th design domain. Essentially, what we want to determine is whether the value of a given $\tilde{\rho}_i$ should be 0 or 1, based upon the value of the corresponding ρ_j. In order to do so, the

filter is defined using a normalized through-the-thickness coordinate system $s(l)$ where l is the given layer number associated with each $\tilde{\rho}_i$.

$$s(l) = \frac{l-1}{n^l} + \frac{1}{2\,n^l}, \quad l \in [1, n^l]. \tag{3}$$

The normalized coordinate system thus defines the boundary or interface where the value of $\tilde{\rho}_i$ changes. In (3), the boundary is located at the center of each layer; provided that all n^l layers have the same thickness. Now, for a given value of $s(l)$, the value of a given $\tilde{\rho}_i$ can be determined using a Heaviside function (4).

$$\tilde{\rho}_i = H_s\left(\rho_j, s(l)\right), \tag{4a}$$

$$H_s\left(\rho_j, s(l)\right) = \begin{cases} 0 & , \rho_j \leq s(l), \\ 1 & , \rho_j > s(l). \end{cases} \tag{4b}$$

However, the formulation in (4) is not differentiable, hence the authors in [1] suggested a smooth approximation of the Heaviside function based on the work by [6].

$$\tilde{\rho}_i = H_s\left(\rho_j, s(l), \beta\right), \tag{5a}$$

$$H_s\left(\rho_j, s(l), \beta\right) = \begin{cases} 1 - \rho_j \left[e^{-\beta(1-s(l)/p_j)} - \left(1 - s(l)/\rho_j\right) e^{-\beta}\right] & , \rho_j \leq s(l), \\ 1 - \left(1-\rho_j\right)\left[1 - e^{-\beta(s(l)-\rho_j)/(1-\rho_j)}\right. & \\ \left. + \left(s(l)-\rho_j\right) e^{-\beta} / \left(1-\rho_j\right)\right] - \rho_j & , \rho_j > s(l), \end{cases} \tag{5b}$$

In (5), β is a parameter controlling the steepness of the Heaviside approximation. The sensitivity of a given function f, with respect to the design variables, ρ_j, is determined by use of the chain rule:

$$\frac{\partial f}{\partial \rho_j} = \frac{\partial f}{\partial \tilde{\rho}_i} \frac{\partial \tilde{\rho}_i}{\partial \rho_j}. \tag{6}$$

Numerical examples and results

The thickness filter formulation makes it possible to optimize the total thickness of a multilayered structure with a single design variable for each design domain. Hence, it is only natural to compare the filter formulation against a single layered plate where for each design domain the actual thicknesses of the plate are used as the design variables. Consequently, two examples are presented in the following. Both examples center around a 1m×1m steel plate with a maximum thickness of 20mm. The plate is modeled with clamped boundary conditions and is subjected to a uniform pressure of 1kPa. The finite element discretization consists of $8x8$ nine node shell elements. For example 1, the plate has been modeled with eight layers per shell element each with a uniform thickness of 2.5mm. For example 2, the plate has been modeled with single layered shell elements, having a maximum thickness of 20mm.

For both examples a minimum thickness has been set to 2.5mm. This ensures that no elements are completely replaced by void. The objective for both examples is to minimize the total mass, subjected to a constraint on the maximum vertical displacement of 0.01mm for the center node.

Figures 2 and 3 show the optimized thickness distribution for Example 1 and Example 2, respectively.

As can be seen on the figures, the examples have converged to nearly identical thickness distributions. In Table 1, the final objective and constraint values are shown. For both examples, the constraint is active and the final mass is within 2% of one another.

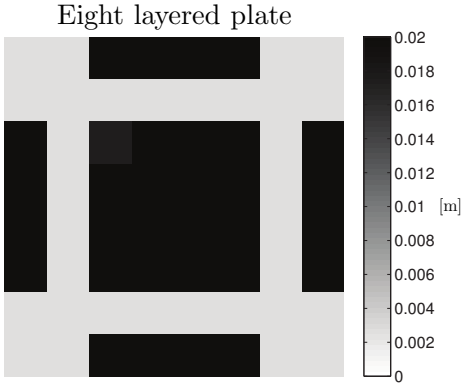

Figure 2. Example 1. Thickness distribution of an eight layered plate optimized with continuous thickness design variables ρ_j

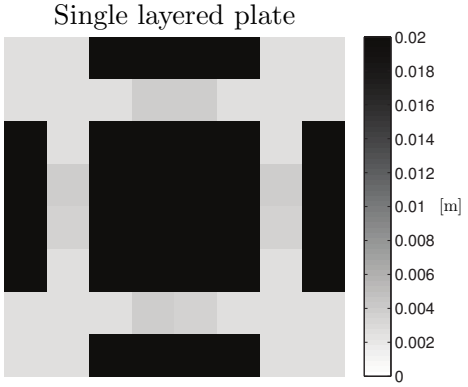

Figure 3. Example 2. Thickness distribution of a single layered plate optimized with the plate thicknesses continuous design variables

	Example 1	Example 2
Final mass	88.0kg	89.5kg
Constraint value	0.01mm	0.01mm

Table 1. Results for Example 1 and Example 2

Conclusion

A new parameterization for performing simultaneous material and thickness variation optimization of laminated composite structures has been presented. The parameterization utilized a casting filter technique originally developed for topology optimization of isotropic structures. The filter makes it possible to avoid explicit constraints for preventing intermediate void in between layers of the laminated structure. Based on the presented preliminary results, the thickness filter formulation behaves as intended. Further details and results for laminated composite structures will be presented at the NSCM26 conference.

References

[1] A. Gersborg and C. S. Andreasen. An explicit parameterization for casting constraints in gradient driven topology optimization. *Structural and Multidisciplinary Optimization*, 44: 875–881, 12/2011 2011. ISSN 1615-147X. 10.1007/s00158-011-0632-0.

[2] C. Hvejsel and E. Lund. Material interpolation schemes for unified topology and multi-material optimization. *Structural and Multidisciplinary Optimization*, 43(6):811–825, 2011.

[3] E. Lund and J. Stegmann. On structural optimization of composite shell structures using a discrete constitutive parametrization. *Wind Energy*, 8(1):109–124, 2005.

[4] S. N. Sørensen and E. Lund. Topology and thickness optimization of laminated composites including manufacturing constraints. *Structural and Multidiciplinary Optimization*, 2013. doi: 10.1007/s00158-013-0904-y.

[5] M. Stolpe and K. Svanberg. An alternative interpolation scheme for minimum compliance topology optimization. *Structural and Multidisciplinary Optimization*, 22(2):116–124, 2001.

[6] S. Xu, Y. Cai, and G. Cheng. Volume preserving nonlinear density filter based on heaviside functions. *Structural and Multidisciplinary Optimization*, 41(4):495–505, 2010. ISSN 1615-147X.

Proceedings of the 26th Nordic Seminar on Computational Mechanics
A. Logg, K.A. Mardal, A. Massing (Eds.)

The investigation of effect of uncertainties on the optimum vibration reduction of rigid rotors with magnetorheological dampers by means of the probability Monte Carlo method

Jaroslav Zapoměl[1], Petr Ferfecki[2]

(1)VŠB-Technical University of Ostrava, Department of Mechanics, 17. listopadu 15, Ostrava-Poruba, Czech Republic, jaroslav.zapomel@vsb.cz
(2)VŠB-Technical University of Ostrava, Centre of Excellence IT4Innovations, 17. listopadu 15, Ostrava-Poruba, Czech Republic, petr.ferfecki@vsb.cz

Summary. To reduce lateral vibrations of rotating machines excited by unbalance forces the damping devices are placed between the rotor and its frame. The advanced technological solution is represented by application of magnetorheological squeeze film dampers. Values of some geometric, technological or operational parameters of rotor systems can be indefinite or slightly variable during the operation. Then they should be treated as uncertain and some probabilistic approach should be used for the investigations. The Monte Carlo method seems to be promising for this purpose.

Key words: rigid rotors, magnetorheological dampers, steady state response, Monte Carlo method

Introduction

Application of magnetorheological damping devices placed between the rotor and its casing makes it possible to control lateral vibrations of rotating machines produced by unbalance forces. The aim is to reach the optimum compromise between reducing the rotor oscillations amplitude and minimizing magnitude of the force transmitted to the rotor frame.

Values of some geometric, technological or operational parameters of rotor systems can be indefinite or slightly variable during the operation. Then the approaches based on stochastic principles should be used for the investigations. The worst scenario method [1], the theory of fuzzy sets and interval mathematics [2], [3], [4], [5], the probability methods [6] and variational procedures belong to them. Unlike the fuzzy set approach that overestimates the influence of uncertainties on behaviour of mechanical systems, the probability method of the Monte Carlo type seems to be more suitable. The results are obtained by means of repeated simulations for randomly generated values of uncertain parameters. The system reliability ψ is defined

$$\psi = 1 - \frac{N_{\mathrm{dis}}}{N_{\mathrm{sat}} + N_{\mathrm{dis}}} \tag{1}$$

where N_{sat}, N_{dis} are the numbers of simulations when all required conditions put on the machine operation are satisfied, are not satisfied.

Specification of the investigated rotor system and the problem

The investigated rotating machine (figure 1) consists of a rigid rotor formed by a shaft and one disc and of a rigid frame. Two magnetorheological squeeze film dampers are used to mount the shaft with the bearing housings flexibly coupled with the rotor casing. The rotor turns

at constant angular speed and is loaded by its weight and by the disc unbalance. The squirrel springs are prestressed to be eliminated their deflection (relative to the bearing housings) caused by the rotor weight. The whole system can be considered as symmetric relative to the disc middle plane.

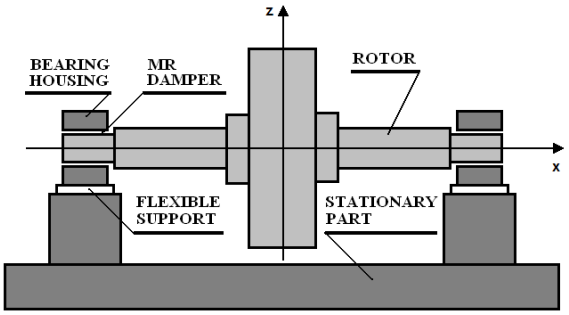

Figure 1. The investigated rotor system.

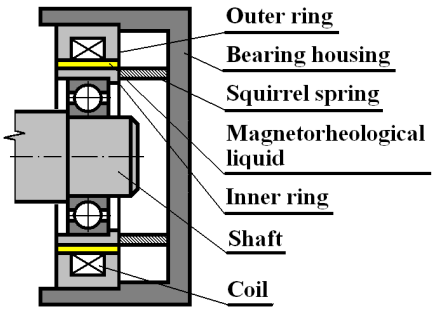

Figure 2. Magnetorheological damper.

The magnetorheological damper (figure 2) is formed by two rings between which there is a layer of magnetorheological fluid. The outer ring is fixed to the damper's body. The inner ring is coupled with the shaft by a rolling element bearing and with the stationary part by a squirrel spring. The lateral vibration of the rotor squeezes the lubricating layer which produces the damping effect. The damper is equipped with an electric coil generating magnetic flux passing through the lubricating oil. As resistance against the flow of the magnetorheological liquid depends on magnetic induction, the change of the current can be used to control the damping force.

The task was to evaluate magnitude of the current keeping amplitude of the disc vibration in the radial direction lower than the allowed value (0.22 mm) at the specified angular speed (200 rad/s) during the rotor steady state operating regime. The force transmitted to the rotor frame should be as low as possible. In the analysis the rotor unbalance and speed of its rotation are uncertain parameters.

In the computational model the rotor, its casing and the bearing housings are considered as absolutely rigid, the squirrel springs and the coupling between the bearing housings and the frame as elastic and linear. Acting of the layer of the magnetorheological oil on the inner and outer rings is represented in the model system by hydraulic forces. The magnetorheological lubricant is modelled by Bingham material. In cavitated areas the pressure is assumed to be equal to those in the ambient space.

To take into account the uncertain character of the specified parameters the approach utilizing the Monte Carlo method has been adopted. The probabilistic distribution of both uncertain parameters was estimated as uniform. Then the equations of motion of the rotor system read

$$m_{\mathrm{r}}\ddot{y}_{\mathrm{r}} + b_{\mathrm{p}}\dot{y}_{\mathrm{r}} + 2k_{\mathrm{d}}y_{\mathrm{r}} - 2k_{\mathrm{d}}y_{\mathrm{b}} = m_{\mathrm{r}}e_{\mathrm{t}}\omega^2\cos(\omega t + \psi_{\mathrm{r}}) + 2F_{\mathrm{mry}} + 2F_{\mathrm{psy}}, \tag{2}$$

$$m_{\mathrm{r}}\ddot{z}_{\mathrm{r}} + b_{\mathrm{p}}\dot{z}_{\mathrm{r}} + 2k_{\mathrm{d}}z_{\mathrm{r}} - 2k_{\mathrm{d}}z_{\mathrm{b}} = m_{\mathrm{r}}e_{\mathrm{t}}\omega^2\sin(\omega t + \psi_{\mathrm{r}}) + 2F_{\mathrm{mrz}} + 2F_{\mathrm{psz}} - m_{\mathrm{r}}g, \tag{3}$$

$$m_{\mathrm{b}}\ddot{y}_{\mathrm{b}} + b_{\mathrm{b}}\dot{y}_{\mathrm{b}} - k_{\mathrm{d}}y_{\mathrm{r}} + (k_{\mathrm{d}} + k_{\mathrm{b}})y_{\mathrm{b}} = -F_{\mathrm{mry}} - F_{\mathrm{psy}}, \tag{4}$$

$$m_{\mathrm{b}}\ddot{z}_{\mathrm{b}} + b_{\mathrm{b}}\dot{z}_{\mathrm{b}} - k_{\mathrm{d}}z_{\mathrm{r}} + (k_{\mathrm{d}} + k_{\mathrm{b}})z_{\mathrm{b}} = -F_{\mathrm{mrz}} - F_{\mathrm{psz}} - m_{\mathrm{b}}g. \tag{5}$$

m_{r}, m_{b} are masses of the rotor and the bearing housing, b_{p} is the coefficient of the rotor external damping, k_{d} is the squirrel spring stiffnesses, k_{b}, b_{b} are the stiffness and damping coefficient of the bearing housing support, e_{t} is eccentricity of the rotor centre of gravity, g is the gravity acceleration, t is the time, y_{r}, z_{r}, y_{b}, z_{b} are displacements of the rotor and bearing housings centres in the horizontal and vertical directions, ω is angular speed of the rotor rotation, ψ_{r} is the phase shift, F_{mry}, F_{mrz}, F_{psy}, F_{psz} are the y and z components of the magnetorheological

damping and prestress forces and (.), (..) denote the first and second derivatives with respect to time.

The hydraulic forces are calculated by integration of the pressure distribution in the film of the magnetorheological oil around the circumference and along the length of the damping element taking into account the cavitation. The pressure in noncavitated regions is governed by solution of the Reynolds equation adapted for Bingham material. The details on its derivation and solution are discussed in [7].

Results of the simulations

In figures 3 and 4 there are depicted the frequency response characteristic referred to the rotor disc centre and dependence of the maximum force transmitted to the rotor frame in the vertical direction for several magnitudes of the applied current. The results show that the high current for velocities lower than approximately the first resonance frequency reduces both amplitude of the rotor vibration and magnitude of the transmitted force. But in the area of higher rotor angular speeds the rising current changes the vibration amplitude only little but considerably rises the transmitted force. As the investigated operating speed is higher than the critical one, the proposed current should be as low as possible but high enough to reduce the vibration amplitude below the allowed value.

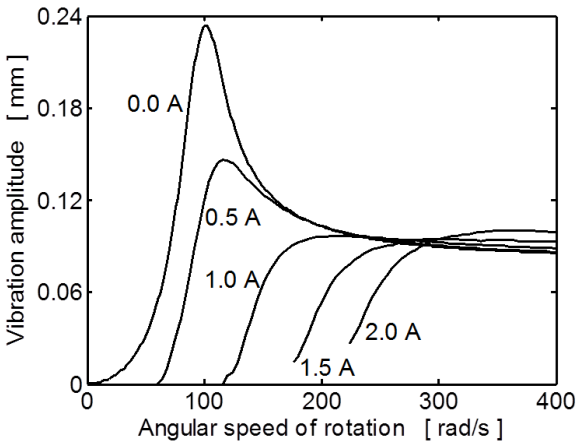

Figure 3. Response characteristic.

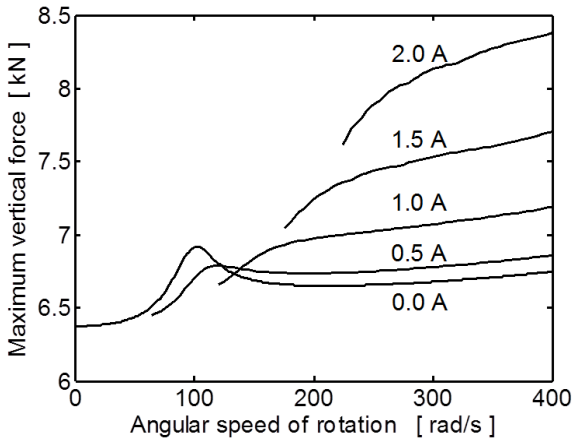

Figure 4. Vertical force versus speed of rotation.

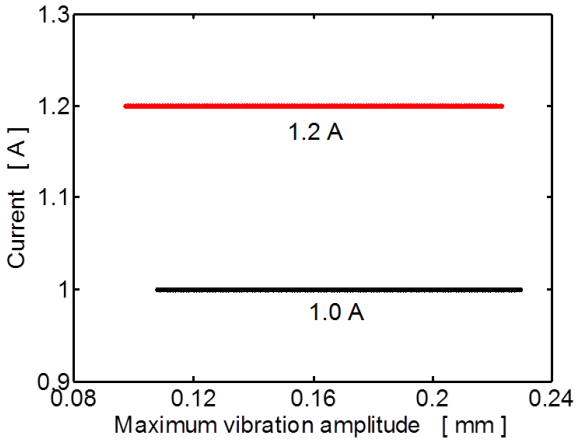

Figure 5. Dispersion of the disc amplitude.

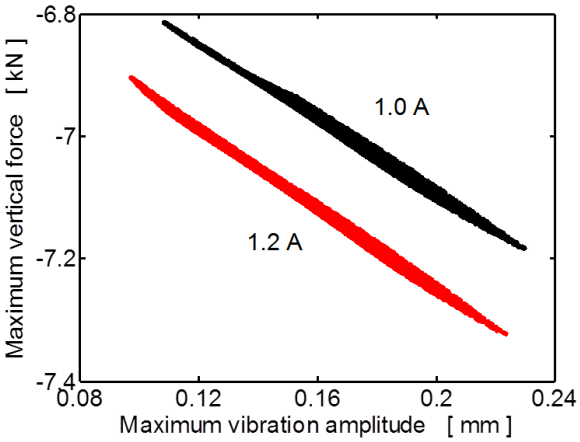

Figure 6. Vertical force-disc displacement dispersion.

Amplitude of the rotor vibration and magnitude of the vertical force transmitted to the rotor frame is evaluated by means of the Monte Carlo method. The results were obtained by performing 10 000 simulations, each for two magnitudes (1.0 A, 1.2 A) of the electric current. Figure 5 shows that in both cases the condition for the allowed value of the oscillation amplitude is not satisfied. Nevertheless, the reliability is comparatively high, 99.0 % and 99.9 % for the currents of 1.0 A and 1.2 A respectively. Increase of the current leads to rising the force transmitted to the rotor frame in the vertical direction by about 1.3 % as evident from figure 6.

Conclusions

The probabilistic Monte Carlo method makes it possible to investigate dynamical behaviour of mechanical systems taking into account the effect of uncertainty of some geometric, design or operational parameters. The results are obtained in the form of intervals of numerical values. It follows from the theory, confirmed by experience, that to obtain the reliable results a large number of computational simulations must be performed which makes this method considerably time consuming.

This work was supported by the research projects MSM 6198910027, CZ.1.05/1.1.00/02.0070.

References

[1] J. Liberdová and J. Zapoměl. Effect of uncertainty of the support stiffness, damping and unbalance excitation on dynamical properties of the turbine rotor of an aircraft engine. *Transactions of the VSB-Technical University of Ostrava*, 56(2):289–294,2010.

[2] L.A. Zadeh. Fuzzy sets. *Information and Control*, 8(3):338–353,1965.

[3] H.-J. Zimmermann. *Fuzzy set theory and its applications*. Kluwer Academic Publishers, Boston/Dordrecht/London, 1996.

[4] D. Moens and D. Vandepitte. Fuzzy finite element method for frequency response function analysis of uncertain structures. *AIAA Journal*, 40(1):126–136,2002.

[5] L. Chen and S.S. Rao. Fuzzy finite-element approach for the vibration analysis of imprecisely-defined systems. *Finite Elements in Analysis and design*, 27(1):69–83,1997.

[6] M.H. Kalos and P.A. Whitlock. *Monte Carlo methods*. Wiley-VCH, 2008.

[7] J. Zapoměl, P. Ferfecki and P. Forte. A computational investigation of the transient response of an unbalanced rigid rotor flexibly supported and damped by short magnetorheological squeeze film dampers. *Smart Materials and Structures*, 21(10):105011,2012.

Proceedings of the 26th Nordic Seminar on Computational Mechanics
A. Logg, K.A. Mardal, A. Massing (Eds.)

Applications of the BEam Cross section Analysis Software (BECAS)

José Pedro Blasques, Robert Bitsche, Vladimir Fedorov, and Martin Eder

Department of Wind Energy, Technical University of Denmark, Frederiksborgvej 399, 4000 - Roskilde, Denmark, jpbl@dtu.dk, robi@dtu.dk, vlfe@dtu.dk, maed.dtu.dk

Summary. A newly developed framework is presented for structural design and analysis of long slender beam-like structures, e.g., wind turbine blades. The framework is based on the BEam Cross section Analysis Software – BECAS – a finite element based cross section analysis tool. BECAS is used for the generation of beam finite element models which correctly account for effects stemming from material anisotropy and inhomogeneity in cross sections of arbitrary geometry. These type of modelling approach allows for an accurate yet computationally inexpensive representation of a general class of three dimensional beam-like structures. Preliminary results are presented where the devised framework is used for stiffness and strength analysis of wind turbine blades, material and structural topology optimization of wind turbine blade cross sections, and evaluation of strain energy release rate in fractured beams. The results show a good agreement with solutions from three-dimensional solid finite element models but require only a fraction of the computation time.

Key words: beam finite elements, wind turbine blades, cross section analysis tools, laminated composite structures

Introduction

The design and certification of wind turbines requires the analysis of a large number of load cases. Each of these load cases corresponds to relatively long time series analysis of the loads and response of the wind turbine. These analyses are typically conducted using specialized wind turbine aero-servo-elastic codes. In here the most important components of the wind turbine are typically modelled using beam finite elements. These type of modelling approach offers a convenient trade off between accuracy and computational efficiency.

The generation of beam finite element matrices entails the determination of the cross section stiffness and mass properties. For isotropic beams with simple geometries (e.g., tower and shaft) the determination of these properties is usually trivial. However, the development of accurate beam models to represent the blades is not so simple. The blades have complex geometries and are made of combinations of different composite materials with different degrees of anisotropy. Simplified approaches have been used in the past to estimate the blade cross section properties. However, these tools do not meet the desired level of accuracy for future blade designs.

The wind turbine blade design and engineering community, in an effort to improve the accuracy of its aeroelastic models, has in recent years looked into new methods for developing high-fidelity beam models to represent the blades. The open source BEam Cross section Analysis Software – BECAS – described here is a result of this effort (see BECAS [1]). BECAS is able to accurately account for effects stemming from material anisotropy and inhomogeneity in cross sections of arbitrary geometry. As a result, it is now possible for blade designers to tailor these properties to improve the aeroelastic performance of the blade.

In the next sections, we will describe the basic BECAS workflow and present different application examples which illustrate the potential of such a tool. We conclude with an outlook into

future extensions and challenges.

The BECAS workflow

A schematic description of a typical BECAS workflow for structural blade analysis and design is described in Figure 1. BECAS is first used in a pre-processing phase to generate the beam finite elements representing the blade in the aeroelastic analysis code. A series of pre-defined cross sections along the blade are analysed. The analysis is based on a finite element mesh of the cross section. The material properties are defined at each element and may present any level of anisotropy. The resulting beam finite elements are used to represent the blades in the wind turbine assembly inside the aeroelastic analysis tool. Finally, based on the cross section forces and moments resulting from the aeroelastic simulations it is possible to recover the detailed three-dimensional stress components or analyse the strain energy release rate, as will be shown in the next sections.

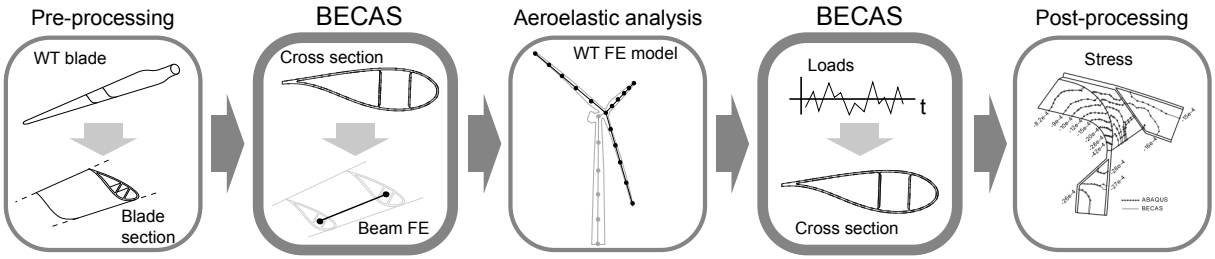

Figure 1. Schematic description of the BECAS workflow for structural analysis and design of wind turbine (WT) blades.

The framework described previously was recently employed in the stiffness and strength design of the DTU 10 MW Reference Wind Turbine (DTU10MW-RWT) (Bak et al. [2]). The geometry and material distribution were automatically generated based on a shell finite element model of the blade. The resulting cross section stiffness and mass properties were employed in the generation of the beam finite element representing the blades in the wind turbine aeroelastic analysis tool HAWC2 (Larsen and Hansen [3]). The strength of the laminates in the blade were analysed based on the resulting aeroelastic loads. The procedure was repeated until the final structural configuration of the blade was obtained.

Applications

The following sections give a brief account of the main developments within the BECAS framework. These are mostly preliminary results intended to illustrate the potential of such a tool.

Stiffness and strength analysis

The first step in the development consisted of the validation of the cross section stiffness and mass properties. Results show that the deformation and eigenfrequencies given by beam finite element models generated using BECAS match closely the results from detailed shell finite element models. Moreover, the three-dimensional stress components on a detailed wind turbine cross section have been analysed. The results from Figure 2 show that the three-dimensional stress components estimated by BECAS match well with that obtained from three-dimensional finite element models.

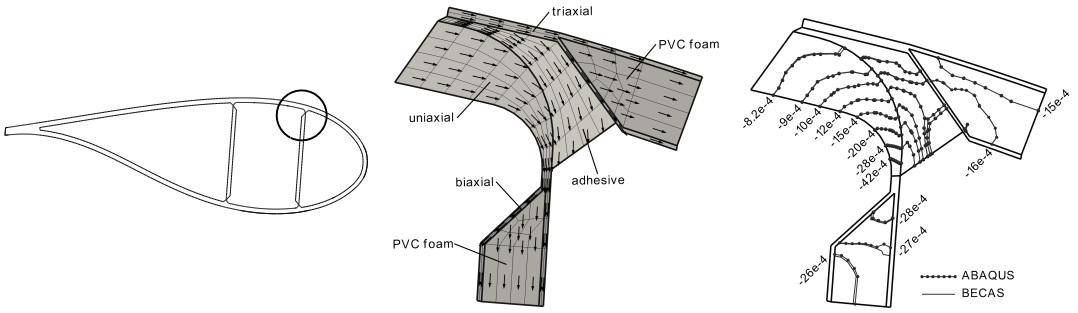

(a) (b) (c)

Figure 2. Analysis of strength in a wind turbine cross section using BECAS. (a) Wind turbine cross section and region of detail. (b) Finite element mesh, and material distribution and orientation at detail. (c) Element strains ϵ_{11} in material coordinate system as obtained by BECAS and a three-dimensional solid finite element model in ABAQUS.

Multi-material topology optimization

An optimal design framework was developed by Blasques and Stolpe [4] combining BECAS and multi-material topology optimization techniques. The optimal design problem concerns the distribution of a limited amount of different materials within a design domain represented by the cross section finite element mesh. A change in the material distribution in the cross

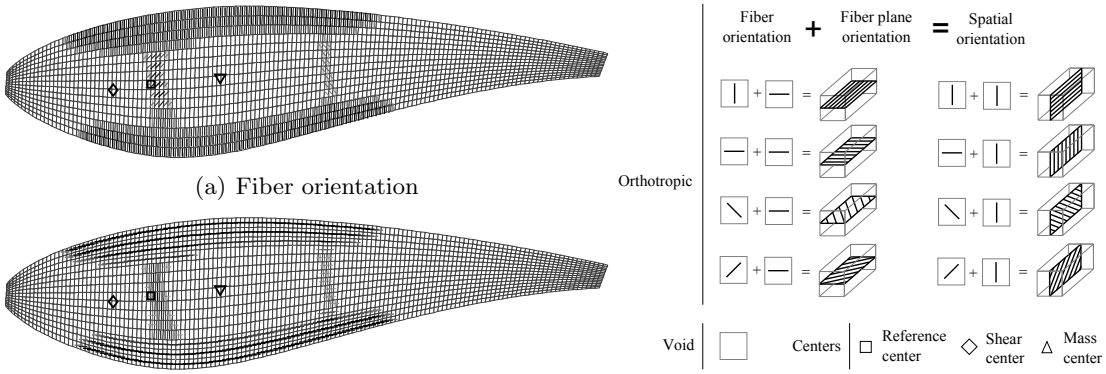

(a) Fiber orientation

(b) Fiber plane orientation

(c) Legend

Figure 3. Optimal material distribution and laminate properties for the load carrying structure of a wing profile cross section subject to 15 static load cases of aerodynamic nature. Solution to the minimum compliance problem with a weight constraint. It is assumed that the outer aerodynamic shell is non-structural and exists around the perimeter of the cross section shape outside the design domain. (a) Fiber orientation. (b) Fiber plane orientation. (c) List of 9 candidate materials (laminated composite material in 8 different directions and void) and legend to figures (a-b) for interpretation of the three-dimensional orientation of the fibers.

section results in a consequent change of its stiffness and mass properties and in turn, of the structural response of the beam. The approach was applied, among other, to the optimization of the material properties and structural topology of an idealized wind turbine blade. The resulting topology presented in Figure 3 agrees well with results reported in the literature using computationally significantly more expensive three-dimensional solid finite element models.

Evaluation of strain energy release rate

The most recent work has focused on the analysis of strain energy release rate (SERR) in fractured beams. The Virtual Crack Closure Technique (Krueger [5]) has been implemented in BECAS. The validation work includes the analysis of SERR for cracks along the beam length

in mono- and bi-material interfaces. The resulting SERR values show a good agreement when compared with three-dimensional solid finite element models (cf. Figure 4).

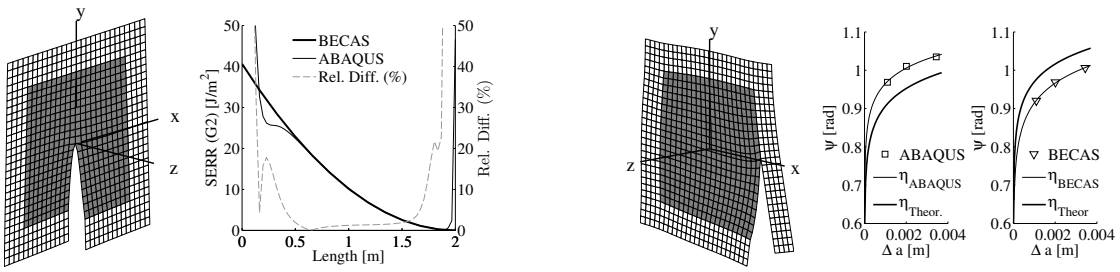

Figure 4. Selected results comparing the VCCT results from BECAS and three-dimensional finite element models in ABAQUS for cantilever beams subjected to tip loads. The origo of the length coordinate is at the clamped end of the beam. Strain energy release rates G1, G2, and G3 are associated with mode 1, 2 and 3 crack opening, respectively. (a-b) Bi-material cross section with crack in the center subjected to transverse force in the x direction. (a) Cross section warping deformation and finite element mesh. (b) Variation of the strain energy release rate GII along the beam length. (c-d) Bi-material cross section with crack at the material interface subjected to tension force in z direction. (c) Cross section warping deformation and finite element mesh. (d) Dundurs parameters as estimated based on measurements for different mesh sizes using BECAS (right) and a solid finite element model in ABAQUS (left).

Current developments and future challenges

Ongoing developments concern mostly the extension of the previously presented results. The strength analysis module is being further extended to address material based fatigue damage estimations and reliability analysis. The main challenge in this module is the incorporation of effects stemming from geometrical non-linearities, e.g., panel buckling for thin-walled cross sections. The topology optimization framework is currently being extended to include aeroelastic stability constraints. The aim in this case is to fully exploit the fact that the analysis of the global response of the beam is relatively inexpensive to consider novel computationally intensive and complex multi-physics constraints. Finally, the aim with the fracture analysis module is to perform multi-scale modelling using loads stemming from aeroelastic analysis simulations to study the development of debond and delamination damage.

References

[1] *User's Manual for BECAS – A cross section analysis tool for anisotropic and inhomogeneous beam sections of arbitrary geometry.* DTU Wind Energy, Roskilde, 2013.

[2] C. Bak et al. *Light Rotor: The 10-MW reference wind turbine.* in Proceedings of EWEA 2012 - European Wind Energy Conference & Exhibition, EWEA - The European Wind Energy Association, 2012.

[3] T.J. Larsen, A.M. Hansen. *How 2 HAWC2, the user's manual.* Risoe National Laboratory. Denmark. Forskningscenter Risoe. Risoe-R, no. 1597, 2007.

[4] J.P. Blasques and M. Stolpe. Multi-material topology optimization of laminated composite beam cross sections. *Composite Structures*, 94(11):3278–3289, 2012.

[5] R. Krueger. Virtual crack closure technique: History, approach, and applications. *Applied Mechanics Reviews*, 57, 2004.

Proceedings of the 26th Nordic Seminar on Computational Mechanics
A. Logg, K.A. Mardal, A. Massing (Eds.)

An effective, robust and parallel implementation of an interior point algorithm for limit state optimization

Niels Dollerup[1], Michaels S. Jepsen[2], and Lars Damkilde[3]

(1)Ph.D. fellow, Niels Bohrs vej 8, 6700 Esbjerg, ndo@civil.aau.dk
(2)Ph.D. fellow, Niels Bohrs vej 8, 6700 Esbjerg, msj@civil.aau.dk
(3)Professor, Niels Bohrs vej 8, 6700 Esbjerg, lda@civil.aau.dk

Summary. The article describes a robust and effective implementation of the interior point optimization algorithm. The adopted method includes a precalculation step, which reduces the number of variables by fulfilling the equilibrium equations a priori. This work presents an improved implementation of the precalculation step, which utilizes the principals of the well-known frontal method. The succeeding optimization algorithm is also significantly optimized, by applying a parallel implementation, which eliminates the exponential growth in computational time relative to the element numbers.

Key words: FEM limit analysis, element renumbering, frontal method, interior point optimization, parallel computing

Introduction

The optimization method described in the article is an efficient implementation of the method by C. Frier and L. Damkilde [1]. The optimization method in the succeeding is based on the well-known limit state lower bound problem, formulated as:

$$\begin{aligned} &\textit{Maximize:} && \alpha && && (1)\\ &\textit{Subjected to:} && \boldsymbol{H}\boldsymbol{\sigma} = \alpha\boldsymbol{r} + \boldsymbol{r}_0 && && \textit{equilibrium equations},\\ & && \boldsymbol{f}_i(\boldsymbol{\sigma}) + \boldsymbol{s} = \boldsymbol{0} \quad i = 1, 2, \cdots, p && && \textit{yield criterions}, \end{aligned}$$

where $\boldsymbol{H}$ is the flexibility matrix describing the continuity and equilibrium conditions, $\boldsymbol{r}$ and $\boldsymbol{r}_0$ are vectors describing the external scalable load applied and the constant load, e.g. body weight. α is the scalar load parameter and $\boldsymbol{\sigma}$ is a vector with the generalized stress variables m_x^i, m_y^i and m_{xy}^i for each control point i. And finally $\boldsymbol{s}$ is a vector with the slack variables for each yield function.

By fulfilling the equilibrium equations a priori, the number of variables in the succeeding optimization is significantly reduced, which of course reduces computational time, cf. [1]. Further, the optimization routine seems to get significantly more robust, as the gradients is less sensitive to changes in the search direction. Due to the limit state formulation the number of equilibrium equations is smaller than the number of variables, thus the set of equations describes an under determined system of equations. The variables in such a system can be divided into two parts, which for structural analysis can be considered as static determined variables and free variables. By realizing this, it is possible to fulfill all equilibrium equations a priori and reduce

the optimization problem, cf. [1]. By introducing the reduction of variables, the optimization problem in (1) reduces to:

$$\begin{aligned} &\textit{Maximize:} && \boldsymbol{b}^T\boldsymbol{\beta} && && (2)\\ &\textit{Subjected to:} && \boldsymbol{f}_i(\boldsymbol{\beta}) + \boldsymbol{s} = \boldsymbol{0} \quad i = 1, 2, \cdots, p && && \textit{yield criterions,} \end{aligned}$$

where $\boldsymbol{b}$ is the weighting of the free stress variables and the scalar load parameter, $\boldsymbol{\beta}$ is a vector with the free stress variables $\boldsymbol{\sigma}_f$ and the load parameter α.

Nonlinear interior point optimization

The optimization problem in equation (1) has been solved by several different optimization algorithms. Focus in recent years has mainly been on the Second-Order Cone Programming (SOCP), implemented by e.g. [2], and the Nonlinear Interior Point Programming (NIPP) method implemented by e.g. [1]. The benefit of the NIPP solver is the robust search for optimality, which is non-dependent of the number of elements. This is not the case for the SOCP solver, which has convergence problems in material optimization for only 540 elements, cf. [2]. The main drawback of the NIPP solver is the relatively slow computational time. Thus a parallel formulation has been implemented in the succeeding.

The optimization problem in (2) can be formulated as a Lagrangian function, due to its primal-dual properties, cf. [1]. To increase the robustness of the search for optimality a barrier function is added to the Lagrangian function:

$$\mathcal{L}(\boldsymbol{\beta}_d, \boldsymbol{s}, \boldsymbol{\lambda}) = -\boldsymbol{b}^T\boldsymbol{\beta} - \mu_k \sum_{i=1}^{p} log(s_i) + (\boldsymbol{f}(\boldsymbol{\beta}) + \boldsymbol{s})^T\boldsymbol{\lambda}. \tag{3}$$

Here, $\boldsymbol{\lambda}$ denotes the cost-variables or in structural terms the strain-velocities, and μ denotes a scalar barrier parameter, for iteration k. The optimal solution to this function is found by the Karush-Kuhn-Tucker (KKT) condition and Newton's method. [1] presents a detailed reduction of the gradient variables, which is included in this implementation. By the reduction method the step direction can be determined by:

$$\boldsymbol{T}\Delta\boldsymbol{\beta} = -\boldsymbol{r}_1 \tag{4}$$

$$\boldsymbol{r}_1 = \nabla \boldsymbol{f}_{\boldsymbol{\beta}}{}^T(\boldsymbol{\beta})\boldsymbol{F}^-1\mu_k - \boldsymbol{b} \tag{5}$$

$$\boldsymbol{T} = \sum_{i=1}^{p} \mu_{k,i} \left(\nabla_{\boldsymbol{\beta}} \boldsymbol{f}_i^T(\boldsymbol{\beta}) \cdot \boldsymbol{f}_i^{-2}(\boldsymbol{\beta}) \cdot \nabla_{\boldsymbol{\beta}} \boldsymbol{f}_i(\boldsymbol{\beta}) - \nabla^2_{\boldsymbol{\beta}\boldsymbol{\beta}} \boldsymbol{f}_i(\boldsymbol{\beta}) \cdot \boldsymbol{f}_i^T(\boldsymbol{\beta}) \right) \tag{6}$$

Where $\boldsymbol{F}$ is $\boldsymbol{f}(\boldsymbol{\beta})$ on diagonal form. By starting the iteration from an initial feasible point with a stress field equal to 0 and a load multiplier α equal to 0, the solution of the first iterations can be determined as:

$$\boldsymbol{\beta}_k = \boldsymbol{\beta}_{k-1} + \theta\eta\Delta\boldsymbol{\beta}. \tag{7}$$

Here, η is the maximum allowable step length, which secures that the yield criterion is not violated and θ is a correction factor which reduces the step length and makes the search more robust.

Equilibrium equations solved a priori with a frontal approach

To achieve an effective assembly and reduction of variables of the flexibility matrix $\boldsymbol{H}$, this article implements an effective mesh renumbering scheme and a frontal approach to assemble $\boldsymbol{H}$ and determine the static and free variables.

An effective numbering of the elements is a prerequisite to get an efficient frontal assembly process. The scheme used for optimization of the element numbers is done in two steps. Step 1; a standard MATLAB Sparse Reverse Cuthill-McKee renumbering optimizes the node numbers and step 2; elements are renumbered by the method described by Sloan [3]. This gives a sparse connectivity pattern of the graph describing the mesh.

In traditional FEM the frontal approach has been used for decades to assemble and solve the system of equations $\boldsymbol{Kd}=\boldsymbol{r}$. The system of equations is assembled by looping over elements and simultaneously eliminating equations and variables which are ready to leave the front. By this method, the front width of the assembly matrix is always kept as narrow as possible, which reduces both computational time and storage capacity. As the flexibility matrix $\boldsymbol{H}$ of the optimization problem is rectangular, the frontal method is adapted to handle a system with more variables than equations. The frontal approach implemented in this work is split in three steps:

1. Determine maximum front size
2. Assemble elements and perform forward substitution in a frontal scheme $[\boldsymbol{H}_s \ \boldsymbol{H}_f]$
3. Perform backward substitution to determine the relation between static and free variables $\boldsymbol{H}'_f = \boldsymbol{H}_s \backslash \boldsymbol{H}_f$

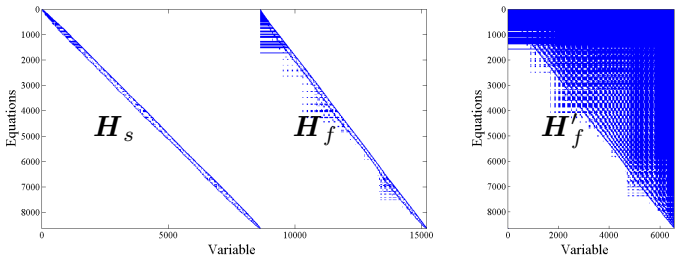

Figure 1. ***(Left)*** Sparsity pattern of the flexibility matrix $\boldsymbol{H}$ after assembly and forward substitution. ***(Right)*** Sparsity pattern of $\boldsymbol{H}'_f$. (1688 elements)

The total stress field in the structure is then determined as a function of the free variables:

$$\boldsymbol{\sigma} = \boldsymbol{B}\boldsymbol{\beta} + \boldsymbol{r}'_0 \tag{8}$$

Here $\boldsymbol{B}$ denotes a matrix $[\boldsymbol{H}'_f \ ; \ \boldsymbol{I}]$, and $\boldsymbol{r}'_0$ is a vector manipulated according to the forward and backward substitution process. As seen from Figure 1, the number of variables $\boldsymbol{\beta}$ in the optimization problem is significantly reduced compared to the original problem formulation in (1).

Optimization process utilizing parallel computing

An evaluation of a sequential implementation of the optimization algorithm above shows that 98% of the computational time of each iteration is consumed by two operations, which includes summing up $\boldsymbol{T}$ and $\boldsymbol{r}_1$ in equation (6) and (5). The computational time to build $\boldsymbol{T}$ and $\boldsymbol{r}_1$ for each iteration, in a sequential order, is dependent on the number of flops per iterations.

$$N \cdot C_p \cdot f \cdot \left((r+1)n^2 + (r^2+2r+6)n\right) \cdot t_0 \tag{9}$$

Here N is the number of elements, Cp is the number of control points per element, f is the number of constraint functions, n is the number of free variables, r is the number of variables in each yield function and t_0 is a hardware constant describing computational time per operation. Tests shows that equation (9) gives a realistic estimate of the computational time per iteration, cf. Figure 2.

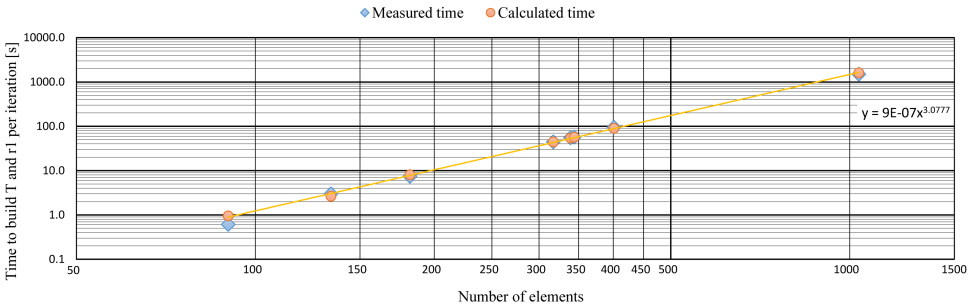

Figure 2. Actual computational time and estimated computational time per iterations in a sequential order.

As seen, the computational time per iteration grows with the element number to the power of 3. The summing process for building $\boldsymbol{T}$ and $\boldsymbol{r}_1$ is ideal for parallelization as each contribution to $\boldsymbol{T}$ and $\boldsymbol{r}_1$ are independent. Thus, the expression in (9) is reduced significantly by parallelizing on two levels. In this context data transfer and overhead time is not considered.

$$\frac{N}{p_2} \cdot C_p \cdot f \cdot \left((r+1)\left(\frac{n}{p_1}\right)^2 + (r^2+2r+6)\frac{n}{p_1} \right) \cdot t_0, \tag{10}$$

where p_1 times p_2 are the number of parallel processes. In this work a parallel scheme which utilizes the properties of equation (10) is implemented, such that the flops is done simultaneously, and consequently the computational time is significantly reduced.

Conclusion

By utilizing the properties of the frontal method and parallel computing, this work has shown that the optimization method by Frier and Damkilde [1] can be significantly optimized with regards to computational time. The implementation seems to be very efficient in both load and material optimization and give robust solutions with more fine meshes (N>1000), which seems to be a challenge when using e.g. the SOCP method [2].

References

[1] C. Frier and L. Damkilde, *A compact formulation of lower bound limit state problems using the interior point method*. In press, 2013.

[2] K. Krabbenhøft, A.V Lyamin and S.W. Sloan, *Formulation and solution of some plasticity problems as conic programs*. International Journal of Solids and Structures, Vol. 44, pp.1533-1549, 2007

[3] S.W. Sloan, *Automatic element reordering for finite element analysis with frontal solution schemes*. International Journal of Solids and Structures, Vol. 19, pp.1153-1181, 1983

Proceedings of the 26th Nordic Seminar on Computational Mechanics
A. Logg, K.A. Mardal, A. Massing (Eds.)

Parameter identification of vibrating beams with elastic boundary conditions

Ljubov Feklistova[1], Helle Hein[1], and Mairit Vikat[1]

(1)University of Tartu, J. Liivi 2, ljubov.feklistova@ut.ee, helle.hein@ut.ee, mairit.vikat@ut.ee

Summary. This article addresses the support parameter identification of vibrating beams with elastic boundary conditions. The problem is frequently encountered in modeling and structural health monitoring. Two solutions are proposed: the first solution is based on the fixed number of first natural frequencies and artificial neural networks; the second one - on the Haar wavelet transform of the mode shapes and neural networks. The results are compared to each other. The significance of the proposed numerical approaches (in comparison to the existing ones) to the inverse problem lies in its relatively fast and precise model-independent parameter predictions.

Key words: Haar wavelet, neural network, elastic boundary conditions, free vibration

Introduction

The free vibration of the elastically constrained beam has been a subject of practical engineering interest for several decades [1, 2, 3]. The frequencies of the vibrations depend on the stiffness parameters of the elastic supports. These parameters change significantly during severe exploitation of the structure and environmental conditions; as a result, the stiffness characteristics can considerably influence the performance of the structures. Therefore, the online monitoring and precise identification of the stiffness parameters are important issues, which have not been widely studied yet.

The calculation of the stiffness parameters from the governing equation of the vibrating beams on elastic supports or with elastic boundary conditions is an inverse problem and cannot be done analytically. Therefore, alternative methods have to be developed. The aim of the present paper is to study the free vibrations of the beams with non-classical elastic boundary conditions and propose a numerical solutions to the problem.

One option is to use an artificial neural network (ANN). It is a simulation of the biological neural network responsible for the learning by examples. The computational model consists of the hidden-layer neurons connected between the input and output neurons. The connections between the neurons are modeled by the weights which are to be determined during the training phase. In the present paper, the hyperbolic tangent sigmoid transfer function is used as an activator to increase the modeling flexibility [4].

Since the accuracy of the predictions depends on the training algorithm and the training data, two approaches are proposed. The first one is based on the fixed number of the first natural frequencies and ANN. In order to decrease the amount of the preparatory data and the calculation time, the Haar wavelet transform was applied to the vibrating mode shapes in the second solution.

The Haar wavelet is the simplest discrete orthogonal wavelet which is discontinuous and resembles a step function. It has been chosen in the present paper due to its ability to perform discrete wavelet transform and efficient preprocessing of the data [5].

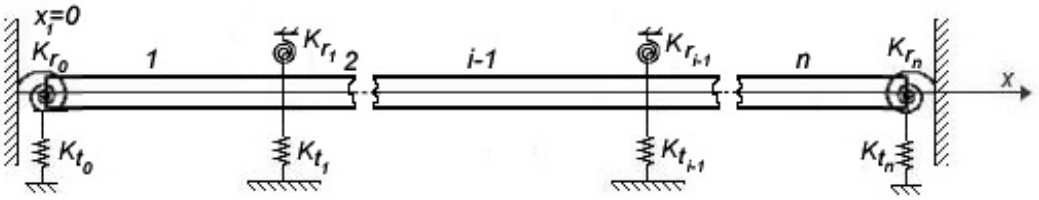

Figure 1. The beam with translational and rotational spring supports.

The present paper is divided into four Sections. The second Section gives an overview of the physical model. Section three introduces the approaches. The numerical examples on the parameter identification using the ANN and Haar wavelets are presented in Section four.

Free vibrations of beams with elastic constraints

A uniform beam with elastic boundaries and an arbitrary number of intermediate elastic supports is shown in Figure 1. It is assumed that the number of the intermediate supports is $n-1$ and the supports are located at the origins of $n-1$ local axial coordinates $x_i, i = 2, \ldots, n$ which are introduced for the i-th beam element of length l_i. The left end of the beam is origin to the coordinate x_1. The restraints are provided by either a translational or rotational spring, or both (see Figure 1), which are characterized by the spring constants K_t or K_r, respectively. Each beam element is considered as Euler-Bernoulli beam. The governing differential equation of the i-th beam element $(i = 1, \ldots, n)$ can be written as:

$$EI\frac{\partial^4 w_i}{\partial x_i^4} - \rho A\frac{\partial^2 w_i}{\partial t^2} = 0, \tag{1}$$

where w_i is the transverse displacement of the i-th beam element, E is the Young's modulus, I is the moment of inertia of the cross-section, ρ is the mass per unit volume, A is the cross-sectional area and t is the time.

The boundary conditions of the beam at the left and right ends are the following:

$$\begin{array}{llll} K_{r_0}\frac{\partial w_1(0,t)}{\partial x_1} & = EI\frac{\partial w_1^2(0,t)}{\partial x_1^2}, & K_{t_0}w_1(0,t) & = -EI\frac{\partial w_1^3(0,t)}{\partial x_1^3}, \\ K_{r_n}\frac{\partial w_n(l_n,t)}{\partial x_n} & = -EI\frac{\partial w_n^2(l_n,t)}{\partial x_n^2}, & K_{t_n}w_n(l_n,t) & = EI\frac{\partial w_n^3(l_n,t)}{\partial x_n^3}, \end{array} \tag{2}$$

where K_{r_0}, K_{t_0} and K_{r_n}, K_{t_n} stand for the rotational and translational spring constants at the left and right ends, respectively.

The equations for the intermediate supports can be written as:

$$\begin{array}{llll} w_i(l_i,t) & = w_{i+1}(0,t), & K_{r_i}\frac{\partial w_i(l_i,t)}{\partial x_i} & = -EI(\frac{\partial w_i^2(l_i,t)}{\partial x_i^2} - \frac{\partial w_{i+1}^2(0,t)}{\partial x_{i+1}^2}), \\ \frac{\partial w_i(l_i,t)}{\partial x_i} & = \frac{\partial w_{i+1}(0,t)}{\partial x_{i+1}}, & K_{t_i}w_i(l_i,t) & = EI(\frac{\partial w_i^3(l_i,t)}{\partial x_i^3} - \frac{\partial w_{i+1}^3(0,t)}{\partial x_{i+1}^3}). \end{array} \tag{3}$$

In (3), the intermediate rotational restraints are characterized by the spring constants K_{r_i}, $i = 1, \ldots, n-1$ and the translational restraints by the spring constants $K_{t_i},\ i = 1, \ldots, n-1$.

Modeling of the system

In the present research paper on the elastic parameter identification, the focus is placed on two approaches based on the natural frequencies, ANN and Haar wavelets. The first complex approach includes the following steps:

- calculation of the first five frequencies

Table 1. Prediction of the stiffness coefficient of the translational spring placed at the left end of the cantilever.

Exact stiffness	Stiffness predicted based on frequencies	Stiffness predicted based on Haar coefficients
57	55.3327	54.8327
145	143.6753	150.2754
225	228.5777	231.8532
297	293.7516	297.0932
337	337.2109	339.1035
393	396.1568	396.1999
441	440.2295	438.4284
481	477.1500	477.2706
505	500.8022	497.5804
553	551.6345	549.9034
617	620.7470	620.1079
729	726.6735	731.1058
777	772.6530	773.4868
801	797.6877	797.6564
913	919.0898	917.7227
χ^2	0.0239	0.0512

- composition of a 110-pattern training set and a 15-unknown-pattern test set
- creation and training of the feed-forward ANN with one hidden layer

The second method is updated to the following steps:

- construction of the first mode shape
- the mode transformation into 16 Haar coefficients
- composition of a 110-pattern training set and a 15-unknown-pattern test set
- creation and training of the feed-forward ANN with one hidden layer

In order to compare the performances of the methods, the chi-square test is performed: the smaller $\boldsymbol{\chi}^2$ is, the more accurate is the prediction. For predicting the stiffness coefficients, the ANNs were created in the MATLAB environment using the Neural Network Toolbox and Intel Pentium III Xeon processor with 2,4 GHz and 3,46 GB of RAM.

Numerical examples

First, the suggested approaches for the elastic parameter identification were applied to the cantilever with a translation spring on the right. The results can be seen in Table 1.

Secondly, the proposed methods were examined on the cantilever with rotational and translational spring support at the distance of 0.2 units from the left end. The NN predicted the stiffness coefficient of the rotational spring; the translational spring coefficient was fixed to 10. The results are presented in Table 2.

Concluding remarks

In the present paper, the free vibrations of the beams with non-classical boundary conditions were studied using two different approaches: the first method was based on the natural frequen-

Table 2. Prediction of the stiffness coefficient of the rotational spring placed in the intermediate of the cantilever.

Exact stiffness	Stiffness predicted based on frequencies	Stiffness predicted based on Haar coefficients
57	54.3689	55.4120
145	145.6795	145.4038
225	224.2490	223.9381
297	299.1908	298.8477
337	337.1403	339.5338
393	390.1646	392.3984
441	439.0274	438.3825
481	482.3506	477.1660
505	508.1855	502.8082
553	556.2718	553.8683
617	616.9037	619.0140
729	724.1373	725.1305
777	774.2796	775.0439
801	800.4138	800.9546
913	917.9655	918.5208
χ^2	0.0190	0.0136

cies and NN; the second one transferred the mode shape into 16 Haar coefficients that were used for the same NN training. The accuracy of the predictions were quite precise and relatively similar to each other (the χ^2 error was near 2 and 5 per cent, respectively); however, the method based on Haar coefficients required five times less data and time.

Acknowledgement

Financial support from the Estonian Science Foundation under Grant ETF 8830 and SF0180008s12 are gratefully acknowledged.

References

[1] H. Saito and K. Mori Vibrations of a beam with non-linear elastic constraints. *Journal of Sound and Vibration*, 66(1):1–8,1979.

[2] J.R. Banerjee and H. Su Development of a dynamic stiffness matrix for free vibration analysis of spinning beams. *Computers & Structures*, 82(23-26):891–2197,2004.

[3] L. Wang, J. Ma, J. Peng, L. Li Large amplitude vibration and parametric instability of inextensional beams on the elastic foundation. *International Journal of Mechanical Sciences*, 67:1–9,2013.

[4] S. Haykin. *Neural networks: a comprehensive foundation*. Prentice Hall, Englewood Cliffs, New Jersey, 1999.

[5] H. Hein, L. Feklistova Computationally efficient delamination detection in composite beams using Haar wavelets. *Mechanical Systems and Signal Processing*, 25(6):2257–2270,2011.

Proceedings of the 26th Nordic Seminar on Computational Mechanics
A. Logg, K.A. Mardal, A. Massing (Eds.)

Implementation of a state-of-the-art cohesive zone element for ANSYS Mechanical

J. Glud[1], E. T. Christensen[1], E. Lindgaard[1], and B. L. V. Bak[1]

[(1)]Department of Mechanical and Manufacturing Engineering, Aalborg University, Fibigerstraede 16, 9220 Aalborg Oest, Denmark, jag@m-tech.aau.dk

Summary. This paper describes the implementation and verification of a state-of-the-art user programmed cohesive zone element in the commercial finite element package ANSYS Mechanical. The user programmed element is benchmarked against the Ansys Mechanical cohesive element, INTER205. Convergence rates are better than INTER205 by 15% to 100% and extra possibilities regarding data output have been added. A standard practice to overcome convergence difficulties when using a coarse mesh with cohesive zone elements is to lower the onset traction. A study is presented which demonstrates that this practice may lead to underestimated load carrying capability.

Key words: cohesive zone modelling, composite structures, user programmed, ANSYS Mechanical, finite element, fracture mechanics.

Introduction

The work presented in this paper is a part of the master thesis project [1]. The master thesis treats the formulation of a cohesive zone finite element and analyses of wrinkle defects using cohesive zone elements. The master thesis was carried out in collaboration with Siemens Wind Power A/S. Siemens Wind Power A/S manufactures wind turbine blades made of glass-epoxy-balsa laminates and the entire blade is cast in a single process using vacuum assisted resin transfer moulding. In the infusion process of large glass-epoxy-balsa composite structures, such as wind turbine blades, several types of manufacturing defects can arise [3]. Among these manufacturing artifacts are wrinkle defects. Wrinkle defects are out-of-plane fiber misaligments, which might initiate delaminations leading to structural collapse of the blade during operation. The occurrence of wrinkle defects presents a great expense in the production of the blades since they are, in most cases, repaired due to lack of reliable methods of estimating the reduction in load carrying capability [3]. In order to characterise whether a given wrinkle defect is detrimental for the structural integrity of the blade, it is necessary to be able to predict the onset of delamination and its development. The cohesive zone modelling (CZM) approach provide such capabilities and was therefore chosen for the analysis of wrinkle defects.

CZM is an indirect way of applying classical fracture mechanics, where the critical energy release rate is represented by the work of tractions acting on the crack faces. The research field within the implementation of CZM into the framework of the finite element method has several contributions. The element presented here is based on the work of [4] and [5].

A user programmed element was chosen for the analysis of wrinkle defects since all options affecting results and convergence rates would be accessible to the user. This is not the case for commercially implemented cohesive finite elements. Among these options can be mentioned: order of integration, mode interaction criterion, computation of tangent stiffness matrix and internal force vector as well as non-standard result output such as element damage and average

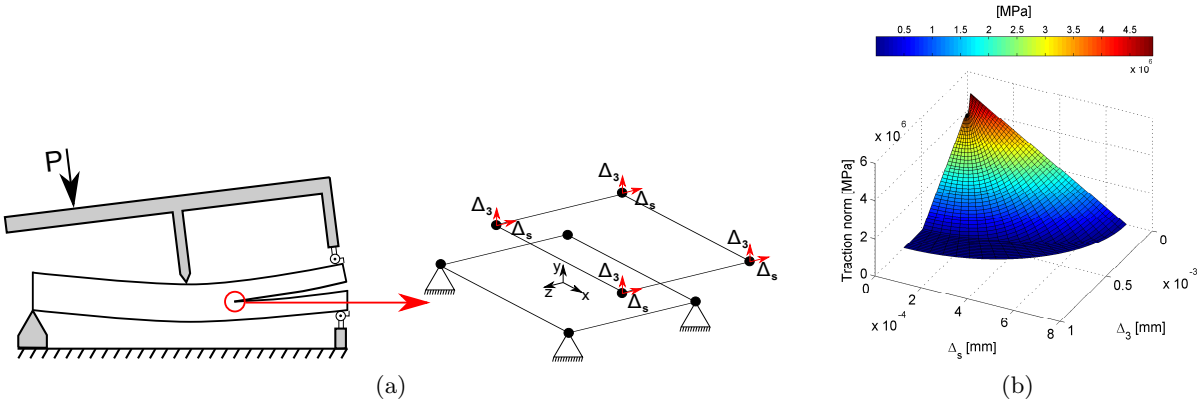

(a) (b)

Figure 1: a) single element model undergoing rigid body translation and rotation as well as relative displacements. b) surface plot of tractions in the relative opening space.

mode mixity. Furthermore, a user programmed element provides a framework in which further research can be conducted. It was chosen to implement the user programmed feature (UPF) in the ANSYS Mechanical finite element package for several reasons. ANSYS Mechanical provides a thorough documentation for implementing user programmable features along with extensive possibilities of accessing the wanted data from the element routine. ANSYS Mechanical also provides tools for plotting results of UPFs and it is possible to create and modify models through the Ansys Parametric Design Language (APDL). APDL is well suited for parametric studies, which come in handy when wrinkle defects of various sizes and compositions are to be analysed. The work carried out regarding analysis of the strength of wrinkle defects is presented in [2].

Element formulation and verification

The developed UPF is a bilinear eight-noded isoparametric element with zero thickness. The element uses a bilinear traction-displacement law and is capable of simulating mixed mode crack development in 3D. The Benzeggagh-Kenane (BK) criterion [9] is used to determine equivalent properties for a given mode mixity as done in [4]. The damage evolution law is based on a single scalar damage parameter and the quadrature rule is 1. order Newton-Cotes. The computation of the tangent stiffness matrix is simplified by neglecting contributions from changing mode mixity and changing geometry from substep to substep. This simplification is made due to computational efficiency and because it is assumed that the mode mixity and geometry will change slowly. Using the UPF the global problem is turned into a nonlinear problem due to the nonlinear constitutive law and nonlinear geometric relations of the crack interfaces. Under displacement control the problem can be solved using the standard Newton-Raphson solver and under load control an equilibrium path tracing algorithm such as e.g. the Arc-Length method has to be used since snapthroughs and snapbacks may occur in simulations.

The element was verified using a two step procedure. In step one the element kinematics along with the material model was verified on a single element model shown to the right in Figure 1a. Different rigid body rotations and translations were applied to the element in order to check if convergent solutions were obtained, and thereby verify that the element kinematics was implemented correctly. For the different configurations tested, a surface plot of the traction norm in the opening space spanned by the relative displacement in the x- and y-direction of the element coordinate system was made. The surface plot of the traction norm in the relative displacement space can be seen in Figure 1b. The implementation of the material law was then validated by comparing the obtained results with a material law programmed in MATLAB.

In step two the element was validated by simulating the physical test specimens; double cantilever beam (DCB), end notch flexure (ENF) and mixed mode bending (MMB) and comparing

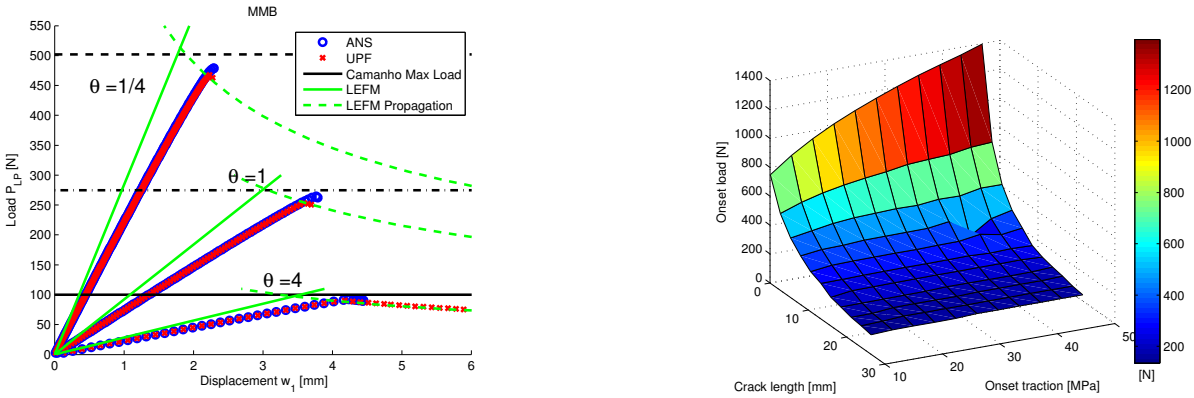

(a) (b)

Figure 2: a) Load-displacement curves for MMB tests with different mode mixities. b) Surface plot of load at which unstable crack growth occurs for varying crack lengths and onset tractions.

	$\theta = 1/4$		$\theta = 1$		$\theta = 4$	
Method	Load [N]	Iterations	Load [N]	Iterations	Load [N]	Iterations
ANS	478.5	457	264.3	390	92.2	276
UPF	467.5	387	253.1	189	90.0	128
LEFM	513.5	-	277.5	-	97.3	-
Experimental	518.7	-	275.4	-	108.1	-

Table 1: Number of iterations used and load at which unstable crack propagation occurs for different mode mixities.

with the INTER205 element (ANS) in ANSYS, Linear Elastic Fracture Mechanics (LEFM) and with experiments from [6]. The FE models are meshed with 1600 elements in the length direction of the specimens in order to obtain convergent solutions for the required onset traction of 80MPa to 100MPa. The results obtained from the MMB tests are shown in Figure 2a. The mode mixity for each test is given as $\theta = \frac{G_I}{G_{II}}$. The UPF element gives the same results as the ANS on most parts of the curves and shows faster convergence (see Table 1). The reason for the difference in results between UPF and ANS is believed to be the different mode interaction criteria used. It is also seen that LEFM predicts a stiffer response and higher load for unstable crack growth. A model using CZ elements becomes more compliant than LEFM predicts because the interfaces in the cohesive zone are allowed to separate some distance defined by the constitive law before crack propagation starts.

Influence of the onset traction on the predicted load carrying capability

Using CZ elements in an FE model can potentially make the model difficult to solve due to convergence difficulties. Substantial research have been carried out in order to overcome such difficulties. Among studies on this subject can be mentioned [4], [5], [7] and [8]. Suggestions for improving the chance of convergence are e.g. modifying the tangent stiffness, lowering the penalty stiffness, increasing order of integration, lowering the onset traction and to use a very fine mesh in the damage process zone.

The DCB, ENF and MMB simulations were meshed with a mesh so fine that it would be impractical to use in the simulations of wrinkle defects. From [7] it is known that one way to use a coarser mesh without sacrifising convergence is to lower the onset tractions. This is because it enlarges the cohesive zone resulting in more elements present in this region. In order

to overcome convergence difficulties when simulating wrinkle defects in [2] the onset tractions were lowered until convergence for a reasonable amount of elements was observed. In order to clarify which influence lowering the onset traction has on the predicted load carrying capability, a parametric study was conducted on the DCB specimen. The parameters varied were initial crack length and the onset traction. The results from the study are shown in the surface plot in Figure 2b. It is clear that for long cracks the choice of onset traction has an insignificant influence on the predicted load for the onset of unstable crack growth. This means that for long cracks, the energy release rate is the governing parameter. It is also observed that the predicted load for a short crack is highly dependent on the choice of onset traction. This is because the length of the cohesive zone is large compared to the crack length and the added compliance from the cohesive zone becomes significant. The study shows that if information regarding crack propagation is sought, lowering the onset traction is an acceptable way of reducing the demand for the required number of elements. However, crack initiation is highly dependent of the onset traction, since crack initiation can be seen as the limit case of decreasing the crack length. This has the implication, that the onset traction can not be lowered arbitrarily in order to obtain convergence if crack initiation is to be examined since, if the onset traction is lowered, non-physical behaviour of the model may be experienced.

References

[1] E. T. Christensen, J. Glud and J. Sjølund. *Formulation of Cohesive Finite Element for Analysing Strength of Wrinkles in Glass-Epoxy Laminates*. Master Thesis, Department of Mechanical and Manufacturing Engineering, Aalborg University, Denmark, 2013.

[2] E. T. Christensen, J. Glud, E. Lindgaard and B. L. V. Bak. *Analysing the Strength of Wrinkle Defects in Glass-Epoxy Laminates*. Proceedings of the 26th Nordic Seminar on Computational Mechanics, Eds. A. Logg, K.A. Mardal, Oslo, Norway, October 23-25, 2013.

[3] M. Leong. *The Influence of Defects on the Failure of Wind Turbine Blades*. Ph.D. Thesis, Department of Mechanical and Manufacturing Engineering, Aalborg University, Denmark, 2012, ISBN: 87-91464-44-7.

[4] A. Turon. *Simulation of Delamination in Composites under Quasi-Static and Fatigue Loading using Cohesive Zone Models*. Ph.D. thesis, Universitat De Girona, Spain, 1st edition, 2006, ISBN: 978-84-690-4372-1.

[5] V. K. Goyal. *Analytical Modeling of the Mechanics of Nucleation and Growth of Cracks*. Ph.D. thesis, Faculty of Virginia Polytechnic Institute and State University, USA, 2002.

[6] P. P. Camanho, C. G. Dávila, and M. F. D. Moura. *Numerical Simulation of Mixed-mode Progressive Delamination in Composite Materials*. Composite Materials, 37(16):1415-1438, 2003.

[7] A. Turon, C. G. Dávila, P. P. Camanho and J. Costa. *An Engineering Solution for Mesh Size Effects in the Simulation of Delamination using Cohesive Zone Models*. Engineering Fracture Mechanics, 74:1665-1682, 2007.

[8] B.L.V. Bak and E. lund. *Reducing the Integration Error of Cohesive Elements*. Proceedings of the 24th Nordic Seminar on Computational Mechanics, Eds. A. Logg, K.A. Mardal, Oslo, Norway, October 3-4, 2011.

[9] M.L. Benzeggagh and M. Kenane. *Measurement of Mixed-Mode Delamination Fracture Toughness of Unidirectional Glass/Epoxy Composites with Mixed-Mode Bending Apparatus*. Composites Science and Technology, 49:439-449, 1996.

Proceedings of the 26th Nordic Seminar on Computational Mechanics
A. Logg, K.A. Mardal, A. Massing (Eds.)

Using 3D gesture controls for interacting with mechanical models

D. Åkesson[1] and J. Lindemann[2]

(1)Division of Structural Mechanics, PO Box 118, 221 00 Lund, daniel.akesson@construction.lth.se
(2)Division of Structural Mechanics, PO Box 118, 221 00 Lund, jonas.lindemann@byggmek.lth.se

Summary. Leap Motion is a 3D gesture-control device that was launched in July 2013. The device can track movement of fingers and hands down to 1/100 mm, it also comes with a software development kit that makes it easy to implement into existing software. This paper describes how the Leap Motion can be implemented into an existing 3D application.

Key words: 3D user interfaces, leap motion, gestures, mechanics software

Introduction

Leap Motion is a 3D gesture-control device with high finger tracking accuracy. Creating 3D user interfaces with mouse and keyboard as input devices have always been challenging both for developers and users. Using 3D gestures using a device like Leap Motion could improve the usability for 3D based user interfaces.

Structural Mechanics in Lund have a long experience in creating user interfaces that support conceptual design by using direct-manipulation. A good example of this is Sketch-a-Frame [1], a 2D FE application for the iPad, where the user can quickly model a geometry using the multi-touch interface of the iPad. As changes are made to the model the result is visualised in real-time, enhancing the users understanding of the structure.

The goal of this work is to bring the same feeling of direct manipulation as in Sketch-a-Frame to three dimensions, using the Leap Motion device.

ObjectiveFrame

ObjectiveFrame is a 3D beam analysis application, that can visualise the response of a structure to a user-defined load in real-time [2]. The application is developed as an educational tool for design-, architecture- and structural mechanics students. The mouse is used as an input device which has limited input interaction in a 3D environment. It is written in C++ with the cross-platform GUI toolkit FLTK [4].

Figure 1. The Leap Motion device in use.

Leap motion

The Leap Motion device (see Figure 1) is placed on the desktop and it then tracks all movement of hands, fingers and tools such as a pen [3]. The interaction area is 0.6m above the device, by 0.6m on each side and by 0.6m in depth on each side (see Figure 3). It can track movements at an accuracy of 1/100 mm. The device consists of two cameras and three infrared LEDs, making the device very slim.

The Leap Motion software development toolkit (SDK) has support for most common programming languages. With the SDK implemented position, velocity and direction for fingertips, hands and tools can be used, making the device easy to implement into existing applications.

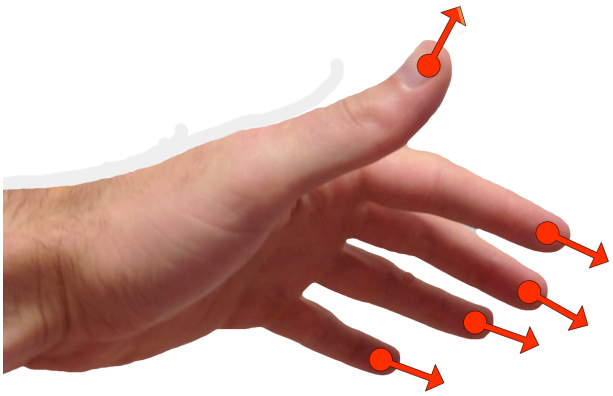

Figure 2. The fingertips direction vectors.

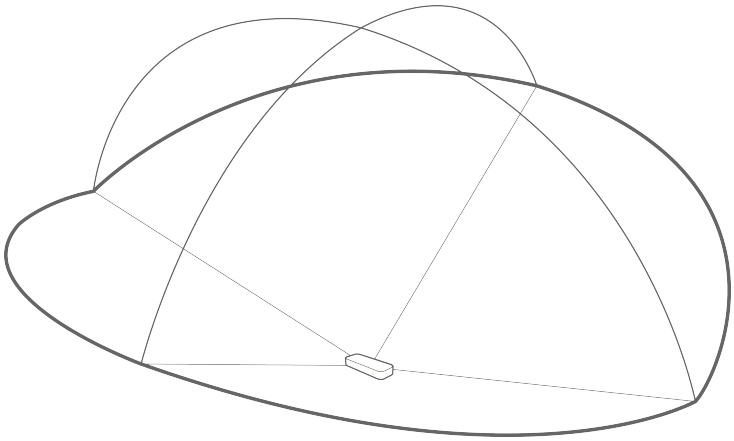

Figure 3. The Leap Motion interaction area.

Implementation in ObjectiveFrame

The Leap Motion SDK is linked to the existing ObjectiveFrame code using CMake [5], the 3D vectors and positions are retrieved are scaled to the ObjectiveFrame coordinate system. When the controller detects two fingers 3D cone objects are visualised with position and direction set to give the user a visual representation of the fingers in the ObjectiveFrame space (see Figure 4). The two fingers can select which node to interact with using a pinch gesture. When a node is selected it can either be moved or its force vector can be altered using the fingers position. Combined with real-time calculations it gives the user a feeling of direct manipulation, enhancing the users understanding of the structural behaviour of the model.

The Leap Motion is also used to change the users viewpoint. If one hand and five fingers are detected the viewpoint will change with the hands velocity and angel. Moving the hand to the left or right rotates the view, moving the hand forward or backward for zoom and tilting the hand changes the vertical angel of the viewpoint. Two hands can be used for panning.

The result is an application where the user can move around in a 3D environment, and interact with the model using only hand gestures.

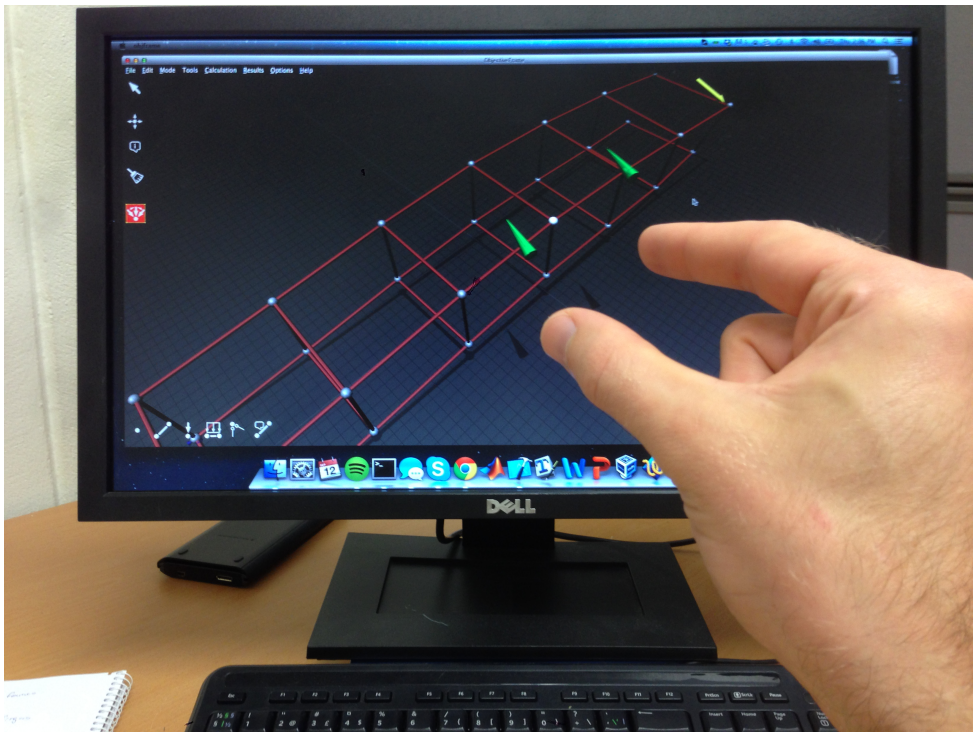

Figure 4. The application with fingers interacting.

References

[1] D. Åkesson. Interaction models for 2D finite element modeling on touch devices *Master's dissertation, Department of Construction Sciences, LTH, Lund*, ISSN 0281-6679 (2013)

[2] J. Lindemann, O. Dahlblom, G. Sandberg. Objective Frame - An educational tool for understanding the behaviour of structures *Proceedings of CONVR 2001*

[3] Leap Motion *http://www.leapmotion.com*

[4] Fast Light Toolkit (FLTK) *http://www.fltk.org*

[5] CMake *http://www.cmake.org/*

Proceedings of the 26th Nordic Seminar on Computational Mechanics
A. Logg, K.A. Mardal, A. Massing (Eds.)

Time-efficient integrator for solving the marine vessel equations of motion by splitting schemes

Elena Celledoni[1] and Nataliya Ramzina[1]

(1)Department of Mathematical Sciences Norwegian University of Science and Technology, 7491 Trondheim, nataliya.ramzina@math.ntnu.no

Summary. In the present study we investigate the applicability of splitting schemes to integrate the equations of motion of a marine vessel model. High order splitting schemes were applied to the numerical solution of a rigid body model subject to torque. The performance of the algorithm has been compared with a classical Runge-Kutta method. The obtained results suggest that the method can compete with traditional solvers for this specific problem.

Key words: Time-efficient integrator, splitting method, marine vessel

Introduction

In the past years we have seen a significant increase in the use of energetic resources, and the search for oil and gas deposits has become increasingly challenging. Locations of the new deposits are often found to be in deep waters which makes oil extraction a more demanding task. One concrete example is the pipe-laying process from marine vessels, where the damaging of the pipes can result in big operational costs.

This marine operation requires high precision in positioning the vessel. The speed and capability of prediction of the dynamical properties of the vessel is crucial in such problems. Vessel location becomes especially important in high waves where errors in numerical simulations could cause critical deformations of the pipes. Those issues are indicating that predicting marine vessel dynamics is a challenging and relevant engineering task.

In the present study we investigate splitting methods applied to a marine vessel model which is taken as an example. For simplicity of modelling, the control inputs of the vessel have been turned off. We start with the formulation of the mathematical model for the marine vessel followed by the description of the numerical scheme. The results are summarised in Figure 1 and future prospects are discussed.

Mathematical formulation

The theoretical background we use in the present work was introduced and developed in [9], [7]. Briefly, the marine vessel has six degrees of freedom (6DOF) and obeys the general equation of motion:

$$M\dot{\boldsymbol{\nu}} + C(\boldsymbol{\nu})\boldsymbol{\nu} + D(\boldsymbol{\nu})\boldsymbol{\nu} + g(\boldsymbol{\eta}) = \boldsymbol{\tau}, \tag{1}$$

where M is the inertia matrix of the system, $\boldsymbol{\nu} = [\mathbf{v}^T \boldsymbol{\omega}^T]^T \in \mathbb{R}^6$ is generalized velocity matrix consisting of linear velocity $\mathbf{v}$ and angular velocity $\boldsymbol{\omega}$, $C(\boldsymbol{\nu})$ is the matrix of Coriolis and centripetal forces, $D(\boldsymbol{\nu})$ is the matrix of damping forces, $\boldsymbol{\eta} = [\mathbf{p}^T \boldsymbol{\theta}^T]^T \in \mathbb{R}^6$ is vector of generalized coordinates expressed in terms of the position vector $\mathbf{p}$ and the vector of Euler angles

$\boldsymbol{\theta} = [\phi, \theta, \psi]^T$, $g(\boldsymbol{\eta})$ is the generalized vector of gravitational and buoyancy forces and moments, and $\boldsymbol{\tau}$ the vector of control forces and environmental disturbances such as wind, waves and currents.

In order to apply the splitting method we now rewrite (1) obtaining the following system of four differential equations of motion:

$$\left.\begin{aligned} \dot{\mathbf{m}} &= \mathbf{m} \times T^{-1}\mathbf{m} + A_1\mathbf{m} + \boldsymbol{\tau}_1, \\ \dot{\mathbf{q}} &= \frac{1}{2}\mathbf{q}\Omega, \\ \dot{\mathbf{v}} &= -\widehat{\omega}\mathbf{v} + \frac{1}{m_v}(A_2\mathbf{v} + \boldsymbol{\tau}_2), \\ \dot{\mathbf{p}} &= \Sigma(\mathbf{q})\mathbf{v}, \end{aligned}\right\} \quad \text{6DOF equations of motion} \tag{2}$$

where $\mathbf{m} = (m_1, m_2, m_3)^T$ is the angular momentum, $T = diag\,(T_1, T_2, T_3)$ is the tensor of inertia, A_1 and A_2 are the matrices of external forces applied to added mass and rigid body respectively, $\boldsymbol{\tau}_1$ and $\boldsymbol{\tau}_2$ are the vectors of input control forces applied to the added mass and rigid body respectively, $\mathbf{q}$ is a unit quaternion describing the rotation of the body, $\Omega = (0, T^{-1}\mathbf{m})$ is a quaternion in the Lie algebra $\mathfrak{s}^3$ and $T^{-1}\mathbf{m} = \boldsymbol{\omega}$ is the angular velocity, $\widehat{\omega}$ is the transformation of the vector $\boldsymbol{\omega} = (\omega_1, \omega_2, \omega_3) \in \mathbb{R}^3$ to the corresponding skew-symmetric matrix, m_v is the mass of the vessel, $\mathbf{p}$ is the position in a spatial frame, $\Sigma(\mathbf{q})$ is the Euler Rodriguez map transforming quaternions into rotation matrices.

We use a quaternion formulation to express the rotation between the laboratory and the vessel-fixed spacial frames. The quaternion formulation avoids kinematic singularities featured for Euler angles and is globally defined, but should be used with care in problems of rigid body attitude control [5].

Numerical integration

The numerical integrator for the equations of motion (2) is performed using splitting schemes as it was developed and successfully applied in several studies ([6], [8], [2]). We have employed Störmer/Verlet and higher order splittings.

The vector field of the vessel model is the sum of two exactly solvable parts, whose flows can be adequately composed by the splitting scheme to achieve high order. The splitting results in two subsystems of ordinary differential equations. The first subsystem is a free rigid body motion[1] and can be integrated exactly. An explicit solution can be obtained by using Jacobi elliptic functions and has been implemented to machine accuracy following the techniques presented in [2], [3], [4]. The remaining part is a system of linear differential equations which could be solved by the standard variation of constants formula. To obtain high order, we adopt optimised splitting techniques devised by Blanes et al. [1] and the result is a very efficient method. The splitting scheme is symmetric.

The control forces during the integration have been turned off for simplicity of the calculations; i.e., the vectors $\boldsymbol{\tau}_1$ and $\boldsymbol{\tau}_2$ have been set to zero.

Results and discussion

All the computations have been performed on a time interval $t = 10s$. The number of integration steps have been set ranging from 2^1 up to 2^9 and equally spaced in logarithmic scale. The solution for comparison have been calculated employing 10^4 integration steps. Splitting schemes of the second, fourth and sixth order have been tested in the current work. The coefficients of splitting schemes are well tabulated in the literature ([1]). The evaluation of CPU time

[1]It includes in fact also the equations for linear velocity which is however constant in this integration.

used for the calculations have been performed directly in MATLAB® by measuring the time interval between the initiation of the algorithm and completion of the calculation. The main output variables of the algorithm are values of momentum, quaternion, velocity and position. All calculation performed on a single core of four-core laptop Lenovo THINKPAD T520 with 2.3GHz and 4GB RAM.

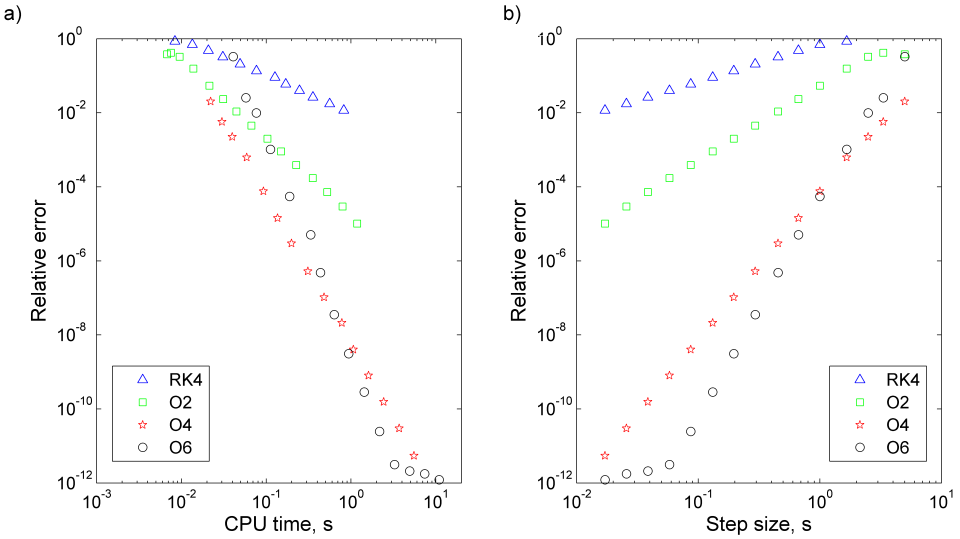

Figure 1. Dependence of the relative error on the CPU time (a) and on the step size (b). Results for the second (□), the fourth (⋆) and the sixth order (◯) splitting schemes as well as for the Runge-Kutta method (△) are plotted. The data for each point is averaged over 10 runs.

The performance of the algorithm is well represented by the plot of the relative error against the CPU time (Figure. 1a). The result for the Runge-Kutta method is plotted in the same coordinates. Those plots exhibit a power law dependence. The slope of the curve is larger for higher orders of the splitting. The curves intersect at relative errors about 10^{-2}; i.e., to achieve precision more than 1% the higher order splitting scheme is more time-efficient. The degeneration of the trend is achieved when the accuracy exceeds about 10^{-12}. This limit is possibly a software-induced effect due to the double-precision computer calculations. The ordinary limit for double-precision arithmetics is about 10^{-16} but larger error accumulates due to the large number of iterations.

The additional gain in computational resources is achieved due to exponential dependence of the error ϵ on the integration time step h so that $\epsilon = ah^n$, where n is order of the splitting and a is a constant depending on the final solution. Such a dependence is shown in Figure. 1b. On the other hand the amount of calculations is proportional to the number of integration steps. Therefore the dependence of the accuracy of calculations on the CPU time is exponential as it is visible from Figure 1a.

Conclusion

In the current work, we applied splitting schemes to resolve the dynamics of a marine vessel. We compared the CPU time required to accomplish the calculations with the relative error of calculations. The results suggest that higher order splitting schemes achieve the aimed precision faster compared to classical Runge-Kutta schemes. The use of splitting schemes became more popular in scientific simulation in the past decade and this study confirms there is a potential for the use of such schemes also in engineering problems.

Acknowledgements

This research was supported by a Marie Curie International Research Staff Exchange Scheme Fellowship within the 7th European Community Framework Programme. The authors would like to acknowledge the support from the GeNuIn Applications project funded by the Research Council of Norway, and part of the work was carried out while the authors were visiting Massey University, Palmerston North, New Zealand and La Trobe University, Melbourne, Australia.

References

[1] S. Blanes and P.C. Moan. Practical symplectic partitioned Runge-Kutta and Runge-Kutta-Nyström methods *Journal of Computational and Applied Mathematics*, 142:313–330, 2002.

[2] E. Celledoni and N. Säfstöm. Efficient time-symmetric simulation of torqued rigid bodies using Jacobi elliptic functions. *Journal of Physics A*, 39:5463–5478, 2006.

[3] E. Celledoni, F. Fassó, N. Säfström and A. Zanna. The exact computation of the free rigid body motion and its use in splitting methods *SIAM Journal on Scientific Computing*, 30:4:2084–2112, 2008.

[4] E. Celledoni and A. Zanna. FRB-FORTRAN routines for the exact computation of free rigid body motions *ACM ToMS*, vol 37 nr. 2 (2010).

[5] N.A. Chaturvedi, A.K. Sanyal and N.H. McClamroch Rigid-Body Attitude Control *IEEE Control Systems Magazine*, 31:3:30–51, 2011.

[6] A. Dullweber, B. Leimkuhler, and R. McLachlan. Symplectic splitting methods for rigid body molecular dynamics. *J. Chem. Phys*, 107:5840–5851, 1997.

[7] T.I. Fossen. *Marine Control Systems*. Marine Cybernetics, 2002.

[8] M. Geradin and A. Cardona. *Flexible Multibody Dynamics*. Wiley and Sons Ltd., 2001.

[9] T. Perez and T.I. Fossen. Kinematic Models for Manoeuvring and Seakeeping of Marine Vessels *Modeling, Identification and Control*, 28:1:19–30, 2007.

Proceedings of the 26th Nordic Seminar on Computational Mechanics
A. Logg, K.A. Mardal, A. Massing (Eds.)

Beam section stiffness properties using 3D finite elements

Philippe Couturier, Steen Krenk, and Jan Høgsberg

Department of Mechanical Engineering,
Technical University of Denmark, Kgs. Lyngby, Denmark
phicout@mek.dtu.dk, sk@mek.dtu.dk, jhg@mek.dtu.dk

Summary. The cross-section properties of a beam is characterized by a six by six stiffness matrix, relating the six generalized strains to the conjugate section forces. The problem is formulated as a single-layer finite element model of a slice of the beam, on which the six deformation modes are imposed via Lagrange multipliers. The Lagrange multipliers represent the constraining forces, and thus combine to form the cross-section stiffness matrix. The theory is illustrated by a simple isotropic cross-section.

Key words: cross-section analysis, coupled beam deformation, anisotropic beam

Introduction

With recent advances in manufacturing capabilities, beams with more complex geometries and materials with general anisotropy are being used in wind turbine blades. While the global response of the blades can be represented by a beam model, the accuracy depends on the use of appropriate description of the cross-section properties, including coupling from e.g. pretwist and material anisotropy. Several theories have been developed to calculate the cross-section properties of beams. Many are based on simplifications which limits their use to simple geometries or isotropic materials [1]. Two methodologies have been found to provide the correct stiffness matrix for most engineering structures which are based on advanced kinematic analysis of beams, namely the theories developed by Giavotto et al. [2] and Hodges and Yu [3], respectively.

This papers presents a method to calculate the cross-section stiffness matrix of the deformation modes of classic beam theory. The method is based on the analysis of a thin slice of the beam, on which the six modes of deformation corresponding to the equilibrium modes are imposed by use of Lagrange multipliers. Each deformation mode corresponds to activating one kinematic degree-of-freedom, while setting the remaining five to zero. Thus, each kinematic load case generates six Lagrange multipliers, representing the section forces needed to impose that particular kinematic mode. Together the six sets of Lagrange multipliers, each with six components, form the cross-section stiffness matrix. The analysis is carried out by a three-dimensional finite element model of a thin slice of the beam. This format enables correct representation of effects like transverse contraction and coupling due to anisotropy.

The slice approach

The properties of a cross-section of a beam can be assessed by considering a thin slice of the beam as shown in Fig. 1. The slice is given a unit thickness for numerical simplification. The slice is characterised by six equilibrium states, namely extension, two homogeneous shear components, torsion, and two homogeneous bending components. The stiffness matrix linking the equilibrium states and their conjugate six deformation modes can be determined by imposing a displacement of the end cross-section planes of the slice and calculating the required forces. The degrees of

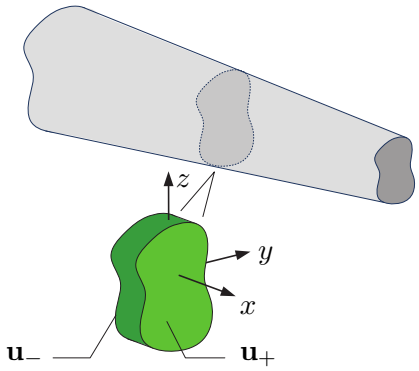

Figure 1. Unit slice of a beam with front and back face

freedom of the slice are defined in terms of the displacements at the front (+) and back (−) face of the slice as $\mathbf{u}_\pm = \left[\mathbf{u}_1^T, \mathbf{u}_2^T, \cdots \mathbf{u}_n^T\right]_\pm^T$, where n is the number of nodes and $\mathbf{u}_i$ defines the 3D displacements at the node i.

The six deformation load cases

The properties of the slice are analysed using the finite element method. Within linear elasticity the stiffness equations of the slice take the following block matrix format

$$\begin{bmatrix} \mathbf{K}_{++} & \mathbf{K}_{+-} \\ \mathbf{K}_{-+} & \mathbf{K}_{--} \end{bmatrix} \begin{bmatrix} \mathbf{u}_+ \\ \mathbf{u}_- \end{bmatrix} = \begin{bmatrix} \mathbf{f}_+ \\ \mathbf{f}_- \end{bmatrix}, \tag{1}$$

The deformation modes are defined in terms of differences in displacement at the two sides of the slice and it is therefore convenient to rewrite the stiffness equations in terms of increments and mean values

$$\Delta\mathbf{u} = \mathbf{u}_+ - \mathbf{u}_-, \qquad 2\bar{\mathbf{u}} = \mathbf{u}_+ + \mathbf{u}_-. \tag{2}$$

Substitution into (1) gives

$$\begin{bmatrix} (\mathbf{K}_{++} - \mathbf{K}_{+-} - \mathbf{K}_{-+} + \mathbf{K}_{--}) & (\mathbf{K}_{++} + \mathbf{K}_{+-} - \mathbf{K}_{-+} - \mathbf{K}_{--}) \\ (\mathbf{K}_{++} - \mathbf{K}_{+-} + \mathbf{K}_{-+} - \mathbf{K}_{--}) & (\mathbf{K}_{++} + \mathbf{K}_{+-} + \mathbf{K}_{-+} + \mathbf{K}_{--}) \end{bmatrix} \begin{bmatrix} \Delta\mathbf{u} \\ 2\bar{\mathbf{u}} \end{bmatrix} = 2\begin{bmatrix} \mathbf{f}_+ - \mathbf{f}_- \\ \mathbf{f}_+ + \mathbf{f}_- \end{bmatrix}. \tag{3}$$

In order to define the deformation of the slice explicitly in terms of the deformation modes, the displacement vector is further transformed as to include the six generalized strains $\boldsymbol{\gamma} = [\varepsilon_x\ \varepsilon_y\ \varepsilon_z\ \kappa_x\ \kappa_y\ \kappa_z]^T$. The components ε_x, ε_y and ε_z represent the axial strain and both generalized shear strains respectively. Similarly, the components κ_x, κ_y and κ_z represent the rate of twist and both bending curvatures respectively. If one uses elements with Hermitian interpolation of the transverse displacements in the axial direction and nodal degrees of freedom defined as $\mathbf{u}_i = [u, v, w, u', v']_i^T$, the transformation is done by defining the difference in displacement, $\Delta\mathbf{u}$, as

$$\Delta\mathbf{u} = \boldsymbol{\Phi}\mathbf{u}_\gamma, \tag{4}$$

where $\mathbf{u}_\gamma = \left[\boldsymbol{\gamma}^T, \Delta u_1', \Delta v_1', \cdots, \Delta u_n', \Delta v_n'\right]^T$. The transformation matrix $\boldsymbol{\Phi}$ takes the form

$$\boldsymbol{\Phi} = \begin{bmatrix} \boldsymbol{\Gamma}_1 & \boldsymbol{\Theta}_1 & & \\ \vdots & & \ddots & \\ \boldsymbol{\Gamma}_n & & & \boldsymbol{\Theta}_n \end{bmatrix}. \tag{5}$$

The matrix $\boldsymbol{\Gamma}_i$ defining the displacement increments and the matrix $\boldsymbol{\Theta}_i$ storing the rotation

increments are defined as

$$\mathbf{\Gamma}_i = \begin{bmatrix} 1 & 0 & 0 & 0 & z_i & -y_i \\ 0 & 1 & 0 & -z_i & 0 & 0 \\ 0 & 0 & 1 & y_i & 0 & 0 \\ 0 & 0 & 0 & 0 & 0 & 0 \\ 0 & 0 & 0 & 0 & 0 & 0 \end{bmatrix}, \qquad \mathbf{\Theta}_i = \begin{bmatrix} 0 & 0 \\ 0 & 0 \\ 0 & 0 \\ 1 & 0 \\ 0 & 1 \end{bmatrix}, \tag{6}$$

where $x_i,\ y_i,\ z_i$ are the global Cartesian coordinates of node i.

Elimination of $\Delta\mathbf{u}$ in (3) by (4) gives

$$\begin{bmatrix} \mathbf{\Phi}^T\mathbf{K}_{11}\mathbf{\Phi} & \mathbf{\Phi}^T\mathbf{K}_{12} \\ \mathbf{K}_{21}\mathbf{\Phi} & \mathbf{K}_{22} \end{bmatrix} \begin{bmatrix} \mathbf{u}_\gamma \\ 2\bar{\mathbf{u}} \end{bmatrix} = 2 \begin{bmatrix} \mathbf{\Phi}^T(\mathbf{f}_+ - \mathbf{f}_-) \\ (\mathbf{f}_+ + \mathbf{f}_-) \end{bmatrix}, \tag{7}$$

where $\mathbf{K}_{ij}$ are the block components of the stiffness matrix in (3).

In order to impose the six deformation modes independently, the values of $\boldsymbol{\gamma}$ are defined via constraints in the form of

$$[\mathbf{C}_\gamma\ \mathbf{C}_f] \begin{bmatrix} \mathbf{u}_\gamma \\ 2\bar{\mathbf{u}} \end{bmatrix}_j = \mathbf{q}_j. \tag{8}$$

The vector $\mathbf{q}_j$ is used to activate one kinematic degree-of-freedom, while setting the remaining five to zero, e.g. for the extension case $\mathbf{q}_1 = [1, 0, 0, 0, 0, 0]^T$. The constraints are added to the system of linear equations using the method of Lagrange multipliers were each constraint is enforced by solving for the associated Lagrange multiplier which acts as the force needed to impose the constraint [4]. As such, if no external forces are applied to the slice, the Lagrange multipliers associated with the generalized strains come out as the generalized forces. Incorporating the constraints and Lagrange multipliers, $\boldsymbol{\lambda}$, to be solved and setting the external forces to zero the system of equations takes the form

$$\begin{bmatrix} \mathbf{\Phi}^T\mathbf{K}_{11}\mathbf{\Phi} & \mathbf{\Phi}^T\mathbf{K}_{12} & \mathbf{C}_\gamma^T \\ \mathbf{K}_{21}\mathbf{\Phi} & \mathbf{K}_{22} & \mathbf{C}_f^T \\ \mathbf{C}_\gamma & \mathbf{C}_f & \mathbf{0} \end{bmatrix} \begin{bmatrix} \mathbf{u}_\gamma \\ 2\bar{\mathbf{u}} \\ \boldsymbol{\lambda} \end{bmatrix}_j = \begin{bmatrix} \mathbf{0} \\ \mathbf{0} \\ \mathbf{q}_j \end{bmatrix}. \tag{9}$$

Using this formulation, the cross-section stiffness matrix can be populated by imposing one displacement mode at a time and solving for the generalized section forces.

It is to be noted that in the case of both shear modes and torsion mode, additional constraints need to be added to enforce that the work is orthogonal to the work done in extension, and both bending cases. Since the internal work equals the external work done by the forces on the nodes, the orthogonality conditions can be expressed as

$$\mathbf{f}_{\pm\alpha}^T\mathbf{u}_{\pm\beta} = 0, \tag{10}$$

where the indices define the displacement modes based on the order set in $\boldsymbol{\gamma}$, i.e. $\alpha = 1,\ 5,\ 6$ and $\beta = 2,\ 3,\ 4$.

Simple example

This section presents the analysis of a square cross-section using an implementation of the methodology described in the previous section. Eight-node elements are used with Hermitian shape functions in the thickness direction. The square has a width of $b = 2$ with a Young's modulus of $E = 1$ and Poisson's ratio of $\nu = 0.3$. The reference axis being at the center, only diagonal terms in the stiffness matrix are non-zero. Furthermore, the diagonal terms come out as EA, GA_y, GA_z, GJ, EI_y, and EI_z, which are the extensional stiffness, shear stiffness about both in-plane axes, the torsional stiffness and bending stiffness about both in-plane axes, respectively.

Table 1. Normalized cross-section stiffness properties for a square

	Mesh size				
	1x1	4x4	9x9	19x19	Analytical
A/b^2	1.000	1.000	1.000	1.000	1.000
$A_y/b^2 = A_z/b^2$	1.000	0.8788	0.8424	0.8353	0.8333
J/b^4	0.1667	0.1479	0.1421	0.1409	0.1408
$I_y/b^4 = I_z/b^4$	0.09619	0.08416	0.08350	0.08338	0.08333

Results obtained using different mesh size and using analytical solutions for isotropic cross-sections are listed in Table 1, illustrating convergence for all parameters towards the analytical solution.

The associated 3D deformation of the six modes are represented graphically in Fig. 2. It can seen that the cubic displacement associated with shear is captured. Furthermore, in the two bending cases, the quadratic curvature in the thickness direction is modelled with the use of a single element via the Hermitian interpolation. Contraction from Poisson's ratio can also be observed.

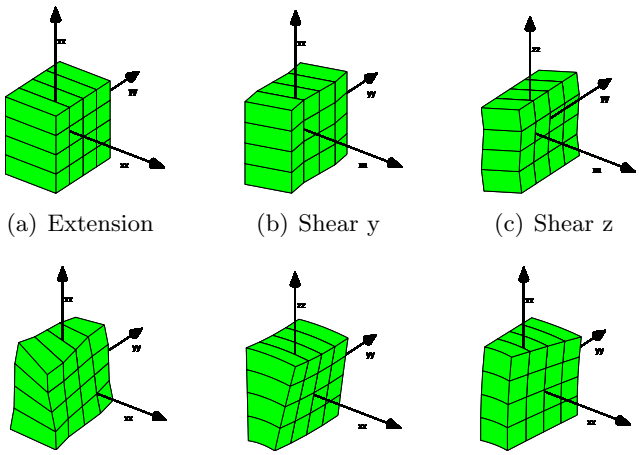

(a) Extension (b) Shear y (c) Shear z

(d) Torsion (e) Bending y (f) Bending z

Figure 2. Elastic beam deformation modes for a square cross-section

References

[1] H. Chen, W. Yu, and M. Capellaro. A critical assessment of computer tools for calculating composite wind turbine blade properties. *Wind Energy*, 13:497–516, 2010.

[2] V. Giavotto, M. Borri, P. Mantegazza, G. Ghiringhelli, V. Carmaschi, G. C. Maffioli and F. Mussi. Anisotropic beam theory and applications. *Computers and Structures*, 16:403–413, 1983.

[3] D. Hodges, W. Yu. A rigorous, engineer friendly approach for modelling realistic, composite rotor blades. *Wind Energy*, 10:179–193, 2007.

[4] R. D. Cook et al., *Concepts and Applications of Finite Element Analysis*. Wiley, 2007.

Proceedings of the 26th Nordic Seminar on Computational Mechanics
A. Logg, K.A. Mardal, A. Massing (Eds.)

Axisymmetric stability of the nonuniform transversely isotropic circular plates

Svetlana Bauer, Eva Voronkova, and Ksenia Ignateva

St. Petersburg State University, Universitetsky prospekt, 28, 198504, St. Petersburg, Russia, s_bauer@mail.ru, voronkova.eva@math.spbu.ru, kseniiaignatieva@gmail.com

Summary. This work is concerned with the numerical study of unsymmetrical buckling of clamped inhomogeneousc plates under uniform pressure. The effect of material heterogeneity on the buckling load is examined. The refined 2D shell theory is employed to obtain the governing equations for buckling of a clamped circular shell. The unsymmetric part of the solution is sought in terms of multiples of the harmonics of the angular coordinate. A numerical method is employed to obtain the lowest load value, which leads to the appearance of waves in the circumferential direction. It is shown that if the elasticity modulus decreases away from the center of a plate, the critical pressure for unsymmetric buckling is sufficiently lower than for a plate with constant mechanical properties.

Key words: axisymmetric equilibrum states, circular plates, buckling

Introduction

Unsymmetric equilibrium states of circular plates appear in a number of either pure engineering (metal or polymer sheets) or biomechanical (human tissue, living cells) applications.

For the first time, unsymmetrical buckling of thin homogeneous circular isotropic plate subjected to surface load was analyzed by Panov and Feodosev in 1948 [6]. Later, Cheo and Reiss examined the same problem [3]. The critical buckling load and the corresponding wave number obtained in [3] and [6] differs significantly from each other. Cheo and Reiss suspected that Panov and Feodos'ev had found unstable unsymmetric state, and underlined the approximation function with two unknown parameters was "too inaccurate to adequately describe the wrinkling of the plate".

This paper is concerned with buckling of a circular plate with varying mechanical characteristics. Such a plate can be used as the simplest model of Lamina Cribrosa (LC) in the human eye. Buckling of the LC in a nonaxisymmetric state in the neighborhood of the edge could cause edamas and folds at the periphery of the LC and loss of sight.

Problem formulation

In dimensionless variables the Ambartsumyan's theory of anisotropic plates for transversely isotropic plates is:

$$\begin{gathered}\phi' + \phi/r + \dot{\psi}/r - L(w,F) - p = 0,\\ g_1 L_1(w) + g_1' \mathcal{L}_1^+(w) - L_{1\phi}(\phi) - L_{1\psi}(\psi) = -\phi,\\ g_1 L_2(w) + g_1' \mathcal{L}_2(w) - L_{2\phi}(\phi) - L_{2\psi}(\psi) = -\psi,\\ g_2 L_3(F) + g_2' \mathcal{L}_3^-(F) + g_2'' \mathcal{L}_1^-(F)\frac{\lambda^2}{2} L(w,w) = 0,\\ (\,)' = \frac{\partial(\,)}{\partial r}, \quad \dot{(\,)} = \frac{\partial(\,)}{\partial \theta}.\end{gathered} \tag{1}$$

Here $w(r,\theta)$, $F(r,\theta)$, $\phi(r,\theta)$, $\psi(r,\theta)$ are the non-dimensional out-of-plane deflection, the Airy stress function and the force functions, respectively, Δ is the Laplacian in polar coordinate, L_i, $\mathcal{L}_i$, $L_{j\phi}$, $L_{j\psi}$, $i = 1\ldots 3,\ j = 1,2$ are linear opetators and

$$L(x,y) = x''\left(\frac{y'}{r} + \frac{\ddot{y}}{r^2}\right) + y''\left(\frac{x'}{r} + \frac{\ddot{x}}{r^2}\right) - 2\left(\frac{\dot{x}}{r}\right)'\left(\frac{\dot{y}}{r}\right)'$$

Dimensionless quantities are related with those with dimensions by the expressions

$$r = \frac{r^*}{R},\ w = \frac{\beta w^*}{h},\ p = \frac{\beta^3 R^4}{E_r^{\mathrm{av}} h^4} p^*,\ F = \frac{\beta^2 F^*}{E_r^{\mathrm{av}} h^3},\ \{\phi,\psi\} = \frac{R^3\beta^3}{12 E_r^{\mathrm{av}} h}\{\phi^*,\psi^*\},\ \beta^2 = 12(1-\nu_r^2). \tag{2}$$

In (2), R and $h\,(h/R \ll 1)$ are the radius and thickness of the plate and E_r and ν_r are Young's modulus and Poisson's ratio, respectively. We assume radial inhomogeneity of the plate, i.e. the in-plane elastic modulus continuously varies from point to point in the radial direction. E_r^{av} is an average value of the elastic modulus in the radial direction

$$E_r^{\mathrm{av}} = \frac{1}{\pi R^2}\int_0^{2\pi}\int_0^R E_r(r) r\,dr\,d\theta, \quad E_r(r) = E_r^0 f(r) \tag{3}$$

and $g_1(r) = E_r^0 f(r)/E_r^{\mathrm{av}}$, $g_2(r) = 1/g_1(r)$.

We suppose that the edge of the plate is clamped but moving freely in the plate's plane. This results in the following set of conditions at $r = 1$

$$w = 0,\ w' = 5\mu_r\phi/2,\ \frac{F'}{r} + \frac{\ddot{F}}{r^2} = -\left(\frac{\dot{F}}{r}\right)' = 0. \tag{4}$$

In addition, all sought-for functions must fulfil the boundedness condition at the center of the plate.

Following [3], we search for solutions of equations (1) in the form

$$\begin{Bmatrix}\phi(r,\theta)\\ w(r,\theta)\\ F(r,\theta)\end{Bmatrix} = \begin{Bmatrix}\phi_s(r)\\ w_s(r)\\ F_s(r)\end{Bmatrix} + \varepsilon\begin{Bmatrix}\phi_n(r)\\ w_n(r)\\ F_n(r)\end{Bmatrix}\cos n\theta, \qquad \psi(r,\theta) = \psi_n(r)\sin n\theta, \tag{5}$$

where $\phi_s(r)$, $w_s(r)$, $F_s(r)$ describe prebuckling axisymmetric state, ε is a small parameter, n is a mode number and $\phi_n(r), \psi_n(r), w_n(r), F_n(r)$ are the non-symmetrical components.

After linearization about an axisymmetric state, the unsymmetric part of the solution is sought in terms of multiples of the harmonics in the angular coordinate. The eigenvalue parameter p appears nonlinearly in the resulting eigenvalue problem. We use the shooting method to solve nonlinear axisymmetric problem together with boundary conditions. To determine the value of p, for which have nontrivial solution, the finite difference method is employed [3]. We regard the smallest of these eigenvalues as the buckling load. The step of the difference grid is chosen so that by reducing the step by 2 the value of the critical load varied less than 1%.

Table 1. Normalized buckling load (p_{cr}/p_0) and corresponding wave numbers for the heterogenous plate.

	$q=0$	$q=-1$	$q=-3$	$q=-5$
p_{cr}/p_0	1	0.76	0.4	0.19
Mode number, n	14	14	15	17

Results and Discussion

In order to study the effect of the varying rate of inhomogeneity on the critical load and buckling mode, we solved the corresponding problem for two different laws of material inhomogeneity: $E=\bar{E}_0 e^{q_1 r}$ and $E=\widehat{E}_0(1+q_2 r)$. The buckling load for unsymmetrical buckling was calculated numerically over a large range of parameters $\bar{E}_0$, $\widehat{E}_0$, $q_{1,2}$, but for constant average value of the in-plane elastic modulus (3). The results are summarized in table 1 and figure 1. The parameter value $q=0$ corresponds to uniform plate with constant Young's modulus. The buckling load of axisymmetric equilibrium states of isotropic homogeneous circular plates is denoted as p_0 ($p_0=64522$).

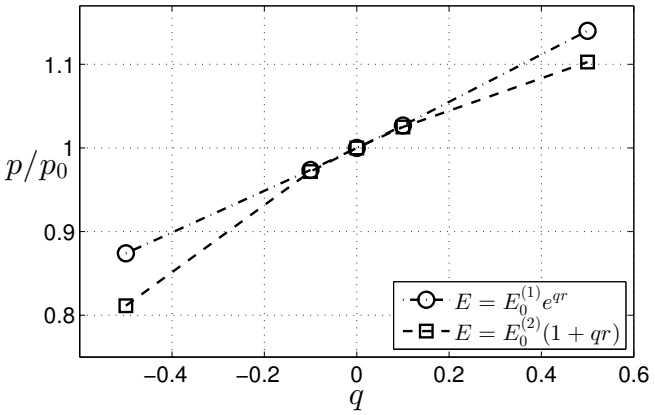

Figure 1. Normalized buckling load of heterogeneous plate. p_0 denotes the buckling pressure for uniform plate

In case $q<0$, the buckling mode shows more and more waves in the circumferential directions as the rate of inhomogeneity $|q|$ increases, see table 1).

For the consecutive wave number we noted closely adjacent values of the critical load, e.g. for the uniform plate the critical loads differ between each other by less than 1% ($p_{\rm cr}=64522$ for $n=14$ and $p_{\rm cr}=64929$ for $n=13$). The heterogeneous plate (with the rate function $f(r)=e^{-4r}$) wrinkles at $p_{\rm cr}=18355$, and the buckling mode has 16 waves, while for 15 waves the critical load is 18416. Thus, the considered plate is sensitive to initial imperfections of form or to initial stresses.

For numerical examples plate properties are taken from literature as material properties of the Lamina Cribrosa (LC) of the human eye [4]: the in-plane modulus and Poisson's ratio are assumed to be $E_r^{\rm av}$ =0.3 MPa, $\nu=0.45$, $h/R=0.1$. Taking the inhomogeneity parameter $q=-5$ we find that the non-axisymmetric buckling occurs under pressure about 60 mm Hg. From a mechanical point of view, folds at the periphery of LC could be annotated by the buckling of the axisymmetric state of the LC in the nonaxisymmetric state.

The problem for an annular plate was also treated. We considered a roller support for the inner edge of the plate, i.e. the edge that can slide along the figure axes without changing the slope, see figure 2

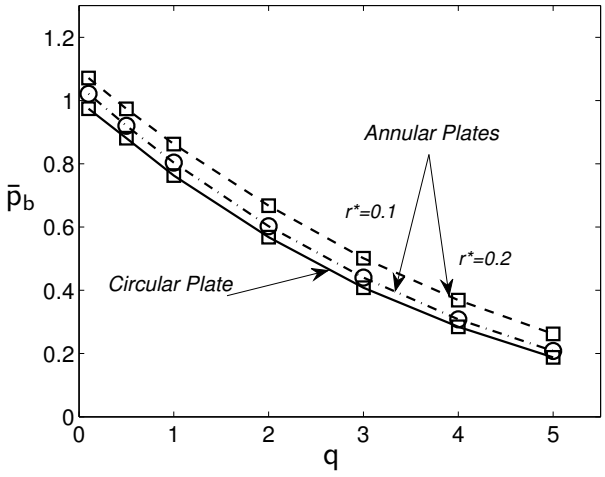

Figure 2. Normalized buckling load vs. degree of non-uniformity for circular (*solid line*) and annular plates (*dashed and dot-dashed lines*). r^* – the inner-to-outer radius ratio; $f(r) = e^{-qr}$.

Conclusions

The critical pressure for unsymmetric buckling is significantly lower than for a plate with constant elastic moduli, if the elastic moduli decrease away from the center of a plate. Number of waves in the circumferential direction increases with the degree of nonuniformity. The folders in the narrow zone at the periphery of the Lamina Cribrosa (LC) of the human eye could be explained by the bucking of the axisymmetric state of LC in the nonaxisymmetric state.

References

[1] S. Ambartsumyam. *Theory of Anisotropic Plates*. Stamford: Technomic publishing, 1970.

[2] S. Bauer. Mechanical models of the development of glaucoma. *Advances in Mechanics of Solid In Memory of Prof E M Haseganu*, Singapore, pp. 195–212, 2006.

[3] L. Cheo and E.Reiss. *Unsymmetrical wrinkling of circuar plates*, Quart. Appl. Math., 31, pp. 75-91, 1973.

[4] M. Edwards and T.Good. *Use of a mathematical model to estimate stress and strain during elevated pressure induced lamina criprosa deformation*, Curr Eye Res, 23, pp. 215-25, 2001.

[5] V. Feodos'ev. *On a method of solution of the nonlinear problems of stability of deformable systems*, J. App. Math. Mech., 27, pp. 392-404, 1963.

[6] D. Panov and V. Feodos'ev. *Equilibrum and loss of stability of shallow shells with large deflections*,(in russian), P.M.M., 31, pp. 75-91, 1948.

Proceedings of the 26th Nordic Seminar on Computational Mechanics
A. Logg, K.A. Mardal, A. Massing (Eds.)

Modeling dual-scale flow-deformation processes in composites manufacturing

Mohammad Rouhi[1], Maciej Wysocki[1], and Ragnar Larsson[2]

(1)Swerea SICOMP, Mölndal, Göteborg
(2)Dept of Applied Mechanics, Chalmers University of Technology, ragnar@chalmers.se

Summary. In present work, we attempt to unify the modeling of different sub-processes under the umbrella of two-phase porous media theory. Two sub processes are considered: (1) the wetting and compaction of individual plies and (2) the overall preform deformation and macroscopic Darcian flow. The idea is to identify a set of relevant constituents, i.e. particles, voids and liquids, and assign them to pertinent media. As to the continuum formulation a few researchers, e.g. Larsson et al. [1], Pillai et al. [2], Li and Tucker [3], have proposed formulations to predict the consolidation as a function of coupled flow and deformation-based two-phase porous media theory, cf. also [4] for a review of recent developments related to large deformation consolidation modeling.

The result is a set of overlapping continuous media, each having its own density-, velocity- and stress field on the macroscopic scale. In addition, we introduce internal variables to describe irreversible micro-processes in the system, such as microscopic infiltration and preform deformation. In this work we extend the previous developments, coupling the preform deformation on different scales to the process of micro infiltration, with respect to the modeling of the microcompaction as well as the Darcian interaction on the macro scale. A coupled displacement-pressure, geometrically non-linear, finite element model is presented. The approach is applied to a representative numerical example where we used parameter values out of the literature and estimates from our own micrographs.

Key words: Poromechanics, Finite Element Analysis, Multiscale modeling

References

[1] R. Larsson, M. Wysocki, and S. Toll, Process–modelling of composites using two-phase porous media theory, Eur. J. Mech. A/Solids, 23, 15–36 (2004).

[2] K. M. Pillai, C. L. Tucker, and F. N. Phelan. Numerical Simulation of Injection/Compression Liquid Composite Moulding. Part 2: Preform Compression, Composites: Part A, 32, 207-220 (2001).

[3] M. Li and C. L. Tucker, Modelling and Simulation of Two-Dimensional Consolidation for Thermoset Matrix Composites. Composites; Part A, 33, 877-892 (2002).

[4] J. Larsson and R. Larsson, "Non-linear analysis of nearly saturated porous media - Theoretical and numerical formulation", Comp. Meth. Appl. Mech. Engng, 191, 3885-3907 (2002).

Proceedings of the 26th Nordic Seminar on Computational Mechanics
A. Logg, K.A. Mardal, A. Massing (Eds.)

Fluid model of crystal plasticity: numerical simulations of 2-turn equal channel angular extrusion

Piotr Minakowski[1], Jaroslav Hron[2]

(1) Mathematical Institute, Charles University Sokolovská 83, 186 00 Prague, Czech Republic, minak@karlin.mff.cuni.cz
(2) Mathematical Institute, Charles University Sokolovská 83, 186 00 Prague, Czech Republic, hron@karlin.mff.cuni.cz

Summary. Considering severe plastic deformation experiments as a motivation, plastic behaviour of crystalline solids is treated as a flow of highly viscous material. We present thermodynamic derivation of the model of rate dependent crystal plasticity including evolution of Cauchy stress. Numerical simulations for 2-turn equal channel angular extrusion are reported. Our approach is purely Eulerian.

Key words: crystal plasticity, Eulerian plasticity, equal channel angular extrusion

Introduction

Within the last 20 years it was recognized that severe plastic deformation of certain material allows to achieve exceptionally high strength accompanied by relatively good ductility. Several metal forming processes achieving severe plastic deformation are now available. We chose ECAE (equal channel angular extrusion) because it is highly suitable for experimental and theoretical studies. Very high strains can be achieved without interruption, one can look at various amount of strains in one specimen.

In presented approach plastic behaviour of crystalline solid is treated as a highly viscous material flow through an adjustable crystal lattice [5]. Looking at severe plastic deformations experiments [1] it seems that crystalline materials at yield behave as a spacial kind of anisotropic, highly viscous fluid.

Model

We present thermodynamic description of the model of rate dependent crystal plasticity including evolution of Cauchy stress. Unlike the standard purely phenomenological approaches [2, 3] we employ ideas of Rajagopal [6] and derive our model on the basis of Gibbs potential.

The system we aim to solve consists of mass conservation (1), balance of angular momentum (2), evolution of Cauchy stress (3) and evolution of slip directions (4),

$$\rho_{,t} + \operatorname{div}(\rho \boldsymbol{v}) = 0, \tag{1}$$

$$\rho \dot{\boldsymbol{v}} + \operatorname{div} \boldsymbol{T} = 0, \tag{2}$$

$$\dot{\boldsymbol{T}} + \boldsymbol{T} \operatorname{div} \boldsymbol{v} + \boldsymbol{W}\boldsymbol{T} - \boldsymbol{T}\boldsymbol{W} = \rho \mathbf{C}(\boldsymbol{D} - \boldsymbol{D}_*), \tag{3}$$

$$\dot{\boldsymbol{s}}_i = \left(\operatorname{grad} \boldsymbol{v} - \sum_i \nu_i \boldsymbol{s}_i \otimes \boldsymbol{m}_i \right) \boldsymbol{s}_i \tag{4}$$

where plastic part of deformation is given by

$$\boldsymbol{D}_* = \sum_i \nu^{(i)} \mathrm{sym}(\boldsymbol{s}_i \otimes \boldsymbol{m}_i),\ \boldsymbol{D} = \mathrm{sym}(\mathrm{grad}\,\boldsymbol{v}),\ \boldsymbol{W} = \mathrm{skew}(\mathrm{grad}\,\boldsymbol{v}).$$

We fulfil the system with definition of slip rates $\nu^{(i)} = \nu_0 \mathrm{sign}(\tau^{(i)}) \left|\frac{\tau^{(i)}}{\tau_c^{(i)}}\right|^{\alpha}$ and hardening law $\dot{\tau_c}^{(i)} = \sum_j H_{ij} |\nu^{(j)}|$. The dots stand for material time derivatives.

Moreover we extend our approach to rate independent model by implicit constitutive relation between slip rate (ν) and resolved shear stress (τ).

Numerical treatment

Inspired by numerical methods of fluid dynamics FEM Eulerian representation is formulated and applied in a solution of a flow adjustment boundary value problem of equal channel angular extrusion.

Time is discretized by one step finite difference. In space we used **P2** for velocity and **P1** for density and slip directions (both continuous) and **P1**-discontinuous for Cauchy stress. Taking advantage of Eulerian formulation our computational domain is 2-turn channel [7]. Boundary conditions on impenetrable, frictionless boundary are imposed by Nitsche's method [9]. To solve the system we employ nonlinear Newton solver with analytic Jacobian.

We present a results of computations (see Figure 1). We can observe that plastic slip occurs only in the vicinity of slip planes (where the channel turns) and in the same region slip systems rotate due to elastic deformation. Density is almost constant although it changes in the neighbour of curved part of the boundary.

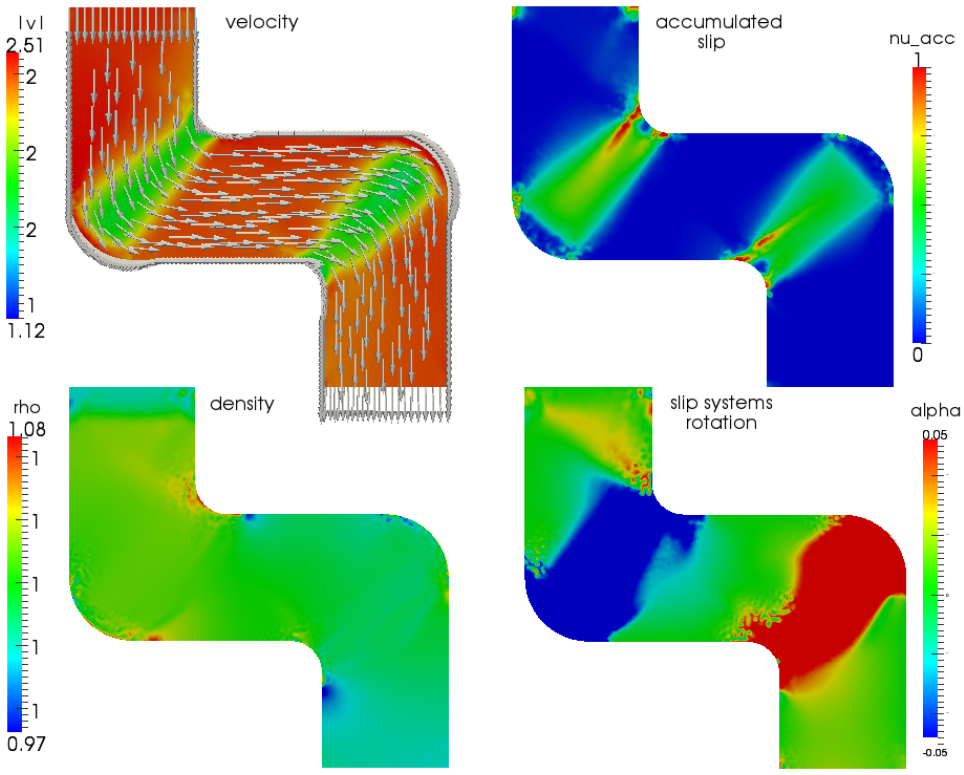

Figure 1. Computed variables: velocity magnitude (top-left), accumulated slip (top-right), density (bottom-left), slip system rotation (bottom-right)

Computations are done in two dimensions and we restrict ourself to the plane-strain case. Due to this fact we consider only three slip systems. In Figure 2 we observe the behaviour of slip systems in the channel. Activation of particular slip system depends on its position relative to slip plane.

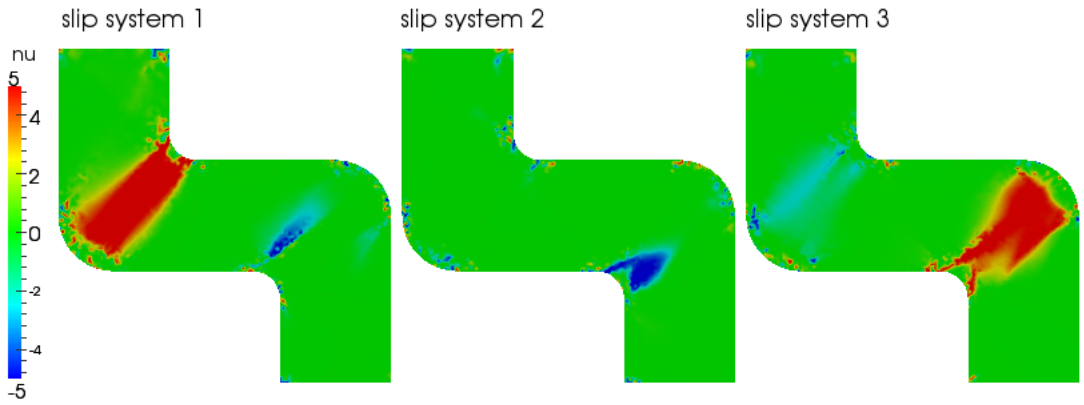

Figure 2. Behaviour of slip systems in the 2-turn channel.

Implementation is done in FEniCS [8]. We compare our results to [4] and [7]. Our novelty are Eulerian formulation, numerical approach and consideration of compressible elasticity.

References

[1] Ruslan Z. Valiev and Terence G. Langdon. *Principles of equal-channel angular pressing as a processing tool for grain refinement.* Progress in Materials Science, 51(7):881–981, 2006.

[2] D. Peirce, R.J. Asaro, and A. Needleman. *Material rate dependence and localized deformation in crystalline solids.* Acta Metallurgica, 31(12):1951–1976, 1983.

[3] R.J. Asaro and A. Needleman. *Overview no. 42 texture development and strain hardening in rate dependent polycrystals.* Acta Metallurgica, 33(6):923–953, 1985.

[4] Oana Cazacu and Ioan R. Ionescu. *Dynamic crystal plasticity: An eulerian approach.* Journal of the Mechanics and Physics of Solids, 58(6):844–859, 2010.

[5] Jan Kratochvíl Martin Kružik and Radan Sedlček *A model of ultrafine microstructure evolution in materials deformed by high-pressure torsion.* Acta Materialia, 57(3):739–748, 2009.

[6] K. R. Rajagopal and A. R. Srinivasa. *A gibbs-potential-based formulation for obtaining the response functions for a class of viscoelastic materials.* Proc. R. Soc. A, 467(2125):39–58, 2011.

[7] A. Rosochowskia, L. Olejnik *Numerical and physical modelling of plastic deformation in 2-turn equal channel angular extrusion* Journal of Materials Processing Technology 125–126 (2002) 309–316

[8] A. Logg, K.-A. Mardal, G. N. Wells et al. *Automated Solution of Differential Equations by the Finite Element Method*, Springer 2012.

[9] Freund, J.; Stenberg, R. *On weakly imposed boundary conditions for second order problems.* Proceedings of the International Conference on Finite Elements in Fluids, pages 327–336.

Proceedings of the 26th Nordic Seminar on Computational Mechanics
A. Logg, K.A. Mardal, A. Massing (Eds.)

Variationally consistent homogenization of viscous flow in a porous medium

Kenneth Runesson[1], Fredrik Larsson[1], and Carl Sandström[1]

(1)Chalmers University of Technology, Department of Applied Mechanics, SE41296 GÖTEBORG, kenneth.runesson@chalmers.se, fredrik.larsson@chalmers.se, carl.sandstrom@chalmers.se

Summary. This paper discusses the model-based homogenization of viscous flow in a porous medium leading to Darcy-type of seepage on the macroscale. Particular focus is placed on the efficiency of weakly periodic boundary conditions on the Representative Volume Element (RVE) where the underlying microstructure is resolved.

Key words: homogenization, seepage, weakly periodic

Introduction

The classical setting of model-based homogenization is considered in this presentation. For the standard quasistatic stress problem based on subscale elasticity, the Hill-Mandel (or macrohomogeneity) condition can be expressed as the "equivalence of virtual work of the fine-scale and the macroscale". How to generalize this condition to a more general class of nonlinear and/or time-dependent coupled field problems involving selective homogenization of the pertinent fields (and balance equations) is not obvious; however, a possibility is offered by the paradigm of Variationally Consistent Homogenization in the spirit of the Variational Multiscale Method, originally proposed by Hughes [1] in a quite different context. The corresponding macrohomogeneity condition is then associated with a Galerkin property of the homogenized problem. As a result, symmetry of macroscale tangent operators is preserved.

Seepage in a rigid porous medium

An important and indeed very classical engineering problem is that of seepage through a rigid or (more generally) deformable porous material, e.g. granular material. In this presentation we adopt (selective) homogenization of incompressible Stokes' flow in the rigid porous medium to obtain Darcy-type of seepage, typically in the FE^2-setting [4]. Only the continuity equation is homogenized, whereas the momentum balance remains completely local, cf. Sandström and Larsson [3]. We adopt (as the point of departure) the concept of weakly periodic fluctuations to formulate boundary conditions on the RVE, cf. Larsson et al. [2], for which the pertinent Hill-Mandel condition is satisfied. Moreover, we discuss how to establish a "macroscale energy density" that serves as the potential for the macroscale (homogenized) drainage velocity.

The explicit expression of the saddle-point problem defining the effective response is given as

$$\inf_{\substack{\boldsymbol{v}\in\mathcal{V}_\square \\ \boldsymbol{\beta}\in\mathcal{B}_\square}} \sup_{p^{\mathrm{S}}\in\mathcal{P}^{\mathrm{S}}_\square} \inf_{\gamma\in\mathcal{G}_\square} \Pi(\boldsymbol{\nabla} p^{\mathrm{M}}, \boldsymbol{v}, p^{\mathrm{S}}, \boldsymbol{\beta}, \gamma) \tag{1}$$

where $\boldsymbol{v}$ is the velocity field, p^{S} is the pressure and $\boldsymbol{\beta}$ and γ are Lagrange multipliers pertinent to the conditions on periodicity on $\boldsymbol{v}$ and p^{S}. Furthermore, we note the explicit dependence on the macroscale pressure gradient $\boldsymbol{\nabla} p^{\mathrm{M}}$. We also note that, by choosing the solution spaces in a suitable way, we are able to produce upper and lower energy bounds. Considering the problem on the pore domain of the RVE, we express the potential as

$$\Pi(\boldsymbol{\nabla} p^{\mathrm{M}}, \boldsymbol{v}, p^{\mathrm{S}}, \boldsymbol{\beta}, \gamma) = \int_{\Omega^{\mathrm{F}}_{\square}} \Phi(\boldsymbol{\nabla} \boldsymbol{v}) \mathrm{d}V - \int_{\Omega^{\mathrm{F}}_{\square}} p^{\mathrm{S}} (\boldsymbol{\nabla} \cdot \boldsymbol{v}) \mathrm{d}V + \int_{\Omega^{\mathrm{F}}_{\square}} \boldsymbol{\nabla} p^{\mathrm{M}} \cdot \boldsymbol{v} \mathrm{d}V - \int_{\Gamma^{\mathrm{F}+}_{\square}} [\![\boldsymbol{v}]\!] \cdot \boldsymbol{\beta} + [\![p^{\mathrm{S}}]\!] \gamma \mathrm{d}S \quad (2)$$

where Φ is the potential pertaining to the viscous material.

Numerical examples

The efficiency of weakly periodic boundary conditions are assessed for an RVE in 3D representing a microstructure with simplified topology. We consider the porespace located in between particles in a BCC arrangement of sphere slightly overlaping. In this particular example, the Lagrange multipliers are discretized as polynomials. Snapshots of the solutions are shown in Figure 1 for different orders of polynomials.

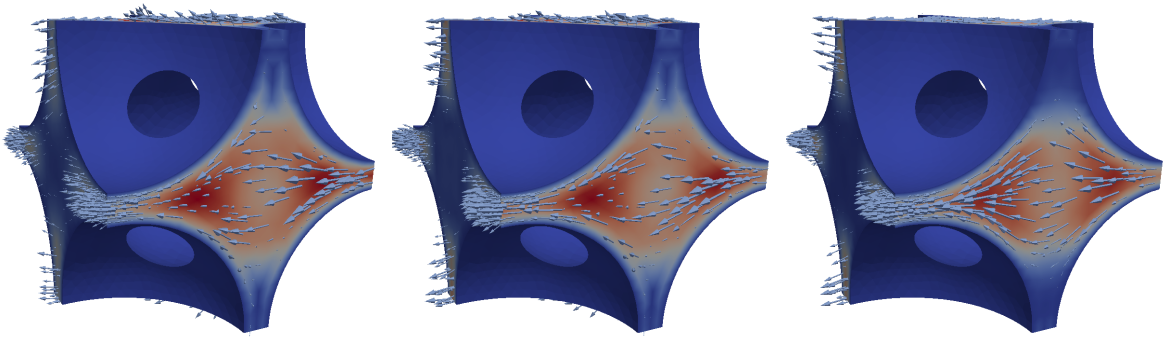

(a) 0th order (b) 2nd order (c) 6th order

Figure 1. Solutions showing the velocity for different orders of polynomial approximations of the Lagrange multipliers

References

[1] T. Hughes. Multi-scale phenomena: Green's functions, the dirichlet-to-neumann formulation, subgrid scale models, bubbles and the origins of stabilized methods. *Computer Meth. Appl. Mech. Engrg.*, 127:387–401, 1995.

[2] F. Larsson, K. Runesson, S. Saroukhani, and R. Vafadari. Computational homogenization based on a weak format of micro-periodicity for rve-problems. *Computer Meth. Appl. Mech. Engrg.*, 200:11–26, 2011.

[3] C. Sandström and F. Larsson. Variationally consistent homogenization of Stokes' flow in porous media. *Int. J. Multiscale Computational Engrg.*, 11:117–138, 2013.

[4] C. Sandström, F. Larsson, K. Runesson, and H. Johansson. A two-scale finite element formulation of Stokes flow in porous media. *Computer Meth. Appl. Mech. Engrg.*, 261-262:96–104, 2013.

Proceedings of the 26th Nordic Seminar on Computational Mechanics
A. Logg, K.A. Mardal, A. Massing (Eds.)

Stress-strained state and the stability of a spherical segment under the influence of a load with a flat base.

Ermakov A. M.

Department of Theoretical and Applied Mechanics, Faculty of mathematics and mechanics
St. Petersburg State University, Saint-Petersburg, Russian Federation, Ermakovamsi@gmail.com

Summary. In this paper the problem of the buckling of the transversal-isotropic segment of spherical shell with the different thicknesses under the influence of the load with a flat base is studied. The spherical segment has a rigid support on the edge and previously has been loaded by internal pressure. The solution of this problem is based on the theory of the shell of moderate thickness by Paly-Spiro. This theory takes into account the influence of the cross section shear and change of the shell thickness. For modelling such large deformations the method of consequent loading is used. In this method, due to the use of linear physical relations, it is possible to trace the non-linear problem at each separate stage to the solution of a linear system. The comparison of the results which were obtained with the use of the method of linearization of non-linear equilibrium equations and the method of minimization of elastic potential of the shell has been done. The problems of stress-strain state of soft and close to soft shells that are under the influence of a load with a flat base are important for analyzing the data related to measuring a very important in ophthalmology characteristic of intraocular pressure.

Key words: nonlinear shell theory, stability, load with a flat base

The problem statement

Let us consider the problem of state-strain state and the loss of stability of the transversally isotropic segment of a spherical shell under the influence of the load with a flat base, see figure 1. The spherical segment has a rigid support on the edge and previously has been loaded by the internal pressure.

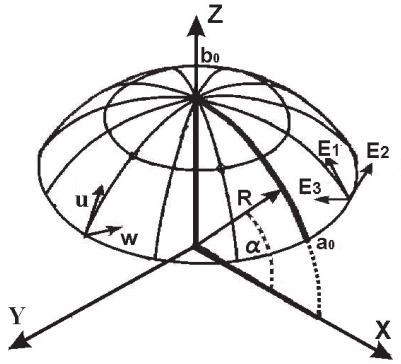

Figure 1. The dual structure of continuum mechanics.

The deformation and loss of stability are considered to be axisymmetric therefore we can take into account only the half of the arc created by the vertical cross section. On the pole point

and the edge the boundary conditions of the symmetry and rigid support were introduced. Thus all the values depend only on one spherical coordinate, $\alpha \in [a_0, \pi/2]$, where a_0 – characterizes the angle of segment opening.

The elastic moduli of the considered shell differ by an order, therefore the theory of anisotropic shells of moderate thicknesses by Paly-Spiro [1] is used. This theory takes into account the influence of cross section shear and the deformation into the direction of the normal to the middle surface and is based on the following hypotheses:

1) a rectilinear element normal to the middle surface of a shell remains rectilinear after the deformation;

2) the cosine of the angle of inclination of the shell of these fibers to the middle surface of the deformed shell equals to the averaged angle of the cross displacement.

The mathematical formulation of the accepted hypotheses resolves to the following equations:

$$\begin{aligned} &u_1 = u + \phi \cdot z, \quad u_3 = w + F(\alpha, z), \\ &\phi = \gamma_1 + \phi_0, \qquad \phi_0 = -\frac{1}{A_1}\frac{\partial w}{\partial \alpha} + k_1 u, \end{aligned} \tag{1}$$

where u_1 and u_3 – tangential and normal displacements of the shell, u and w – displacements of the middle surface, φ – turning angle of the normal in plane (α, z); φ_0 – turning angle of the normal to the medial surface; γ_1 – shear angle. The function F(α, z) characterizes length change of the normal to the medial surface.

The methods of solution

The deformations which appear under the influence of the load with a flat base are large and we need the geometrical non-linear shell theory to describe them. However, the construction of the solution of the non-linear theory equations presents a significant difficulty [2, 3]. Therefore the solution of this problem is based on the method of consequent loading.

In this method pressure P is presented as the sum of monotonous consequent loadings:

$$P = \Delta P_1 + \Delta P_2 + ... + \Delta P_n \qquad (\Delta P > 0, n >> 1). \tag{2}$$

Thus the geometrically non-linear problem is reduced to a consequent solution of linear problems for a previously loaded shell of revolution. The original stress strain state of the shell was defined by the results of the previous loadings $\sum_{i=1}^{N} \Delta P_i$.

At each stage only the part of all the loading ΔP_i is applied to the shell so that the deformations should stay small. We take into account the fact that at previous stage of the loading each point of the original surface changed its own position and thickness. It needs recalculating Lame coefficients A_1, A_2, curvatures k_1, k_2, the new law of distribution of function of thicknesses h. Besides, the values of the stress strain state of the shell obtained at the previous stages of the loading are included in the resulting equation. The adding loads ΔP_1, ΔP_2, ΔP_3 must be small in comparison with that values which the upper critical load corresponds to.

In this work the method of consequent loading is presented in two ways. The first of them is the method of linearization of non-linear equilibrium equations [1] and the second - the method of minimization of elastic potential of the shell [4]. These ways of the problem solution give us the different approaches to the estimation of the critical load.

In the first method the system of differential equations of the equilibrium of shell is solved at the each separate stage of the loading. The right part of the system except the next addition of the load ΔP_i takes into account the forces and deformations from the previous step of loading. We presume that the critical load corresponds to the case when ΔP_i=0 the system ceases to be an identical. Non-trivial solutions appear due to the influence of the internal forces.

In the second approach the solution is obtained by minimization of elasticity potential of the shell with use of the Ritz numerical method. The displacements are represented as the

functional series which satisfy the boundary conditions. Having the partial derivatives of the elasticity potential for the each member of the series of the displacement functions, we obtain the system of non-linear differential equations. To solve the obtained system of non-linear algebraic equations, the continuation method by the loading parameter ΔP_i is used. In the result all solution is reduced to the system of linear algebraic equations for the members of the series of the displacement functions. The loss of stability takes place when the resulting matrix of this system becomes degenerate. In this case the post–critical state is obtained by the change of the parameter.

The comparison of the results which were obtained with the use of these methods is done. For both methods we defined the dependence of the load contact area on the influence of the internal pressure, thickness and the curvature radius of the spherical shell segment. The distributions of the stress strain state for different values of the load are constructed. The possible appearance of exfoliation in the area of the contact with the flat base is studied. This problem may have a biomechanical application.

Numerical simulation

Let us introduce the comparison of the results which were obtained with the use of considered methods for the problem of deformation of the cornea of the eye. In the Maklakov method of tonometry a human eye is deformed by flat base load of the bar. The diameter of the contact zone with cornea is measured and the measured diameter length is used in estimating the intraocular pressure (IOP). When the intraocular pressure is not very high and the thickness of an eye shell (cornea) is small (for example, after refractive surgery) the cornea may buckle and detach from tonometer. It leads to errors in estimates of intraocular pressure[5].

The cornea average curvature radius R=8 mm, its foundation radius is constant and equal R_{os}=5.25 mm, thickness h changes linearly from h_a=1 mm at the edge of segment to h_b=0.5 mm at the pole point. For elastic modulus, cross–section shear, and poisson's ratios these values was taken [6, 7] : $E_1 = E_2 = 7 \cdot 10^4$ Pa, $E_3 = 7 \cdot 10^2$ Pa, $G = 7 \cdot 10^3$ Pa, $\nu_{21} = \nu_{31} = \nu_{12} = \nu_{32} = 0.4$, $\nu_{13} = \nu_{23} = 0.01$.

We consider that these geometrical parameters correspond to the case when the cornea is under the influence of IOP of 22 mm.Hg. (1 mm.Hg.= 133.3 Pa). Therefore firstly we consider the shell of a smaller height. It is loaded by negative IOP. The geometry of obtained form is considered to be initial. The forces which act in it are equated to zero and it is loaded by the similar but positive load. The new shell is higher than a previous one but it is taken into account the influence of internal pressure.

For modelling the influence of the bar we introduce the function which takes into account that the load acts only in straightened area on the top. In the case of appearance of displacement which leads to exfoliation of the shell from the bar the negative load starts acting. This negative load takes off the part of the overall load from the exfoliated surface [8].

Conclusions

Let us consider deformations and the distribution of normal stress in the contact area corresponding to them. It should be noted that the general views of the distribution of normal stress of reviewed methods is almost similar.

a) Under the influence of the small load 0.75 gm the main stress is concentrated in the vicinity of the pole and decreases exponentially towards the edges.

b) In the case of load increase up to 3.5 gm the normal stress redistributes and the unloaded area in the vicinity of the pole appears.

c) For the given value of load of 10 gm, we can see a slightly loaded ring area. The main surface stresses act only at the edge of the loaded area and at the pole point.

Table 1. The comparison of the radiuses of contact area .

Thickness at the pole point h_b (mm)	0.5	0.465	0.43	0.395	0.36
The method of minimization R_{out}	3.00	3.04	3.08	3.12	3.17
The method of linearization R_{out}	2.97	3.00	3.05	3.10	3.15

d) When the loading is being continued (15 gm), the distribution of the load obtains a more complex shape.

e) In the case of solving this problem with the use of the method of lineralization the shell may lose the stability as this method takes into account the force ΔT_1 evidently. Also the system corresponding to it has the higher order. The force ΔT_1 reaches significantly large values in the vicinity of the pole point. This can make the shell fall down inside – lose the stability.

The table 1 presents the values of radiuses, of the contact area of the shell with a bar of 10 gm. R_{out} for different values of the thickness in the vicinity of the pole h_b mm. curvature radiuses which are equal to R=8.5-h_b mm. These calculations may help to model the consequences of keratometric operations, because in the course of these operations a layer of tissue is cut off the top the cornea. As one can see, the reduction of the value of thickness h_b at the pole leads to the increase of the contact area R_{out}. It may contribute to error in measurement IOP. Radiuses received by method of linearization are less then radius received by method of minimization of elastic potential, which can be explained by direct accounting of effort function ΔT_1 in the first method. When the linearization method is used, unloaded or slightly loaded areas appear earlier (at a lower level of pressure), then in the case when the minimization method is used.

References

[1] O.M. Paliy and V.E. Spiro. *Anisptropic shells in shipbildung. Theory and analysis*. Sudostroenie, Leningrad, 1977.

[2] V.I. Feodosev. On a Method of Solution of the Nonlinear Problems of Stability of Deformable Systems. *Journal of Applied Mathematics and Mechanics Russian Academy of Sciences*, 27(2):265–274,1963.

[3] E. Lavendelis. *Design of Rubber-Technical Construction Elements*. Mashinostroenie, Moscow, 1997.

[4] V.V. Karpov, D.A. Baranova and R.T. Berkaliyev. *The program complex for studying stability of shells*. SPbGASU, Saint-Petersburg, 2009.

[5] S.M. Bauer, B.A. Zimin and P.E. Tovstik. *The program complex for studying stability of shells*. St. Petersburg State University Press, Saint-Petersburg, 2000.

[6] S.E. Avetisov, I.A. Bubnova and A.A. Antonov. The study of the effect of the corneal biomechanical properties on the intraocular pressure measurement. *State research institute of eye diseases RAMS*, 4:30–33,2009.

[7] E.N. Iomdina. Mechanical properties of human eye. *Modern problems in biomechanics*, 11:183–201,2006.

[8] B. Ya. Kantor. *Contact Problems of Nonlinear Theory of Shells of Revolution*. Naukova Dumka, Kiev, 1990.

Proceedings of the 26th Nordic Seminar on Computational Mechanics
A. Logg, K.A. Mardal, A. Massing (Eds.)

Modelling ship grounding with finite elements

Ole J. Hareide[1], Lars Brubak[1,2], and Torstein Pettersen[1]

(1)Section for Ship Structures and Concepts, Maritime Advisory, Det Norske Veritas, Norway.
E-mail: ole.jakob.hareide@dnv.com
(2)Mechanics Division, Department of Mathematics, University of Oslo, Norway

Summary. Numerical simulations using non-linear finite element analysis have been performed to study ship grounding. The results are compared with experimental tests which were performed in USA in 1995 and good agreement is achieved. This illustrates that non-linear FE analysis can be used to estimate damage extent in a grounding scenario.

Key words: Ship grounding, FEA, non-linear analysis

Introduction

Every year ships run aground around the world. The potential for damage is huge, both in economic and ecological terms. With the ability to simulate ship groundings with finite element software and assess the strength of a ship against such incidents there is a huge potential to be gained. Similar studies for collision scenarios by using non-linear finite element analysis have been performed by Notaro et. al [1, 2].

A detailed picture of a ship's performance in a grounding situation can be used in the design of the ship. The results do, however, depend on correct material parameters and the use of a correct coefficient of friction in addition to a very detailed description of the geometry. There is not much data to be found from real events so to verify that the model is indeed giving reasonable results, a series of analyses has been run against results obtained from scale tests performed in the USA in 1995 [3].

Background

A series of model scale test was performed at the Naval Surface Warfare Center in the US in 1995. Four different steel configurations of double bottom structures were built in 1:5 scale and used to evaluate the performance when impacted into a concrete cone used to simulate a rock on the seabed. The models were mounted to a rail cart and released down a slight incline in order to build up velocity and hit the rock at a speed of 14 knots. In a double hull configuration there is generally not a danger for a cargo spill if the inner hull is not breached, so the double bottom models were mounted at a pitch angle of approx. 3.2° in the test rig to ensure a gradual vertical increase in the damage depth and eventually a rupture of the inner hull. The output from the experiments, which have been used to compare the finite element results against, were force-displacement and energy-displacement curves.

FE model and analysis procedure

A detailed model of one of the double bottom scale models was created in Abaqus/Explicit v6.11 [4]. Of the four models tested the one chosen for modelling in Abaqus was the configuration

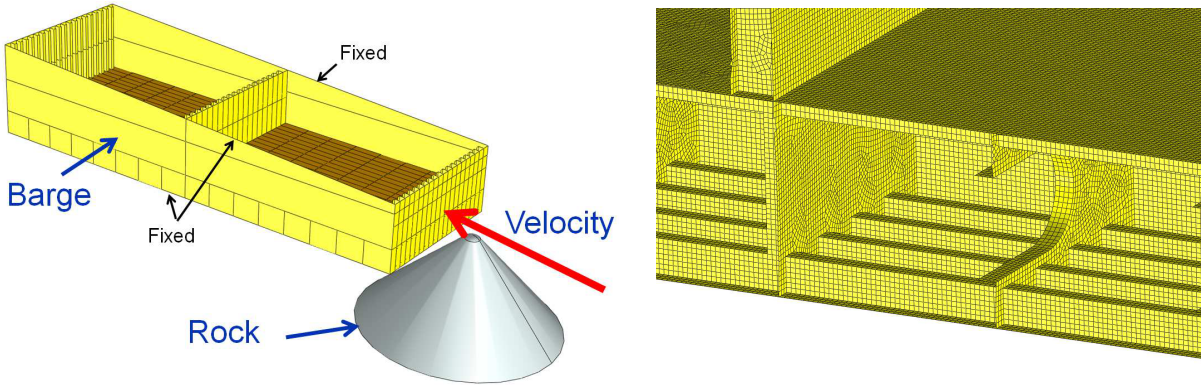

(a) (b)

Figure 1. (a) A barge impacting into a rock and (b) the detail level and mesh for the barge where stiffeners, girders and bulkheads are included.

most resembling the double bottom of a traditional tanker as shown in Fig. 1. The model consisted of two cargo holds divided by a stiffened bulkhead. On either end of the hold there were also stiffened bulkheads. The double bottom consisted of a longitudinal girder in the centre and seven transverse frames under each hold. The rock was modelled as a rigid body with a cone shape. First-order reduced-integration shell elements were used with a fine mesh size of around 10x10mm in a fine area where the rock would impact and 50x50mm in the rest of the model. The reason for such a fine mesh, which is in the order of three times the thickness, was to accurately capture the failure mechanisms such as rupture, folding and crushing of plates and stiffeners.

The material used in the model was an ASTM A569 isotropic steel with a Young's modulus of $E = 206000$MPa, Poisson's ratio of $\nu = 0.3$ and density of $\rho = 7.9 \times 10^3$kg/m^3. Plasticity was included with a yield stress of $\sigma_y = 283$MPa. In order to model the rupture of the steel as the rock passed through the model a tensile failure criterion was added to the material definition, which after tensile strain of 0.278 will simulate necking behaviour in the material and linearly degrade an element's stiffness down to zero over a damage displacement, defined here as 3.2mm additional displacement after necking occurs. When the element's stiffness has reached zero it was visually removed from the analysis.

The coefficient of friction is difficult to measure from a grounding experiment due to other energy dissipating mechanisms such as tearing and folding of the structure. Typical values of steel against rock ranging from 0.4 to 0.7 were used here, and the choice of this coefficient can have a large impact on the dissipation of energy.

The analyses were run with Abaqus/Explicit with an initial velocity of 14 knots applied to the model. Along with the mass of the structure an additional mass was added to the model to account for the weight of the testing rig used in the scale model tests. Using an initial kinetic energy (as opposed to the constant velocity) approach meant that the kinetic energy would be dissipated by the impact and that the model would come to a halt when the dissipated energy equalled the initial kinetic energy. The upper two longitudinal edges in the structure were fixed in order to keep them rigid during the analysis.

Results and discussion

The results from the analyses are shown here in Fig. 2. Both energy and force curves are plotted against the displacement of a reference point placed in the rear of the model. The kinetic energy will drop as the energy dissipation increases. From the force curve, several smaller spikes and

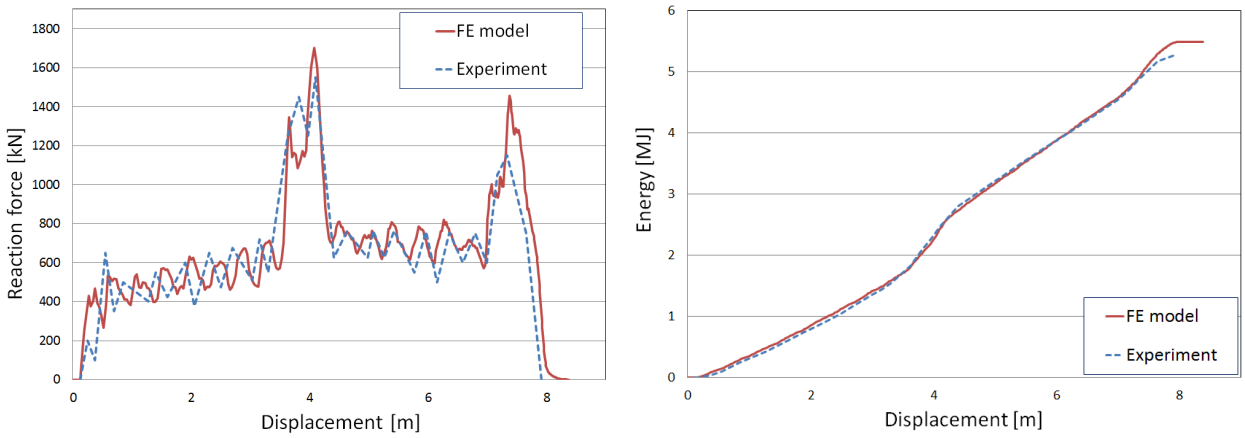

(a) (b)

Figure 2. (a) Reaction force and (b) absorbed energy versus grounding distance.

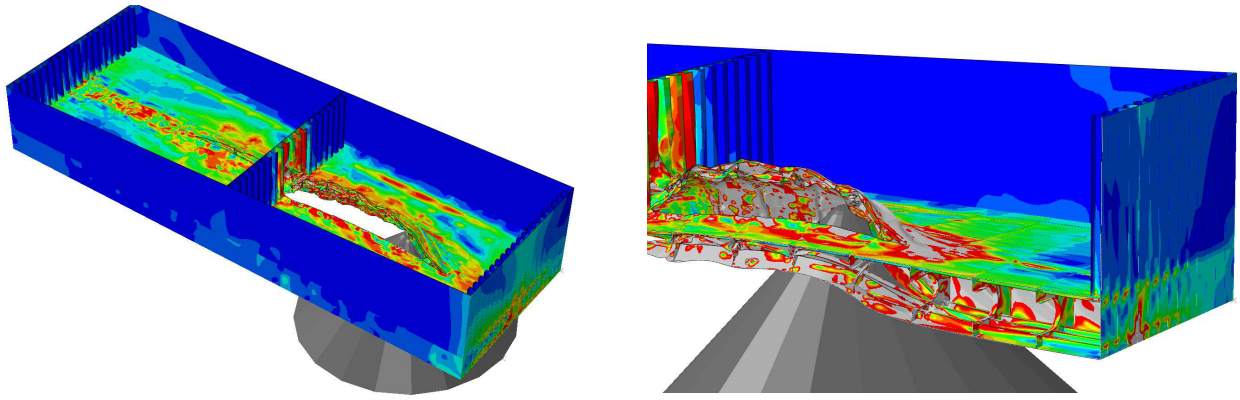

(a) (b)

Figure 3. (a) Damage extent of the barge and (b) close-up view of the damages.

the two large spikes are observed, corresponding to the structure resisting deformations as the rock passed through the several smaller transverse frames and the two cargo hold bulkheads at the centre and the aft. There is also an overall increasing trend in the registered force which is due to the pitch angle.

The absorbed energy can be found by integrating the reaction force over the grounding distance and thus it can be seen to also have a slightly higher absorption rate (energyabsorption pr. meter) around the two bulkheads than in the cargo holditself.

The total dissipated energy can be broken down into several components such as friction, plastic deformation, elastic strain and energy gone into tearing elements apart. In the analyses that were run it is seen that most of the energy is dissipated by plastic deformation and friction while the other aforementioned energies that make up the rest are relatively small. The ratio between the energy going into friction and plastic deformation varies depending on the coefficient of friction, as was mentioned above.

The damages are shown in Fig. 3 and it can be seen that the deformations are very large. This illustrates that non-linear finite element computations can be used to estimate the damage extent with reasonable accuracy. From what can be read from the pictures of the experimental test [3], the damages are very similar to what was found in the present finite element analysis. In Fig. 4, close-up views of the deformations in the longitudinal girder and in the area close to the transverse bulkhead are shown.

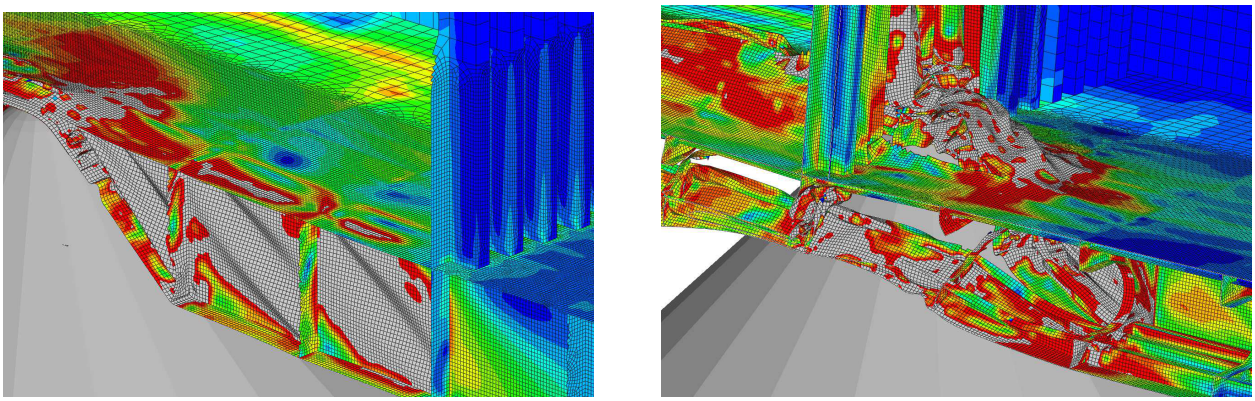

(*a*) (*b*)

Figure 4. Close-up view of (*a*) the deformation in the longitudinal girder, which is a typical skewed folding pattern from shear deformations and (*b*) the deformations at the transverse bulkhead.

Conclusion

Finite element analysis for a grounding scenario has been performed and computed results are compared and verified with experimental test data from a steel 1:5 scale model. Results show that the simulation can accurately predict the damage extent and yield the same energy dissipation rate.

Acknowledgments

The authors would like to thank dr. Eivind Steen, Tom K. Østvold, Gabriele Notaro and Alessio Prestileo at Det Norske Veritas (DNV), for their interest, suggestions and valuable discussions throughout the study.

References

[1] G.Notaro, K. Brinchmann, E. Steen and N. Oma. *Evaluation of the Fendering Capabilities of the SPS for an Offshore Application*, ICCGS 2013 Conference, Trondheim, Norway, 2013.

[2] G.Notaro, T.K. Østvold, E. Steen and N. Oma. *Collision Damages and Residual Hull Girder Strength of a Ship Shaped FPSO*, PRADS 2013 Conference, Changwon City, Korea, 2013

[3] James L. Rodd. Observations on Conventional and Advanced Double Hull Grounding Experiments *Proceedings of the International Conference on Design and Methodologies for Collision and Grounding Protection of Ships*. San Francisco, California, 1996

[4] ABAQUS/Standard, *User Manual Version 6.11* volume Hibbitt, H. D. and Karlsson, B. I. and Sorensen, I. Hibbit, Karlsson and Sorenson Inc., Pawtucket; 2012.

Proceedings of the 26th Nordic Seminar on Computational Mechanics
A. Logg, K.A. Mardal, A. Massing (Eds.)

FEM simulation of cold deforming pipe into flange

Assoc. Prof. Jan Henriksen[1], Prof. Michael R. Hansen[2]

(1)Department of Engineering and Science, University of Agder,Grimstad, Norway , jan.henriksen@uia.no
(2)Department of Engineering and Science, University of Agder, Grimstad, Norway, michael.r.hansen@uia.no

Summary. In this paper the usefulness of finite element analysis (FEA) as a tool for predicting the cold forming pipe-flange connection process of Quickflange AS is investigated. The Quickflange technology is based on plastic cold expansion/deformation of the pipe into a modified standard flange by use of a cold forming tool. The technology represents a highly feasible alternative to welding that has been the technology of choice for connection of subsea flanges for decades. Experimental work is presented for both model parameter identification and model verification. Comparing with test results the FEA model is in good accordance in terms of applied hydraulic pressure for the process and at the same time computational time consumption is acceptable. Further work, will focus on the ability of the model to predict the key performance parameters of the cold flanged connection.

Key words: flange, cold forming, Finite Element Method

Introduction

It is expected that the use of flange to pipe connection technology utilizing cold deformation of the pipe for subsea applications will make installation, inspection and maintenance of subsea pipelines safer and more cost effective than with current state-of-the art flanging technology, i.e., welding. The Quickflange technology is based on plastic cold expansion/deformation of the pipe into a modified standard flange by use of a cold forming tool. In order to to fully exploit this technology there is a need for a better fundamental knowledge about, and understanding of, the elasticity and plastic deformation of the metals and alloys used in the pipe and flange. Especially, the ability to model plasticity as well as spring back effects is crucial in order to predict the important parameters of the cold flanging process. The use of finite element analysis has been widely used to describe processes similar to the one investigated in this paper. FE-analysis allows for the assessment of spring back effects in different types of forming processes due to its ability to reflect parameters such as stress, strain and temperature in deforming bodies [1]. There are numerous examples of finite element modeling of sheet metal bending where the spring back effect is most pronounced. Such publications are often focused on minimizing the spring back effect in order to predict numerically rather than empirically. Some recent publications on this subject are [2], [3] and [4]. In processes involving forming of pipes, Zheng et al [5] has used finite element analysis (FEA) to predict the inner coating of pipes by means of cold forming obtaining good correlation with experimental data. Other manufacturing processes that has received attention in recent years is the FE-modeling of the sequential plate punching when manufacturing large welded pipes, [6], and the rolling of pipe, [7], pipe bending, [8], or pipe extrusion, [9]. A common goal for these research activities is the desire to use FEA to predict and optimize processes. Also, experimental verification is normally introduced to validate numerical results. It seems that the commercial software packages Abaqus and LS Dyna are used almost exclusively. In this work Finite Element Method is used to model the process using Abaqus. By combining FEA, parameter identification and experimental work, this paper investigates whether the cold flanging technology of Quickflange AS can be satisfactorily predicted by means

of Finite Element Method. The main emphasis has been on the hydraulic pressure load during the process.

Considered process

The technology is based on plastic cold expansion/deformation of the pipe into a modified standard flange by use of a hydraulic flanging tool, see figure 1.

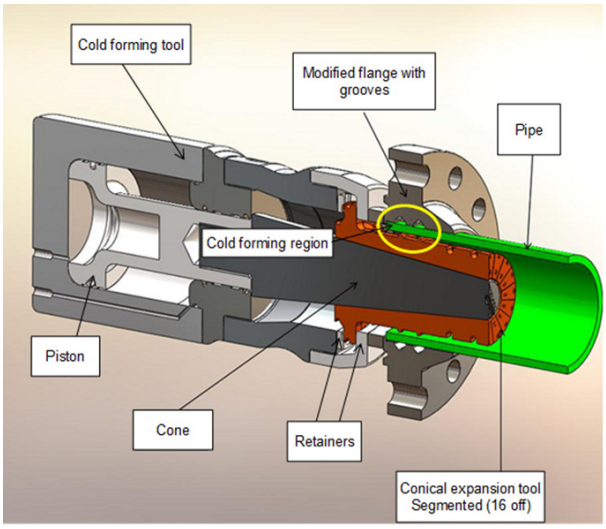

Figure 1. The main components employed in the process connecting pipe to flange.

The pipe is positioned inside a modified flange with grooves. Inside the pipe, a segmented expansion tool is held fixed in axial direction by means of retainers. The expansion tool consists of a number of segments that together form a cylinder with an inner conical shape. During cold flanging, the segments separate in tangential direction and, simultaneously, dilate in radial direction by means of a cone that slides inside the expansion tool. The radial dilation forces the pipe to cold deform into the groves of the flange. The cone is driven by a hydraulically actuated double acting piston that is also used to pull the cone back and allow the expansion tool to retract. Therefore, the main components of the cold forming tool are the retainers, the conical expansion tool (segments), the cone and the hydraulically actuated piston.

Modeling, simulation and experimental test

In general, an ASME WN CL900 6" Schedule 80 flange connections with API 5L X52 pipe quality is subjected to simulation and testing.

A dynamic non-linear 90° finite element model of the flange, pipe and segments is built up utilizing symmetry about the xy- and xz-plane as presented in figure 2. The explicit solver in Abaqus is applied for the analysis. This solver has proven to perform well for metal forming simulations with complex contact conditions. C3D8R linear brick elements with reduced integration are applied for all parts in the simulation. Enhanced hourglass control is applied for all elements. The mesh is refined in all contact areas between bodies with sharp edges as in the contact area between the pipe and flange groove. Elements applied for the segments are modeled as rigid connected to a reference point at the back of each segment. Boundary conditions are applied to the flange and pipe at the symmetry planes restricting the nodes to translate normal to symmetry plane. A cylindrical coordinate system is applied for the segment reference points restricting each reference point to translate/rotate at all degrees of freedom except in radial direction. Each segment is set to move 5.35 mm in radial direction using a smooth ramp function

going from zero to 5.35 mm and back to 4.28mm. This is sufficient to move the segments away from the pipe after deformation of the pipe.

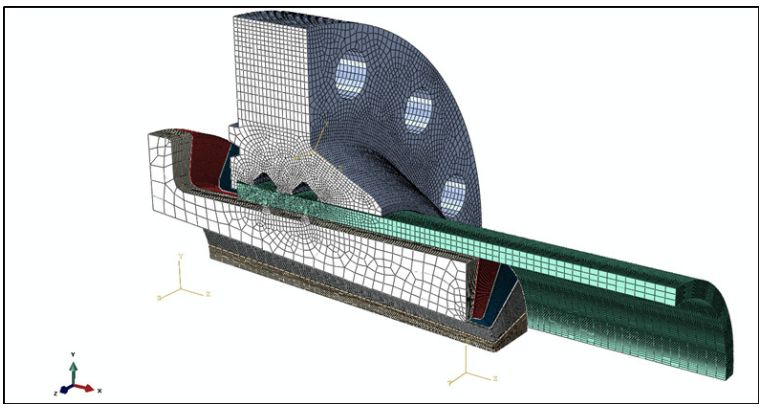

Figure 2. Finite element model presenting mesh.

A step period of 0.03s is applied for the analysis. In order to avoid excessive reduction of stable time increment due to large element deformations in the simulation, semi-automatic mass scaling is applied for all elements in the step. Elements adjacent to the flange grooves will be subjected to large deformations. Mass scaling is applied for all elements every 10 increment throughout the entire step experiencing stable time increment below $7.68 * 10^{-8}$s. This value is found by experience to give acceptable simulation time with small kinetic energy level for the deforming material. A friction coefficient of 0.3 in all directions is applied between all surfaces in contact. A general contact algorithm in Abaqus is applied.

Results

The simulation was solved on a laptop with Intel i7 quad core 2.3GHz CPU with 20 GB RAM. The model is built up by 583363 C3D8R elements and the simulation time was 2h and 40 min. The simulation time is considered sufficiently short to facilitate sensitivity analysis and design optimization of flange geometry which was considered important in model development. Based on discussions within the company a maximum simulation time of 3h had been set up as target.

Figure 3 present pump pressure versus cone axial displacement for one of the six tests. Both tested values and simulated values are included. All simulations show that artificial strain energy is approximately 1% of internal energy for the model, hence hourglassing of the elements is not considered to be a problem. The kinetic energy for all simulations is less than 1% of the internal energy of the model. Therefore the applied mass scaling scheme is considered to be acceptable.

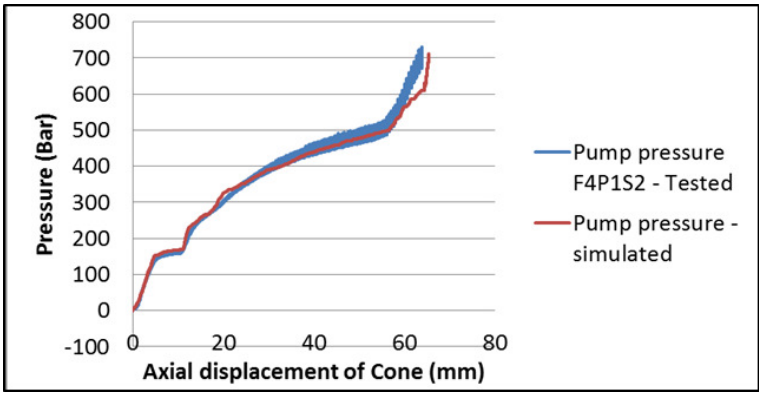

Figure 3. Pump pressure versus cone axial displacement for one of the six tests.

Conclusion

In this work FEA is examined as a possible tool for model based prediction of the cold flanging technology of Quickflange AS. Experimental work has been utilized for both model parameter identification and model verification. Comparing with test results the FEA model is in good accordance in terms of applied hydraulic pressure for the process within reasonable computational time consumption. The accuracy ensures that the process requirements regarding the hydraulic power supply can be assessed within $\pm 10\%$ which is highly satisfactory. The analysis time is less than 3 hours on a high-end laptop which makes it feasible for the model to be used in everyday work. Sensitivity analyses also revealed that the friction between Segments/pipe and pipe/flange has limited or no impact on the required hydraulic load pressure which strongly improves usefulness of the model as a predictive tool. Further work, will focus on the ability of the model to predict the key performance parameters of the cold flanged connection.

References

[1] S. Kobayashi, S. Oh, and T. Altan. *Metal Forming and the Finite Element Method*. Oxford University Press, New York, 1989, ISBN 0195044029.

[2] Anggono, A.D. Combined method of spring-forward and spring-back for die compensation acceleration. *4th International Conference on Modeling, Simulation and Applied Optimization (ICMSAO), Kuala Lumpur, Malaysia, 2011, p. 1-6*, 10.1109/ICMSAO.2011.5775496.

[3] H.-S. Park and T. V. Anh. Finite Element Analysis of roll forming process of aluminum automotive component. *International Forum on Strategic Technology (IFOST), Ulsan, Korea, 2010, p. 5-9*, 10.1109/IFOST.2010.5667921.

[4] D. Lei, et al. Research on Numerical Simulation for Automotive Panel Forming and Springback Based on Dynaform. *Third International Conference on Measuring Technology and Mechatronics Automation (ICMTMA'11), Shanghai, China, 2011, Volume 3, 2011, p. 55-58*, 10.1109/ICMTMA.2011.585.

[5] Z. Dezhi et al. Forming Force Calculation and Experimental Study on Hydro-Forming Process of Lined Steel Pipe. *Third International Conference on Measuring Technology and Mechatronics Automation (ICMTMA'11), Shanghai, China, 2011, Volume 2, p. 246-250*, 10.1109/ICMTMA.2011.349.

[6] Y. Gao, Q. Li, and L. Xiao. Numerical Simulation of JCO/JCOE Pipe Forming. *2009 WRI World Congress on Computer Science and Information Engineering, Los Angeles, USA, 2009, Volume 2, p. 233-237*, 10.1109/CSIE.2009.675.

[7] Y. Zhao, E. Yu, and T. Yan. Deformation analysis of seamless steel tube in cross rolling piercing process. *2010 International Conference on Computer Design and Applications (ICCDA), Quinhuangdao, China, 2010, Volume 3, p. 320-323*, 10.1109/ICCDA.2010.5541258.

[8] J. Meihui, T. Chengtong, and W. Wengang. Spatial shape prediction of multi-bends metal tube bending. *2011 IEEE International Conference on Computer Science and Automation Engineering (CSAE), Shanghai, China, 2011, Volume 2, p. 770-775*, 10.1109/CSAE.2011.5952615.

[9] K. Chen, et al. Numerical simulation for pipe forming in multi-process hot extrusion. *9th International Conference on Computer-Aided Industrial Design and Conceptual Design, Kunming, China, 2008, p. 685-687*, 10.1109/CAIDCD.2008.4730657.

Proceedings of the 26th Nordic Seminar on Computational Mechanics
A. Logg, K.A. Mardal, A. Massing (Eds.)

Design of Ultra High Performance Fiber Reinforced Concrete shells

Michael S. Jepsen[1], Soren Heide Lambertsen, Lars Damkilde.

(1)Division of Structures and Materials, Aalborg University Esbjerg Denmark, msj@civil.aau.dk

Summary. The paper treats the redesign of the float structure of the Wavestar waver energy converter. Previously it was designed as a glass fiber structure, but due to cost reduction requirements a redesign has been initiated. The new float structure will be designed as a double curved Ultra High Performance Fiber Reinforced Concrete shell. The major challenge in the design phase has been securing sufficient stiffness of the structure while keeping the weight at a minimum. The weight/stiffness issue has been investigated by means of the finite element method, to optimize the structure regarding overall deformation and buckling resistance.

Key words: UHPFRC, Ultra-thin double curved shell, Linear buckling analysis.

Main ideas

The basic idea of the Wave star wave energy concept is to generate power by the motion of the waves, letting a float structure follow the wave elevations. This displaces the floats up and down. The floats are connected to an arm structure, which are mounted on a hull structure, see figure 1. The float displaces the arm position vertically and as the arm moves vertically it drives a hydraulic cylinder which is attach to the top surface of the arm structure. Inside the hydraulic cylinder a piston follows the displacement of the arm. The piston pumps hydraulic oil into a common manifold system, collecting the oil pressure from each hydraulic pump mounted on each arm. The manifold creates an even flow of high oil pressure into a hydraulic motor that drives an electric motor directly. The concept behind the Wavestar WEC was formulated back in 2000 by Niels and Kjeld Hansen and has since proved its feasibility at open sea. Thus a redesign of the

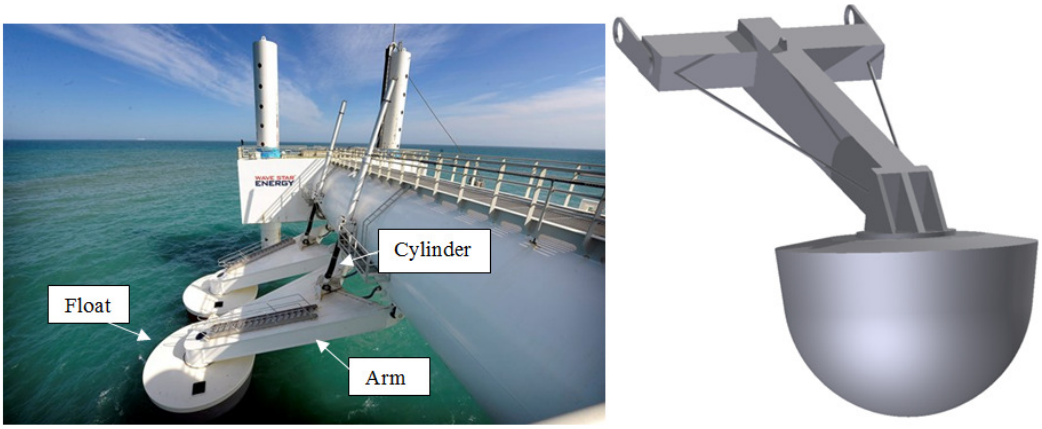

Figure 1. Right - The current WSE prototype of steel arm and glass fiber float. Left - UHPFRC design.

arm and float is initiated, see figure 1, to improve the structure and avoid the problems made evident on the first prototype. The major concern is how to lower the overall cost and increase the durability of the float structure. In the current design of the structure several problems has been recognized during manufacturing and installation[1]. The current design of the Wavestar float is a complex glass fibre structure. The structural design can be seen in figure 2 and it consists of an outer double curved 5 meter in diameter shell hemisphere which is connected to the top cap. Inside the float a complex system of thin bracing walls secures the rigidity of the structure. The complexity in manufacturing the glass fibre floats has been a major issue for the

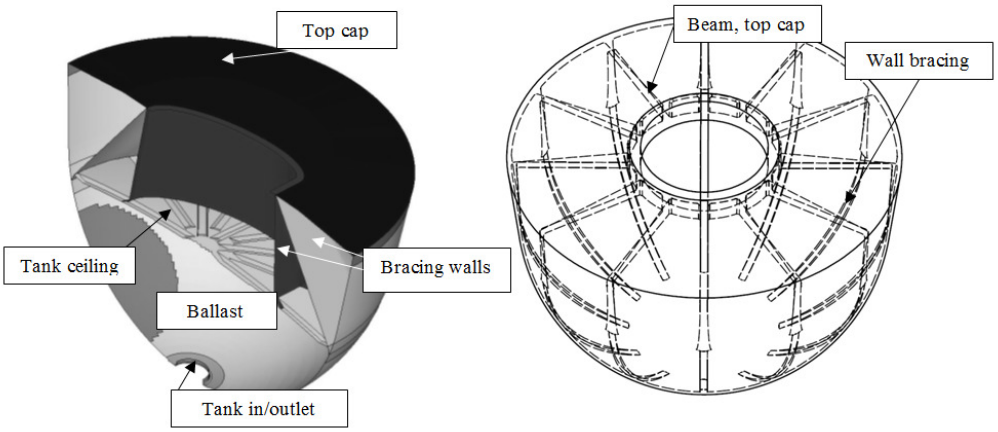

Figure 2. Left - Existing glass fiber float, Right - Ultra High Performance Fiber Reinforced concrete float.

Wave Star project, because a full scale Wave Star wave energy converter will consist of 20 floats. Thus a series production is a necessity to reduce the overall cost. This requirement has initiated a structural optimization where the current material configuration of the float has been changed from glass fibre to an Ultra High Performance Fibre Reinforced Concrete structure.

New Design Material

Choosing the UHPFRC as the main material makes it possible to accommodate the need for series production and increase the durability [2]. The float will be cast in two parts, one hemisphere and one top cap. The composition of the UHPFRC utilized in the project is a mortar with quartz sand, and steel fibre contents up to 6 vol. % straight steel fibres of 12 mm in length and 0.4 mm in diameter. Generally the UHPFRC matrix has compression capacities above 120 MPa. Increasing the compressive strength of concrete causes highly brittle failure modes. This is abbreviated by means of the fibre addition. The fibres increase the overall ductility and the ultimate tensile strength capacity, which is approximately 1/10 of the compressive strength. In figure 3 the material behavior is illustrated by means of direct tensile tests. When the first micro crack opens, the fibers inside the crack prevents further crack opening, because less energy is needed to open another micro crack. The development of multiple micro cracks causes strain hardening which is a very desirable material property in the design of civil engineering structures.

Design principles of the UHPFRC float

The basic idea is to create a UHPFRC float as seen in figure 2 where the outer geometry is adopted from the existing float. While the outer geometry is kept, the entire load carrying system inside the float is changed. In the new design no ballast tank is necessary, due to the increased weight of the structure. This means that no secondary support structure has to be

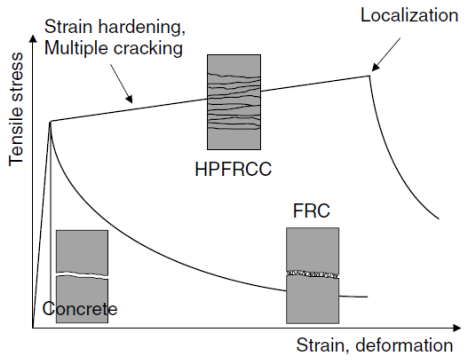

Figure 3. Strain hardening effect of the UHPFRC materials [3].

provided inside the float. Consequently a more efficient load carrying system can be achieved. In the new design, the internal forces are carried in the bracing system situated in the walls, see figure 2. The external forces at the shell or the top cap will be transferred to the cap beams. The beams are connected to the inner ring, which connects the float to the transition piece and arm. This gives an effective load carrying system, where the external forces on the shell structure is transferred directly into the inner ring as normal forces and bending moment in the top cap beams. Here the cap shell also contributes in carrying the normal forces, by membrane effect. Bending of the cap will be carried by the beams. One of the major concerns of the new design has been the weight/stiffness ratio. To investigate the design linear buckling analysis was carried out, to secure that the final design has sufficient buckling stiffness, which is of great importance in thin shell structures.

Computational issues

The structural analysis of the float is carried out in ANSYS Workbench 14.5. The first finite element model is designed to reveal which load conditions that will govern the design regarding weight and stiffness. In figure 4 the float model can be seen and it is initially analysed as a linear elastic structure discretised by ANSYS SOLID186 which is a 20 node element. The model is furthermore discretised by means of adaptive meshing, which has revealed geometrical spots with high stress gradients. This has been of special concern due to the geometrical design of both the internal bracing and the hatch in the top cap, see figure 4 right. In the design of the

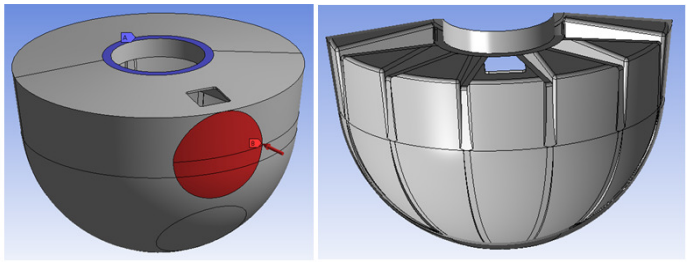

Figure 4. Left - (Blue) Boundary condition, (Red) Pressure load, Right - Internal bracing.

float, great effort has been directed to estimate the governing load conditions and how they can be applied to the model. In figure 4 the red area illustrates the pressure load, which simulates the slamming wave load on the top part of the double curved shell. Several load conditions has been investigated, but the case sketched in figure 4 cause the most critical condition regarding buckling [4]. In the structural investigation the pressure load is situated between two internal bracings. The resulting span between the two bracings in combination with the hole cut out for

the hatch make this section sensitive to a significant compressive stress field in the membrane plane. The design optimization of the internal geometry of the float, concerns primarily the number of bracings. The number of bracings has to be kept at a minimum to secure minimum weight. The final number of bracings was achieved by means of a linear elastic buckling analysis,

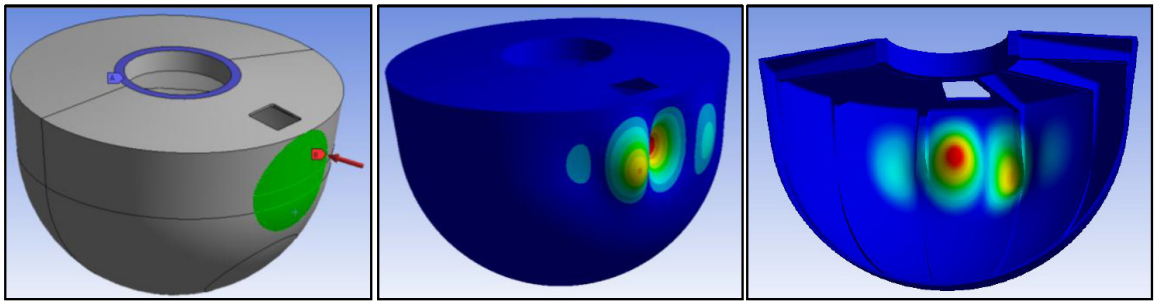

Figure 5. Left - Boundary condition, Right - Pressure load.

treated as an eigenvalue problem in ANSYS Workbench. For the most critical load case a load factor of 14 was achieved and clearly depicts the high buckling resistance of the structure. The float design has converged to an initial design with a weight of 9.7 tons, where 1.5 tons is the bracing in the double curved shell and in the top cap.

Result

The float structure has initially been investigated by means of linear elastic analysis, where the overall deformations of the UHPFRC structure have been considered. It has to be emphasized that the current float model does not take eventual rebar reinforcement into account and relies solely on the elastic properties of the UHPFRC material. The new design has a very desirable load carry system, where the loads primarily is obtained in the thin shell and translated into normal forces and flexure of the beams in the top cap. The arrangement of the internal bracing gives high rigidity against buckling, as can be seen in figure 5.

Conclusion

The redesign of Wavestar float has been investigated and a more efficient load carrying system has been achieved. The design has shown high rigidity to the environmental loadings, where especially the slamming loading is a governing condition. The number of internal bracings is optimized regarding stiffness and weight, and it can be concluded that 12 bracings are sufficient to cope with the overall deformation criterion and the buckling resistance.

References

[1] M. S. Jepsen, L. Damkilde, N. A. Hansen, B. Aarup. Increasing the durability and lowering the overall cost of wave energy converters using Ultra High Performance Concrete, *EWTEC2013,* Conference proceedings, 2013.

[2] B. Aarup, L. Rom. CRC - Applications of Fibre Reinforced High Performance Concrete, *In press.*

[3] G. Fischer, V. C. Li. Effect of fiber reinforcement on the response of structural members, *Engineering Fracture Mechanics*, volume 74, 2007, pages 258-272.

[4] M. S. Jepsen, L. Damkilde. Wavestar C5 prototype - Structural analysis of the UHPFRC float, *Design document*, Rev. 10-06-2013.

Proceedings of the 26th Nordic Seminar on Computational Mechanics
A. Logg, K.A. Mardal, A. Massing (Eds.)

Modelling of the stochastic dynamic behaviour of the Bergsøysund Bridge

Knut Andreas Kvåle[1], Ole Øiseth[2], and Ragnar Sigbjörnsson[3]

(1)Department of Structural Engineering, NTNU, knut.a.kvale@ntnu.no
(2)Department of Structural Engineering, NTNU, ole.oiseth@ntnu.no
(3)Department of Structural Engineering, NTNU, ragnar.sigbjornsson@ntnu.no

Summary. A study on the hydroelastic modelling of pontoon bridges is presented, and exemplified with the Bergsøysund Bridge. The structural modelling is based on the finite element method using the FE-software ABAQUS; the fluid-structure interaction, as well as the wave action, are modelled applying linearized potential theory represented by the DNV HYDROD WADAM software. The main emphasis is put on the stochastic response analysis within the framework of the power spectral density method. The accuracy of the presented modelling is outlined. Convergence of the response obtained by modal technique is dealt with.

Key words: frequency domain, floating bridge, Bergsøysund, modal dynamics

Introduction

The Norwegian Public Roads Administration (NPRA) is currently working on plans for rebuilding *Highway E39* along the Norwegian west-coast. This route stretches 1100 km between the cities Kristiansand and Trondheim, and incorporates multiple crossings of deep fjords, which today are operated by eight ferry connections [4]. Floating bridges of the pontoon type are proposed as feasible options for such crossings. In connection with the NPRA's project, the objective is to carry out verification of the accuracy of the modelling methods used to assess the overall dynamic behaviour of floating structures exposed to environmental action, especially due to locally wind generated waves.

Outline of general theoretical modelling

Within the framework of a Finite Element Method (FEM) formulation, the equations of motion for the floating bridge can be written as:

$$[\mathbf{M}_s]\{\ddot{\mathbf{u}}(t)\} + [\mathbf{C}_s]\{\dot{\mathbf{u}}(t)\} + [\mathbf{K}_s]\{\mathbf{u}(t)\} = \{\mathbf{p}_h(t)\}, \tag{1}$$

where $\{\mathbf{p}_h\}$ is the hydroelastic action, including the fluid-structure interaction as well as the wave action, $[\mathbf{M}_s]$ the structural mass matrix, $[\mathbf{C}_s]$ the structural damping matrix, $[\mathbf{K}_s]$ the structural stiffness matrix, and $\{\mathbf{u}(t)\}$ represents the displacements of the degrees of freedom defined for the system [3]. Hence, the floating elements contribute with forces from the interaction between the water and the structure. These forces are dependent on displacements, velocities and accelerations of the pontoons, which give rise to hydrodynamic mass, damping and stiffness. In the frequency domain, this results in the following total system matrices:

$$[\mathbf{M}(\omega)] = [\mathbf{M}_s] + [\mathbf{M}_h(\omega)], \quad [\mathbf{C}(\omega)] = [\mathbf{C}_s] + [\mathbf{C}_h(\omega)], \quad [\mathbf{K}] = [\mathbf{K}_s] + [\mathbf{K}_h]. \tag{2}$$

Assuming harmonic oscillating response, the following equations of motion for the coupled system are obtained:

$$[\mathbf{M}(\omega)]\{\ddot{\mathbf{u}}(t)\} + [\mathbf{C}(\omega)]\{\dot{\mathbf{u}}(t)\} + [\mathbf{K}]\{\mathbf{u}(t)\} = \{\mathbf{p}(t)\}, \tag{3}$$

where $\{\mathbf{p}(t)\}$ represents the wave excitation force vector acting on the pontoons. As stated in Langen and Sigbjörnsson [1], the displacements and forces can be expressed within the theory of stochastic processes using generalized harmonic decomposition:

$$\{\mathbf{u}(t)\} = \int_{-\infty}^{\infty} e^{i\omega t} d\{\mathbf{Z_u}(\omega)\}, \quad \{\mathbf{p}(t)\} = \int_{-\infty}^{\infty} e^{i\omega t} d\{\mathbf{Z_p}(\omega)\}, \tag{4}$$

where $\{\mathbf{Z_p}(\omega)\}$ and $\{\mathbf{Z_u}(\omega)\}$ are the spectral processes corresponding to the response vector and the load vector, respectively. Using the principles of superposition Equation 3 can, hence, be rewritten as follows:

$$\int_{-\infty}^{\infty} \underbrace{\left(-\omega^2 [\mathbf{M}(\omega)] + i\omega [\mathbf{C}(\omega)] + [\mathbf{K}]\right)}_{[\mathbf{H}(\omega)]^{-1}} e^{i\omega t} d\{\mathbf{Z}_u(\omega)\} = \int_{-\infty}^{\infty} e^{i\omega t} d\{\mathbf{Z_p}(\omega)\}. \tag{5}$$

Langen and Sigbjörnsson [1] express the cross-spectral densities of the displacement $\{\mathbf{u}(t)\}$ and the wave action $\{\mathbf{p}(t)\}$ as:

$$[\mathbf{S_u}(\omega)] = E[d\{\mathbf{Z_u}(\omega)\} d\{\mathbf{Z_u}(\omega)\}^*], \quad [\mathbf{S_p}(\omega)] = E[d\{\mathbf{Z_p}(\omega)\} d\{\mathbf{Z_p}(\omega)\}^*], \tag{6}$$

where the operator $[\cdot]^*$ is used as complex conjugate and matrix transpose. Combining this with Equation 5 gives:

$$[\mathbf{S_u}(\omega)] = [\mathbf{H}(\omega)] [\mathbf{S_p}(\omega)] [\mathbf{H}(\omega)]^* . \tag{7}$$

Here, the excitation spectral density matrix can be obtained from a given wave spectral density describing the geometry of the wavy sea surface (see *e.g.* [2]). To explore the hydroelastic properties of the fluid-structure system, it can be beneficial to introduce the excitation as a white noise given by a frequency independent auto-spectral density (identity) matrix and zero cross-spectral density matrices.

Furthermore, the coherence function and the correlation coefficient corresponding to the processes x and y, with standard deviances σ_x and σ_y, and covariance σ_{xy}, are respectively defined as [1]:

$$\gamma_{xy}(\omega) = \frac{|S_{xy}(\omega)|^2}{S_x(\omega) S_y(\omega)}, \quad \rho_{xy} = \frac{\sigma_{xy}}{\sigma_x \sigma_y}. \tag{8}$$

Computational modelling

An ABAQUS/CAE[5] truss model of the Bergsøysund Bridge developed by Sindre M. Hermstad was used. This model is shown in Figure 1. The structural modal system properties, such as mode shapes, damping ratios and natural frequencies, were extracted from this model. Contributions from the floating elements to the overall system stiffness, damping and mass, were calculated using DNV HYDROD WADAM[7]. These contributions were thereafter transformed to modal space using the modal shapes retrieved from the FE-model. The established system properties formed the basis for response calculations, that were performed applying a MATLAB computer code specially developed for the purpose.

Numerical results

Figure 2 shows the response spectral densities for heave of pontoons 1 to 3 induced by assumed load spectral densities. Above the diagonal, the coherence spectra are plotted. Figure 3 displays selected response spectral densities from the white noise calculations, with different number of modes included.

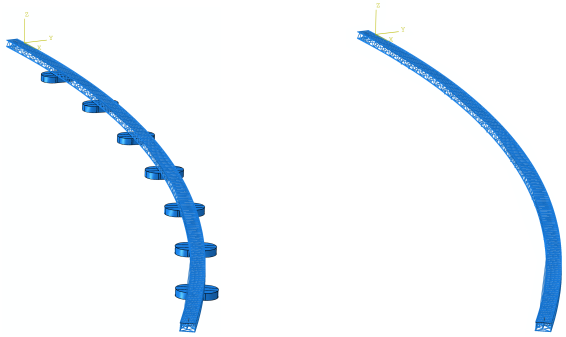

(a) Entire model, with pontoons.

(b) Bridge truss used to find the structural properties from ABAQUS.

Figure 1. FE-model used for calculations of structural properties in ABAQUS/CAE.

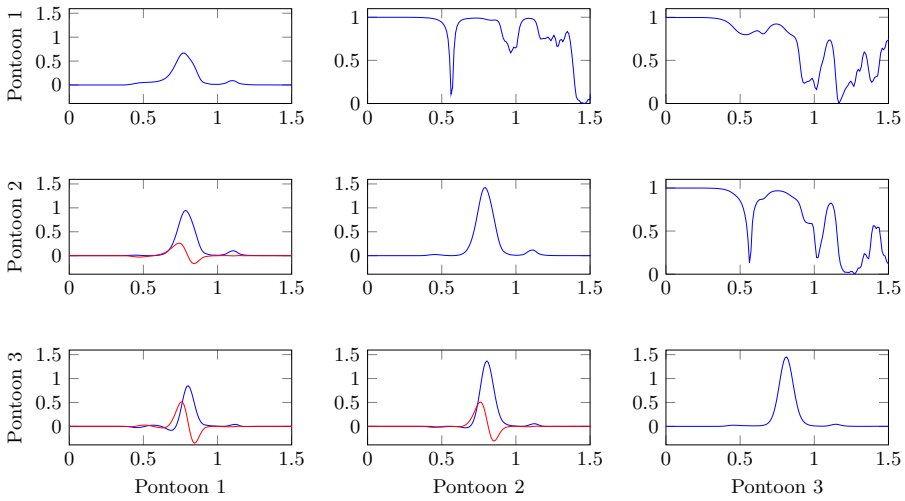

Figure 2. Response spectral densities for heave response (DOF 3) of the first 3 pontoons of the Bersøysund Bridge induced by assumed wave spectral densities. The auto-spectral densities are found on the diagonal, while the cross-spectral densities are plotted below the diagonal and the coherence spectra above the diagonal. The x-axes show the frequency in $\frac{rad}{s}$, and the y-axes show the cross-spectral densities of the displacements in $\frac{m^2 s}{rad}$, except for the coherence plots above the diagonal, which have dimensionless y-axes in the range 0 to 1 (see Equation 8). Blue plots show real parts, while red plots show imaginary parts of the cross-spectral densities.

Discussion and concluding remarks

Based on the white noise approximation it is seen that the response spectra of the Bergsøysund Bridge model approaches convergence when approximately 20 modes are included. When assumed sea load spectra are enforced (dominating period equal to 10 s), approximately 30 modes give near-converged results. On the other hand, the 100 modes used on the Bergsøysund Bridge model at most, did not introduce considerable computation time. In general, it is found that for sea states with short dominating period a higher number of modes are needed than for the long periodic ones. Furthermore, the number of modes required depends also on the response quantity under consideration, *e.g.* the acceleration response requires more modes than the displacement response. Similar applies to internal forces.

The response is sensitive to the crest length of the waves. In the case displayed in Figure 2, it is seen that the response induced by long crested waves results in response with high correlation ($\rho \approx 0.9$ between the responses of pontoon 1 and 2); furthermore, it is seen that the coherence is

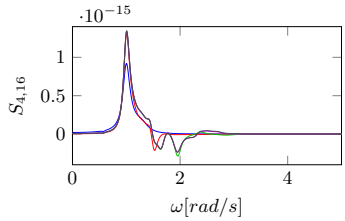

(a) Cross-spectrum between DOF 4 on pontoon 1 and DOF 4 on pontoon 3.

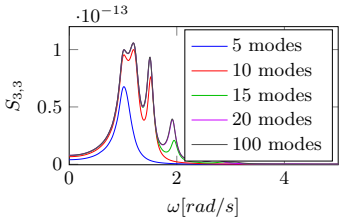

(b) Auto-spectrum of DOF 3 on pontoon 1.

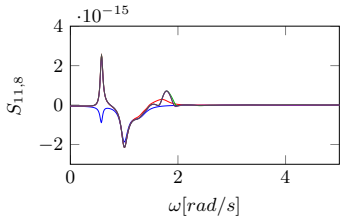

(c) Cross-spectrum between DOF 5 on pontoon 2 and DOF 2 on pontoon 2.

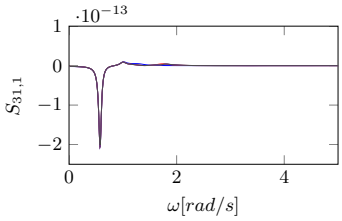

(d) Response spectrum between DOF 1 on pontoon 6 and DOF 1 on pontoon 1.

Figure 3. Selected cross- and auto-spectral densities for the Bergsøysund Bridge, with different number of modes included in the calculations. Only real parts of the spectra are plotted. Because the white noise loading is assumed unity, the units of the response spectra are $\frac{s^4}{kg^2}$.

very high, which is characteristic when the dominating wave period is long as in this case (about 10 s). For a wave field with shorter characteristic periods, this changes, and the result is lower correlation and smaller coherence, which is important to account for in fatigue computations.

The sea state used to create Figure 2 is not characteristic for the Bergsøysund environments. Therefore, the next step is to compare response measurements of the Bergsøysund Bridge with calculated response based on wave spectral densities representing the real sea state in the Bergsøysund, which is apparently characterised by locally generated wind seas.

Furthermore, by the means of system identification applying response measurements, modal parameters such as damping ratios, natural frequencies and modal shapes need to be determined. The identified system will then be used to calibrate the presented computational hydroelastic model, and thereby quantify the uncertainties of the methods applied.

References

[1] Ivar Langen and Ragnar Sigbjörnsson. *Dynamisk analyse av konstruksjoner*. Tapir, Trondheim, 1979.

[2] Ivar Langen and Ragnar Sigbjörnsson. *On the stochastic dynamics of floating bridges*. Engineering Structures, 2, 1980, 209-216.

[3] Ivar Langen. *Frequency domain analysis of a floating bridge exposed to irregular short-crested waves*. SINTEF, Trondheim.

[4] Olav Elleveset. *Project Overview Coastal Highway Route E39*. Norwegian Public Roads Administration, 2012.

[5] Abaqus/CAE, *version 6.12-1*. Dassault Systèmes, 2011, software.

[6] MATLAB, *version 2013a*. The MathWorks, Inc., 2012, software.

[7] Wadam HydroD. DNV, software.

Proceedings of the 26th Nordic Seminar on Computational Mechanics
A. Logg, K.A. Mardal, A. Massing (Eds.)

Ionic strength induced swelling for determination of thin polymer film elastic properties

Victorien Prot[1], Hrafn Mar Sveinsson[2], Kamila Gawel[2], Ming Gao[2],
Bjørn Skallerud[1] and Bjørn Torger Stokke[2]

(1)Biomechanics Division, Department of Structural Engineering, The Norwegian University of Science and Technology, NTNU, NO-7491 Trondheim, Norway, victorien.prot@ntnu.no
(2)Biophysics and Medical Technology, Department of Physics, The Norwegian University of Science and Technology, NTNU, NO-7491 Trondheim, Norway

Summary. Deposition of polymers at the surface of an ionic hydrogel is conventionally used to tailor properties of the composite material for application within for instance drug release and cell encapsulation. Here we describe a method for determination of the mechanical properties of a thin polymer film deposited on an ionic hydrogel core.

Key words: thin-film, hydrogel, finite element analysis

Introduction

Selective deposition of polymers at the surface of an ionic hydrogel is conventionally used to tailor properties, e.g., barrier properties, of the composite material for application within for instance drug release and cell encapsulation. The impact of such a layer on the the mechanical properties of the structure is largely unknown. By combination of high resolution monitoring of ionic strength induced swelling properties of the hydrogel core before and after polymer deposition and inverse finite element modelling, we suggest an approach to extract information on the equivalent mechanical properties of the layer. The constraining of the hydrogel swelling by a 4 and 8 chitosan-alginate composite multilayer was used as a basis for estimating mechanical properties of these materials. The approach also required thickness measurements of the polymer film as obtained by confocal imaging.

Methods

Experimental procedure

Hemi-ellipsoidal hydrogels (radius about 50-60 μm) of co-polymerized AAM and AMPSA were synthesized covalently attached to the end of an optical fiber. Then chitosan-alginate multilayers composed of four and eight polymer bilayers were deposited on the anionic acrylamide-based hydrogel core in a 150 mM NaCl solution at pH$\sim$5.4 after pre-equilibration of the hydrogel.
A high resolution interferometric technique (Invivosense) was employed for monitoring the optical length changes of non-modified hydrogel and hydrogel with deposited multilayers upon variation of ionic strength in immersing solution.
The interferometric setup consisted of an optical fiber of diameter $2R_f = 125\mu$m with a hydrogel physically bound at one end and a connector/adapter system at the other. See [1, 2] for further information.

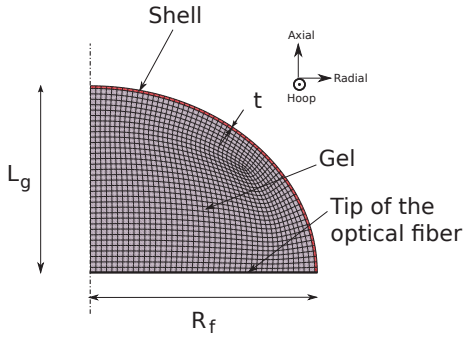

Figure 1. Finite element models. Model 1 corresponds to the anionic gel without polymer coating ($t = 0$). Model 2 corresponds to the anionic gel with polymer coating ($t \neq 0$).

Material constitutive models

In order to describe the mechanical behavior of the anionic gel used in this study, we use the following free energy function U [3]:

$$U = \frac{1}{2}Nk_BT\left(I_1 - 3 - 2\ln(J)\right) + \frac{k_BT}{v_s}\left((J-1)\ln\left(1-\frac{1}{\mathrm{J}}\right) + \chi\left(1-\frac{1}{\mathrm{J}}\right)\right) + \gamma C_{A^-} + k_BT\left[\sum_{\alpha\neq s} C_\alpha\left(ln\frac{C_\alpha}{Jc_\alpha^{ref}} - 1\right) + C_{AH}\ln\left(\frac{C_{AH}}{C_{A^-}+C_{AH}}\right) + C_{A^-}\ln\left(\frac{C_{A^-}}{C_{A^-}+C_{AH}}\right)\right] \quad (1)$$

where N is the network crosslink density, v_S the volume per solvent molecule, k_B is the Boltzmann constant, χ the Flory-Huggins parameter and γ the molar heat of dissociation. C_α and c_α^{ref} are the nominal and reference concentrations, respectively, of the different mobile species (protons H^+, positive ions $+$, negative ions$-$). C_{AH} and C_{A^-} are the nominal concentrations of the associated group AH and dissociated group A^-, respectively. J is the Jacobian of the deformation and I_1 is the first principal invariant of the right Cauchy-Green deformation tensor $\mathbf{C}$. Further details on the use of this constitutive material law can be found in [3].
The average mechanical behavior of the multilayers is modeled with the following strain energy W function proposed by Ehret and Böl [4] for biofilms,

$$W = \frac{C_0}{4}\Omega\left(\frac{1}{1-\Lambda\sqrt{I_1/3}} - \Lambda\left(\sqrt{\frac{I_1}{3}} - 2\Lambda\frac{I_1}{3} + \Lambda^2\left(\frac{I_1}{3}\right)^{3/2}\right)\right) + W_0, \quad (2)$$

$$\text{with} \qquad \Omega = \frac{L}{l_p}, \quad \Lambda = \frac{r_0}{L} \quad \text{and} \quad r_0^2 = 2l_p^2\left(\frac{L}{l_p} - 1 + e^{-L/l_p}\right), \quad (3)$$

where L is the contour length, l_p the persistence length and r_0 the end-to-end distance between two junctions in the reference configuration. W_0 is a constant term calculated such as $W(I_1 = 3) = 0$. C_0 is a material parameter to be determined in the present study representing the equivalent elastic properties of the chitosan-alginate multilayers. The multilayers are modeled as fully incompressible. The constitutive material model defined by eq.(2) was implemented in an ABAQUS user-subroutine UHYPER.

Inverse finite element modelling

A finite element model was used to simulate the ionic strength induced swelling of the anionic hydrogel with and without polymer coating (see Fig, 1). The network crosslink density N and the Flory-Huggins parameter χ of the hydrogel (AMPSA) used in this work were identified by fitting the length of the hydrogel sensor L_g^{FE} (model 1, Fig 1) computed using the finite element software ABAQUS to the length L_g^{exp}. L_g^{exp} was measured during our swelling experiment

Table 1. Parameters of the ionic hydrogel (APSMA)

	vN	χ	pKa	f	t	$L^{exp}_{g,0.15}$ (μm)
AMPSA	3.3e-3	0.48	2.0	0.022	0	54.0

Table 2. Elastic parameter C_0 (eq.(2))for the deposited shells with 4 and 8 bilayers (Chitosan-alginate)

		$C_0/(k_BT/v)$	l_p (nm)	L (nm)	t (μm)	$L^{exp}_{g,0.15}$ (μm)
Chitosan-alginate	4 bilayers	2.1e-2	15	250	0.8±0.2	54.7
	8 bilayers	2.6e-2	15	250	0.8±0.2	50.2

with varying salt concentration (varying $\bar{c}_+$) and constant pH (constant $\bar{c}_{H^+}$) and the hydrogel bound to the optical fiber without deposited polymer layer. The fitting was performed using the *lsqnonlin* function in the Optimization Toolbox of the commercial software MATLAB together with the trust-region-reflective algorithm.
Then, the material parameter C_0 in eq.(2) of the thin polymer layer deposited on the surface of the ionic hydrogel is determined using a similar numerical procedure and using the network crosslink density N and the Flory-Huggins parameter χ for the ionic hydrogel found previously and the finite element model 2 , see Figure 1.

Results

The identified material parameters obtained with the FE constrained model for the ionic hydrogel (AMPSA) and the deposited shells with 4 and 8 bilayers (Chitosan-alginate) are summarized in Tables 1 and 2.

Comparisons between experiments and numerical simulations using the identified parameters, provided in Figure 2, show satisfying agreement.

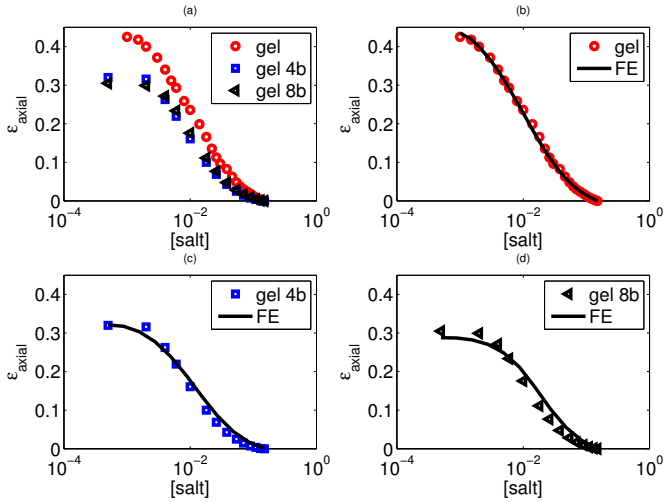

Figure 2. Comparison between the axial strain $\epsilon_{axial} = (L_g - L_{g,0.15})/L_{g,0.15}$ of the hydrogel measured during experiments at different levels of salt concentration and the one computed from finite element analyses with the fitted parameters from Tables 1 and 2. Red circles, blue squares and black triangles correspond to experimental results for the gel without deposited layer, the gel with four and eight bilayer chitosan-alginate coating, respectively. The solid lines correspond to the numerical results.

Concluding remarks

We develop a method to characterize multilayer thin films material properties from finite element analysis. Experimental measurements of the deformations of the hydrogel and the thickness of the deposited thin film are used as inputs to determine the crosslink densities of the hydrogel first and the elastic property of deposited multilayer in a second step. This can be achieved by means of an inverse modeling approach using a nonlinear least square technique. The method is applied to a hemi-ellipsoidal hydrogel with chitosan and alginate multilayers. It may easily be employed with other types of geometries and polymer films. Therefore, this method can be adapted to the experimental set-up available. Moreover, the numerical method described in this study may be used with other kinds of constitutive material models.

References

[1] V. Prot, H. M. Sveinsson, K. Gawel, M. Gao, B. Skallerud, and B. T. Stokke. Swelling of a hemi-ellipsoidal ionic hydrogel for determination of material properties of deposited thin polymer films: an inverse finite element approach. *Soft Matter*, 9:5815–5827, 2013.

[2] S. Tierney, D. R. Hjelme, and B. T. Stokke. Determination of swelling of responsive gels with nanometer resolution. fiber-optic based platform for hydrogels as signal transducers. *Analytical Chemistry*, 80(13):5086–5093, 2008.

[3] R. Marcombe, S. Cai, W. Hong, X. Zhao, Y. Lapusta, and Z. Suo. A theory of constrained swelling of a ph-sensitive hydrogel. *Soft Matter*, 6:784–793, 2010.

[4] A. E. Ehret and M. Böl. Modelling mechanical characteristics of microbial biofilms by network theory. *J. R. Soc. Interface*, 10(78):20120671, 2013.

Proceedings of the 26th Nordic Seminar on Computational Mechanics
A. Logg, K.A. Mardal, A. Massing (Eds.)

How accurate is classical shell theory as a model of a spherical dome?

Juhani Pitkäranta

Aalto University, School of Science, Department of Mathematics and Systems Analysis
P.O. Box 11100, FI-00076 Aalto, juhani.pitkaranta@aalto.fi

Summary. We study the accuracy of classical shell bending theory for spherical domes as compared to the full three dimensional elasticity theory. The analysis is based on variational methods and on the Hypercircle theorem of the linear theory of elasticity.

Key words: shell theory, verification & validation, variational methods

Introduction

In [1] the accuracy of a classical engineering model for a shell roof was studied in case of the so called *Girkmann problem*, a textbook example presented in [2]. In the Girkmann problem the roof consists of a spherical dome stiffened by a foot ring, and the problem is to find the horizontal force and moment acting at the junction of the dome and the ring when the roof is loaded by its own weight, see Figure 1. The material of the structure is assumed homogeneous and linearly elastic with Yuong modulus $\nu = 0$. In [1] the accuracy of the classical model was tested against the full axisymmetric 3D linear elastic model of the roof.

Shell bending theory

We focus here on the subproblem of the Girkmann problem where the stiffening ring is removed and only the spherical shell remains. In the subproblem we want to evaluate the horizontal shift (Λ) and the rotation (Ψ) of the edge of the dome due to given axisymmetric tractions acting at the edge of the dome. The classical shell bending theory gives the solution in the form

$$E\Lambda = k_{11}R + k_{12}M, \quad E\Psi = -k_{12}R - k_{22}M, \tag{$\star$}$$

where E is the Young modulus and R, M are the force and moment per unit length at the edge due to the tractions acting there. The coefficients k_{ij} depend on the thickness (d) of the dome, the radius (r_0) of its midsurface and the opening angle (α) of the dome. Approximate expressions for k_{ij} were historically found manually using simplified shell bending theory [2, 3]. In [1] it was demonstrated that even more accurate expressions are manually computable using asymptotic expansions.

The problem we pose is: Suppose we know the coefficients k_{ij} in model ($\star$) precisely as corresponding to classical shell bending theory with no simplifications. Then how accurate is such a model as compared to the full 3D axisymmetric linear elastic model? We approach this problem by mathematical error analysis that is based on the Hypercircle theorem of linear elasticity. In this way we obtain rigorous, computable error bounds.

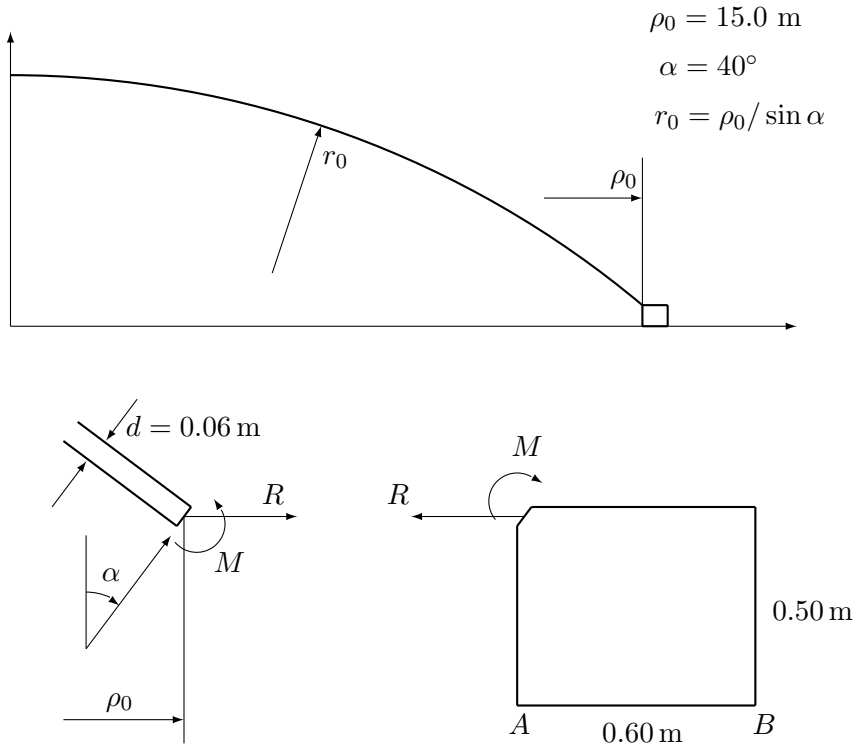

Figure 1. The Girkmann problem. Cross-section of the structure.

Results

In the 3D linear elastic model we need to specify the normal and shear stress distributions at the edge more closely, since only the horizontal stress resultant R and moment M are referred to in ($\star$). We consider kind of edge conditions:

A. *Soft edge*: No kinematic constraints. The stresses σ_θ and $\tau_{r\theta}$ (spherical coordinates) are specified as

$$\sigma_\theta(\alpha, r) = \frac{r_0}{r}\left[\frac{R cos\alpha}{d} - \frac{12M}{d^3}(r - r_0)\right],$$
$$\tau_{r\theta}(\alpha, r) = \frac{r_0}{r} \cdot \frac{R\sin\alpha}{d}.$$

B. *Hard edge*: For the displacements, only rigid horizontal deflection (Λ) and rotation (Ψ) are allowed at vertical profiles of the edge, so that

$$U_\theta(\alpha, r) = \Lambda\cos\alpha + \Psi(r - r_0), \quad U_r(\alpha, r) = \Lambda\sin\alpha.$$

For the stresses only the two resultant conditions are specified:

$$\int_{r_0-d/2}^{r_0+d/2} [\cos\alpha\,\sigma_\theta(\alpha, r) + \sin\alpha\,\tau_{r\theta}(\alpha, r)]\, r dr = r_0 R,$$
$$\int_{r_0-d/2}^{r_0+d/2} \sigma_\theta(\alpha, r)(r - r_0)\, r dr = -r_0 M.$$

The kinematic constraint of case B holds in classical shell theory, so the two cases A,B differ only in the 3D model.

In the error analysis we use the fact that classical shell bending theory follows from the 3D energy principle when enforcing the kinematic assumptions of classical shell theory, that is: U_θ varies linearly in r and U_r is constant in r. This allows us to derive direct energy bounds for the gaps of the spring coefficients k_{ij} in between the two models. Applying the Hypercircle theorem to such bounds we obtain the following result.

Theorem 1. *Let k_{ij} be the spring coefficients in $(\star)$ according to the 3D model and let k_{ij}^S be the coefficients according to classical shell bending theory. Then the following error bounds hold:*

$$0 \le \frac{k_{ii} - k_{ii}^{\mathrm{S}}}{k_{ii}^{\mathrm{S}}} \le \frac{\sqrt{3}}{10} \cdot \frac{d}{r_0} + \mathcal{O}\left(\frac{d}{r_0}\right)^{3/2}, \quad i = 1, 2,$$
$$\frac{|k_{12} - k_{12}^{\mathrm{S}}|}{k_{12}^{\mathrm{S}}} \le \frac{\sqrt{6}}{10} \cdot \frac{d}{r_0} + \mathcal{O}\left(\frac{d}{r_0}\right)^{3/2}.$$

In Table 1 we give the spring coefficients k_{ij}^{S} and the bounds for $|k_{ij} - k_{ij}^{\mathrm{S}}|$ according to Theorem 1 for the Girkmann problem where $d/r_0 = 0.0026$. (The remainder terms in the bounds are computable as well, but these are insignificant.) In the table, k_{12} and k_{22} are given in the units [cm] and [cm^2], respectively (k_{11} is dimensionless). The coefficients k_{ij}^{S} were computed by 1D FEM and also confirmed manually by using the improved engineering bending theory of [1].

Table 1. Spring coefficients and error bounds in the Girkmann problem

i, j	11	12	22
$k_{ij}^{\mathrm{S}} =$	8343	144.68	5.0115
$\lvert k_{ij} - k_{ij}^{\mathrm{S}}\rvert \le$	4	0.09	0.0023

We conclude that classical shell bending theory is very accurate — indeed so accurate that it is not easy to beat by modern 3D FEM tools. In the context of the original Girkmann problem, software tests referred to in [1] lead to similar conclusions.

References

[1] J. Pitkäranta, I. Babuška, and B. Szabó, The dome and the ring: Verification of an old mathematical model for the design of a stiffened shell roof, *Computers and Mathematics with Applications*, 64(1):48–72, 2012.

[2] K. Girkmann, *Flächentragwerke*, Third Edition. Springer, Wien, 1954.

[3] D.P. Billington, *Thin Shell Concrete Structures*. McGraw-Hill, New York, 1965.

Proceedings of the 26th Nordic Seminar on Computational Mechanics
A. Logg, K.A. Mardal, A. Massing (Eds.)

Resonances and mode shapes of the human vocal tract during vowel production

Atle Kivelä[1], Juha Kuortti[1], and Jarmo Malinen[1]

[(1)]Aalto University, School of Science, Department of Mathematics and Systems Analysis, P.O. BOX 11100, FI-00076 AALTO, {atle.kivela, juha.kuortti, jarmo.malinen}@aalto.fi

Summary. We show that higher vowel formants may consist of multiple acoustic resonances. We compute the Helmholtz resonances of the vocal tract (VT) using FEM. The resulting resonance and pressure information is then compared to formants extracted from recorded vowel phonation. It is observed that the pure longitudinal modes appear in the sequence of all acoustic modes in an order that depends on the vowel even in a single test subject.

Key words: vocal tract, resonance, formants, FEM, MRI

Introduction

It is well known that the two or three lowest vowel formants $F_1, F_2, \ldots$ (in increasing order of frequency) are sufficient to distinguish between vowels in most cases. The formants, determined from sound samples, correspond closely to the acoustic resonance frequencies $R_1, R_2, \ldots$ of the human vocal tract (VT). The relevance of the higher formants and resonances (i.e., $n \geq 4$) has been a subject of study for a long time. The most recent findings are due to computational modelling of the VT acoustics in 3D geometries that have been obtained using X-ray computer tomography (CT) [7, 8].

The purpose of this article is to model VT acoustics using a 3D Helmholtz resonance model and Finite Element Method (FEM) for its numerical solution. Resonances obtained from the Helmholtz model are compared to (i) the resonances obtained from Webster's horn model with one spatial dimension, and (ii) the spectral envelopes extracted from sound samples from the same test subject. We observe that the Finnish vowel [œ] has transversal components in resonances R_4, R_5, R_6, and these form a cluster that gets experimentally recognised as just a single formant F_4. In this data, the lowest transversal resonance takes always place in piriform sinuses and not in the mouth cavity, see [6]. We remark that the positions of the longitudinal resonance frequencies in the sequence of all resonance frequencies vary, depending on the vowel geometry even in the same subject (see Fig. 1).

The computational geometries for this article have been obtained using Magnetic Resonance Imaging (MRI). Using MRI is not as straightforward as CT since osseous structures (such as maxillae and teeth) do not show up in the images. Further, the MRI machine produces a lot of acoustic noise which makes simultaneous speech recording more difficult [2, 3]. However, MRI can be used to make a large number of measurements from the same subject not having a medical condition that would justify the use of ionising radiation.

Methods

We use 3D geometries of the VT and a MATLAB-based FEM solver for the Helmholtz equation (1). The raw MRI data is first vectorised as described in [1]. In addition to Eq. (1), more simple acoustic resonance model Eq. (3) is used. The latter model accounts only for the longitudinal acoustic resonances. Hence, identification of pure longitudinal acoustic resonances from Eq. (1) can be carried out by comparison, without inspecting 3D eigenfunctions of Eq. (1) individually. Finally, Linear Predictive Coding (LPC) is used to determine spectral envelopes from recorded sound samples, and their peaks are compared to the computed resonances $R_1, R_2, \ldots$.

Helmholtz equation

We solve the acoustic resonances by first solving the Helmholtz problem

$$\begin{cases} \lambda^2\Phi_\lambda = c^2\Delta\Phi_\lambda \quad \text{on} \quad \Omega, \quad \Phi_\lambda = 0 \quad \text{on} \quad \Gamma_1, \\ \frac{\partial\Phi_\lambda}{\partial\nu} = 0 \quad \text{on} \quad \Gamma_2, \quad \text{and} \quad \lambda\Phi_\lambda + c\frac{\partial\Phi_\lambda}{\partial\nu} = 0 \quad \text{on} \quad \Gamma_3, \end{cases} \tag{1}$$

where the speed of sound is denoted by c, $\Omega \in \mathbb{R}^3$ is the interior volume of the VT whose boundary $\partial\Omega = \Gamma_1 \cup \Gamma_2 \cup \Gamma_3$ consists of the mouth opening Γ_1, the VT tissue walls Γ_2, and the (virtual) control surface Γ_3 right above the glottis. The exterior normal derivative is denoted by $\frac{\partial}{\partial\nu}$ and the solution Φ_λ is the velocity potential, giving the acoustic pressure by $\rho\lambda\Phi_\lambda$ where ρ is the density of air.

The variational formulation of Eq. (1) can be turned into a quadratic eigenvalue problem as shown in [4]. The matrices for the eigenvalue problem are constructed using FEM with piecewise linear shape functions and tetrahedral meshes with approximately 10^5 elements. We obtain the stiffness matrix $\mathbf{K}$, the mass matrix $\mathbf{M}$, and the matrix $\mathbf{P}$ which presents the absorbing glottis boundary condition in Eq. (1). The discretised eigenvalue problem can be written as

$$\lambda^2\mathbf{K}\mathbf{x}(\lambda) + \lambda c\mathbf{P}\mathbf{x}(\lambda) + c^2\mathbf{M}\mathbf{x}(\lambda) = 0. \tag{2}$$

The imaginary parts of the smallest eigenvalues give resonance frequencies $R_1, R_2, \ldots$ (in increasing order of frequency), and the longitudinal resonances are identified from these by comparing them to the resonances obtained from (3).

Resonance version of Webster's horn model

Using the 3D wave equation is impractical for modelling acoustics of the VT in high temporal and spatial resolution. The classical Webster's horn model is computationally much lighter, and in some special geometries even analytic solutions are possible [9]. For Webster's model, a tubular domain is defined by a parameterised centreline and corresponding cross-sectional areas $A(s)$ as shown in Fig. 2. The resonances of Webster's horn model can then be obtained from the eigenvalue problem

$$\lambda^2\psi_\lambda = \frac{c^2\Sigma(s)^2}{A(s)}\frac{\partial}{\partial s}\left(A(s)\frac{\partial\psi_\lambda}{\partial s}\right) \quad \text{for} \quad s \in [0, \ell], \tag{3}$$

where ℓ is the length of the VT, and the function $\Sigma(s)$ has been introduced in [5] for taking into account the centreline curvature. The Webster's velocity potential ψ_λ corresponds to the 3D velocity potential given by (1). We solve Eq. (3) numerically by using piecewise linear elements and end point conditions at $s = 0, \ell$ corresponding to the boundary conditions in Eq. (1).

Eqs. (1)–(3) are solved numerically using sufficiently many elements so that all computed resonances can be regarded as accurate.

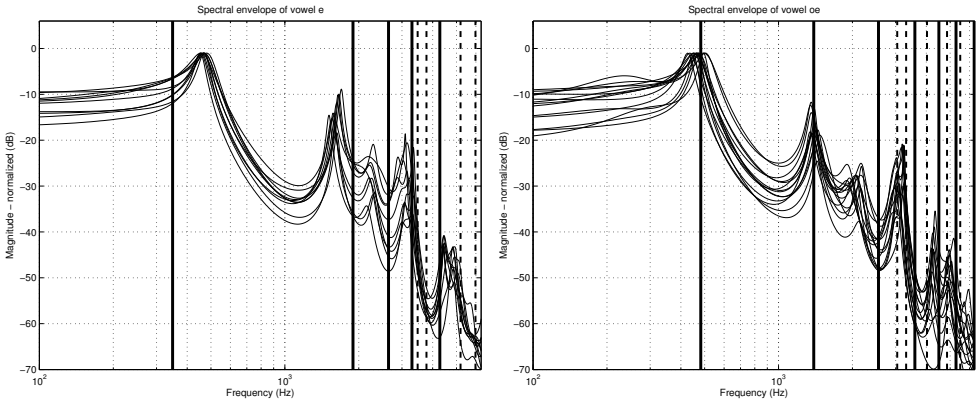

Figure 1. The spectral envelopes of Finnish vowels [œ,e] recorded in an anechoic chamber. These curves differ only slightly from those recorded during the MRI [3]. The solid vertical lines represent longitudinal resonances while the dashed lines represent transversal resonances, both computed from Eq. (1).

LPC

Spoken vowels can be identified based on wide bandwidth acoustic energy concentrations around discrete frequencies in the power spectrum of the measured signal. Such energy peak locations $F_1, F_2, \ldots$ (in increasing order of frequency) are called formants, and they are related to the frequencies $R_1, R_2 \ldots$ computed from Eq. (1). In measured signals, formants can discriminated from harmonic overtones of the fundamental glottal frequency by the fact that formants, indeed, have much wider bandwidth. Thus, smoothing of the power spectrum allows the formants to be usually extracted with good accuracy.

The most popular method of spectral smoothing in speech science is LPC. LPC is a forward predictor FIR filter whose frequency response gives an estimate for the spectral envelope of the signal; the poles of the filter can be regarded as a practical definition of formant locations. LPC is mathematically equivalent to fitting a low-order rational function $R(s)$ to the power spectrum function on the imaginary axis. Thus, plotting the values of $|R(i\omega)|$ for real ω yields the desired smoothing of the power spectrum, and formant frequencies $F_1, F_2, \ldots$ correspond then to the imaginary parts of the poles of $R(s)$.

Results

The LPC spectral envelopes and resonance frequencies $R_1, R_2, \ldots$ up to 4 kHz for Finnish vowels [œ, e] are shown in Fig. 1. Some of the resonances are identified as longitudinal by Webster's horn model, and they are plotted with solid lines in Fig. 1. The remaining resonances from Eq. (1) are regarded as transversal, and this behaviour can be observed from the acoustic pressure distributions shown in Fig. 2.

Results presented here and in [7, 8] confirm that higher formants may consist of a cloud of longitudinal and transversal resonances. This clustering phenomena appears to be significant from the fourth formant onwards. As expected, the first and second formants can be reliably identified with the resonances of Webster's horn model.

Conclusions

The resonances from Eq. (1) differ somewhat from those extracted from experimental data. Apart from the lowest formant F_1 (where the formant extraction from speech signal is most error-prone), the discrepancy is likely to be caused by the unrealistic acoustic impedance at mouth in Eq. (1) as discussed in [4].

The full classification of the resonance structure of the VT in various vowel configurations requires additional effort and a combined MRI/sound data set from several test subjects. An-

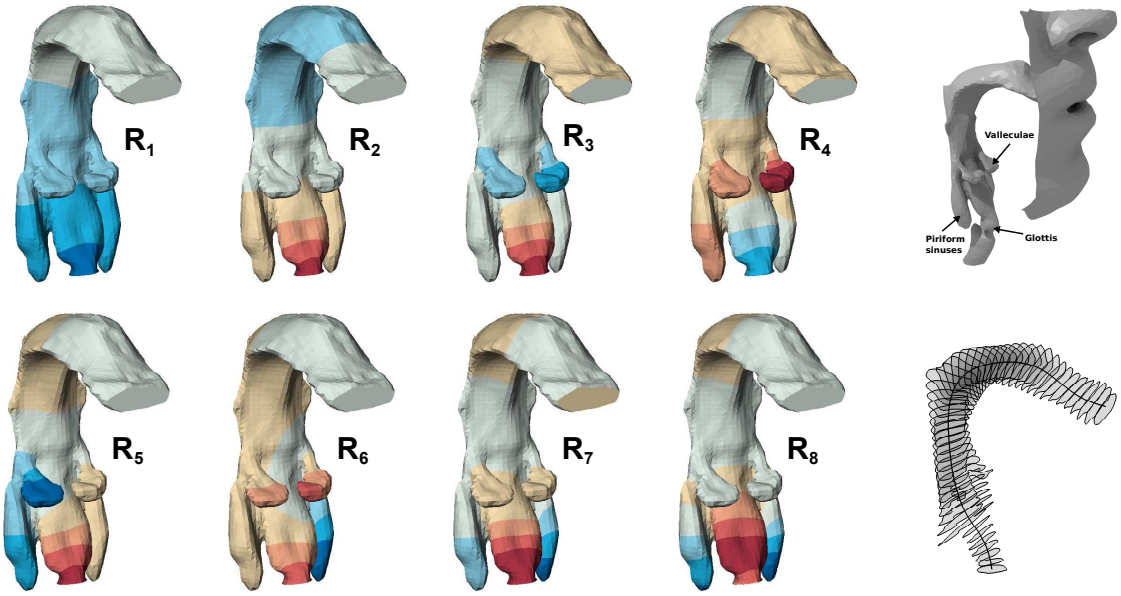

Figure 2. Modes of the first eight resonances for vowel [œ], the surface mesh with face, and an example of a generated area function.

other interesting challenge is the study of the singer's formant in sopranos and tenors where similar resonance clustering is expected to take place.

References

[1] D. Aalto, J. Helle, A. Huhtala, A. Kivelä, J. Malinen, J. Saunavaara, and T. Ronkka. Algorithmic surface extraction from MRI data: modelling the human vocal tract. In *BIODEVICES*, 2013.

[2] D. Aalto, J. Malinen, P. Palo, O. Aaltonen, M. Vainio, R.-P. Happonen, R. Parkkola, and J. Saunavaara. Recording speech sound and articulation in MRI. In *BIODEVICES*, 2011.

[3] D. Aalto, O. Aaltonen, R.-P. Happonen, P. Jääsaari, A. Kivelä, J. Kuortti, J.-M. Luukinen, J. Malinen, T. Murtola, R. Parkkola, J. Saunavaara, T. Soukka, and M. Vainio. Measurement of acoustic and anatomic changes in oral and maxillofacial surgery patients. 2013. arXiv:1309.2811.

[4] A. Hannukainen, T. Lukkari, J. Malinen, and P. Palo. Vowel formants from the wave equation. *J. Acoust. Soc. Am. Express Letters*, 122(1):EL1–EL7, 2007.

[5] T. Lukkari and J. Malinen. Webster's equation with curvature and dissipation. arXiv 1204.4075, 2013 (submitted).

[6] J. Sundberg. Articulatory interpretation of the "singing formant". *J. Acoust. Soc. Am.*, 55(4):838–844, 1974.

[7] T. Vampola, J. Horáček, A.-M. Laukkanen, and J. Švec. Finite element modelling of vocal tract changes after voice therapy. *Applied and Computational Mechanics*, 5(1), 2011.

[8] T. Vampola, J. Horáček, A.-M. Laukkanen, and J. Švec. Human vocal tract resonances and the corresponding mode shapes investigated by three-dimensional finite-element modelling based on CT measurement. *Logopedics Phoniatrics Vocology*, pages 1–10, 2013.

[9] A. Webster. Acoustic impedance, and the theory of horns and of the phonograph. *Proc. Natl. Acad. Sci. USA*, 5:275–282, 1919.

Proceedings of the 26th Nordic Seminar on Computational Mechanics
A. Logg, K.A. Mardal, A. Massing (Eds.)

Isogeometric Collocation Methods for 1D thin structures

Carlo Lovadina[1]

(1) University of Pavia, Via Ferrata 1, 27100 Pavia, Italy, carlo.lovadina@unipv.it

Summary. We study isogeometric collocation methods for 1D thin structures, focusing on the simplest example of the Timoshenko beam problem, and considering a mixed formulation. In particular, we show that locking-free solutions are obtained, independently on the approximation degrees selected for the unknown fields.

Key words: Timoshenko beam model, isogeometric collocation methods, locking-free schemes.

Introduction

Isogeometric Analysis (IGA) is an idea, firstly introduced by Hughes et al. [4, 5], to fill the gap between Computational Mechanics and Computer Aided Design (CAD). The key feature of IGA is to extend the Finite Element Method (FEM) representing the geometry by spline functions typically used by CAD systems, and then invoking the isoparametric concept to define field variables. As a consequence, the computational domain exactly reproduces the CAD description of the physical domain.

Within the framework of IGA, collocation methods have been proposed in [1] as an appealing high-order low-cost alternative to standard Galerkin approaches. In [3] we initiate the investigation about the IGA collocation methods for the approximation of thin structure problems: the aim of this paper is to report on the results detailed in that paper.

We focus on the simple case of an initially straight planar Timoshenko beam. Despite its simplicity, the numerical approximation of this problem often presents some difficulties, especially when dealing with FEM in connection with low-order schemes. Indeed, one has to avoid the so-called *shear locking phenomenon*, which arises when the beam thickness parameter becomes "small". Within the FEM framework, several options to overcome *shear locking* are nowadays well-established. For example, ad-hoc reduced integration of the shear energy term can be used. Alternatively (and, sometimes, equivalently), the employment of discrete schemes based on a suitable *mixed formulation* can be of great advantage. However, the use of a mixed formulation does not solve the problem by itself: the discrete approximation spaces must be carefully chosen to avoid shear locking, and to prevent the occurrence of *spurious modes*.

On the contrary, it has been shown in [3] that suitable isogeometric collocation methods can be designed, leading to *locking-free schemes without the need of any compatibility condition between the selected discrete spaces*. Therefore, the convergence behaviour, *uniform in the thickness parameter*, is dictated only by the approximation features of the discrete spaces. We note that this very appealing property is deeply linked to the collocation method adopted and not only a consequence of the isogeometric approach.

Timoshenko beam equations

We consider an initially straight, planar, elastic, and homogenous beam. The beam axis is assumed to occupy the interval $[a, b]$. Following the Timoshenko model [6], we introduce a *suitably scaled* mixed formulation, where the unknown variables are the displacements $v(x)$ (usually referred to as deflections), the rotations $\varphi(x)$, and the *scaled* shear strain $\tau(x)$. Assuming for simplicity, but without loss of generality, clamped boundary conditions, the equations to be solved are the following:

$$\begin{cases} \tau'(x) = \alpha q(x), & x \in]a, b[, \\ -\varphi''(x) + \tau(x) = 0, & x \in]a, b[, \\ v'(x) + \varphi(x) - \alpha^{-1} t^2 \tau(x) = 0, & x \in]a, b[, \\ v(a) = v(b) = 0, \\ \varphi(a) = \varphi(b) = 0, \end{cases} \tag{1}$$

where $q(x)$ represents the transversal load, α is a positive parameter depending on the material properties and on the cross section geometry, and t is a slenderness parameter.

Isogeometric collocation methods for the Timoshenko beam

In this section, we present our collocation methods for the Timoshenko beam, which are implemented in the spirit of isogeometric collocation methods, as introduced in [1] and further developed in [2]. Before proceeding, we need to introduce the p_φ-degree B-spline space $\Phi_h \subset C^2(a, b)$, used for the rotation approximation, and associated with the knot vector

$$\{\xi_1^\varphi = 0, ..., \xi_{n_\varphi + p_\varphi + 3}^\varphi = 1\}. \tag{2}$$

Analogously, we introduce the p_v-degree B-spline space

$$V_h \subset C^2(a, b), \tag{3}$$

used for the deflection approximation, and associated with the knot vector

$$\{\xi_1^v = 0, ..., \xi_{n_v + p_v + 3}^v = 1\}. \tag{4}$$

Finally, we define the p_τ-degree B-spline space

$$\Gamma_h \subset C^1(a, b), \tag{5}$$

used for the shear stress approximation, and associated with the knot vector

$$\{\xi_1^\tau = 0, ..., \xi_{n_\tau + p_\tau + 1}^\tau = 1\}. \tag{6}$$

Furthermore, we introduce suitable sets of collocation points in $[a, b]$:

$$\begin{cases} \mathcal{N}(\Phi_h'') = \{x_1, x_2, \ldots, x_{n_\varphi}\}, \\ \mathcal{N}(V_h') = \{y_1, y_2, \ldots, y_{n_v+1}\}, \\ \mathcal{N}(\Gamma_h') = \{z_1, z_2, \ldots, z_{n_\tau - 1}\}. \end{cases} \tag{7}$$

Mixed discretization

We now introduce our collocation method based on the mixed formulation (1). Given the finite dimensional spaces Φ_h, V_h and Γ_h, together with the collocation points introduced in (7), the discretized problem reads as follows.

$$\begin{cases} \text{Find } (\varphi_h, v_h, \tau_h) \in \Phi_h \times V_h \times \Gamma_h \text{ such that:} & \\ \tau_h'(z_i) = \alpha q(z_i), & z_i \in \mathcal{N}(\Gamma_h') \\ -\varphi_h''(x_j) + \tau_h(x_j) = 0, & x_j \in \mathcal{N}(\Phi_h'') \\ v_h'(y_k) + \varphi_h(y_k) - \alpha^{-1} t^2 \tau_h(y_k) = 0, & y_k \in \mathcal{N}(V_h') \\ v_h(a) = v_h(b) = 0, & \\ \varphi_h(a) = \varphi_h(b) = 0. & \end{cases} \tag{8}$$

Notice that problem (8) is a linear system of $(n_\varphi + n_v + n_\tau + 4)$ equations for $(n_\varphi + n_v + n_\tau + 4)$ unknowns.

Error estimates

We make the following fundamental assumption on the collocation points.

Assumption 0.1 (Stable interpolation) *There exists a constant C_{int}, independent of the knot vectors, such that the following holds. For all functions θ, w, and r in $C^0(a,b)$ there exist unique interpolating functions*

$$\begin{aligned} &\theta_{II}(x_j) = \theta(x_j) \qquad \forall\ x_j \in \mathcal{N}(\Phi_h''), \quad \theta_{II} \in \Phi_h'', \\ &w_{III}(x_j) = w(x_j) \qquad \forall\ z_i \in \mathcal{N}(V_h'), \quad w_{III} \in V_h', \\ &r_I(x_j) = r(x_j) \qquad \forall\ y_k \in \mathcal{N}(\Gamma_h'), \quad r_I \in \Gamma_h', \end{aligned}$$

with the bounds

$$\begin{aligned} &||\theta_{II}||_{L^\infty)} \leq C_{int} ||\theta||_{L^\infty}, \\ &||w_{III}||_{L^\infty} \leq C_{int} ||w||_{L^\infty}, \\ &||r_I||_{L^\infty} \leq C_{int} ||r||_{L^\infty}. \end{aligned}$$

The following error estimate, uniform in the thickness parameter t, has been proved in [3].

Theorem 0.1 *Let (φ, v, τ) and (φ_h, v_h, τ_h) represent the solutions of problem* (1) *and* (8)*, under Assumption 0.1 on the collocation points. Then it holds*

$$||\varphi - \varphi_h||_{W^{2,\infty}} + ||v - v_h||_{W^{1,\infty}} + ||\tau - \tau_h||_{W^{1,\infty}} \leq C h^\beta \, |q|_{W^{\beta,\infty}} \tag{9}$$

with

$$\beta = \min(p_v, p_\tau, p_\varphi - 1), \tag{10}$$

and where the constant C is independent of the knot vectors and the thickness parameter t.

References

[1] F. Auricchio, L. Beirão da Veiga, T.J.R. Hughes, A. Reali, G. Sangalli. Isogeometric Collocation Methods. *Mathematical Models and Methods in Applied Sciences*, **20**, 2075–2107, 2010.

[2] F. Auricchio, L. Beirão da Veiga, T.J.R. Hughes, A. Reali, G. Sangalli. Isogeometric collocation for elastostatics and explicit dynamics. *Computer Methods in Applied Mechanics and Engineering*, in press. DOI:10.1016/j.cma.2012.03.026.

[3] L. Beirão da Veiga, C. Lovadina, A. Reali. Avoiding shear locking for the Timoshenko beam problem via isogeometric collocation methods. *Computer Methods in Applied Mechanics and Engineering*, **241-244**, 38–51, 2012.

[4] J.A. Cottrell, T.J.R. Hughes, Y. Bazilevs. *Isogeometric Analysis. Towards integration of CAD and FEA*. Wiley, 2009.

[5] T.J.R. Hughes, J.A. Cottrell, Y. Bazilevs. Isogeometric analysis: CAD, finite elements, NURBS, exact geometry, and mesh refinement. *Computer Methods in Applied Mechanics and Engineering*, **194**, 4135–4195, 2005.

[6] S. P. Timoshenko. On the correction factor for shear of the differential equation for transverse vibrations of bars of uniform cross-section. *Philosophical Magazine*, **41**, 744–746, 1921.

Proceedings of the 26th Nordic Seminar on Computational Mechanics
A. Logg, K.A. Mardal, A. Massing (Eds.)

Girkmann problem: shell elements vs. solid elements

Antti H. Niemi and Julien Petit

Aalto University, School of Engineering, Department of Civil and Structural Engineering
P.O. Box 12100, FI-00076 Aalto, antti.h.niemi@aalto.fi

Summary. We present computational results for the so called Girkmann benchmark problem involving a spherical shell stiffened with a foot ring. In particular, we compare the accuracy of finite element formulations based directly on the three-dimensional theory of elasticity to formulations based on dimensionally reduced structural models. We conclude that, in the Girkmann problem, shell elements are very economical and can be recommended instead of solid elements. Nevertheless, we express concern over the membrane behaviour of the lowest-order shell elements.

Key words: verification & validation, shell elements, *hp*-adaptivity, concrete structures

Introduction

Shell finite element formulations involve various explicit and implicit modelling assumptions that extend beyond the limits of mathematical convergence theory currently available, see [1]. However, thanks to modern computation technology, such as the *hp*-adaptive finite element method [2, 3], shell analysis can also be based directly on three-dimensional elasticity theory. Such approach rules out the modelling errors arising from the simplifications of dimensionally reduced structural models but requires in general more degrees of freedom for the discrete model. Also, if simplified representations of the stress state such as the stress resultants are needed, they must be post-processed from the three-dimensional stress field.

Girkmann problem

A model problem called the *Girkmann problem*, which was revived some time ago, highlights the above complications rather dramatically, see [4–7]. The problem involves a concrete structure consisting of a spherical dome stiffened by a foot ring under a dead gravity load, see Fig. 1. The task is to determine the values of the shear force and the bending moment at the junction between the dome and the ring as well as the maximum bending moment in the dome.

The problem was initially presented and solved analytically in the text book [8]. More recently, in the bulletin of the International Association of Computational Mechanics (IACM) [9], the problem was posed as a computational challenge to the finite element community. The purpose of the challenge was to find out how the process of verification, that is the process of building confidence that an approximative result is within a given tolerance of the exact solution to the mathematical model, is carried out by the community given the Girkmann problem. The results, that are summarized in [4, 10], without attribution and details on how verification was actually performed, are scandalous. Out of the 15 results submitted, 11 have a very large dispersion and are not within any acceptable tolerance of the reference values computed in [4–6] using different models and formulations.

So far detailed verification studies have been published for the axisymmetric models based on elasticity theory as well as axisymmetric dimensionally reduced models. In [4], the *p*-version

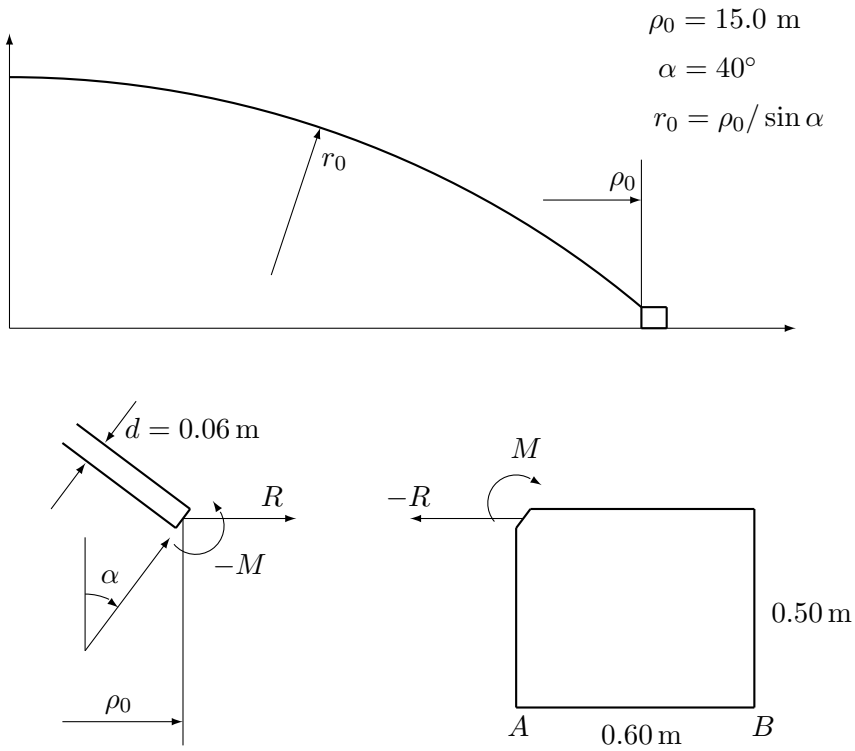

Figure 1. The Girkmann problem. Cross-section of the structure.

of FEM was used in conjunction with the extraction procedure of [11] to compute accurate values for the quantities of interest. Similar approach with the *hp*-version of FEM was taken in [5], where also the axisymmetric *h*-version with selective reduced integration was successfully employed to discretize the dimensionally reduced model.

In the present work, we use the Girkmann problem to benchmark general 3D shell elements. Namely, we model a quarter of the dome as shown in Fig. 2 and use different type of shell elements to approximate the deformation. We use the bilinear and biquadratic shell elements of LUSAS finite element analysis software as well as the bilinear shell element proposed in [12].

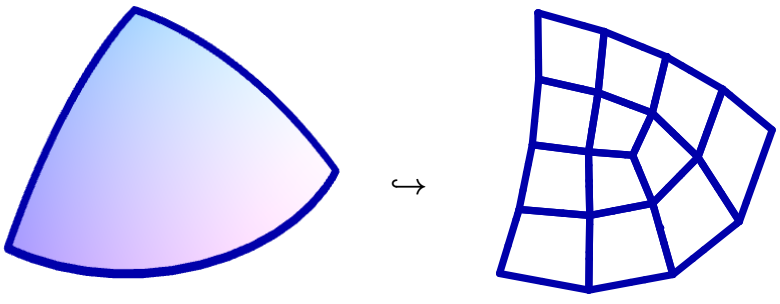

Figure 2. Bilinear finite element representation of the Girkmann dome.

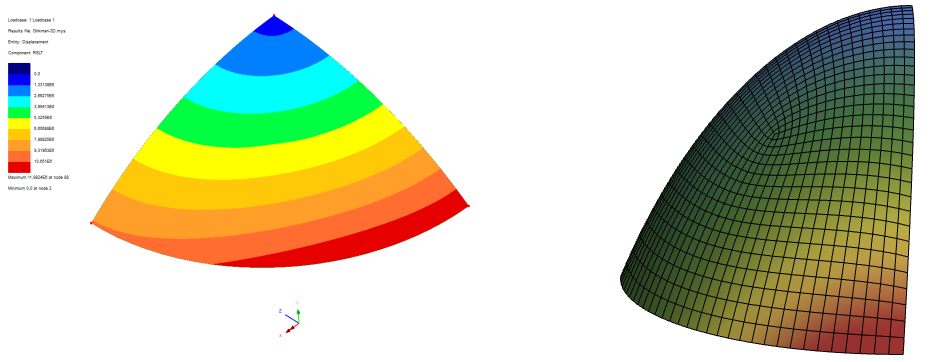

QTS4 MITC4S

Figure 3. Solution using bilinear shell elements - membrane part

	N	$E\Lambda$	$E\Psi$	k_{11}	k_{21}	k_{22}
MITC4S of [12]	16	-2.247e6	8.833e5	6.927e3	1.147e4	-4.341e4
	32	-2.294e6	9.273e5	7.930e3	1.379e4	-4.877e4
	64	-2.302e6	9.277e5	8.249e3	1.454e4	-5.057e4
	128	-2.300e6	9.295e5	8.318e3	1.477e4	-5.097e4
	N	$E\Lambda$	$E\Psi$	k_{11}	k_{21}	k_{22}
QTS4 of LUSAS	16	-2.467e6	7.697e5	6.236e3	9.914e3	-3.882e4
	32	-2.333e6	8.887e5	7.658e3	1.316e4	-4.702e4
	64	-2.313e6	9.139e5	8.167e3	1.435e4	-5.011e4
	128	-2.307e6	9.181e5	8.327e3	1.477e4	-5.152e4
	N	$E\Lambda$	$E\Psi$	k_{11}	k_{21}	k_{22}
Reference values		-2.300e6	9.338e5	8.345e3	1.477e4	-5.113e4

Table 1. Convergence of the inverse spring coefficients with bilinear elements.

Convergence studies

In the first phase, we rule out any modelling errors arising from the shell-solid intersection at the junction by using the force method associated to the free-body splitting of Fig. 1. That is, we study the convergence of the inverse spring coefficients k_{ij}^{shell} and displacements $\Lambda^{\text{shell}}, \Psi^{\text{shell}}$ in the expansions

$$E\Lambda^{\text{shell}} = E\Lambda_0^{\text{shell}} + k_{11}^{\text{shell}} R + k_{12}^{\text{shell}} M,$$
$$E\Psi^{\text{shell}} = E\Psi_0^{\text{shell}} + k_{21}^{\text{shell}} R + k_{22}^{\text{shell}} M,$$

where Λ^{shell} and Ψ^{shell} denote the horizontal displacement and rotation of the shell at the junction, respectively, and R, M are the unknown reactions.

Our first observation is that when computing the first terms Λ_0^{shell} and Ψ_0^{shell} in the expansions with bilinear elements, *there is no convergence*! This is reflected in Fig. 3 which shows that axisymmetry of the solution is lost for the bilinear QTS4 element of LUSAS and MITC4S of [12]. However, convergence occurs in the sense of average displacement over the whole junction line as shown in Table 1. Based on these values and a consistent model for the ring, see [6], rather accurate values of the stress resultants can be computed, see Table 2.

Model/Element type	Q (N/m)	M (Nm/m)	$M_{\max}$	$\theta_{\max}$
Solid / ICES *hp*-FEM	943.7	-36.79	254.9	38.14
3D Shell / MITC4S	944.7	-37.66	251.7	38.13

Table 2. Summary of numerical results

References

[1] D. Chapelle and K.-J. Bathe. *The Finite Element Analysis of Shells - Fundamentals*. Springer Berlin Heidelberg, 2011.

[2] L. Demkowicz. *Computing with hp-ADAPTIVE FINITE ELEMENTS. Volume 1 One and Two Dimensional Elliptic and Maxwell Problems*. Chapman and Hall/CRC, 2006.

[3] R. Tews and W. Rachowicz. "Application of an automatic hp adaptive Finite Element Method for thin-walled structures". In: *Computer Methods in Applied Mechanics and Engineering* 198 (2009), pp. 1967–1984.

[4] B. A. Szabó et al. "The problem of verification with reference to the Girkmann problem". In: *Engineering with Computers* 26 (2009), pp. 171–183.

[5] A. H. Niemi et al. "Finite element analysis of the Girkmann problem using the modern hp-version and the classical h-version". In: *Engineering with Computers* 28 (2012), pp. 123–134.

[6] J. Pitkäranta, I. Babuška, and B. Szabó. "The dome and the ring: Verification of an old mathematical model for the design of a stiffened shell roof". In: *Computers & Mathematics with Applications* 64 (2012), pp. 48–72.

[7] P. R. Devloo et al. "Application of a combined continuous–discontinuous Galerkin finite element method for the solution of the Girkmann problem". In: *Computers & Mathematics with Applications* 65 (2013), pp. 1786–1794.

[8] K. Girkmann. *Flächentragwerke*. Springer Vienna, 1963.

[9] J. Pitkäranta, I. Babuška, and B. Szabó. "The Girkmann Problem". In: *IACM Expressions* 22 (2008), p. 28.

[10] J. Pitkäranta, I. Babuška, and B. Szabó. "The Problem of Verification with reference to the Girkmann Problem". In: 24 (2009), pp. 14–15.

[11] I. Babuška and A Miller. "The post-processing approach in the finite element method-part 1: Calculation of displacements, stresses and other higher derivatives of the displacements". In: *International Journal for Numerical Methods in Engineering* 20 (1984), pp. 1085–1109.

[12] A. H. Niemi. "A bilinear shell element based on a refined shallow shell model". In: *International Journal for Numerical Methods in Engineering* 81 (2009), pp. 485–512.

Proceedings of the 26th Nordic Seminar on Computational Mechanics
A. Logg, K.A. Mardal, A. Massing (Eds.)

Robust finite element methods for Biot's consolidation model

Jeonghun Lee

Aalto University, Department of Mathematics and Systems Analysis, Espoo, Finland,
jeonghun.lee@aalto.fi

Summary. We propose new locking-free finite element methods for Biot's consolidation model by coupling nonconforming and mixed finite elements. We show a priori error estimates of semidiscrete and fully discrete solutions. The main advantage of our method is that a uniform-in-time pressure error estimate is provided with an analytic proof. In our error analysis, we do not use Grönwall's inequality, so the exponentially growing factors in time do not appear in the error bounds.

Key words: Biot's consolidation model, nonconforming finite elements, poroelasticity, locking-free

Introduction

Biot's consolidation model describes deformation of saturated elastic porous media and viscous fluid flow in the porous media, simultaneously. In studies of numerical solutions for Biot's model with continuous Galerkin finite elements, nonphysical pressure oscillations of numerical solutions are observed [1, 2, 3]. This nonphysical pressure oscillation phenomenon is called poroelasticity locking and various numerical methods have been suggested to resolve it [4, 7, 5]. Most of these numerical methods use nonconforming elements or discontinuous Galerkin methods with stabilization techniques. Although some numerical results of the methods illustrate that they are locking-free, the complete a priori error analysis is achieved with the assumption that the constrained specific storage coefficient, denoted by c_0, is uniformly positive. However, in a heuristic analysis [12] the locking phenomena occur when c_0 is vanishing or very close to 0, so the analysis is not enough to guarantee that the methods are locking-free.

In our work we propose a new locking-free finite element scheme for Biot's consolidation model. In our numerical scheme we obtain an a priori error estimate of the pressure in $L^\infty([0,T];L^2)$ norm without assuming uniformly positive c_0, so the error analysis confirms that our method is locking–free.

Biot's consolidation model

Consider a bounded domain $\Omega \subset \mathbb{R}^n$, $n = 2, 3$, with piecewise smooth boundary. We use $\boldsymbol{u}$, p, $\boldsymbol{f}$, g to denote the displacement of porous media, fluid pressure, body force, source/sink density function of fluid, respectively. The governing equations of quasistatic Biot's consolidation model are

$$-\operatorname{div} \mathcal{C}\epsilon(\boldsymbol{u}) + \alpha \nabla p = \boldsymbol{f}, \tag{1}$$

$$c_0 \dot{p} + \alpha \operatorname{div} \dot{\boldsymbol{u}} - \operatorname{div}(\underset{\sim}{\boldsymbol{\kappa}} \nabla p) = g, \tag{2}$$

in which $\mathcal{C}$, $c_0 \geq 0$, $\underset{\sim}{\boldsymbol{\kappa}}$, $\alpha > 0$ denote the elastic stiffness tensor, the constrained specific storage coefficient, the hydraulic conductivity tensor which is positive definite, and the Biot–Willis constant, respectively. Here $\dot{p}$, $\dot{\boldsymbol{u}}$ stand for the time derivatives of p, $\boldsymbol{u}$.

To define boundary conditions we consider two partitions of $\partial\Omega$,

$$\partial\Omega = \Gamma_p \cup \Gamma_f, \qquad \partial\Omega = \Gamma_d \cup \Gamma_t,$$

and assume that Γ_d is of positive measure. We assume that boundary conditions are

$$p = 0 \text{ on } \Gamma_p, \quad -\underset{\sim}{\boldsymbol{\kappa}}\nabla p \cdot \boldsymbol{n} = 0 \text{ on } \Gamma_f, \quad \boldsymbol{u} = 0 \text{ on } \Gamma_d, \quad \underset{\sim}{\boldsymbol{\sigma}}\boldsymbol{n} = 0 \text{ on } \Gamma_t, \tag{3}$$

for all time, where $\boldsymbol{n}$ is the outward unit normal vector field on $\partial\Omega$ and $\underset{\sim}{\boldsymbol{\sigma}} := \mathcal{C}\epsilon(\boldsymbol{u}) + \alpha p I$ is the Cauchy stress tensor. We also assume that the initial data of $\boldsymbol{u}$, p and $\boldsymbol{f}$ satisfy the compatibility condition (1).

Variational formulation

For simplicity we set $\alpha = 1$ and $\underset{\sim}{\boldsymbol{\kappa}}$ is the identity tensor. By introducing a new unknown $\boldsymbol{z} := \nabla p$ in (1) and (2), we have a new system

$$-\operatorname{div}\mathcal{C}\epsilon(\boldsymbol{u}) + \nabla p = \boldsymbol{f}, \tag{4}$$
$$\boldsymbol{z} - \nabla p = 0, \tag{5}$$
$$c_0\dot{p} + \operatorname{div}\dot{\boldsymbol{u}} - \operatorname{div}\boldsymbol{z} = g. \tag{6}$$

Defining

$$\Sigma = \{\boldsymbol{u} \in H^1(\Omega;\mathbb{R}^n) \,|\, \boldsymbol{u}|_{\Gamma_d} = 0\},$$
$$V = \{\boldsymbol{z} \in H(\operatorname{div},\Omega) \,|\, \boldsymbol{z}\cdot\boldsymbol{n}|_{\Gamma_t} = 0\},$$
$$W = L^2(\Omega),$$

the variational formulation of (4)-(6) is to seek $(\boldsymbol{u}, \boldsymbol{z}, p) \in \Sigma \times V \times W$ such that

$$a(\boldsymbol{u},\boldsymbol{v}) - (p, \operatorname{div}\boldsymbol{v}) = (\boldsymbol{f},\boldsymbol{v}), \qquad \boldsymbol{v} \in \Sigma, \tag{7}$$
$$(\boldsymbol{z},\boldsymbol{w}) + (p, \operatorname{div}\boldsymbol{w}) = 0, \qquad \boldsymbol{w} \in V, \tag{8}$$
$$(c_0\dot{p}, q) + (\operatorname{div}\dot{\boldsymbol{u}}, q) - (\operatorname{div}\boldsymbol{z}, q) = (g, q), \qquad q \in W, \tag{9}$$

in which $a(\boldsymbol{u},\boldsymbol{v}) = (\mathcal{C}\epsilon(\boldsymbol{u}), \epsilon(\boldsymbol{v}))$.

Finite element spaces

We assume that our triangular mesh is shape regular. The finite element space $V_h \subset V$ the lowest order Raviart–Thomas element and $W_h \subset W$ is the piecewise constant element. For Σ_h we use vector-valued nonconforming H^1 finite elements, say Mardal–Tai–Winther type elements, which are originally developed for Stokes–Darcy flow problems [8, 9]. The discrete H^1 norm for Σ_h is defined by

$$\|\boldsymbol{v}\|_{1,h}^2 = \sum_{T\in\mathcal{T}_h} \|\nabla\boldsymbol{u}\|_{0,T}^2 + \sum_{E\in\mathcal{E}_h} \frac{1}{h_E}\|[\![\boldsymbol{u}]\!]\|_{0,E}^2, \tag{10}$$

in which $\mathcal{T}_h$, $\mathcal{E}_h$ are the set of triagnles/tetrahedra and the set of edges/faces, respectively. Here, if $E \subset \partial\Omega$, then the jump $[\![\boldsymbol{u}]\!]$ on E means the trace of $\boldsymbol{u}$.

The Mardal–Tai–Winther type elements satisfy a discrete Korn's inequality, and the pair (Σ_h, W_h) satisfies the inf-sup condition with the above discrete H^1 norm and the L^2 norm. It

turns out that these features are very useful to develop robust numerical schemes for Biot's consolidation model.

Rectangular Martal–Tai–Winther type elements [5] and higher order triangular Mardal–Tai–Winther type elements [10] are developed. Therefore our approach can be extended to rectangular meshes and triangular meshes with higher order elements.

Differential algebraic equations and compatibility conditions

The semidiscrete problem corresponding to the system (7)-(9), is not a system of ordinary differential equations, so existence and uniqueness of its solutions should be treated carefully. In particular, the algebraic equations (7) and (8) give a compatibility condition on initial data. We say that numerical initial data is compatible if it satisfies the compatibility conditions given by the corresponding discrete equations of (7) and (8). We prove that the semidiscrete problem of (7)-(9) has a unique solution if its initial data is compatible.

The compatibility of numerical initial data is also important for robustness of time discretization schemes. If the initial data of differential algebraic equation is not compatible, then the Crank–Nicolson scheme, which is absolutely stable, may give a spurious numerical solution because numerical solutions do not satisfy the algebraic equations in all time steps. To avoid this problem, we show that we can always find a compatible numerical initial data which is close to the original initial data.

Semidiscrete and fully discrete error estimates

We use $\|\boldsymbol{u}\|_{L^\infty([0,T];H^1_h)}$ to denote the standard space-time norm with the discrete H^1 norm in (10). Let $(\boldsymbol{u}, \boldsymbol{z}, p)$ and $(\boldsymbol{u}_h, \boldsymbol{z}_h, p_h)$ be the exact and semidiscrete solutions. If the exact solution is sufficient regular, then we have

$$\|\boldsymbol{u} - \boldsymbol{u}_h\|_{L^\infty([0,T];H^1_h)} + \|\boldsymbol{z} - \boldsymbol{z}_h\|_{L^2([0,T];L^2)} + \|p - p_h\|_{L^\infty([0,T];L^2)} = O(h).$$

In our error analysis, to avoid Grönwall's inequality, we adapt the energy estimates of linear evolutionary partial differential equations to our differential algebraic equation.

For the fully discrete solutions we use the Crank–Nicolson scheme with time step Δt. Let N be the last time step. Defining $t_j = j\Delta t$ for integer $0 \le j \le N$ and denoting the fully discrete solution at j-th time step by $(\boldsymbol{U}^j, \boldsymbol{Z}^j, P^j)$, we have

$$\sup_{0\le j\le N} \|\boldsymbol{u}(t_j) - \boldsymbol{U}^j\|_{1,h} + \sum_{0\le j\le N} \|\boldsymbol{z}(t_j) - \boldsymbol{Z}^j\|_0^2 + \sup_{0\le j\le N} \|p(t_j) - P^j\|_0 = O(h + (\Delta t)^2).$$

In the error analysis of fully discrete solutions there is an additional technical difficulty arising from time discretization. It is mainly due to the fact that the c_0-weighted L^2 norm of p is not an upper bound of $\|p\|_0$ because c_0 is not uniformly positive. We are able to handle this problem in the help of the inf-sup condition of (Σ_h, W_h) and the error estimate of $\boldsymbol{u}$.

References

[1] Vermeer, P. A. and Verruijt, A. *An accuracy condition for consolidation by finite elements. International Journal for Numerical and Analytical Methods in Geomechanics*, 5(1):1–14,1981.

[2] Reed, M. B. *An investigation of numerical errors in the analysis of consolidation by finite elements. International Journal for Numerical and Analytical Methods in Geomechanics*, 8(3):243–257,1984.

[3] Zienkiewicz, O. C. and Shiomi, T. *Dynamic behaviour of saturated porous media; The generalized Biot formulation and its numerical solution. International Journal for Numerical and Analytical Methods in Geomechanics*, 8(1):71–96,1984.

[4] Phillips, Phillip Joseph and Wheeler, Mary F. *A coupling of mixed and discontinuous Galerkin finite-element methods for poroelasticity*, *Computational Geosciences*, 12(4):417–435,2008.

[5] Chen, Yumei and Luo, Yan and Feng, Minfu *Analysis of a discontinuous Galerkin method for the Biot's consolidation problem*, *Applied Mathematics and Computation*, 219(17):9043–9056,2013.

[6] Biot, M. A. and Willis, D. G. *The elastic coefficients of the theory of consolidation*, *J. Appl. Mech.*, 24:594–601,1957.

[7] Yi, Son-Young *A coupling of nonconforming and mixed finite element methods for Biot's consolidation model*, *Numerical Methods for Partial Differential Equations*, *published online, http://dx.doi.org/10.1002/num.21775*, 2013.

[8] Mardal, Kent Andre and Tai, Xue-Cheng and Winther, Ragnar *A robust finite element method for Darcy-Stokes flow*, *SIAM J. Numer. Anal.*, 40(5):1605–1631,2002.

[9] Tai, Xue-Cheng and Winther, Ragnar *A discrete de Rham complex with enhanced smoothness*, *Calcolo*, 43(4):287–306,2006.

[10] Guzmán, Johnny and Neilan, Michael *A family of nonconforming elements for the Brinkman problem*, *IMA Journal of Numererical Analysis*, 32(4):1484–1508,2012.

[11] Zhang, Shiquan and Xie, Xiaoping and Chen, Yumei *Low order nonconforming rectangular finite element methods for Darcy-Stokes problems*, *J. Comput. Math.*, 27(2-3):400-424,2009.

[12] Phillips, Phillip Joseph and Wheeler, Mary F. *Overcoming the problem of locking in linear elasticity and poroelasticity: an heuristic approach*, *Computational Geosciences*, 13(1):5–12,2009.

Proceedings of the 26th Nordic Seminar on Computational Mechanics
A. Logg, K.A. Mardal, A. Massing (Eds.)

On the numerical solution of a micropolar continuum model

Reijo Kouhia[1], Antti H. Niemi[2]

(1)Tampere University of Technology, Department of Engineering Design
P.O. Box 589, FI-33101 Tampere, reijo.kouhia@tut.fi
(2)Aalto University, School of Engineering, Department of Civil and Structural Engineering
P.O. Box 12100, FI-00076 Aalto, antti.h.niemi@aalto.fi

Summary. A simple numerical test for two low-order standard Lagrange type elements for the polar-continuum model in 3-D is performed.

Key words: micropolar continuum, finite element method

Introduction

The ordinary Cauchy continuum model cannot describe effects originating from the microstructure of a material, such as the size-effect. After the first trials by Woldemar Voigt [14] and the brothers Eugene and Francois Cosserat [2] for generalizing the Cauchy continuum model, it took more than a half century for growing interest to the generalized continuum models [1, 5, 9, 6, 13].

Micropolar continuum

Equilibrium equations

For the micropolar continuum the following local forms of the equilibrium equations can be obtained

$$\frac{\partial \sigma_{ji}}{\partial x_j} + \rho b_i = 0, \tag{1}$$

$$\frac{\partial \mu_{ji}}{\partial x_j} + \rho c_i + \epsilon_{ijk}\sigma_{jk} = 0, \tag{2}$$

where $\boldsymbol{\sigma}$ and $\boldsymbol{\mu}$ stand for force- and moment stress tensors, $\boldsymbol{b}, \boldsymbol{c}$ are the body force and moment per unit mass, respectively. In general, the force stress and moment stress tensors are not symmetric. The alternating tensor is denoted as ϵ_{ijk} and ρ is the mass density.

Constitutive equations

For centrosymmetric material the linear constitutive equations for the force-stress σ_{ij} and the couple-stress μ_{ij} can be written as [3, 12, 10]

$$\sigma_{ij} = C^{(\gamma)}_{ijkl}\gamma_{kl}, \qquad \mu_{ij} = C^{(\kappa)}_{ijkl}\kappa_{kl}, \tag{3}$$

where the Cosserat's first strain tensor γ_{ij} and microcurvature tensor κ_{ij} are defined as

$$\gamma_{ij} = u_{j,i} - \epsilon_{kij}\varphi_k, \quad \text{and} \quad \kappa_{ij} = \varphi_{j,i}, \tag{4}$$

in which $\boldsymbol{\varphi}$ is the independent microrotation field. The material stiffness tensors for an isotropic solid can be expressed as

$$C^{(\gamma)}_{ijkl} = \lambda\delta_{ij}\delta_{kl} + \mu(\delta_{ik}\delta_{jl} + \delta_{il}\delta_{jk}) + \mu_{\mathrm{c}}(\delta_{ik}\delta_{jl} - \delta_{il}\delta_{jk}), \tag{5}$$

$$C^{(\kappa)}_{ijkl} = \alpha\delta_{ij}\delta_{kl} + \beta(\delta_{ik}\delta_{jl} + \delta_{il}\delta_{jk}) + \gamma(\delta_{ik}\delta_{jl} - \delta_{il}\delta_{jk}). \tag{6}$$

In addition to the classical Lamé constants λ, μ, there are four additional material parameters: $\mu_{\mathrm{c}}, \alpha, \beta$ and γ. However, a more comprehensible set of constants are the Young's modulus $E = \mu(3\lambda + 2\mu)/(\lambda + \mu)$, the shear modulus μ, and [8, 10, 11]

$$\text{the characteristic length in torsion} \qquad \ell_{\mathrm{t}} = \sqrt{\frac{\beta}{\mu}}, \tag{7}$$

$$\text{the characteristic length in bending} \qquad \ell_{\mathrm{b}} = \sqrt{\frac{\beta+\gamma}{4\mu}}, \tag{8}$$

$$\text{the coupling number} \qquad N = \sqrt{\frac{\mu_{\mathrm{c}}}{\mu+\mu_{\mathrm{c}}}}, \tag{9}$$

$$\text{and the polar ratio} \qquad \psi = \frac{\beta}{\beta + \frac{1}{2}\alpha}. \tag{10}$$

The allowed range for the dimensionless parameters N and ψ are

$$0 \le N \le 1, \quad \text{and} \quad 0 \le \psi \le \frac{3}{2}, \tag{11}$$

Determination of the four additional constants is a major problem for practical applications. Neff et al. [10, 11] have inroduced so called conformally invariant curvature state, which reduces the number of additional material parameters to two and which also facilitates a stable estimation of them. For conformally invariant curvature state, the curvature tensor is purely deviatoric and symmetric, thus

$$\gamma = 0, \qquad \beta = \mu\ell_{\mathrm{t}}^2, \qquad \alpha = -\tfrac{2}{3}\mu\ell_{\mathrm{t}}^2. \tag{12}$$

The conformally invariant curvature state corresponds thus to the upper limit of the polar ratio, i.e. $\psi = \frac{3}{2}$. Notice that in this case $\ell_{\mathrm{b}} = \frac{1}{2}\ell_{\mathrm{t}}$. It also results in a non-sigular behaviour of stiffening in torsion and bending, see Figure 1, where the stiffening effect in pure bending of a straight beam with circular cross-section is shown. The singular behaviour of the non-conformally invariant curvature state is clearly seen. The analytical solution in given in [7].

Numerical solution

The virtual work expression for the polar continua can be written as

$$\int_V \left[\left(-\nabla\cdot\boldsymbol{\sigma}^T - \rho\boldsymbol{b}\right)\cdot\delta\boldsymbol{u} + \left(-\nabla\cdot\boldsymbol{\mu}^T - \boldsymbol{\epsilon}:\boldsymbol{\sigma} - \rho\boldsymbol{c}\right)\cdot\delta\boldsymbol{\phi} \right] \mathrm{d}V = 0. \tag{13}$$

After integration by parts and utilizing the divergence theorem, it transforms into the form suitable for finite element approximation

$$\int_V \left[\boldsymbol{\sigma} : \left((\nabla\delta\boldsymbol{u})^T - \mathrm{skew}(\delta\boldsymbol{\varphi}) \right) + \boldsymbol{\mu} : (\nabla\delta\boldsymbol{\varphi})^T \right] \mathrm{d}V - \int_S (\boldsymbol{t}\cdot\delta\boldsymbol{u} + \boldsymbol{m}\cdot\delta\boldsymbol{\varphi})\,\mathrm{d}S = 0. \tag{14}$$

As an example a straight beam with square cross-section is solved with both 27-node triquadratic and 8-node trilinear standard C_0-elements. The beam is divided in ten equal elements and loading is a uniform traction in the vertical direction at the free end of the beam. The

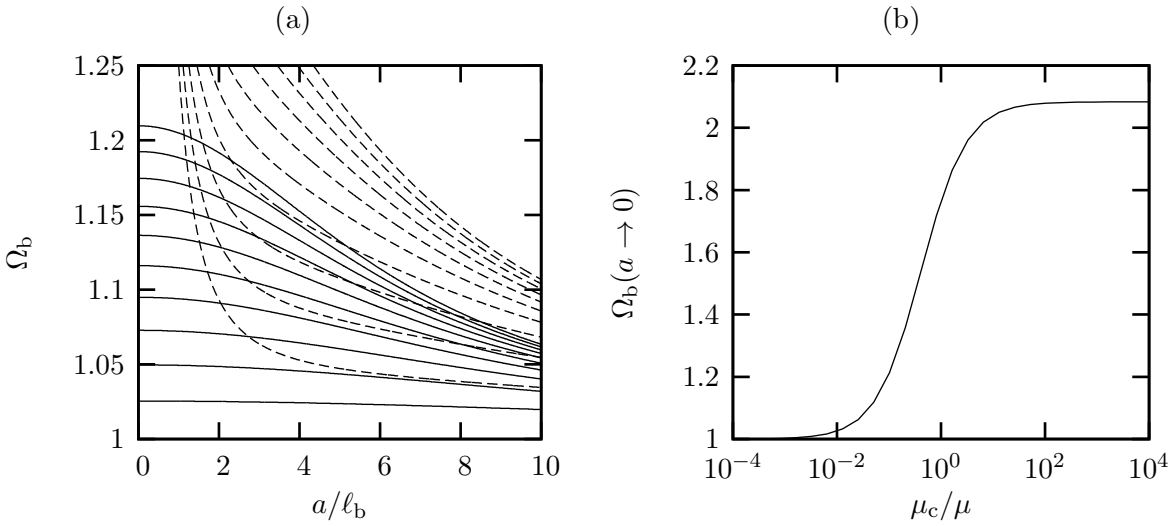

Figure 1. (a) Ratio of bending rigidity of the polar continuum versus standard Cauchy's continuum model Ω_b as a function of the radius a of the beam's cross-section with different values of the coupling modulus μ_c; from bottom to top $\mu_\mathrm{c}/\mu = 0.01, 0.02, 0.03, \ldots, 0.09, 0.1$. Conformally invariant curvature case ($\beta = 4\mu\ell_\mathrm{b}^2, \gamma = 0$) shown by solid lines and the case with parameters $\gamma = 0.01\beta$ indicated by dashed lines. (b) Limit value of Ω_b when $a \to 0$ as a function of the coupling modulus μ_c for the conformally invariant curvature state.

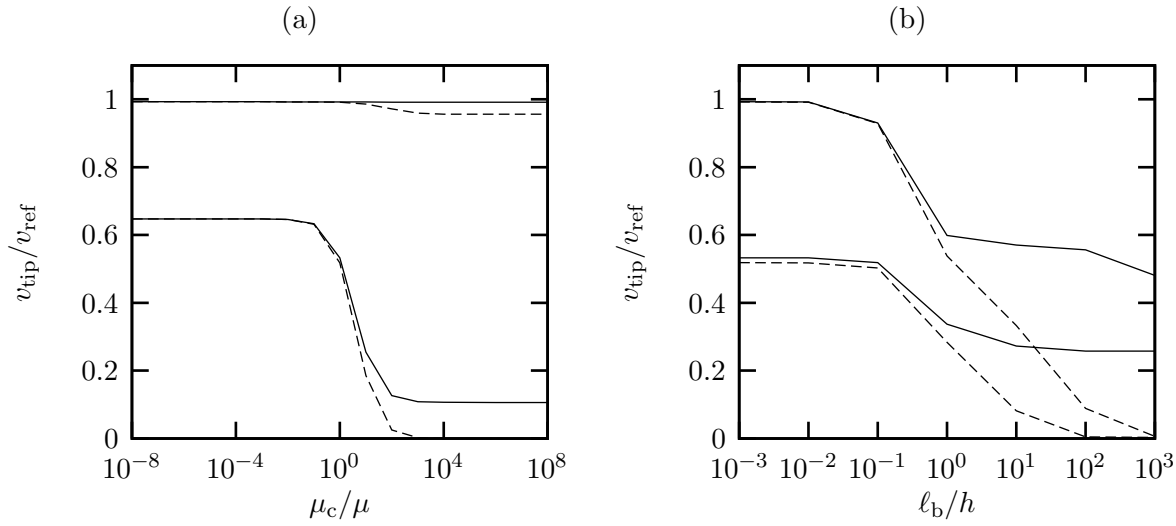

Figure 2. (a) The effect of the coupling modulus μ_c to the tip displacement of the cantilever beam. The reference value is the tip deflection according to the Euler-Bernoulli beam model: $v_\mathrm{ref} = FL^3/3EI$. The material length in bending is $\ell_\mathrm{b} = h/200$, where h is the cross-section height. The upper two curves correspond to solutions with triquadratic elements and the lower ones with trilinear elements. Solid lines indicate solutions where the rotations are free at the clamped edge and the dashed line where they are supressed. (b) The effect of internal length scale ℓ_b on the FE solution: $\mu_\mathrm{c} = \mu$.

length to height ratio of the beam is $L/h = 10$. Two different types of boundary conditions are computed; both the rotations and displacements are supressed at the clamped edge or only the displacements are supressed. Only conformally invariant curvature state is considered.

It is clearly seen from the Figure 2(a) that the trilinear elements lock also earlier as expected from standard continuum in the limit $\mu_c \to \infty$. The behaviour of the quadratic element is also peculiar for the fully clamped case, Figure 2(b). However, it should be noted that the analytical solution is unknwon for this case.

References

[1] E.L. Aero, E.V. Kuvshinskii, Fundamental equations of the theory of elastic media with rotationally interacting particles. *Soviet Physics, Solid State*. **2**, 1961, 1272–1281.

[2] E. Cosserat, F. Cosserat, *Théorie des Corps Deformables*, A. Herman & Sons, Paris, 1909. *Theory of Deformable Bodies* translation D.H. Delphenich, available at `www.uni-due.de/hm0014/Cosserat files/Cosserat09 eng.pdf`

[3] A.C. Eringen, *Microcontinuum Field Theories: I. Foundations and Solids*, Springer, New York, 1999.

[4] R.D. Gauthier, W.E. Jahsman, A quest for micropolar elastic constants, *Journal of Applied Mechanics*, **42**, 1975, 369–374.

[5] A.E. Green, R.S. Rivlin, Multipolar continuum mechanics. *Archives of Rational Mechanics and Analysis*. **17** (2), 1964, 113–147.

[6] W.T. Koiter, Couple stresses in the theory of elasticity I, II. *Prodeedings of the Koninklijke Nederlandse Akademie van Wetenschappen B*, **67**, 1964, 17–44.

[7] G.V. Krishna Reddy, N.K. Venkatasubramanian, On the flexular rigidity of a micropolar elastic circular cylinder. *Journal of Applied Mechanics*, **45**, 1978, 429–431.

[8] R.S. Lakes, Experimental methods for study of Cosserat elastic solid and other generalized elastic continua. Continuum Models for Materials with Microstructure, H.B. Mühlhaus (Ed.), Wiley, 1995, 1–25.

[9] R.D. Mindlin, Micro-structure in linear elasticity. *Archives of Rational Mechanics and Analysis*. **16** (1), 1964, 51–78.

[10] P. Neff, J. Jeong, A new paradigm: the linear isotropic Cosserat model with conformally invariant curvature energy. *Zeitschrift für Angewandte Mathematik und Mechanik*, **89**(2), 2009, 107–122.

[11] P. Neff, J. Jeong, A. Fischle, Stable identification of Linear isotropic Cosserat parameters: bounded stiffness in bending and torsion implies invariance of curvature. *Acta Mechanica*, **211**, 2010, 237–249.

[12] W. Nowacki, *Theory of Asymmetric Elasticity*, PWN - Polish Scientific Publishers, Varsova, Pergamon Press, Oxford, 1986. (Polish original 1971.)

[13] R.A. Toupin, Theories of elasticity with couple-stress. *Archives of Rational Mechanics and Analysis*. **17** (2), 1964, 85–112.

[14] W. Voigt, Theoretische Studien über die Elasticitätsverhältnisse der Krystalle, *Abhandlungen der Königlichen Geselshaft der Wissenshaften zu Göttingen*, Vol. 24, Göttingen, 1887.

Proceedings of the 26th Nordic Seminar on Computational Mechanics
A. Logg, K.A. Mardal, A. Massing (Eds.)

Modelling of multiple delaminations in shells using XFEM

Jim Brouzoulis[1] and Martin Fagerström[2]

(1)Department of Applied Mechanics, Chalmers University of Technology, Göteborg, Sweden, jim.brouzoulis@chalmers.se
(2)Department of Applied Mechanics, Chalmers University of Technology, Göteborg, Sweden, martin.fagerstrom@chalmers.se

Summary. A shell element which can account for multiple internal delaminations is presented. The shell kinematics is enriched based on the eXtended Finite Element Method (XFEM) and the element is verified against numerical tests.

The oral presentation will include three numerical examples and the kinematics will be explained in greater detail.

Key words: multiple delaminations, XFEM, shell theory

Introduction

There is an ever increasing interest in utilising Fiber Reinforced Polymers (FRP) in the automotive industry, especially for structural components. This calls for computational tools which can be used for the evaluation of crashworthiness. One key point is the need for computational efficiency as the models are generally very complex. Furthermore, there is a multitude of failure mechanisms which may be triggered in a layered composite, during impact or crash, with multiple delaminations being one of the primary mechanisms.

It is therefore of high importance to be able to model delaminations in a computationally efficient manner, especially for a large number of laminae. In fact, to be able to simulate the progressive failure of FRP components is a necessity for such components to be competitive within the automotive industry, as *e.g.* stated in the ERTRAC Research and Innovation Roadmap for Safe Road Transport [1].

In view of this, this work is a first step towards developing a computationally efficient shell element which can account for multiple (interlaminar) delaminations. Such an element may be constructed by enriching a suitable shell element with discontinuous shape functions in accordance with the XFEM, cf. [2] for a similar approach. Note that the present approach is similar to a layerwise model where displacements jumps are hierarchically added to the displacements field, cf. *e.g.* [3].

Continuous shell kinematics

To set the stage, we first briefly describe the underlying shell kinematics for a non-delaminated shell, which in the subsequent section then will be extended to allow for arbitrarily many delaminations.

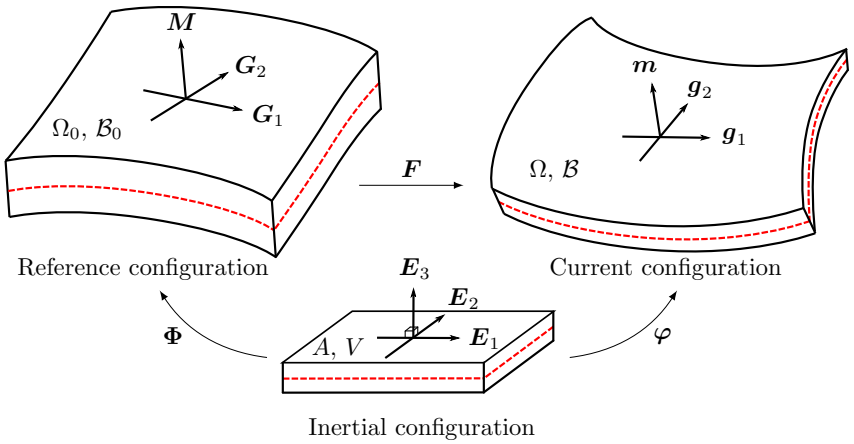

Figure 1: Mappings of shell model defining undeformed and deformed shell configurations relative to inertial Cartesian frame.

Initial shell geometry and convected coordinates

As a staring point, the initial configuration B_0 of the shell is considered parameterised in terms of convected (covariant) coordinates (ξ_1, ξ_2, ξ) as

$$\mathcal{B}_0 = \Big\{ \boldsymbol{X} := \boldsymbol{\Phi}(\boldsymbol{\xi}) = \bar{\boldsymbol{\Phi}}(\bar{\boldsymbol{\xi}}) + \xi \boldsymbol{M}(\bar{\boldsymbol{\xi}}) \quad \text{with } \bar{\boldsymbol{\xi}} \in A \text{ and } \xi \in \tfrac{h_0}{2}[-1,1] \Big\} \tag{1}$$

where we introduced the contracted notation $\boldsymbol{\xi} = (\xi_1, \xi_2, \xi)$ and $\bar{\boldsymbol{\xi}} = (\xi_1, \xi_2)$ and where the mapping $\boldsymbol{\Phi}(\boldsymbol{\xi})$ maps the inertial Cartesian frame into the undeformed configuration, cf. Figure 1. Furthermore, A is the midsurface of the inertial configuration. In Eq. (1), the mapping $\boldsymbol{\Phi}$ is defined by the midsurface placement $\bar{\boldsymbol{\Phi}}$ and the outward unit normal vector field $\boldsymbol{M}$ (with $|\boldsymbol{M}| = 1$). The coordinate ξ is associated with this direction and h_0 is the initial thickness of the shell.

Current shell geometry

The current (deformed) geometry is in the present formulation described by the time dependent deformation map $\boldsymbol{\varphi}(\boldsymbol{\xi}, t) \in \mathcal{B}$ of the inertial Cartesian frame as

$$\boldsymbol{x}(\boldsymbol{\xi}, t) = \bar{\boldsymbol{\varphi}}(\bar{\boldsymbol{\xi}}, t) + \xi \boldsymbol{m}(\bar{\boldsymbol{\xi}}, t) + \frac{1}{2}\xi^2 \gamma(\bar{\boldsymbol{\xi}}, t) \boldsymbol{m}(\bar{\boldsymbol{\xi}}, t) \tag{2}$$

where the mapping is defined by the midsurface placement $\bar{\boldsymbol{\varphi}}$, the spatial director field $\boldsymbol{m}$ and an additional scalar thickness inhomogeneity strain γ, cf. Figure 1. As it can be seen, the specification of the current configuration corresponds to a second order Taylor expansion along the director field, involving the inhomogeneity strain γ, thereby describing inhomogeneous thickness deformation effects of the shell. In particular, the pathological Poisson locking effect is avoided in this fashion.

XFEM extension for multiple delaminations

As stated above, the primary focus of the current work is to develop a shell element formulation able to represent arbitrarily many delaminations within one element. Consequently, the above basic shell kinematics need to be extended to allow for displacement and director discontinuities across each delamination interface. For this purpose, we propose herein a kinematical extension

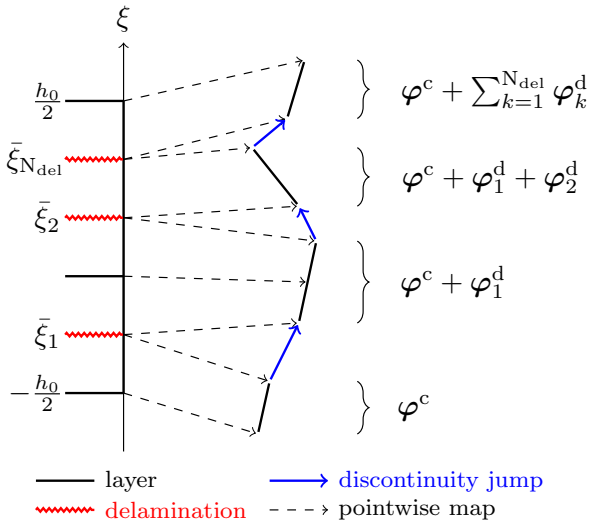

Figure 2: Illustration of a laminate subject to multiple delaminations.

in line with the XFEM (or partition of unity concept) such that the deformation map into the spatial deformed configuration is subdivided into one continuous and one discontinuous part as

$$\boldsymbol{x}(\boldsymbol{\xi}, t) = \boldsymbol{\varphi}^{\mathrm{c}}(\boldsymbol{\xi}, t) + \boldsymbol{\varphi}^{\mathrm{d}}(\boldsymbol{\xi}, t) \tag{3}$$

where the continuous part takes on the same form as the underlying non-delaminated shell element

$$\boldsymbol{\varphi}^{\mathrm{c}}(\boldsymbol{\xi}, t) = \bar{\boldsymbol{\varphi}}^{\mathrm{c}}(\bar{\boldsymbol{\xi}}, t) + \xi \boldsymbol{m}^{\mathrm{c}}(\bar{\boldsymbol{\xi}}, t) + \frac{1}{2}\xi^2 \gamma(\bar{\boldsymbol{\xi}}, t) \boldsymbol{m}^{\mathrm{c}}(\bar{\boldsymbol{\xi}}, t) \tag{4}$$

As for the discontinuous part, it is considered as a sum of enrichments – one for each delamination – according to the XFEM, however restricted only to discontinuous enrichment of the midsurface placement and the director field. Hence, in the case of $\mathrm{N_{del}}$ delaminations through the thickness, the discontinuous part takes on the following form

$$\boldsymbol{\varphi}^{\mathrm{d}}(\boldsymbol{\xi}) = \sum_{k=1}^{\mathrm{N_{del}}} \mathcal{H}_{\mathrm{S}}\left(S_k(\boldsymbol{X}, t)\right) \left(\bar{\boldsymbol{\varphi}}_k^{\mathrm{d}}(\bar{\boldsymbol{\xi}}, t) + \xi \boldsymbol{m}_k^{\mathrm{d}}(\bar{\boldsymbol{\xi}}, t)\right) = \mathcal{H}_{S_k} \left(\bar{\boldsymbol{\varphi}}_k^{\mathrm{d}} + \xi \boldsymbol{m}_k^{\mathrm{d}}\right) \text{ (sum over } k) \tag{5}$$

In Eq. (5), $\mathcal{H}_{\mathrm{S}}(S_k(\boldsymbol{X})) = \mathcal{H}_{S_k}$ is introduced as the standard Heaviside function pertaining to the particular delamination surface Γ_{S_k}. Furthermore, S_k is an associated level set function defining the position $\bar{\xi}_k$ (in thickness direction) of this surface.

Numerical example

To illustrate the proposed kinematics, a numerical example is presented below. This example concerns simulation of the common double cantilever beam (DCB) test with the purpose of validating the kinematics of the element under progressive delamination.

The problem consists of a beam, composed of two laminae, which has an initial crack (delamination zone) of length $a = 3$ mm, see Figure 3 for a description. The length of the beam is $L = 200$ mm, has a height of $h = 3$ mm and a width of $w = 15$ mm.

Since this example focus on the growth of a single delamination, only one set of discontinuous dofs $\{\bar{\boldsymbol{x}}_1^{\mathrm{d}},\ \boldsymbol{m}_1^{\mathrm{d}}\}$ needs to be added to the solution field of the nodes within the delamination zone Γ_k^S. In order to model the progressive growth of the delamination a bilinear cohesive zone, is inserted between the two laminae. The fracture energy associated with mode I loading of the cohesive zone is set to $\mathcal{G}_{\mathrm{Ic}} = 400$ N/m in this example.

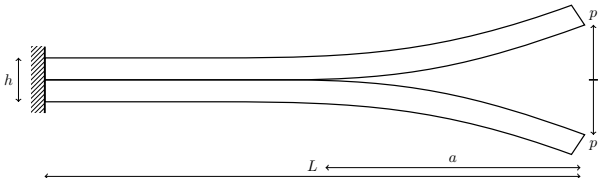

Figure 3: Geometry of the DCB test.

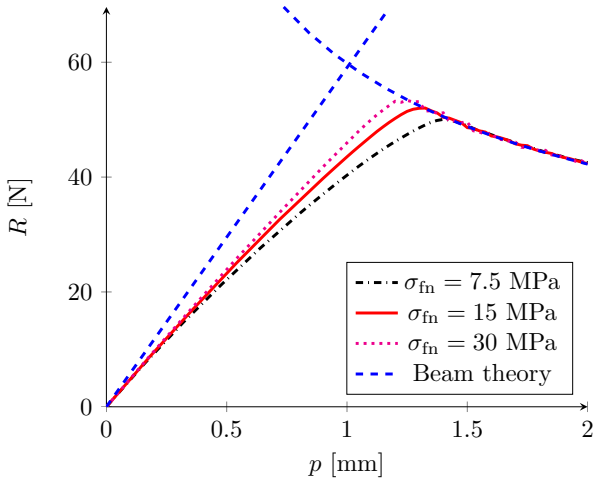

Figure 4: Reaction force for DCB simulation with cohesive zone.

The beam is modelled using 384 quadratic triangular elements with an increased mesh density in the region close to the delamination front. The free ends of the beam are subjected to prescribed displacements in the vertical direction with a magnitude p and the resulting reaction force R is registered. In Figure 4, the reaction forces corresponding to three values of the interface strength (of the cohesive zone) $\sigma_{\text{fn}} = \{15,\ 30,\ 45\}$ MPa are shown. Also, a reference solution obtained from Euler-Bernoulli beam theory is indicated. As can be seen from the figure, the load–reaction curves correspond rather well with beam theory, more so during the delamination phase. It can thus be concluded that the proposed shell element is capable of an accurate representation of progressive delamination.

Acknowledgement

The research leading to these results receives funding from the European Community's Seventh Framework Programme (FP7/2007-2013) under grant agreement no. 314182 (the MATISSE project). This publication solely reflects the authors' views. The European Community is not liable for any use that may be made of the information contained herein.

References

[1] ERTRAC. Research and Innovation Roadmap for Safe Road Transport. http://www.ertrac.org/pictures/downloadmanager/6/50/ertrac-researchinnovation-roadmaps_60.pdf, 2013.

[2] R. de Borst and Remmers and J.J.C Remmers. Computational modelling of delamination. *Composites Science and Technology*, 66(6):713–722, 2006

[3] D.H. Robbins and J.N. Reddy. Variable kinematic modelling of laminated composite plates. *International Journal for Numerical Methods in Engineering*, 39:2283–2317,1996.

Proceedings of the 26th Nordic Seminar on Computational Mechanics
A. Logg, K.A. Mardal, A. Massing (Eds.)

Newton-type method for the variational discretization of topology optimization problems

Anton Evgrafov[1]

(1)Department of Applied Mathematics and Computer Science, Technical University of Denmark, Matematiktorvet 303B, Kgs. Lyngby, DK–2800 Denmark

Summary. We present a locally quadratically convergent optimization algorithm for solving topology optimization problems. The distinguishing feature of the algorithm is to treat the design as a smooth function of the state and not vice versa as in the traditional nested approach to topology optimization, which we achieve by inverting a part of perturbed optimality conditions for the problem. In this way, the computational bottleneck is conveniently shifted from evaluating the merit function to a direction finding subproblem. The latter involves solving certain linearized PDEs, and the computational effort is similar to that of finding a gradient of the merit function in the traditional nested approach. We illustrate the performance of the algorithm on benchmark topology optimization problems in fluid mechanics.

Key words: topology optimization, variational discretization, Newton's algorithm

Introduction

Topology optimization has matured enormously in the past quarter of a century, and has been successfully adapted by a variety of industries, most notably automobile and aerospace. Furthermore, recent advances in manufacturing technologies have made it possible to directly fabricate the designs computed by the optimization algorithm. Coupled with the improvements in computing methodology and computer hardware, these enable topology optimization to be used not only at conceptual and preliminary, but also at final design stages. The latter usage puts considerable requirements on the accuracy of the designs computed using this approach.

On the one hand, the classes of mathematical programming algorithms capable of producing highly accurate solutions in a reasonable number of iterations, that is, those exhibiting local superlinear or quadratic convergence, in the nutshell are based on exact or approximate Newton's iteration for the system of optimality conditions for the problem under consideration. Their global convergence is ensured by one of the several well established mechanisms, such as linesearches, trust regions, and/or filters.

On the other hand, modern successful algorithms (that is, the ones requiring tens to hundreds iterations/FEM evaluations to converge to solutions with moderate accuracy as opposed to thousands to millions iterations needed by many non-derivative search based methods) for topology optimization are often based on the first order approximations. For some methods widely used in practice, their convergence is enforced using very simple heuristic devices, which do not guarantee that the resulting limit points do in fact satisfy the optimality conditions.

There are, of course, very good reasons for this. The scarsity of methods utilizing the exact second-order information in the typical formulations of high-fidelity topology optimization problems is owing to the enormous number of optimization variables combined with the fact that the elements of the Hessian are (a) expensive to compute and (b) impossible to store owing to the fact that the matrix is fully populated. (One could of course try to resort to limited-memory quasi-Newton methods, but they do not seem to perform favourably when compared

with the best first order separable convex approximation algorithms.) The reluctance to rely upon convergence-enforcing safeguards, such as linesearches, is owing to (c) the expensiveness of function evaluations, which involves solving one or several, possibly non-linear, PDEs governing the physical system under consideration.

In what follows we outline an alternative solution approach to topology optimization problems, which quite elegantly avoids the difficulties (a), (b), and (c). We then demonstrate its behaviour on some benchmark problems in topology optimization of flow domains for viscous incompressible flows.

The model problem, its variational discretization, and the solution algorithm

The model problem

We consider the classical problem of topology optimization applied to fluid mechanics, namely the problem of finding the shape of a flow domain of a given volume, which minimizes the power dissipation of a viscous fluid passing through it [1].

More precisely, we are given an open bounded polyhedral domain $\Omega \in \mathbb{R}^d$, $d \in \{2, 3\}$ with Lipschitz boundary $\partial\Omega$, the flow velocity at the boundary $\boldsymbol{u}_0 \in [H^{1/2}(\partial\Omega)]^d$ satisfying the compatibility condition $\int_{\partial\Omega} \boldsymbol{n} \cdot \boldsymbol{u}_0 = 0$, volumetric forces $\boldsymbol{f} \in [L^2(\Omega)]^d$, and a volume fraction $\gamma \in]0, 1[$. We introduce the convex set of admissible designs $G = \{\, \rho \in L^\infty(\Omega) \mid \int_\Omega \rho = \gamma|\Omega|, \text{ and } 0 \le \rho \le 1, \text{ a.e. in } \Omega \,\}$ and the trial space of velocities $V = \{\, \boldsymbol{u} \in [H^1(\Omega)]^d : \boldsymbol{u}|_{\partial\Omega} = \boldsymbol{u}_0 \,\}$. We will use a monotone convex function $\alpha : [0, 1] \mapsto [0, \bar{\alpha}]$ mapping designs to the inverse permeability coefficient of Brinkmann equations, $\alpha(\rho) = \bar{\alpha} q[(q + 1)/(\rho + q) - 1]$, where $\bar{\alpha}$ and q are positive parameters. We will be interested in solving the following problem:

$$\begin{aligned} \underset{(\boldsymbol{u},\rho)\in V\times G}{\text{minimize}} \quad & J(\boldsymbol{u}, \rho) = \frac{1}{2}\int_\Omega \operatorname{grad}\boldsymbol{u} : \operatorname{grad}\boldsymbol{u} + \frac{1}{2}\int_\Omega \alpha(\rho)\boldsymbol{u}\cdot\boldsymbol{u} - \int_\Omega \boldsymbol{f}\cdot\boldsymbol{u}, \\ \text{subject to} \quad & \operatorname{div}\boldsymbol{u} = 0. \end{aligned} \tag{1}$$

It is well known that this problem admits solutions [1], which are unfortunately not unique owing to the non-convexity of the penalization term $\frac{1}{2}\int_\Omega \alpha(\rho)\boldsymbol{u}\cdot\boldsymbol{u}$.

The standard way of solving this problem, see for example [1], is to introduce the *reduced* cost $j(\rho) := \min_{\boldsymbol{u}} J(\boldsymbol{u}, \rho)$, where minimization is carried out over all solenoidal fields in V, and then minimize $j(\rho)$ over all admissible designs $\rho \in G$. This method suffers from the difficulties (a), (b), (c) outlined above; indeed, every evaluation of $j(\rho)$ involves solving a system of partial differential equations, which constitutes the set of optimality conditions for minimizing J w.r.t. $\boldsymbol{u}$ for a fixed ρ.

The barrier problem and its variational discretization

In the spirit of interior-point methods we introduce a small parameter $\mu > 0$ and a perturbation of the problem (1)

$$\begin{aligned} \underset{(\boldsymbol{u},\rho)\in V\times L^\infty(\Omega)}{\text{minimize}} \quad & J_\mu(\boldsymbol{u}, \rho) = J(\boldsymbol{u}, \rho) - \mu\int_\Omega \log[\rho(1-\rho)], \\ \text{subject to} \quad & \operatorname{div}\boldsymbol{u} = 0, \text{ and } \int_\Omega \rho = \gamma|\Omega|. \end{aligned} \tag{2}$$

Let $L_\mu : V \times L^\infty(\Omega) \times L^2_0(\Omega) \times \mathbb{R} \to \mathbb{R}$,

$$L_\mu(\boldsymbol{u}, \rho, p, \lambda) = J_\mu(\boldsymbol{u}, \rho) - \int_\Omega p \operatorname{div}\boldsymbol{u} + \lambda\left[\int_\Omega \rho - \gamma|\Omega|\right], \tag{3}$$

be the Lagrangian for the problem (2). We introduce the variational discretization of the problem (2) by considering a pair of finite-dimensional subspaces $V^h \times Q^h$ of $V \times L^2_0(\Omega)$ satisfying

the LBB condition for the incompressibility constraint and then by studying the stationarity of L_μ on $V^h \times G \times Q^h \times \mathbb{R}$. Note that we do not explicitly discretize the design space (which is inspired by the variational discretization concept of [2]), but this does not prevent us from solving the problem on a computer.

Indeed, for a given pair $(\boldsymbol{u}^h, \lambda^h) \in V^h \times \mathbb{R}$, whenever we need the value of $\rho_{\boldsymbol{u}^h,\lambda^h}(\boldsymbol{x})$ at a point $\boldsymbol{x} \in \Omega$ where $\boldsymbol{u}^h$ is continuous, we simply solve the following scalar non-linear equation:

$$\frac{\partial L}{\partial \rho}(\boldsymbol{x}) = \frac{1}{2}\alpha'(\rho(\boldsymbol{x}))\boldsymbol{u}^h(\boldsymbol{x}) \cdot \boldsymbol{u}^h(\boldsymbol{x}) - \frac{\mu}{\rho(\boldsymbol{x})} + \frac{\mu}{1-\rho(\boldsymbol{x})} + \lambda^h = 0. \tag{4}$$

Note that the problems (4) are completely independent from each over for different values of $\boldsymbol{x}$ and may be solved very efficiently in a parallel computing environment. In a computer implementation of our algorithm the equation (4) is solved in each Gaussian quadrature point.

The Newton's algorithm for the barrier problem

We initialize the solution $(\boldsymbol{u}^h, p^h)$ by solving the discretized Stokes problem for the given boundary conditions and volumetric forces, and set $\lambda^h = 100$. At every iteration, we linearize the equations of stationarity of L_μ around the current approximation $(\boldsymbol{u}^h, \rho_{\boldsymbol{u}^h,\lambda^h}, p^h, \lambda^h)$. We eliminate the equations concerning the stationarity w.r.t. ρ by taking the appropriate Schur complement. (This does not destroy the sparsity of the left-hand side because the equations (4) are independent from each other.) We solve the reduced system for a search direction $(\delta\boldsymbol{u}^h, \delta p^h, \delta\lambda^h)$; this requires solving a Brinkmann-like system of PDEs, and the computational effort is comparable with one gradient evaluation in the standard nested approach to topology optimization. The linesearch is then performed for the augmented Lagrangian merit function

$$\phi(\alpha) = J_\mu(\boldsymbol{u}_\alpha, \rho_\alpha) + \lambda_\alpha\left[\int_\Omega \rho_\alpha - \gamma|\Omega|\right] + \frac{\nu}{2}\left[\int_\Omega \rho_\alpha - \gamma|\Omega|\right]^2, \tag{5}$$

where $(\boldsymbol{u}_\alpha, \rho_\alpha, \lambda_\alpha) = (\boldsymbol{u}^h + \alpha\delta\boldsymbol{u}^h, \rho_{\boldsymbol{u}^h+\alpha\delta\boldsymbol{u}^h,\lambda^h+\alpha\delta\lambda^h}, \lambda^h + \alpha\delta\lambda^h)$, and $\nu > 0$ is a penalty parameter. After a step-length satisfying the Wolfe's conditions has been found, we update the current approximation. Should the search direction fail to be a descent direction for the merit function, we perturb the Hessian so that it is positive definite on the null space of the linearized constraints and recompute the search direction. If necessary, we also increase ν.

Numerical experiments

We test the numerical performance of our algorithm on the benchmark problems described in [1]. In all problems, the computational domain Ω is either a unit square or a rectangle; $\mu = 10^{-3}$, $\bar{\alpha} = 2.5 \cdot 10^4$, $q = 0.1$. We use a heuristic non-monotone strategy for updating ν, which is basically kept at a value slightly above the current estimate of the Lagrange multipliers at the beginning of every step. We test the method on both structured (S, in which case we report the number of subdivisions of the shorter side of the rectangle) and quasi-uniform unstructured (U, in which case we report the largest diameter of the element) conforming meshes of triangles in our experiments. We also use well-known LBB-stable pairs of elements for the spaces $V^h \times Q^h$, namely "mini", Taylor–Hood (TH), and non-conforming Crouzeix–Raviart (CR). For the design discretization, we use Gaussian quadrature exact for polynomials of order 3 for CR elements, and of order 7 for "mini" and TH elements. We terminate the algorithm when either $\|\delta\boldsymbol{u}^h\|_{[H^1(\Omega)]^d}/\|\boldsymbol{u}^h\|_{[H^1(\Omega)]^d} < 10^{-10}$, or when the directional derivative of J_μ is smaller than 10^{-12}. In all cases we observe local superlinear convergence predicted by the theory. The method is implemented mostly in Python using FEniCS tools [3].

The results are summarized in Table 1, where we also compare them with the traditional nested algorithm, stopped after a much more relaxed criterion of function values changing less than 10^{-5} as reported in [1].

Table 1. Numerical performance of the method. Problem names are taken from [1], "rugby (0.8)" refers to "rugby ball" problem with a volume fraction $\gamma = 0.8$. Dbl. pipe (S) and (L) refer to the "double pipes" problem with the domain length of 1.0 and 1.5, respectively. Discretizations are reported as S/U (structured or unstructured) X is the size of mesh (number of elements along one axis for structured meshes/diameter of the larges element for unstructured) "element" (finite element family). J_μ^* is the optimal value and #it is the number of optimization iterations.

Problem →	Diffuser		Pipe bend		Rugby (0.8)		Dbl. pipe (S)		Dbl. pipe (L)	
Discretization ↓	J_μ^*	#it	J_μ^*	#it	J_μ^*	#it	J_μ^*	#it	J_μ^*	#it
$S50$ [1]	30.59	29	10.01	64						
$S100$ [1]	30.46	33	9.76	85	31.75	47	25.67	61	27.64	236
$S100$CR	30.27	14	9.37	33	31.31	13	21.00	28	22.87	28
$S100$TH	30.44	14	9.56	34	31.43	14	21.71	33	23.65	29
$S100$Mini	30.53	13	9.72	32	31.55	12	22.03	26	24.02	32
$S200$Mini	30.47	14	9.66	33	31.46	12	21.93	29	23.90	30
$U0.01$Mini	30.50	14	9.65	34	31.47	12	21.93	30	23.90	28

Conclusions and extensions

Our numerical experiments suggest that (i) the number of algorithmic iterations is virtually independent from the utilized mesh and finite element discretization; (ii) our algorithm outperforms the standard nested approach on this suite of problems at least by a factor of two in terms of the number of iterations, which is very promising if this can be extrapolated to other problems.

The fast local convergence of the algorithm may of course be utilized for the path-following applications, such as for example solving a sequence of problems with $(\bar{\alpha}^{-1}, q^{-1}, \mu) \to (0, 0, 0)$. We have successfully tested this approach also in connection with adaptive refinement based on the PDE-form of the problem's optimality conditions (i.e., also following the parameter $h \to 0$). Finally, and perhaps even more importantly, the algorithm trivially extends to power minimization of non-Newtonian fluids while maintaining the same step complexity, thus providing a very efficient way of solving these optimization problems constrained with non-linear PDEs.

References

[1] Thomas Borrvall and Joakim Petersson. Topology optimization of fluids in Stokes flow. *Internat. J. Numer. Methods Fluids*, 41(1):77–107, 2003.

[2] M. Hinze. A variational discretization concept in control constrained optimization: the linear-quadratic case. *J. Computational Optimization and Applications*, 30:45–63, 2005.

[3] A. Logg, G.N. Wells, and J. Hake. *DOLFIN: a C++/Python Finite Element Library, Automated Solution of Differential Equations by the Finite Element Method*, volume 84 of *Lecture Notes in Computational Science and Engineering*, chapter 10. Springer, 2012.

Proceedings of the 26th Nordic Seminar on Computational Mechanics
A. Logg, K.A. Mardal, A. Massing (Eds.)

On generalized boundary conditions in virtual testing of micro-heterogeneous materials

Fredrik Larsson[1]

[(1)]Chalmers University of Technology, Department of Applied Mechanics, SE41296 GÖTEBORG, fredrik.larsson@chalmers.se

Summary. This paper introduces novel boundary conditions for computational homogenization with application to the linear Poisson problem. The novel boundary conditions pertain to generalized Dirichlet and Neumann type boundary conditions and can be used to obtain upper and lower bounds on the effective (up-scaled) coefficients.

Key words: Computational homogenization, Random media, Boundary conditions

Introduction

This contribution concerns the issue of determining effective properties for (micro)heterogenous random media. Typical applications include the determination of effective mechanical properties for elastic composites or effective heat conductivity in bi-phasic media.

Adopting so-called first order homogenization of random media, the randomness of the underlying subscale vanishes on the macroscale due to the separation of scales assumption. More specifically, the effective properties on the macroscale are defined by the response of an infinite-sized Representative Volume Element (RVE) inside which all imposed macroscale variables vary smoothly. In practice, using numerical simulations, one has to restrict to sampling of finite sized Statistical Volume Elements (SVEs). Using virtual testing, it is well known that the effective properties can be bounded from above and below by the classical assumptions of Dirichlet and Neumann boundary conditions, see e.g. [1, 2]. Furthermore, by adopting periodic boundary conditions, accurate estimates of the effective properties can be obtained. However, for the latter, no control of the quality exists.

When considering problems with increasing contrast of the properties of the phases, the classical bounds mentioned above deteriorate. The limit case of infinite contrast, corresponding to a problem on a "perforated" domain, the classical conditions may be impossible to apply.

In this contribution, we shall present a novel approach to construct alternative bounds for virtual testing of random media with large-contrast constituent properties. The new bounds arise from generalizations of the classic assumptions pertinent to Dirichlet and Neumann boundary conditions, in that the solution (or flux) is restricted on each SVE boundary. The extension follows from adopting different strategies for determining the appropriate shape of such restricted boundary fields.

Model problem and homogenization

We consider the linear Poisson problem of determining $u(\boldsymbol{x})$ satisfying

$$\begin{aligned} \operatorname{Div} \boldsymbol{q} &= b, && (1)\\ \boldsymbol{q} &= -k(\boldsymbol{x}) \operatorname{Grad} u, && (2) \end{aligned}$$

where $k(\boldsymbol{x})$ is the realization of a random field.

Assuming separation of scales, we may consider the effective problem on a macroscale as

$$\begin{aligned} \operatorname{Div} \bar{\boldsymbol{q}} &= \bar{b}, & (3) \\ \bar{\boldsymbol{q}} &= -\bar{\boldsymbol{k}} \cdot \operatorname{Grad} \bar{u}, & (4) \end{aligned}$$

where $\bar{\boldsymbol{k}}$ is the up-scaled (homogenized) effective coefficient tensor and $\bar{b}$ is the effective load (not discussed further here).

The problem we consider is now how to compute $\bar{\boldsymbol{k}}$ for known random process generating $k(\boldsymbol{x})$. More general, we may seek the effective relation $\bar{\boldsymbol{q}}(\bar{\boldsymbol{g}})$ for a non-linear problem, expressed in terms of the macroscale gradient $\bar{\boldsymbol{g}} := \operatorname{Grad} \bar{u}$.

Virtual testing denotes the procedure of studying a number of realizations of $k(\boldsymbol{x})$ on finite sized SVEs $\Omega_\square$. Solving equations 1,2 on $\Omega_\square$ for $b = 0$ together with suitable boundary conditions defines the effective response of the SVE realization, $\bar{\boldsymbol{q}}_\square(\bar{\boldsymbol{g}})$.

Generalized boundary conditions

The generalized Dirichlet boundary conditions can be stated as follows:

$$u = \bar{\boldsymbol{g}} \cdot [\boldsymbol{x} + \boldsymbol{\psi}] \quad \text{on } \partial\Omega_\square, \tag{5}$$

for known effective gradient $\bar{\boldsymbol{g}}$, where $\boldsymbol{\psi}$ is a pre-computed fluctuation on each natural subdivision of the boundary. Here, $\boldsymbol{\psi}$ is constructed such that the average gradient of u inside $\Omega_\square$ is guaranteed to be $\bar{\boldsymbol{g}}$. In practice, $\boldsymbol{\psi}$ is computed from a boundary value problem defined on the boundary, in order to approximate a suitable fluctuation corresponding to a constant flux along the boundary. Setting $\boldsymbol{\psi} = \boldsymbol{0}$ returns the classical Dirichlet conditions.

The generalized Neumann boundary conditions, on the other hand, can be stated as follows:

$$q_n := \boldsymbol{q} \cdot \boldsymbol{n} = \bar{\boldsymbol{q}} \cdot [\phi \boldsymbol{n}] \quad \text{on } \partial\Omega_\square, \tag{6}$$

for known effective flux, $\bar{\boldsymbol{q}}$, where ϕ is a pre-computed fluctuation on each natural subdivision of the boundary. Here, the fluctuation ϕ is required to satisfy that the average of the flux $\boldsymbol{q}$ inside $\Omega_\square$ is exactly $\bar{\boldsymbol{q}}$. In order to compute a suitable fluctuation, ϕ is computed locally corresponding to a uniform gradient across the boundary. Setting $\phi = 1$ returns the classical Neumann conditions.

It can be shown that, under mild restrictions, any choice of $\boldsymbol{\psi}$ and ϕ based on pointwise local information, i.e. coefficient $k(\boldsymbol{x})$, renders statistical bounds on the effective properties.

Numerical examples

A few numerical examples for the Poisson problem in 2D will be presented at the conference, illustrating the behavior of the proposed method.

References

[1] T.I. Zohdi, P. Wriggers, *Introduction to Computational Micromechanics*, Springer, 2005.

[2] M. Ostoja-Starzewski, *Microstructural Randomness and Scaling in Mechanics of Materials*, Chapman & Hall/CRC Taylor & Francis Group, 2007.

Proceedings of the 26th Nordic Seminar on Computational Mechanics
A. Logg, K.A. Mardal, A. Massing (Eds.)

Explicit fourth-order stiffness representation in non-linear dynamics

Steen Krenk

Department of Mechanical Engineering, Technical University of Denmark
Building 403, Nils Koppel's Alle, DK-2800 Kongens Lyngby, Denmark
sk@mek.dtu.dk

Summary. In momentum-based time integration methods, the internal forces appear naturally as an approximate representation of the time integral of the internal forces over the integration interval. It is highly desirable that this force integral also represents the increment of the internal energy. A simple global form of the effective internal force is presented, in which it is represented by its algebraic mean value plus a higher order term in the form of the product of the increment of the tangent stiffness matrix at the interval end-points and the corresponding displacement increment. This explicit representation is of fourth order, and leads to the exact energy increment for systems with quartic internal energy function.

Key words: time integration, energy conservation, non-linear dynamics

Introduction

Traditionally, time integration algorithms in structural dynamics have been based on increments over the time integration interval $h = \Delta t$ and various weighted mean values, typically in the two-parameter format developed by Newmark [1], or in the extended α-modifications of the basic format, see e.g. [2]. These algorithms were initially formulated for linear problems, and their properties characterized by spectral analysis. In the case of non-linear problems the basic collocation format, in which the state variable increments are expressed in terms of averages of forces corresponding to specific times t_n, suffers from the basic weakness that the corresponding energy increment over the time interval can not be expressed in this format. Thus, the collocation format intrinsically breaks with the property of energy conservation for non-linear problems.

About two decades ago an alternative approach to time integration algorithms in dynamics was developed based on representing the time integral of the state-space equations of motion. The original development by Simo and co-workers [3] was based on the observation that in linear elasticity with Green strains the effective internal force over a time increment can be represented via the product of the mean value of the strain gradient and the mean value of the stress. The procedure was later generalized to non-linear elasticity by Gonzalez [4], using a stiffness representation similar to that of the classic BFGS method. These methods provide momentum and energy balance within a second-order time accurate scheme. However, the format has the drawback that the internal force is formed in terms of a product of averages at the element level, and therefore requires reformulation of traditional element procedures, in which the internal force is formed for a particular state associated with the discrete points t_n used in the time integration algorithm. It was later shown by Krenk [5, 6] that in the case of linear elasticity with Green strains energy conservation could be attained by supplementing the mean value of the internal forces with an additional stiffness term formed by the increment of the geometric stiffness matrix. This term can be formed at the global level, and thus permits inclusion as a simple modification of existing finite element codes.

The present paper develops a fourth-order representation of the internal force in terms of values of the internal force and the tangent stiffness matrix at the integration interval end-points at t_n and t_{n+1}. The result is based on Taylor series expansions, and therefore does not require any special format of the internal energy. For energy functions that are up to quartic in the displacement components the energy is conserved exactly, and otherwise to the fourth order.

Momentum based state-space equations

Consider a mechanical system, described in terms of displacements contained in the column vector $\mathbf{u}$. The internal forces are assumed to be given in terms of the potential $G(\mathbf{u})$ in the form

$$\mathbf{g}(\mathbf{u}) = \boldsymbol{\nabla}_{\mathbf{u}} G(\mathbf{u}) \tag{1}$$

where $\boldsymbol{\nabla}_{\mathbf{u}}$ denotes the derivatives with respect to the displacement components of $\mathbf{u}$. For convenience the resulting components are defined to be in column format. The mass matrix $\mathbf{M}$ is assumed to be constant, as e.g. for models using isoparametric elements. The corresponding equation of motion is

$$\mathbf{M}\ddot{\mathbf{u}}(t) + \mathbf{C}\dot{\mathbf{u}}(t) + \mathbf{g}(\mathbf{u}) \;=\; \mathbf{f}(t) \tag{2}$$

where $\mathbf{f}(t)$ is the load vector, and $\mathbf{C}$ is a matrix representing linear viscous damping.

It is convenient to introduce the velocity $\mathbf{v} = \dot{\mathbf{u}}$ and work in terms of the state-space variables $[\,\mathbf{u}^T, \mathbf{v}^T\,]$. The equation of motion can then be expressed by the following symmetric set of first-order differential equations,

$$\begin{bmatrix} \mathbf{C} & \mathbf{M} \\ \mathbf{M} & \mathbf{0} \end{bmatrix} \begin{bmatrix} \dot{\mathbf{u}} \\ \dot{\mathbf{v}} \end{bmatrix} + \begin{bmatrix} \mathbf{g}(\mathbf{u}) \\ -\mathbf{M}\,\mathbf{v} \end{bmatrix} = \begin{bmatrix} \mathbf{f}(t) \\ \mathbf{0} \end{bmatrix} \tag{3}$$

The key step in momentum based integration methods is the use of a time integrated form of these equations, here expressed as

$$\begin{bmatrix} \mathbf{C} & \mathbf{M} \\ \mathbf{M} & \mathbf{0} \end{bmatrix} \begin{bmatrix} \Delta\mathbf{u} \\ \Delta\mathbf{v} \end{bmatrix} + h \begin{bmatrix} \mathbf{g}_* \\ -\mathbf{M}\,\bar{\mathbf{v}} \end{bmatrix} = h \begin{bmatrix} \bar{\mathbf{f}} \\ \mathbf{0} \end{bmatrix} \tag{4}$$

where $\mathbf{g}_* \simeq h^{-1} \int \mathbf{g}\, dt$ and the time mean values of $\mathbf{v}$ and $\mathbf{f}$ are represented by their algebraic mean.

The important point now is to identify a suitable definition of the representative mean value $\mathbf{g}_*$, such that it also satisfies the energy increment relation

$$\Delta G \;=\; \Delta\mathbf{u}^T \boldsymbol{\nabla}_{\mathbf{u}} G_* \;=\; \Delta\mathbf{u}^T \mathbf{g}_* \tag{5}$$

In [3] and [4] this problem was solved for a linear/non-linear elastic body via properties in the mean state at $t_{n+1/2}$, while [5] obtained an explicit expression in terms of the increment of the geometric stiffness for a linear elastic body with Green strains. In the following section a general expression for $\mathbf{g}_*$ of order four is obtained for a general potential function $G(\mathbf{u})$ in terms of the increment of the full stiffness matrix.

Representation of the internal force

The present representation of $\mathbf{g}_*$ is obtained from a suitably modified form of the Taylor expansion of the potential $G(\mathbf{u})$. For this purpose the displacement increment is parameterized over the time interval $[t_n, t_{n+1}]$ as

$$\mathbf{u} \;=\; \mathbf{u}_{n+1/2} + \xi\Delta\mathbf{u} \tag{6}$$

This gives the following expression for the energy increment

$$\Delta G \;=\; \int_n^{n+1} \mathbf{g}(\mathbf{u})^T \, d\mathbf{u} \;=\; \Delta\mathbf{u}^T \int_{-1/2}^{1/2} \mathbf{g}(\mathbf{u}_{n+1/2} + \xi\Delta\mathbf{u}) \, d\xi \tag{7}$$

The internal force is now expanded in terms of ξ as

$$\mathbf{g}(\mathbf{u}) \;=\; \mathbf{g}(\mathbf{u}_{n+1/2}) \;+\; \xi\mathbf{g}'(\mathbf{u}_{n+1/2}) \;+\; \tfrac{1}{2}\xi^2\mathbf{g}''(\mathbf{u}_{n+1/2}) \;+\; \cdots \tag{8}$$

When substituting this expansion into the integral in (7) it is seen that only the even powers of ξ contribute, and when including only the first two contributing terms

$$\Delta G \;=\; \Delta\mathbf{u}^T \Big[\mathbf{g}(\mathbf{u}_{n+1/2}) \;+\; \tfrac{1}{24}\mathbf{g}''(\mathbf{u}_{n+1/2}) \;+\; \mathrm{O}(h^4) \Big] \tag{9}$$

where it has been used that $\Delta\mathbf{u}$ is of order h, and that each derivative with respect to ξ introduces a factor $\Delta\mathbf{u}$ of order h. The terms inside the square brackets define the effective internal force as

$$\mathbf{g}_* \;=\; \mathbf{g}(\mathbf{u}_{n+1/2}) \;+\; \tfrac{1}{24}\mathbf{g}''(\mathbf{u}_{n+1/2}) \;+\; \mathrm{O}(h^4) \tag{10}$$

The first term in this representation is evaluated in the mean displacement state $\mathbf{u}_{n+1/2}$. This would be a serious drawback, and this term is therefore reformulated by use of the Taylor expansion (8) to express the algebraic mean of the internal force,

$$\tfrac{1}{2}[\,\mathbf{g}_{n+1} + \mathbf{g}_n\,] \;=\; \mathbf{g}(\mathbf{u}_{n+1/2}) \;+\; \tfrac{1}{8}\mathbf{g}''(\mathbf{u}_{n+1/2}) \;+\; \mathrm{O}(h^4) \tag{11}$$

When this relation is used to eliminate $\mathbf{g}_{n+1/2}$ in (10) the effective force is expressed as

$$\mathbf{g}_* \;=\; \tfrac{1}{2}[\,\mathbf{g}_{n+1} + \mathbf{g}_n\,] \;-\; \tfrac{1}{12}\mathbf{g}''(\mathbf{u}_{n+1/2}) \;+\; \mathrm{O}(h^4) \tag{12}$$

The final task now is to obtain a representation of the second term without explicit reference to the mean state $\mathbf{u}_{n+1/2}$.

The second term is expressed in terms of the increment of the tangent stiffness, $\Delta\mathbf{K}$. In order to obtain this expression the first derivative of the internal force with respect to the non-dimensional parameter ξ is expressed as

$$\mathbf{g}'(\mathbf{u}) \;=\; \frac{d\mathbf{g}}{d\mathbf{u}}\Delta\mathbf{u} \;=\; \mathbf{K}(\mathbf{u})\Delta\mathbf{u} \tag{13}$$

In the present formulation the displacement increment $\Delta\mathbf{u}$ is fixed, and the second derivative of the internal force with respect to the non-dimensional parameter ξ therefore follows as

$$\mathbf{g}''(\mathbf{u}) \;=\; \frac{d\mathbf{K}}{d\xi}\Delta\mathbf{u} \;\simeq\; \frac{\Delta\mathbf{K}}{\Delta\xi}\Delta\mathbf{u} \;=\; \Delta\mathbf{K}\Delta\mathbf{u} \tag{14}$$

Substitution of this representation into the expansion (12) then gives the final form

$$\mathbf{g}_* \;=\; \tfrac{1}{2}\big[\,\mathbf{g}_{n+1} + \mathbf{g}_n\,\big] \;-\; \tfrac{1}{12}\Delta\mathbf{K}\,\Delta\mathbf{u} \;+\; \mathrm{O}(h^4) \tag{15}$$

In this form the effective internal force is expressed to fourth order entirely by the internal force and the stiffness matrix at the integration interval end-points. The form of this representation is similar to that obtained in [5] for the special case of linear easticity in terms of the Green strain, where the second term was given in terms of the increment of the geometric stiffness as $-\frac{1}{4}\Delta\mathbf{K}_g\,\Delta\mathbf{u}$. However, the present result dos not require any special form of the energy function, and no separation of the stiffness matrix is involved.

Fourth-order conservation algorithm

The discretized form (4) of the equations of motion is now expressed by use of the fourth-order representation (15) of the internal force, whereby

$$\begin{bmatrix} \mathbf{C} - \frac{1}{12}h\Delta\mathbf{K} & \mathbf{M} \\ \mathbf{M} & \mathbf{0} \end{bmatrix} \begin{bmatrix} \Delta\mathbf{u} \\ \Delta\mathbf{v} \end{bmatrix} + \frac{h}{2} \begin{bmatrix} \mathbf{g}(\mathbf{u}_{n+1}) + \mathbf{g}(\mathbf{u}_n) \\ -\mathbf{M}\,\mathbf{v}_{n+1} - \mathbf{M}\,\mathbf{v}_n \end{bmatrix} = h \begin{bmatrix} \bar{\mathbf{f}} \\ \mathbf{0} \end{bmatrix} \tag{16}$$

The viscous damping in terms of $\mathbf{C}$ can be replaced or supplemented by an algorithmic damping by inserting additional terms in the diagonal of the first block matrix, following the procedure in [6].

In the solution procedure the the velocity $\mathbf{v}_{n+1}$ is eliminated in the first equation by use of the second, and a non-linear equation is obtained in $\mathbf{u}_{n+1}$. Subsequently, the velocity $\mathbf{v}_{n+1}$ is obtained from the second equation, using the now known value of $\mathbf{u}_{n+1}$.

The present conservative time integration procedure with fourth-order stiffness representation is illustrated by some simple examples, demonstrating the improved time representation in the solution, as well as the use in problems with internal energy representation that is not directly of fourth degree in the displacements.

References

[1] N.M. Newmark. A method of computation for structural dynamics. *Journal of the Engineering Mechanics Division, ASCE*, 85:67–94 1959.

[2] J. Chung and G.M. Hulbert. A time integration algorithm for structural dynamics with improved numerical dissipation: The generalized α method. *Journal of Applied Mechanics*, 60:371–375, 1993.

[3] J.C. Simo and N. Tarnow. The discrete energy-momentum method. Conserving algorithms for elastodynamics. *Zeitschrift für angewandte Mathematik und Physik*, 43:757–792, 1992.

[4] O. Gonzalez. Exact energy and momentum conserving algorithms for general models in nonlinear elasticity. *Computer Methods in Applied Mechanics and Engineering*, 190:1763–1783, 2000.

[5] S. Krenk. The role of geometric stiffness in momentum and energy conserving time integration. *International Journal for Numerical Methods in Engineering*, 71:631–651, 2007.

[6] S. Krenk. *Non-linear Modeling and Analysis of Solids and Structures*, Cambridge University Press, Cambridge, UK, 2009.

Proceedings of the 26th Nordic Seminar on Computational Mechanics
A. Logg, K.A. Mardal, A. Massing (Eds.)

A second order fast sweeping method for the Eikonal equation

Miroslav Kuchta[1,2], Mikael Mortensen[1,3]

(1)University of Oslo; Moltke Moes vei 35 0851 Oslo, Norway
(2)mirok@math.uio.no, (3)mikaem@math.uio.no

Summary. In this work the first order fast sweeping method of J. Qian at el. [*SINUM*, 45(1):83–107,200] for solving the Eikonal equation on unstructured triangular meshes is recast into an optimization problem. We show that the new formulation is equivalent with the old one and present how it can be used to derive a second order method. Furthermore, we present a new local geometrical solver that is potentially cheaper and applicable to higher order finite elements.

Key words: Eikonal equation, fast sweeping, reinitialization

Motivation

A popular choice for modeling the evolution of an interface separating two phases is the level-set method, where the interface $\gamma \in \mathbb{R}^{n-1}$ represents a zero contour of function $\phi : (\Omega \times \mathbb{R}) \mapsto \mathbb{R}^n$, Ω being domain of interest in $\mathbb{R}^2$ or $\mathbb{R}^3$. The level-set function can be chosen arbitrarily, but a popular choice is to make it a signed distance function. If $\boldsymbol{u}$ is the velocity at the interface, then the evolution of ϕ is governed by

$$\frac{\partial \phi}{\partial t} + \boldsymbol{u} \cdot \nabla \phi = 0. \tag{1}$$

Common finite elemet methods for solving (1) are Streamline-Upwind/Petrov-Galerkin(SUPG) and discontinuous Galerkin(DG). Regardless of the approach, the signed distance property of the level-set function is gradually lost during the computation unless the function is reinitialized.

An alternative to the interface capturing level-set methods are the front tracking methods. One such front tracking method is proposed in [2], where γ is seeded with particles and ordinary differential equations for the evolution of a particle's position $\boldsymbol{x}_0$, normal vector $\boldsymbol{n}$ and curvature tensor $\nabla \boldsymbol{n}$ are derived from (1). Solving this system or equations for all particles, one obtains rich information about the interface that can be used to set the level-set values in the nodes of a Eulerian mesh. For cells containing particles, the value at node $\boldsymbol{x}$ is computed from a Taylor expansion

$$\phi(\boldsymbol{x}) = \boldsymbol{n} \cdot (\boldsymbol{x} - \boldsymbol{x}_0) + \frac{1}{2}(\boldsymbol{x} - \boldsymbol{x}_0) \cdot \nabla \boldsymbol{n} \cdot (\boldsymbol{x} - \boldsymbol{x}_0) + \mathcal{O}(h^3), \tag{2}$$

where h is a typical mesh size. The level-set function in the rest of the domain is then updated by a fast sweeping method [3] that solves the Eikonal equation

$$|\nabla \phi| = 1. \tag{3}$$

We aim to combine traditional solvers of (1) with the particle method of [2] and use particles to reinitialize the level-set function in a narrow band around the interface. It follows from (2) that the method for setting ϕ in the intersected cells is third order accurate. Thus, in this region

particles are an excellent tool for reinitialization of the level-set function. To verify this claim we have implemented the particle-based method and level-set methods based on SUPG and DG. An option to reinitialize the level-set function using particles was added to the latter two solvers. All the solvers were then compared using the Zalesak disk test case. The results are summarized in Figure 1. An improvement in the solution of SUPG and DG due to reinitialization is evident.

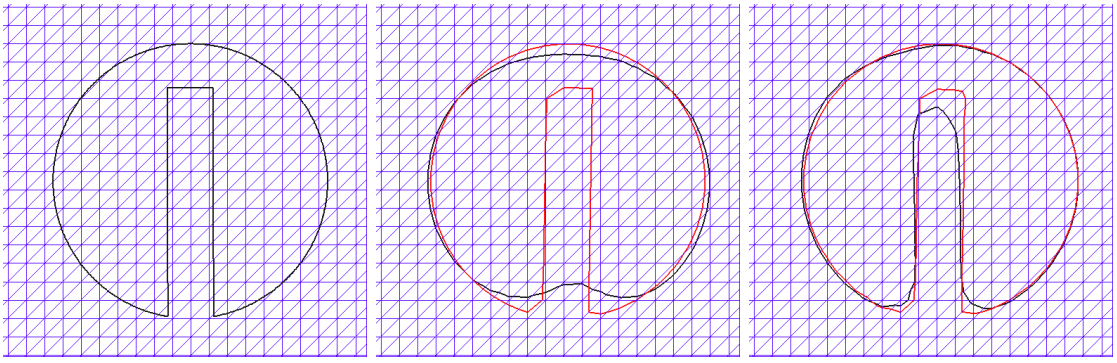

(a) (b) (c)

Figure 1: Zalesak disk test case. Comparison of zero level-set position after one disk rotation. Mesh with 50×50 cells and 1000 particles was used. Result of a traditional solver is denoted with black line. Red line denotes result of a solver with the level-set function reinitialized in the intersected cells at every time step. (a) Oriented particles. (b) SUPG. (c) DG.

To keep the order of accuracy from the intersected cells in the rest of the narrow band a third order accurate method for solving the Eikonal equation is required. However, if only the first term is kept in (2), a second order accurate method will be sufficient. In the remainder of this article we show how such a method can be constructed.

Geometrical solver

The fast sweeping method [3] solves the Eikonal equation on a structured rectangular grid by sweeping through the domain and by applying to the ordered Eulerian nodes a local solver based on finite differences. This procedure is repeated until ϕ is not altered by a new sweep. The method thus does not adhere so strictly to the Huygens principle and there is not need to keep a heap-like structure with the closest points. As a result complexity of the method is $\mathcal{O}(M)$, M being the number of nodes in the mesh, which should be compared with $\mathcal{O}(M \log M)$ complexity of the fast marching method. Ordering of the nodes on a rectangular grid is given naturally by their indices. On an unstructured mesh there is no natural ordering of the nodes and the lack of structure renders finite differences practically unusable. In [1], a fast sweeping method for unstructured triangular meshes is proposed. The method uses ordering of the nodes determined by their distance from a predefined set or reference points and the local Eikonal solver is based on geometrical reasoning.

The local geometrical solver [1] works as follows (see Figure 2a). Given triangle $\boldsymbol{ABC}$ with known values of ϕ at vertices $\boldsymbol{A}$ and $\boldsymbol{B}$ such that $\phi_A < \phi_B$ update the value ϕ_C by (i) computing the angle θ, (ii) computing $h = |\boldsymbol{C}-\boldsymbol{P}_G| = a\sin(\alpha-\theta)$ and (iii) $\phi_C = \min(\phi_C, h+\phi_B)$. Assuming that the triangle is acute, we can see that increasing θ can make $\boldsymbol{C}$ closer to the plane. In such case, updating ϕ_C from $\boldsymbol{A}$ and $\boldsymbol{B}$ violates the causality principle that is valid for the Eikonal equation; nodes closer to the front update those that are further away. We refer readers to the original paper to see how such cases are handled.

To recast the geometrical solver into an optimization problem, note that the correct value $\phi_C = |\boldsymbol{C} - \boldsymbol{C}'| = |\boldsymbol{P}_O - \boldsymbol{C}'| + |\boldsymbol{P}_O - \boldsymbol{C}|$ and the distance $|\boldsymbol{P}_O - \boldsymbol{C}'|$ is obtained from the linear interpolant of ϕ_A, ϕ_B on the edge c evaluated at $\boldsymbol{P}_O$. Moreover, since the update vector $\boldsymbol{C} - \boldsymbol{C}'$

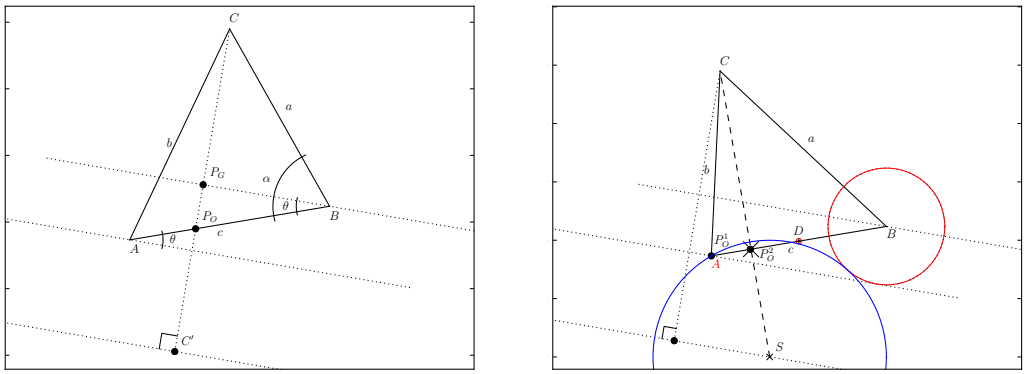

(a) (b)

Figure 2: Local Eikonal solvers. (a) Distance of vertex $\boldsymbol{C}$ from the plane with point $\boldsymbol{C}'$ is to be computed from known values of ϕ_A, ϕ_B. Linear minimization method seeks intersect $\boldsymbol{P}_O$. Geometrical solver is based on $\boldsymbol{P}_G$. Both methods end up updating vertex $\boldsymbol{C}$ using $\boldsymbol{C}'$. (b) Distance of vertex $\boldsymbol{C}$ from point $\boldsymbol{S}$ is to be computed from known values of ϕ_A, ϕ_B and ϕ_D. Linear method approximates circular wavefront by a plane and the local solver fails to find the correct intersect. Quadratic method approximates wavefront using distance from additional point $\boldsymbol{D} = 0.5(\boldsymbol{A} + \boldsymbol{B})$. Intersect $\boldsymbol{P}_O^2$ found by the method is almost identical to the true one denoted by cross. Inverse problem for higher order geometrical solvers: from known values of ϕ_A, ϕ_D, ϕ_C point S can be found as a center of blue circle which passes through $\boldsymbol{A}$ and is tangent to the red circles. The center can be used to update ϕ_C.

passes through $\boldsymbol{P}_O$, the point is a solution to the problem of finding a point on the wavefront with the closest distance to $\boldsymbol{C}$.

Proof of the equivalence of the two formulations is based on two observations: (i) Let $\boldsymbol{P} : [0,1] \mapsto \mathbb{R}^2$, $\boldsymbol{P}(t) = \boldsymbol{A}t + \boldsymbol{B}(1-t)$, then $t = (\phi_B - \phi_A)/|\boldsymbol{P} - \boldsymbol{B}|$. (ii) For $\boldsymbol{P}_G$ found by geometrical solver $\cos(\alpha - \theta) = |\boldsymbol{P}_G - \boldsymbol{B}|/|\boldsymbol{C} - \boldsymbol{B}|$. Combining (i) and (ii) with a definition of θ yields that

$$t_G = \frac{|\boldsymbol{C} - \boldsymbol{B}| \cos(\alpha - \theta)}{|\boldsymbol{A} - \boldsymbol{B}| \cos(\theta)}. \tag{4}$$

To finish the proof it remains to show that t_G is a minimizer of $\psi(t) = \phi_A t + \phi_B(1-t) + |\boldsymbol{C} - \boldsymbol{P}|$. This is indeed true, but the calculations will no be presented here.

The minimization method was implemented using FEniCS [4]. A function space constructed from cG_1 finite elements was used for ϕ and all the cell-node connectivity was provided by FEniCS's functionality. The method was tested using the problem of finding the distance to two circles (see [1]). Results are summarized in Table 1 and confirm first order convergence of the method. Note that at most three iterations were required for convergence.

Table 1: Convergence rates of the first order minimization method measured using L^1 and L^2 norms. Uniform mesh with $N \times N$ triangles was used. Convergence of iteration process was measured in L^∞ norm and the absolute tolerance was set to machine precision.

N	L^1-rate	L^2-rate	Iter.
8	–	–	2
16	0.83	0.95	2
32	0.98	1.05	2
64	0.92	0.97	3
128	0.95	0.98	3
256	0.98	0.99	3

Second order method

As a consequence of the Huygens principle, the accuracy of local solvers of the Eikonal equation depends solely on the approximation of the wavefront. In the minimization framework, a method of arbitrary accuracy can in principle be designed by using an interpolant of the same order. A second order accurate local solver could thus be constructed in the following way (cf. Figure 2): Given triangle $\boldsymbol{ABC}$ with unknown value ϕ_C find an edge c, $\boldsymbol{C} \notin c$, with three known values of ϕ. If such an edge exists, find t_O that is a minimizer of $\psi(t) = \phi_A(1-t)(1-2t) + 4\phi_D t(1-t) + \phi_B t(2t-1) + |\boldsymbol{C} - \boldsymbol{P}|$ with $\boldsymbol{P}(t) = \boldsymbol{A}t + \boldsymbol{B}(1-t)$ and $t \in [0,1]$. If $\psi(t_O) > \min(\phi_A)$ then update $\phi_C = \min(\phi_C, \psi(t_O))$.

Figure 2b shows that our quadratic local solver gives a more accurate update than the linear one. Moreover, for a simple test case such as the one portrayed in the figure, second order convergence can be obtained. We implemented a fast sweeping method based on the quadratic solver using cG_2 finite elements. To get the necessary cell-node, node-edge, edge-cell connectivity FEniCS' built-in functions were used. Early results from the tests are promising but we have noticed that the numerical solution tends to produce undershoots. We believe the issue is related to properties of the quadratic Lagrange interpolant and can be addressed by enforcing causality in the local solver or in the sweeping strategy, perhaps, by different choice of reference points.

In the second order method, the number of calls to the local solver has grown substantially since more nodes have to be updated, and for midpoints the solver must take into account two edges. Therefore, computational cost of the local solution becomes of interest and a method based on geometrical reasoning might be an alternative to the optimization. In Figure 2, the problem of finding distance from vertex $\boldsymbol{C}$ to source $\boldsymbol{S}$ can be thought of as a problem of finding the source. The latter is a type of Apollonius' problem as we are asking for a circle that passes through vertex $\boldsymbol{A}$ and is tangent to circles centered at $\boldsymbol{D}$ and $\boldsymbol{B}$ with radii $\phi_D - \phi_A$ and $\phi_B - \phi_A$ respectively. The cost of this search might be lower than that of optimization. We should note however that such a geometrical solver is not equivalent to the above minimization problem. This can be seen from the fact that unlike the geometrical solver, quadratic Lagrange interpolation produces wavefronts that are not perfect circles. Also note that a geometrical solver would be exact in the problem depicted in Figure 2b.

Conclusions and future work

The minimization framework appears to be a promising source of higher order methods for the solution of the Eikonal equation. In this article, we proposed a local quadratic solver and a new geometrical solver. Both solvers will be implemented into fast sweeping methodss in the near future. Since the core idea of the geometrical solver is very close to the Huygens principle we believe that it can be used as a foundation for higher order methods.

References

[1] J. Qian, Y. Zhang and H. Zhao. Fast sweeping methods for Eikonal equations on triangular meshes. *SIAM Journal on Numerical Analysis*, 45(1):83–107,2007.

[2] S. Ianniello and A. Di Mascio. A self-adaptive oriented particles Level-Set method for tracking interfaces. *Journal of Computational Physics*, 229(4):1353–1380,2010.

[3] H. Zhao. A fast sweeping method for Eikonal equations. *Mathematics of Computation*, 74(250):603–627,2004.

[4] A. Logg, K.-A. Mardal, G. N. Wells et al. *Automated Solution of Differential Equations by the Finite Element Method*. Springer, 2012.

Proceedings of the 26th Nordic Seminar on Computational Mechanics
A. Logg, K.A. Mardal, A. Massing (Eds.)

The average Lagrangian method

Eirik Hoel Høiseth[1]

[(1)]Department of Mathematical Sciences NTNU, 7491 Trondheim, Norway, eirikhoe@math.ntnu.no

Summary. We consider the *average Lagrangian method*, a variational integrator with integral averaging, for use on highly oscillatory problems. When applying particular quadrature rules to approximate the integrals, the method coincides with the variational IMEX method presented in [1]. We test these methods against an energy preserving method, and two trigonometric integrators from [2].

Key words: time integration, highly oscillatory problems, variational integrators, geometric integration, trigonometric integrators

Introduction

Many physical systems satisfy a Lagrangian variational principle, meaning their dynamics are governed by a Lagrangian function $L(\boldsymbol{q}, \dot{\boldsymbol{q}})$. Furthermore, systems in Lagrangian mechanics often have components acting on different time scales, posing a challenge for traditional numerical integrators. Such *highly oscillatory problems* with Lagrangian

$$L(\boldsymbol{q}, \dot{\boldsymbol{q}}) = \dot{\boldsymbol{q}}^T \boldsymbol{M}\, \dot{\boldsymbol{q}} - U(\boldsymbol{q}) - W(\boldsymbol{q}), \tag{1}$$

where the potential energy is the sum of a "fast" potential W and a "slow" potential U, are encountered in for example molecular dynamics. Finding integrators whose timestep is not limited by the scale of the fast oscillations, but still captures the relevant dynamics, is therefore of great interest.

Variational integrators

Hamilton's principle states that the correct solution path for systems in Lagrangian mechanics is obtained by finding the trajectory $\boldsymbol{q}(t)$ that minimizes the action integral.

$$\int_{t_0}^{t_N} L(\boldsymbol{q}(\xi), \dot{\boldsymbol{q}}(\xi))\, d\xi, \quad \text{subject to fixed endpoints} \quad \boldsymbol{q}(t_0) = \boldsymbol{q}_0,\ \boldsymbol{q}(t_N) = \boldsymbol{q}_N.$$

A standard result shows that this minimization problem is equivalent to the Euler-Lagrange equations

$$\frac{d}{dt}\frac{\partial L}{\partial \dot{\boldsymbol{q}}} = \frac{\partial L}{\partial \boldsymbol{q}}. \tag{2}$$

Such systems lend themselves readily to *variational integrators*, a class of geometric numerical methods obtained directly from the Lagrangian. Variational integrators approximate the continous solution path $\boldsymbol{q}(t)$ by a discrete sequence of points $\{\boldsymbol{q}_n\}_{n=0}^N$ with $\boldsymbol{q}_i \approx \boldsymbol{q}(t_i) = \boldsymbol{q}(t_0 + ih)$. Upon replacing the action integral with a suitable discrete action integral

$$L_h(\boldsymbol{q}_n, \boldsymbol{q}_{n+1}) \approx \int_{t_n}^{t_{n+1}} L(\boldsymbol{q}(\xi), \dot{\boldsymbol{q}}(\xi))\, d\xi,$$

the discretized Hamilton principle amounts to minimizing the discrete action sum

$$S_h(\{\boldsymbol{q}_n\}_{n=0}^N) = \sum_{n=0}^{N-1} L_h(\boldsymbol{q}_n, \boldsymbol{q}_{n+1}), \quad \text{subject to } \boldsymbol{q}_0,\, \boldsymbol{q}_N \quad \text{fixed.}$$

This procedure yields the discrete Euler Lagrange (DEL) equations, which can be written in the following way by introducing discrete momentum variables $\boldsymbol{p}_n$

$$\boldsymbol{p}_n = -\frac{\partial L_h}{\partial \boldsymbol{q}_{n+1}}(\boldsymbol{q}_n, \boldsymbol{q}_{n+1}), \quad \boldsymbol{p}_{n+1} = \frac{\partial L_h}{\partial \boldsymbol{q}_n}(\boldsymbol{q}_n, \boldsymbol{q}_{n+1}). \tag{3}$$

Variational integrators preserve, by construction, a discrete version of the Lagrangian variational structure. Consequently, they are automatically symplectic and momentum-preserving, with good long-time energy behavior [3].

Introduction of methods

Variational methods

For a highly oscillatory Lagrangian (1), the average Lagrangian (AL) method uses

$$L_h^{\mathrm{AL}}(\boldsymbol{q}_n, \boldsymbol{q}_{n+1}) = \boldsymbol{v}_{n+\frac{1}{2}}^T \boldsymbol{M} \boldsymbol{v}_{n+\frac{1}{2}} - h\int_0^1 U(\boldsymbol{a}(\xi; \boldsymbol{q}_n, \boldsymbol{q}_{n+1}))\, d\xi - h\int_0^1 W(\boldsymbol{a}(\xi; \boldsymbol{q}_n, \boldsymbol{q}_{n+1}))\, d\xi, \tag{4}$$

where $\boldsymbol{a}(\xi; \boldsymbol{q}_n, \boldsymbol{q}_{n+1}) \equiv (1-\xi)\boldsymbol{q}_n + \xi \boldsymbol{q}_{n+1}$ and

$$\boldsymbol{v}_{n+\frac{1}{2}} \equiv \frac{\boldsymbol{q}_{n+1} - \boldsymbol{q}_n}{h}. \tag{5}$$

The DEL equations (3) corresponding to L_h^{AL} can then be written

$$\begin{aligned}
\boldsymbol{M}\boldsymbol{v}_{n+\frac{1}{2}} &= \boldsymbol{p}_n - h\int_0^1 \frac{\partial U}{\partial \boldsymbol{q}}(\boldsymbol{a}(\xi; \boldsymbol{q}_n, \boldsymbol{q}_{n+1}))f_1(\xi)\, d\xi - h\int_0^1 \frac{\partial W}{\partial \boldsymbol{q}}(\boldsymbol{a}(\xi; \boldsymbol{q}_n, \boldsymbol{q}_{n+1}))f_1(\xi)\, d\xi, \\
\boldsymbol{q}_{n+1} &= \boldsymbol{q}_n + h\boldsymbol{v}_{n+\frac{1}{2}}, \\
\boldsymbol{p}_{n+1} &= \boldsymbol{M}\boldsymbol{v}_{n+\frac{1}{2}} - h\int_0^1 \frac{\partial U}{\partial \boldsymbol{q}}(\boldsymbol{a}(\xi; \boldsymbol{q}_n, \boldsymbol{q}_{n+1}))f_2(\xi)\, d\xi - h\int_0^1 \frac{\partial W}{\partial \boldsymbol{q}}(\boldsymbol{a}(\xi; \boldsymbol{q}_n, \boldsymbol{q}_{n+1}))f_2(\xi)\, d\xi.
\end{aligned} \tag{6}$$

with $f_1(\xi) \equiv 1 - \xi$ and $f_2(\xi) \equiv \xi$.

We can approximate the integrals in (4) using the trapezoidal rule for the first, involving U, and the midpoint rule for the second, involving W. This produces the implicit-explicit (IMEX) variational integrator introduced in [1], with discrete Lagrangian

$$L_h^{\mathrm{IMEX}}(\boldsymbol{q}_n, \boldsymbol{q}_{n+1}) = \boldsymbol{v}_{n+\frac{1}{2}}^T \boldsymbol{M} \boldsymbol{v}_{n+\frac{1}{2}} - h\frac{U\left(\boldsymbol{q}_{n+1}\right) + U\left(\boldsymbol{q}_n\right)}{2} - hW\left(\frac{\boldsymbol{q}_{n+1} + \boldsymbol{q}_n}{2}\right)$$

Testing out other quadrature rules to approximate the integrals, is still work in progress.

Average vector field method

Given the system of ordinary differential equations (ODEs)

$$\dot{\boldsymbol{y}} = \boldsymbol{f}(\boldsymbol{y}), \quad \boldsymbol{y}(0) = \boldsymbol{y}_0 \in \mathbf{R}^n,$$

the *average vector field (AVF) method* is defined as

$$\boldsymbol{y}_{n+1} = \boldsymbol{y}_n + h\int_0^1 \boldsymbol{f}((1-\xi)\boldsymbol{y}_n + \xi \boldsymbol{y}_{n+1})\, d\xi.$$

Suppose $\boldsymbol{f}(\boldsymbol{y}) = \boldsymbol{S}\nabla H(\boldsymbol{y})$ with $\boldsymbol{S}$ a constant skew-symmetric matrix. The Hamitonian, H, is then conserved along both the exact and the discrete numerical solution [5]. Using position and momentum variables, $\boldsymbol{y} = [\boldsymbol{q}^T, \boldsymbol{p}^T]^T$, Hamilton's equations, equivalent to (2), has this form. Applying AVF to Hamilton's equations for (1) can be written as (6), with $f_1(\xi) = f_2(\xi) \equiv 1/2$.

Table 1. Functions defining the considered trigonometric integrators. Here $\text{sinc}(\xi) = \sin(\xi)/\xi$. Note that $\psi_0(\xi)$ and $\psi_1(\xi)$ are defined by the symmetry requirements $\psi(\xi) = \text{sinc}(\xi)\psi_1(\xi)$ and $\psi_0(\xi) = \cos(\xi)\psi(\xi)$

Name	$\psi(\xi)$	$\phi(\xi)$	$\psi_0(\xi)$	$\psi_1(\xi)$
(B)	$\text{sinc}(\xi)$	1	$\cos(\xi)\text{sinc}(\xi)$	1
(E)	$\text{sinc}^2(\xi)$	1	$\cos(\xi)\text{sinc}^2(\xi)$	$\text{sinc}(\xi)$

Trigonometric integrators

The highly oscillatory system of second order ODEs

$$\ddot{\boldsymbol{q}} + \boldsymbol{\Omega}^2 \boldsymbol{q} = \boldsymbol{g}(\boldsymbol{q}), \quad \text{with} \quad \boldsymbol{\Omega} = \begin{pmatrix} \boldsymbol{0} & \boldsymbol{0} \\ \boldsymbol{0} & \omega \boldsymbol{I} \end{pmatrix}, \quad \omega \gg 1, \tag{7}$$

matches the Euler Lagrange equations (2) for the system (1) in the particular case

$$\boldsymbol{g}(\boldsymbol{q}) = -\nabla U(\boldsymbol{q}), \quad W(\boldsymbol{q}) = \boldsymbol{q}^T \boldsymbol{\Omega}^2 \boldsymbol{q}, \quad \boldsymbol{M} = \boldsymbol{I}.$$

A trigonometric integrator for the system (7), has the one step form

$$\begin{aligned} \boldsymbol{q}_{n+1} &= \cos(h\boldsymbol{\Omega})\boldsymbol{q}_n + \boldsymbol{\Omega}^{-1}\sin(h\boldsymbol{\Omega})\dot{\boldsymbol{q}}_n + \frac{1}{2}h^2 \boldsymbol{\Psi}\boldsymbol{g}_n, \\ \dot{\boldsymbol{q}}_{n+1} &= -\boldsymbol{\Omega}\sin(h\boldsymbol{\Omega})\boldsymbol{q}_n + \cos(h\boldsymbol{\Omega})\dot{\boldsymbol{q}}_n + \frac{1}{2}h^2 \left(\boldsymbol{\Psi}_0 \boldsymbol{g}_n + \boldsymbol{\Psi}_1 \boldsymbol{g}_{n+1}\right), \end{aligned} \tag{8}$$

where $\boldsymbol{g}_n = g(\boldsymbol{\Phi}\boldsymbol{q}_n)$, $\boldsymbol{\Phi} = \phi(h\boldsymbol{\Omega})$, $\boldsymbol{\Psi} = \psi(h\boldsymbol{\Omega})$, $\boldsymbol{\Psi}_0 = \psi_0(h\boldsymbol{\Omega})$ and $\boldsymbol{\Psi}_1 = \psi_1(h\boldsymbol{\Omega})$. We consider two common such integrators, method (B) and (E) from [2]. The real valued and even functions, $\phi(\xi)$, $\psi(\xi)$, $\psi_0(\xi)$ and $\psi_1(\xi)$, that defines these integrators, are given in Table 1. The methods are symmetric by construction, and (B) is also symplectic.

It was shown in [4] that the variational IMEX method is a *modified trigonometric integrator*, i.e. it can be written on the form (8), but with a modified fast frequency $\tilde{\omega}$.

Numerical results

We compare the presented methods on the well known highly oscillatory Fermi-Pasta-Ulam (FPU) problem, as stated and analyzed in [2]. In suitable variables, the problem has Hamiltonian

$$\begin{aligned} H(\boldsymbol{x}, \boldsymbol{y}) = &\frac{1}{2}\sum_{i=1}^{m}(y_{0,i}^2 + y_{1,i}^2) + \frac{\omega^2}{2}\sum_{i=1}^{m} x_{1,i}^2 \\ &+ \frac{1}{4}((x_{0,1} - x_{1,1})^4 + \sum_{i=1}^{m-1}(x_{0,i+1} - x_{1,i+1} - x_{0,i} - x_{1,i})^4 + (x_{0,m} + x_{1,m})^4) \end{aligned} \tag{9}$$

All methods are second order accurate in position for small timesteps. However global error is a poor quantity to evaluate, since the system is chaotic. In Figure 1 the numerical trajectories for the oscillatory energies and Hamiltonian (total energy) are shown for this problem.

It is shown in [2] that trigonometric integrators struggle to capture all the dynamic properties of the FPU system. They also often suffer from artificial resonances. In method (E), the slow exchange of energy between the stiff springs happens too slow. Method (B) captures the correct exchange rate to leading order, see again [2]. However, unlike method (E), it suffers from wide resonance bands, making it unusable for a significant region of stepsizes. Both trigonometric integrators conserve H to leading order away from resonances.

The AVF method preserves H up to round off error by construction, but has problems capturing the correct energy exhange rate. The AL method fares slightly better than the AVF method with respect to the energy exhange rate, but we observe poor energy conservation for large stepsizes due to instability. The variational IMEX method resembles the reference solution. In [4] it is proved that for problems (7), this method has no artificial resonances, conserve H to second order, and captures the slow energy exchange to leading order.

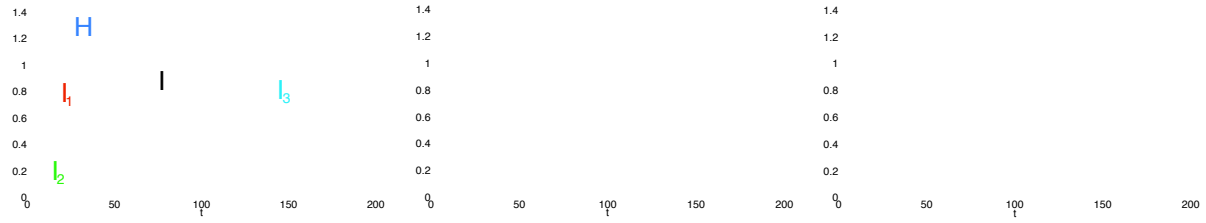

(a) Reference solution (b) Trigonometric integrator (B) (c) Trigonometric integrator (E)

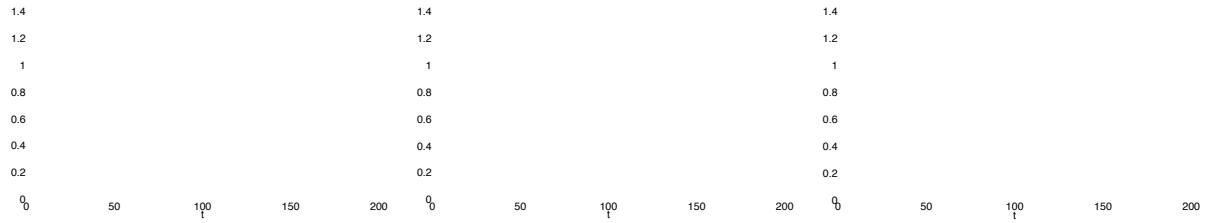

(d) Average Lagrangian (e) Average vector field (f) Variational IMEX

Figure 1. Comparison of methods on the highly oscillatory Fermi-Pasta-Ulam problem (9), with $m = 3$, $\omega = 50$ and $h = 0.03$. Initial conditions are as in [2]. For all methods we plot the evolution of the Hamiltonian H, the oscillatory energy of the individual stiff springs I_1, I_2 and I_3, and the total oscillatory energy $I = \sum_{j=1}^{N} I_j = I_0 + \mathcal{O}(\omega^{-1})$, which is an adiabatic invariant. The energy transfer between stiff springs occurs on the slow timescale $\mathcal{O}(\omega)$.

Conclusions

We have compared a selection of methods on a well known highly oscillatory test problem. The IMEX method appears to outperform the other methods for the FPU problem. It performs well with respect to the considered measures, and avoids the drawbacks of the other methods. The introduced Average Lagrangian method suffers from instability for this problem, when the stepsize becomes large with respect to the fast oscillations. However, preliminary experiments indicate that the AL and AVF methods may compare favourably to the IMEX method for certain highly oscillatory Lagrangian systems (1).

References

[1] A. Stern and E. Grinspun. Implicit-explicit variational integration of highly oscillatory problems. *Multiscale Model. Simul.*, 7(4):1779-1794, 2009.

[2] E. Hairer, C. Lubich and G. Wanner. *Geometric Numerical Integration.* Springer Berlin, Heidelberg, New York, second edition, 2006.

[3] J. E. Marsden and M. West. Discrete mechanics and variational integrators. *Acta Numerica* 10:357-514, 2001.

[4] R. I. McLachlan and A. Stern. Modified trigonometric integrators. *Preprint. arXiv:1305.3216 [math.NA]*, 2013.

[5] G. R. W. Quispel and D. I. McLaren A new class of energy-preserving numerical integration methods. *J. Phys. A: Math. Theor.* 41(4):045206, 2008.

Proceedings of the 26th Nordic Seminar on Computational Mechanics
A. Logg, K.A. Mardal, A. Massing (Eds.)

Some recent results on mixed formulations and shell models

Dominique Chapelle[1]

(1)Inria Saclay Ile-de-France, Palaiseau, France, dominique.chapelle@inria.fr

Summary. In this lecture, I will present some recent results obtained on two different – albeit related – topics of interest in this conference and special session. The first topic lies in the context of parameter-dependent mixed formulations as arises in structural mechanics, and concerns a sharp ellipticity condition for ensuring the convergence – together with the classical inf-sup condition – of the solution when the parameter considered tends to zero, such as in the asymptotic analysis of structural models when the parameter in question represents the thickness of the structure [4]. The second subject concerns the asymptotic analysis of so-called 3D-shell models, for which strong convergence results have been recently obtained [7], thereby improving on earlier results [5, 4], and further substantiating the 3D-shell concept which has already raised much interest in engineering applications due to its versatility and modeling accuracy.

Key words: Mixed formulations; shell modeling; 3D-shells; ellipticity condition; inf-sup condition

Ellipticity condition for parameter-dependent mixed formulations

This work – carried out in collaboration with K.J. Bathe – pertains to the analysis of parameter-dependent mixed formulations of the type
Find $(U^\varepsilon, \Sigma^\varepsilon)$ *in* $\mathcal{V} \times \mathcal{T}^+$ *such that*

$$\left\{ \begin{array}{l} A(U^\varepsilon, V) + B(V, \Sigma^\varepsilon) = F(V), \quad \forall V \in \mathcal{V} \\ B(U^\varepsilon, \Xi) - \varepsilon^2 D(\Sigma^\varepsilon, \Xi) = 0, \quad \forall \Xi \in \mathcal{T}^+ \end{array} \right. \tag{1}$$

where A, B and D denote bilinear forms defined on the Sobolev spaces $\mathcal{V}$ and $\mathcal{T}^+$ – with A and D symmetric – F is a linear form defined on $\mathcal{V}$, and ε represents a small dimensionless model parameter with

$$0 < \varepsilon \leq \varepsilon_{\max},$$

and e.g. related to the thickness of the structure in structural mechanics, or to the inverse of the bulk modulus in nearly-incompressible formulations.

Under certain assumptions to be specified, this sequence of solutions parametrized by ε can be shown to converge – when ε tends to zero – to the solution of the following limit mixed formulation
Find (U, Σ) *in* $\mathcal{V} \times \mathcal{T}$ *such that*

$$\left\{ \begin{array}{l} A(U, V) + B(V, \Sigma) = F(V), \quad \forall V \in \mathcal{V} \\ B(U, \Xi) = 0, \quad \forall \Xi \in \mathcal{T} \end{array} \right. \tag{2}$$

where $\mathcal{T}$ is another Sobolev space less regular than $\mathcal{T}^+$, with continuous and dense inclusion $\mathcal{T}^+ \subset \mathcal{T}$.

It was soon realized in the development of mixed formulations that the classical conditions ensuring the well-posedness of (2), namely, the inf-sup condition pertaining to B and the ellipticity of A on the subspace

$$\mathcal{V}_0 = \{V \in \mathcal{V} \mid B(V, \Xi) = 0, \quad \forall \Xi \in \mathcal{T}\},$$

see in particular [2], are not sufficient for guaranteeing convergence of $(U^\varepsilon, \Sigma^\varepsilon)$ to (U, Σ) when ε tends to zero, and similar difficulties hold for associated discrete mixed formulations. As a consequence, classical earlier such convergence results were established under stronger – or more restrictive – assumptions, such as that A be coercive over the whole space $\mathcal{V}$, or $\mathcal{T}^+ = \mathcal{T}$. For plate and shell models, however, such conditions do not hold.

I will thus present an alternative ellipticity condition which, together with the classical inf-sup condition, can be shown to provide a set of necessary and sufficient conditions for the desired convergence, with a natural counterpart in a discrete setting, see details in [3, 4]. As we will see, a possible technique of proof consists in using a stabilized mixed formulation as in [6].

Strong convergence of 3D-shell models

Most mathematical models and finite elements considered for shell structures are based on the Reissner-Mindlin kinematical assumption, namely, stating that any material line originally transverse to the shell mid-surface in the reference configuration remains "rigid" (i.e. straight and of preserved length) during the whole deformation process, see [1] and references therein. This leads to so-called "5-parameter models", in which the variational unknowns correspond to the 3D displacements of the mid-surface and the rotations of the transverse material lines, with some well-known technicalities to effectively parameterize the rotations, especially when finite transformations are considered. Furthermore, in these formulations another assumption must be used – sometimes implicitly – concerning the stress state, namely that through-the-thickness stresses vanish, which may be quite difficult to handle for nonlinear constitutive laws, and non-physical in many applications (one may think e.g. of metal forming), notwithstanding the well-known paradox of the conflicting assumption of vanishing through-the-thickness strain [4]. To circumvent these various limitations, higher-order kinematical assumptions can be used. More specifically, when considering quadratic variations of displacements across the thickness, we can obtain shell models of the utmost interest and that feature the following major advantages, in particular [5]:

- no stress assumption need – nor in fact should – be made, hence we can directly use general 3D constitutive laws;
- considering the same kinematical assumptions for all the displacement components has important practical consequences, since Cartesian coordinates can then be used for all nodal unknowns in the corresponding finite element procedures, and no rotation handling is needed any longer;
- of course, more accurate physical behaviors can be represented, in particular when large through-the-thickness deformations are concerned.

In the lecture, I will outline the derivation of 3D-shell formulations, and show how mathematical analysis can bring most valuable insight into the models and their physical behaviors. In particular, I will discuss how the first of the above highlights (i.e. no stress assumption) can be rigorously justified by a complete asymptotic analysis of the shell formulation, and this analysis also more generally substantiates the model validity for thin structures. Namely, by this asymptotic analysis we are able to establish that shell model solutions have the same limit behaviors as 3D elasticity solutions [8] when considering sequences of problems with decreasing

thickness parameters, for a fixed structure midsurface. This so-called *asymptotic consistency* holds throughout the tremendous diversity of behaviors that shell structures are able to undergo – depending on their geometries and boundary conditions, in particular – with the two main types of asymptotic behaviors given by membrane- and bending-dominated states [9, 4]. Moreover, this asymptotic analysis result has recently been enhanced by establishing complete *strong convergence* results [7].

References

[1] K.J. Bathe. *Finite Element Procedures*. Prentice Hall, Englewood Cliffs, 1996.

[2] F. Brezzi and M. Fortin. *Mixed and Hybrid Finite Element Methods*. Springer-Verlag, New York, 1991.

[3] D. Chapelle and K.J. Bathe. On the ellipticity condition for model-parameter dependent mixed formulations. *Computers & Structures*, 88:581–587, 2010.

[4] D. Chapelle and K.J. Bathe. *The Finite Element Analysis of Shells – Fundamentals*. Springer, second edition, 2011.

[5] D. Chapelle, A. Ferent, and K.J. Bathe. 3D-shell finite elements and their underlying model. *Math. Models Methods Appl. Sci.*, 14(1):105–142, 2004.

[6] D. Chapelle and R. Stenberg. Stabilized finite element formulations for shells in a bending dominated state. *SIAM J. Numer. Anal.*, 36(1):32–73, 1998.

[7] Dominique Chapelle and Annabelle Collin. Strong convergence results for the asymptotic behavior of the 3D-shell model. *Journal of Elasticity*, 2013.

[8] P.G. Ciarlet. *Mathematical Elasticity - Volume III: Theory of Shells*. North-Holland, Amsterdam, 2000.

[9] J. Pitkäranta, Y. Leino, O. Ovaskainen, and J. Piila. Shell deformation states and the finite element method: a benchmark study of cylindrical shells. *Comput. Methods Appl. Mech. Engrg.*, 128:81–121, 1995.

Proceedings of the 26th Nordic Seminar on Computational Mechanics
A. Logg, K.A. Mardal, A. Massing (Eds.)

On Hierarchical Error Estimators for Shell Problems

Harri Hakula and Tomi Tuominen

Aalto University, Department of Mathematics and System Analysis, FI–00076 Aalto, Finland, Harri.Hakula@aalto.fi, Tomi.A.Tuominen@aalto.fi

Summary. This article discusses the issues related to choosing an appropriate hierarchic error indicator for *hp*-FEM solution of shell problems. For problems subject to strong locking, it is advantageous to emphasize edge modes if the initial polynomial order is low. Overall the ideal situation is when the locking is detected a priori and the polynomial order has been set sufficiently high allowing the use of local indicators.

Key words: shells, *hp*-FEM, error estimation

Introduction

Shell structures and in particular thin shell structures remain the most challenging simple structures from the computational point of view. The basic source of numerical difficulties in shell problems is the small dimensionless parameter, the effective thickness of the shell that appears, e.g., in the energy formulation based on any classical dimension reduction model. The effective thickness of the shell is defined as $t = d/L$, where d is the actual thickness of the shell and L is the length scale one is trying to resolve, for instance, the diameter of the domain or the characteristic length in a boundary layer. Shell is considered (effectively) thin when $t \ll 1$. Shells exhibit a rich variety of boundary layers, including internal layers, each of which has its own characteristic length. Indeed, the solution of any linear shell problem can be viewed as a linear combination of characteristic features.

The geometry of the shell, kinematic constraints, and loading are all factors affecting the activation of characteristic features. Thus, the shells of revolution are an excellent subset of shell problems for mathematical study of thin shell problems since different types of Gaussian surfaces are easy to generate. Furthermore, through appropriate parameterization the computations can be carried out in exact geometry.

One of the challenges in shell problems is to avoid numerical locking. Here, we let the higher-order FEM alleviate the locking and accept that some thickness dependent error amplification or locking factor, $K(t) \geq 1$, is unavoidable. For *hp*-FEM solution one can derive a simple error formulation

$$\text{error} \sim K(t)(h/L)^p,$$

where h is the mesh spacing, and p is the degree of the elements. It is possible that $K(t)$ diverges as t tends to zero, with the worst case being for pure bending problems: $K(t) \sim 1/t$. Of course, for $K(t) \sim 1$ one can expect the *hp*-solution to be optimal in the sense of approximation theory. This simple error formula also suggest why higher-order methods are advantageous in shell problems: the mesh over-refinement in the "worst" case is $\sim (1/t)^{1/p}$, which for a fixed $t = 1/100$, say, indicates that for $p = 4$ the requirement is moderate in comparison to the case of $p = 1$. For a more detailed discussion on this and further references, see [1].

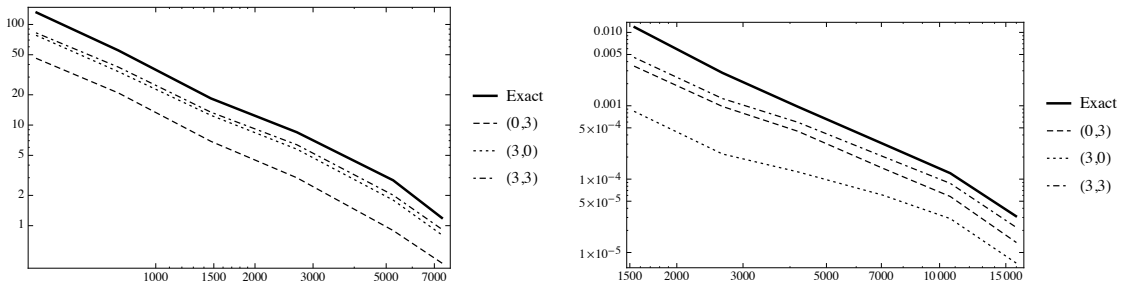

Figure 1. Free cylinder with $t = 1/100$: Comparison of error indicators through seven adaptive steps. Initial polynomial orders: (left: $p = 2$, right: $p = 4$). Notice the relative order of $(0, 3)$ and $(3, 0)$ in the two cases.

In this paper we study the performance of hierarchical error estimators in relation to shell problems. Since the basis functions of the standard *hp*-methods are hierarchic, the idea of using hierarchic enrichments of approximation spaces is natural [2]. However, the central question is how to choose the extra degrees of freedom in terms of polynomial orders. Here we use the notation (e, b) to indicate the choice of polynomial orders $p + e$ and $p + b$ for edges and bubbles, respectively, when p is the underlying polynomial order. Of course, any choice of type $(0, b)$ is of special interest, because in these cases the elemental indicators can be computed in parallel.

Our conclusion is that for problems subject to strong locking, it is advantageous to emphasize edge modes if the initial polynomial order is low. Overall the ideal situation is when the locking is detected a priori and the polynomial order has been set sufficiently high allowing the use of local indicators.

Hierarchic Error Estimation

Our test cases are cylindrical shells of the seminal study by Pitkäranta and co-workers [3]. The adaptive *hp*-algorithm is adapted from the one documented in our previous work [4]. All results are given in terms of squared energy. The two initial polynomial orders $p = 2$ and $p = 4$ are chosen to represent the scenarios where the locking is ignored and taken into account, respectively.

Here we present results of an ensamble study of twelve indicators, (e, b), $e = 0, \ldots, 3, b = 0, \ldots, 3$. The benchmark shell is the free Pitkäranta cylinder, which is known to exhibit the strongest locking. In Figure 1 the estimated errors for three representative indicators $(3, 0)$, $(0, 3)$, and $(3, 3)$ are shown over seven adaptive steps for two initial polynomial orders $p = 2$ and $p = 4$, with the same initial mesh. Notice, that the indicators are consistent, that is, the respective graphs never cross, but the relative order between $(3, 0)$ and $(0, 3)$ is changed. This is in line with our intuition, since for lower polynomial orders detecting the long scale responsible for the locking requires an indicator which spans the whole domain. In the case of initial $p = 4$, the local indicators such as $(0, 3)$ perform well, because the underlying solution has effectively captured the long scale.

The analysis above is supported by Figures 2 and 3, where it is clear that the adaptive algorithm has *h*-refined the mesh over the whole computational domain for initial $p = 2$, whereas for initial $p = 4$ the *h*-refinement is concentrated at the boundary layer. Notice, that in the eye-ball norm all indicators are performing satisfactorily in comparison with the exact energy error shown in the upper left hand corner.

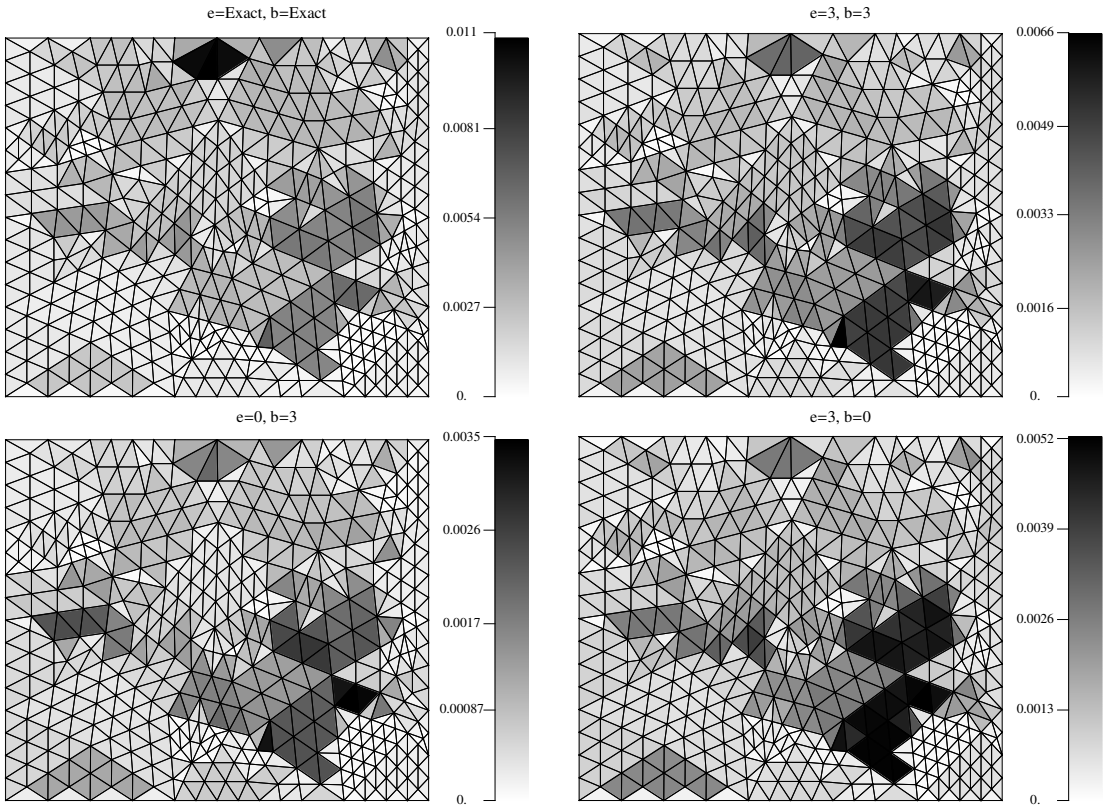

Figure 2. Free cylinder with $t = 1/100$: Error indicators after seven adaptive steps. Initial $p = 2$.

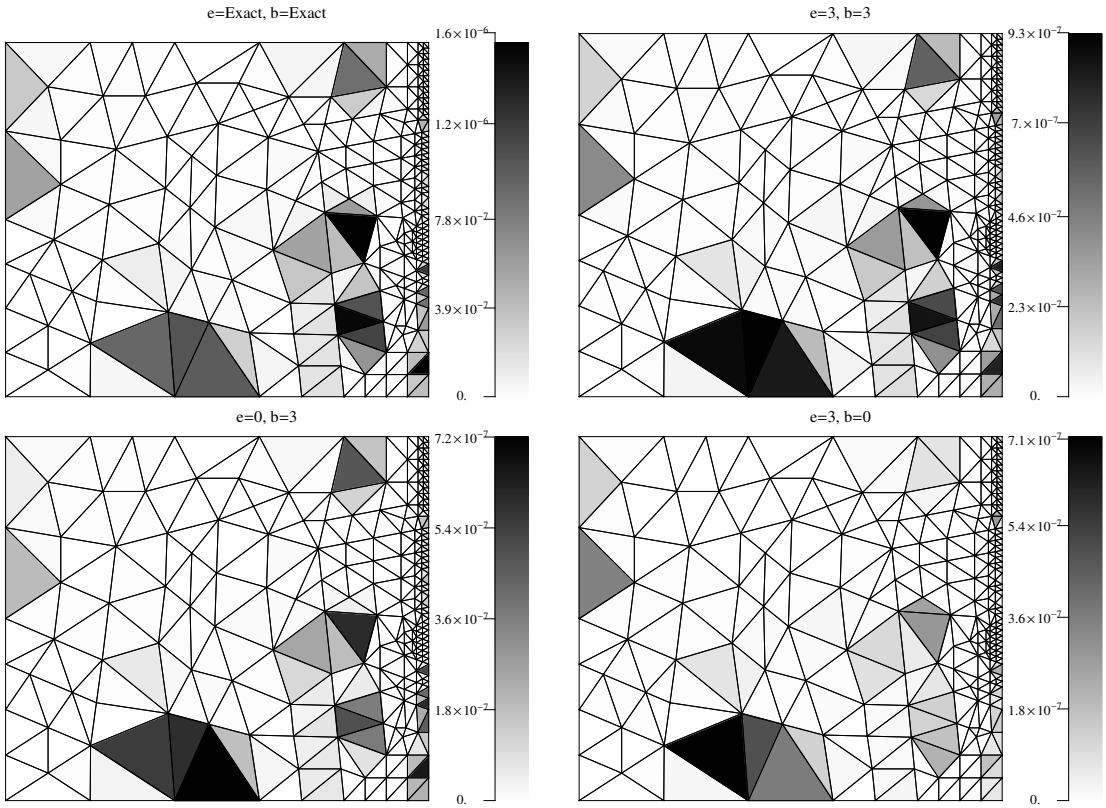

Figure 3. Free cylinder with $t = 1/100$: Error indicators after seven adaptive steps. Initial $p = 4$.

Conclusions and Future Work

The initial results are well aligned with our a priori expectations. In the case of strong locking and low polnomial order, the local enrichment in the form of $(0, b)$ does not perform well. One remedy for this situation is to probe for energy distribution with a minimal mesh and sufficiently high polynomial order, $p = 4$, say. If the problem turns out to be bending-dominated, it is beneficial to start with a higher initial polynomial order.

At the moment we do not have a clear picture of the cost/benefit ratio between different indicators when the whole adaptive algorithm is considered. Addressing this shortcoming is of high priority.

References

[1] H. Hakula, Y. Leino, and J. Pitkäranta, Scale resolution, locking, and high-order finite element modelling of shells, *Computer Methods in Applied Mechanics and Engineering*, 133:157–182:1996.

[2] B. Szabo and I. Babuška, *Finite Element Analysis*, Wiley, 1991.

[3] J. Pitkäranta, Y. Leino, O. Ovaskainen, and J. Piila, Shell Deformation states and the Finite Element Method: A Benchmark Study of Cylindrical Shells, *Computer Methods in Applied Mechanics and Engineering*, 128:81–121:1995.

[4] H. Hakula, and T. Tuominen, Mathematica Implementation of the High Order Finite Element Method Applied to Eigenproblems, *To appear in Computing*, 2013.

Proceedings of the 26th Nordic Seminar on Computational Mechanics
A. Logg, K.A. Mardal, A. Massing (Eds.)

Locking free parametric continuous/discontinuous FEM for the Mindlin–Reissner plate

Peter Hansbo[1] and Mats G. Larson[2]

(1)Department of Mechanical Engineering, Jönköping University, SE-551 11 Jönköping, Sweden, peter.hansbo@jth.hj.se
(2)Department of Mathematics and Mathematical Statistics, Umeå University, SE-901 87 Umeå, Sweden, mats.larson@math.umu.se

Summary. We develop a finite element method with continuous displacements and discontinuous rotations for the Mindlin-Reissner plate model on quadrilateral elements. To avoid shear locking, the rotations must have the same polynomial degree in the parametric reference plane as the parametric derivatives of the displacements, and obey the same transformation law to the physical plane as the gradient of displacements. We prove optimal convergence, uniformly in the plate thickness, and provide numerical results that confirm our estimates.

Key words: Mindlin-Reissner plate, finite element method, quadrilateral element, locking

Introduction

The Reissner-Mindlin equations is a model of the displacement of a moderately thick plate under transversal load. The unknows are the normal displacement field u and the rotation field $\boldsymbol{\theta}$ of a normal fiber. The difficulty with this model, from a numerical point of view, is the matching of the approximating spaces for $\boldsymbol{\theta}$ and u. As the thickness $t \to 0$, the difference $\nabla u - \boldsymbol{\theta}$ must tend to zero, which, for naive choices of spaces, leads to a deterioration of the approximation known as locking or in this case shear locking since the difficulty emanates from the term involving the shear energy. The situation is particularly difficult if we wish to use low order approximations.

Here, we propose to use finite element spaces that are rich enough to satisfy the shear constraint exactly while maintaining optimal approximation properties. This idea was first proposed by Hansbo and Larson [3], where continuous piecewise quadratics for the displacements and discontinuous piecewise linears for the rotations were used in a discontinuous Galerkin formulation. In this contribution we extend the method of [3] to quadrilateral elements. We show that, with the proper definition of the finite element space for the rotations, we can satisfy the equation $\nabla u - \boldsymbol{\theta} = 0$ exactly while maintaining optimal approximation properties and thus together with stability we obtain optimal a priori error estimates uniformly in the thickness parameter.

Using continuous tensor product quadratics for the displacements the suitable space for the rotations consists of discontinuous parametric vector polynomials that are also mapped in the same way as the gradient of elements. The mapping is the rotated, or covariant, Piola mapping that preserves tangent traces, and naturally appears in the context of curl conforming elements, see [2]. The interpolation error estimates on quadrilaterals are based on the observation that tensor product polynomials mapped with a bilinear map contain complete polynomials, cf. [1], and thus the estimates follows from the Bramble–Hilbert lemma and scaling.

The Reissner-Mindlin Plate Model

Energy Functional

Consider a plate with thickness t occupying a convex polygonal domain Ω in $\mathbb{R}^2$, which is clamped at the boundary $\partial\Omega$. Denoting by u the transverse displacement, $\boldsymbol{\theta}$ the rotation of the median surface, t the thickness, and $t^3\, g$ the transverse surface load, and defining the bending energy $a(\cdot,\cdot)$ by

$$a(\boldsymbol{\theta},\boldsymbol{\vartheta}) := \int_\Omega \boldsymbol{\sigma}(\boldsymbol{\theta}) : \boldsymbol{\varepsilon}(\boldsymbol{\vartheta})\, d\Omega \tag{1}$$

where $\boldsymbol{\varepsilon}$ is the curvature tensor $\varepsilon_{ij}(\boldsymbol{\theta}) = \frac{1}{2}(\frac{\partial\theta_i}{\partial x_j} + \frac{\partial\theta_j}{\partial x_i})$ and $\boldsymbol{\sigma}(\boldsymbol{\theta}) := 2\mu\boldsymbol{\varepsilon}(\boldsymbol{\theta}) + \lambda\nabla\cdot\boldsymbol{\theta}\,\mathbf{1}$ is the moment tensor, the transverse displacement and rotation vector are solutions to the following variational problem: find $(u,\boldsymbol{\theta}) \in H_0^1(\Omega)\times[H_0^1(\Omega)]^2$ such that

$$a(\boldsymbol{\theta},\boldsymbol{\vartheta}) + \frac{\kappa}{t^2}(\nabla u - \boldsymbol{\theta}, \nabla v - \boldsymbol{\vartheta}) = (g, v), \quad \forall (v,\boldsymbol{\vartheta}) \in H_0^1(\Omega)\times[H_0^1(\Omega)]^2 \tag{2}$$

where $(\cdot,\cdot)$ denotes the $L^2(\Omega)$ inner product, $H^k(\Omega)$ are the usual Sobolev spaces, and the functions in $H_0^1(\Omega)$ have zero trace on the boundary $\partial\Omega$. Finally, λ and μ are material parameters and k a shear correction factor.

The Finite Element Method

Let $\mathcal{K}^h = \{K\}$ be a family of quasiuniform partitions of Ω into convex quadrilaterals $K = \boldsymbol{F}_K(\widehat{K})$ with mesh parameter h.

In order to define our finite element spaces we define a continuous parametric finite element space V_{D}^h for the displacement u and determine a space $\boldsymbol{V}_{\mathrm{R}}^h$ of discontinuous piecewise parametric functions for the rotations $\boldsymbol{\theta}$ such that

$$\nabla V_{\mathrm{D}}^h \subseteq \boldsymbol{V}_{\mathrm{R}}^h \tag{3}$$

in order to be able to satisfy the equation $\boldsymbol{\theta} - \nabla u = 0$ exactly, when the thickness tends to zero.

Thus, let $\widehat{K}$ be the reference unit square and $Q_{k,l}(\widehat{K})$ the space of tensor product polynomials of order k and l in each variable, more precisely

$$Q_{k,l}(\widehat{K}) = \mathrm{span}\{\widehat{x}^\alpha\widehat{y}^\beta \ :\ 0\le\alpha\le k, 0\le\beta\le l\} \tag{4}$$

and $Q_k(\widehat{K}) = Q_{k,k}(\widehat{K})$. For each $K\in\mathcal{K}^h$ let $\boldsymbol{F}_K : \widehat{K}\to\mathbf{R}^2$ be the bilinear, i.e., $\boldsymbol{F}_K \in [Q_1(\widehat{K})]^2$, mapping such that $K = \boldsymbol{F}_K(\widehat{K})$. We define the space of parametric tensor product polynomials on K by

$$V_{\mathrm{D},K} = \{p : K\to\mathbf{R} \ :\ p = \widehat{p}\circ\boldsymbol{F}_K^{-1}\} \tag{5}$$

and the corresponding space on $\mathcal{K}^h$ of continuous piecewise parametric tensor product polynomials

$$V_{\mathrm{D}}^h = \{v : \Omega\to\boldsymbol{R} : v|_K \in V_{\mathrm{D},K}\ \forall K\in\mathcal{K}^h, v\in C(\Omega)\} \tag{6}$$

Turning to the space for the rotations we recall that, since $p = \widehat{p}\circ\boldsymbol{F}_K^{-1}$, we have

$$\nabla p(x) = DF_K^{-\mathrm{T}}\widehat{\nabla}\widehat{p}(\widehat{x}) = DF_K^{-\mathrm{T}}\widehat{\nabla}\widehat{p}(\boldsymbol{F}_K^{-1}(x)) \tag{7}$$

where $\widehat{\nabla}$ is the gradient in the reference coordinates. Introducing the rotated or covariant Piola mapping

$$\boldsymbol{R}_K : \widehat{\boldsymbol{V}}_{\mathrm{R}} \ni \widehat{\boldsymbol{\theta}} \mapsto D\boldsymbol{F}_K^{-\mathrm{T}}\widehat{\boldsymbol{\theta}}\circ\boldsymbol{F}_K^{-1} \in \boldsymbol{V}_{\mathrm{R}} \tag{8}$$

we have $\nabla p(x) = DF_K^{-\mathrm{T}}\widehat{\nabla}\widehat{p}(\widehat{x}) = \boldsymbol{R}_K\widehat{\nabla}\widehat{p}(\widehat{x})$. We are thus led to defining the following space for the rotations

$$\boldsymbol{V}_{\mathrm{R},K} = \boldsymbol{R}_K\widehat{\boldsymbol{V}}_{\mathrm{R}} \tag{9}$$

where $\widehat{\boldsymbol{V}}_{\mathrm{R}}$ is a space on the reference unit square $\widehat{K}$ that satisfies

$$\widehat{\nabla}\widehat{V}_{\mathrm{D},K} = Q_{1,2}(\widehat{K}) \times Q_{2,1}(\widehat{K}) \subseteq \widehat{\boldsymbol{V}}_{\mathrm{R},K} \tag{10}$$

We finally define the space of discontinuous mapped parametric functions

$$\boldsymbol{V}_{\mathrm{R}}^h = \{\boldsymbol{\theta} : \Omega \to \boldsymbol{R}^2 : \boldsymbol{v}|_K \in \boldsymbol{V}_{\mathrm{R},K}\ \forall K \in \mathcal{K}^h\} \tag{11}$$

Let $\mathcal{E}^h = \{E\}$ be the set of edges in the mesh $\mathcal{K}^h$. We split $\mathcal{E}^h$ into two disjoint subsets

$$\mathcal{E}^h = \mathcal{E}_I^h \cup \mathcal{E}_B^h \tag{12}$$

where $\mathcal{E}_I^h$ is the set of edges in the interior of Ω and $\mathcal{E}_B^h$ is the set of edges on the boundary $\partial\Omega$. Further, with each edge we associate a fixed unit normal $\boldsymbol{n}$ such that for edges on the boundary $\boldsymbol{n}$ is the exterior unit normal. We denote the jump of a function $\boldsymbol{v} \in \boldsymbol{V}_{\mathrm{R}}^h$ at an edge E by $[\boldsymbol{v}] = \boldsymbol{v}^+ - \boldsymbol{v}^-$ for $E \in \mathcal{E}_I^h$ and $[\boldsymbol{v}] = \boldsymbol{v}^+$ for $E \in \mathcal{E}_B^h$, and the average $\langle \boldsymbol{v} \rangle = (\boldsymbol{v}^+ + \boldsymbol{v}^-)/2$ for $E \in \mathcal{E}_I^h$ and $\langle \boldsymbol{v} \rangle = \boldsymbol{v}^+$ for $E \in \mathcal{E}_B^h$, where $\boldsymbol{v}^{\pm}(\boldsymbol{x}) = \lim_{\epsilon \downarrow 0} \boldsymbol{v}(\boldsymbol{x} \mp \epsilon\, \boldsymbol{n})$ with $\boldsymbol{x} \in E$.

The method takes the form: find $(u^h, \boldsymbol{\theta}^h) \in V_{\mathrm{D}}^h \times \boldsymbol{V}_{\mathrm{R}}^h$ such that

$$a_h(\boldsymbol{\theta}^h, \boldsymbol{\vartheta}) + \frac{\kappa}{t^2}\left(\nabla u^h - \boldsymbol{\theta}^h, \nabla v - \boldsymbol{\vartheta}\right) = (g, v) \quad \forall (v, \boldsymbol{\vartheta}) \in V_{\mathrm{D}}^h \times \boldsymbol{V}_{\mathrm{R}}^h \tag{13}$$

Here the bilinear form $a_h(\cdot,\cdot)$ is defined by

$$\begin{aligned} a_h(\boldsymbol{\theta}^h, \boldsymbol{\vartheta}) \;=\; & \sum_{K \in \mathcal{K}^h} (\boldsymbol{\sigma}(\boldsymbol{\theta}^h), \boldsymbol{\varepsilon}(\boldsymbol{\vartheta}))_K \\ & - \sum_{E \in \mathcal{E}_I^h \cup \mathcal{E}_B^h} (\langle \boldsymbol{n} \cdot \boldsymbol{\sigma}(\boldsymbol{\theta}^h) \rangle, [\boldsymbol{\vartheta}])_E + (\langle \boldsymbol{n} \cdot \boldsymbol{\sigma}(\boldsymbol{\vartheta}) \rangle, [\boldsymbol{\theta}^h])_E \\ & + (\mu + \lambda)\, \gamma \sum_{E \in \mathcal{E}_I^h \cup \mathcal{E}_B^h} (h_E^{-1} [\boldsymbol{\theta}^h], [\boldsymbol{\vartheta}])_E \end{aligned}$$

where γ is a positive constant, h_E is defined by

$$h_E = \left(|T^+| + |T^-|\right)/(2\,|E|) \quad \text{for } E = \partial T^+ \cap \partial T^- \tag{14}$$

with $|K|$ the area of K, on each edge, and $(\cdot,\cdot)_\omega$ is the $L^2(\omega)$ inner product with $\omega = K, E$.

Numerical Example

We consider the exact solution to a clamped Reissner–Mindlin plate on the unit square given by $u = u_0 + u_r$, where

$$u_0 = \frac{1}{3} x^3 (x-1)^3 y^3 (y-1)^3$$

corresponds to the Kirchhoff solution as $t \to 0$, and

$$u_r = \frac{2t^2}{5(1-\nu)} (y^3(y-1)^3 x(x-1)(5x^2 - 5x + 1) + x^3(x-1)^3 y(y-1)(5y^2 - 5y + 1)),$$

and rotations

$$\theta_x = (y^3(y-1)^3 x^2 (x-1)^2 (2x-1)), \quad \theta_y = (x^3(x-1)^3 y^2 (y-1)^2 (2y-1)).$$

We let $E = 180$ GPa and $\nu = 0.3$ and do a study of convergence on a sequence of self-similar trapezoids (following [1]), as indicated in Fig. 1 (left). We consider a continuous

Q_2–approximation of the displacements, and the rotations in a reference coordinate system, using the covariant map, are

$$\widehat{\theta}_{\widehat{x}}^h \in \text{span}\{1, \widehat{x}, \widehat{y}, \widehat{x}\widehat{y}, \widehat{y}^2, \widehat{x}\widehat{y}^2\}, \quad \widehat{\theta}_{\widehat{y}}^h \in \text{span}\{1, \widehat{x}, \widehat{y}, \widehat{x}\widehat{y}, \widehat{x}^2, \widehat{y}\widehat{x}^2\}.$$

For a standard bilinear map the components of $\widehat{\boldsymbol{\theta}}$ are instead given in physical coordinates. In our implementation, we have used the same approximating polynomials; thus, for the bilinear map

$$\widehat{\theta}_x^h \in \text{span}\{1, \widehat{x}, \widehat{y}, \widehat{x}\widehat{y}, \widehat{y}^2, \widehat{x}\widehat{y}^2\}, \quad \widehat{\theta}_y^h \in \text{span}\{1, \widehat{x}, \widehat{y}, \widehat{x}\widehat{y}, \widehat{x}^2, \widehat{y}\widehat{x}^2\}.$$

The convergence is given for $\|u - u^h\|_{L_2(\Omega)}$. As t becomes smaller, the bilinear map eventually suffers from locking, as illustrated in Fig. 1 (right) in the case $t = 10^{-4}$. The covariant map is unaffected by the size of t. Note the spurious increase in convergence of the unmapped solution which is due to alleviation of locking as the mesh size decreases.

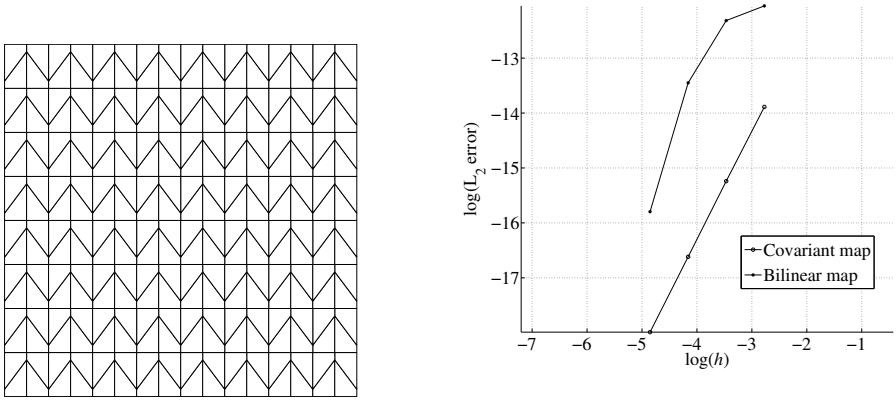

Figure 1. First computational mesh and in a sequence and L_2-convergence for the different maps.

Concluding Remarks

From the numerical example it is clear that the use of a standard bilinear map for the rotations leads to locking on insufficiently fine meshes, where the required fineness is connected to the thickness of the plate. In contrast, the rotated Piola map leads to optimal convergence and is free from locking on coarse meshes.

References

[1] D. N. Arnold, D. Boffi, and R. S. Falk. Approximation by quadrilateral finite elements. *Math. Comp.*, 71(239):909–922, 2002.

[2] R. S. Falk, P. Gatto, and P. Monk. Hexahedral $H(\text{div})$ and $H(\text{curl})$ finite elements. *ESAIM Math. Model. Numer. Anal.*, 45(1):115–143, 2011.

[3] P. Hansbo and M. G. Larson. A P^2-continuous, P^1-discontinuous finite element method for the Mindlin-Reissner plate model. In *Numerical mathematics and advanced applications*, pages 765–774. Springer Italia, Milan, 2003.

Proceedings of the 26th Nordic Seminar on Computational Mechanics
A. Logg, K.A. Mardal, A. Massing (Eds.)

Mesh dependent norm analysis of a simple rectangular elasticity element with weakly symmetric stress

Mika Juntunen and Jeonghun Lee

Aalto University School of Science
Department of Mathematics and Systems Analysis
P.O. Box 11100, FI-00076 Aalto, Finland
mika.juntunen@aalto.fi, jeonghun.lee@aalto.fi

Summary. We show a mesh-dependent norm analysis of mixed finite elements for the linear elasticity with weakly symmetric stress. Based on this analysis, we construct a three dimensional rectangular element with minimal number of degrees of freedom that has the optimal order of convergence for all unknowns.

Key words: linear elasticity, weak symmetry, finite element method, FEM, rectangular element, error analysis

Introduction

We construct a simple three dimensional rectangular element, analogous to the simplified 2D element in [1], that has 36 stress, 3 displacement and 3 rotation DOFs on each cube. For the stability analysis we use the mesh-dependent norm idea of [3] and [4] combined with the discrete Korn's inequalities shown in [2]. The stability analysis shows that the stress space must contain the trace of rigid body motions at element interfaces. This information provided by the mesh-dependent norm analysis is the key for defining the stress space with minimal number of degrees of freedom.

Consider the problem

$$\hat{A}\sigma = \epsilon(u), \quad -\operatorname{div}\sigma = f \quad \text{in } \Omega, \quad \text{and} \quad u = 0 \quad \text{on } \partial\Omega.$$

Here $\Omega \subset \mathbb{R}^3$ is a bounded domain with polygonal boundary and $\hat{A}$ is a bounded positive definite stiffness tensor with the standard symmetry. Extend $\hat{A}$ as identity for skew-symmetric matrices and denote this tensor as A. The associated weak problem is: Find $(\sigma, u, \gamma) \in H(\operatorname{div}, \Omega; \mathbb{R}^{3\times3}) \times L^2(\Omega; \mathbb{R}^3) \times L^2(\Omega; \mathbb{R}^{3\times3}_{\text{skw}})$ such that

$$\mathcal{A}(\sigma, \tau) + \mathcal{B}(u, \gamma; \tau) = 0, \qquad \tau \in H(\operatorname{div}, \Omega; \mathbb{R}^{3\times3}), \tag{1}$$

$$-\mathcal{B}(v, \eta; \sigma) = (f, v), \qquad (v, \eta) \in L^2(\Omega; \mathbb{R}^3) \times L^2(\Omega; \mathbb{R}^{3\times3}_{\text{skw}}), \tag{2}$$

where

$$\mathcal{A}(\psi, \tau) := (A\psi, \tau) \quad \text{and} \quad \mathcal{B}(v, \eta; \tau) := (v, \operatorname{div}\tau) + (\eta, \tau). \tag{3}$$

Here $(\cdot, \cdot)$ denotes the L^2 inner product over Ω.

Formal definition of the finite element spaces

Let $\mathcal{T}_h$ denote the rectangular mesh on Ω and K an element in $\mathcal{T}_h$. By $\mathcal{P}_k(G;\mathbb{X})$ for $G \subset \Omega$, we denote $\mathbb{X}$–valued polynomials of degree $\leqslant k$ on G. On a face F of K, we use $RM(F) \subset \mathcal{P}_1(F;\mathbb{R}^3)$ to denote the trace space of rigid body motions of K on F and use

$$\widetilde{RM}(F) := \{\xi \in RM(F) \mid (\xi, q)_F = 0,\ q \in \mathcal{P}_0(F;\mathbb{R}^3)\}$$

to denote the subspace of $RM(F)$ which is orthogonal to $\mathcal{P}_0(F;\mathbb{R}^3)$. In addition, we define

$$\widetilde{RM}_h(\partial K) := \{\xi : \partial K \mapsto \mathbb{R}^3) \mid \xi|_F \in \widetilde{RM}(F;\mathbb{R}^3) \text{ for a face } F \text{ of } K\}.$$

The finite element spaces are

$$\Sigma_h = \{\tau \in H(\operatorname{div}, \Omega;\mathbb{R}^{3\times 3}) \mid \tau|_K \in \Sigma_K,\ K \in \mathcal{T}_h\}, \tag{4}$$

$$U_h = \{v \in L^2(\Omega;\mathbb{R}^3) \mid v|_K \in \mathcal{P}_0(K;\mathbb{R}^3),\ K \in \mathcal{T}_h\}, \tag{5}$$

$$\Gamma_h = \{\eta \in L^2(\Omega;\mathbb{R}^{3\times 3}_{\mathrm{skw}}) \mid \eta|_K \in \mathcal{P}_0(K;\mathbb{R}^{3\times 3}_{\mathrm{skw}}),\ K \in \mathcal{T}_h\}. \tag{6}$$

Let $RT_0(K)$ be the space of lowest order rectangular Raviart–Thomas shape functions on K and define

$$\Sigma_K = \mathcal{RT}_0(K) + B(K) \quad \text{where} \quad \mathcal{RT}_0(K) := \begin{pmatrix} RT_0(K) \\ RT_0(K) \\ RT_0(K) \end{pmatrix} \subset \mathcal{P}_1(K;\mathbb{R}^{3\times 3}). \tag{7}$$

The $B(K)$ denotes the additional shape functions that fulfill the following Lemma 1.

Lemma 1. *Let $K \in \mathcal{T}_h$ and ν be the unit outward normal vector field on ∂K. There exists a vector space $B(K) \subset \mathcal{P}_2(K;\mathbb{R}^{3\times 3})$ such that*

$$\operatorname{div} B(K) = 0, \tag{8}$$

$$\{\tau\nu|_{\partial K} \mid \tau \in B(K)\} = \widetilde{RM}_h(\partial K), \tag{9}$$

and the map $\tau \mapsto \tau\nu|_{\partial K}$ from $B(K)$ to $\widetilde{RM}_h(\partial K)$ is bijective, which implies $\dim B(K) = 18$.

The degrees of freedom of $\tau \in \Sigma_K$ are

$$\tau \mapsto \int_F \tau\nu \cdot q\, ds, \quad q \in \mathcal{P}_0(F;\mathbb{R}^3), \qquad (6 \times 3 = 18 \text{ DOFs}) \tag{10}$$

$$\tau \mapsto \int_F \tau\nu \cdot q\, ds, \quad q \in \widetilde{RM}(F), \qquad (6 \times 3 = 18 \text{ DOFs}) \tag{11}$$

for a face F of K and the unit outward normal vector ν on F.

The practical implementation of $B(K)$ is omitted here but there are natural shape functions for each face that fulfill Lemma 1 and are associated to the degrees freedom (11).

Mesh dependent norms and stability

Let $\mathcal{RM}(K)$ denote the space of rigid body motions on $K \in \mathcal{T}_h$ and define

$$\mathcal{RM}_h = \{v \in L^2(\Omega;\mathbb{R}^3) \mid v|_K \in \mathcal{RM}(K),\ K \in \mathcal{T}_h\}.$$

For $\eta \in \Gamma_h$, $\eta|_K$ is a constant skew-symmetric matrix on every $K \in \mathcal{T}_h$, so we can find a unique $r_\eta \in \mathcal{RM}_h$ such that

$$\operatorname{grad}_h r_\eta = \eta, \tag{12}$$

$$\int_K r_\eta\, dx = 0, \quad K \in \mathcal{T}_h, \tag{13}$$

where grad_h denotes the element-wise gradient.

Let $\mathcal{F}^\circ$ be the set of faces of $\mathcal{T}_h$ in the interior of Ω, $\mathcal{F}^\partial$ be the set of faces on $\partial\Omega$, and denote by $\mathcal{F} = \mathcal{F}^\circ \cup \mathcal{F}^\partial$ the set of all faces. For a piecewise polynomial g, we define

$$[\![g]\!] = \begin{cases} \text{the jump of } g \text{ over } F, & \text{if } F \in \mathcal{F}^\circ, \\ g, & \text{if } F \in \mathcal{F}^\partial. \end{cases} \tag{14}$$

The mesh-dependent norms, analogous to [3], are

$$\|\tau\|_{0,h}^2 = \sum_{F\in\mathcal{F}} h_F \|\tau\nu_F\|_F^2, \tag{15}$$

$$\|(v,\eta)\|_h^2 = \sum_{F\in\mathcal{F}} h_F^{-1} \|[\![v + r_\eta]\!]\|_F^2, \tag{16}$$

for $\tau \in \Sigma_h$ and $(v,\eta) \in U_h \times \Gamma_h$, where h_F denotes the size of face F and ν_F denotes a unit normal vector on F.

It is clear [3] that $\|\cdot\|_{0,h}$ is equivalent to the $L^2(\Omega)$ norm $\|\cdot\|_\Omega$ in Σ_h. To see that $\|(\cdot,\cdot)\|_h$ is a norm in the finite element spaces, we need the discrete Korn's inequality [2, estimate (1.22)].

Theorem 2 (Stability)**.** *$\mathcal{A}(\cdot,\cdot)$ is continuous on Σ_h and there exists $c > 0$ such that $\mathcal{A}(\tau,\tau) \geqslant c\|\tau\|_{0,h}^2$ for $\tau \in \Sigma_h$. $\mathcal{B}(\cdot,\cdot;\cdot)$ is continuous on $U_h \times \Gamma_h \times \Sigma_h$ and for any $0 \neq (v,\eta) \in U_h \times \Gamma_h$, one can find $\tau \in \Sigma_h$ satisfying*

$$\mathcal{B}(v,\eta;\tau) \geqslant \|(v,\eta)\|_h^2 \quad \textit{and} \quad \|\tau\|_{0,h} \leqslant \|(v,\eta)\|_h. \tag{17}$$

Proof. Clearly

$$\begin{aligned} |\mathcal{A}(\psi,\tau)| &= |(A\psi,\tau)| \leqslant c\|\psi\|\|\tau\| \leqslant c\|\psi\|_{0,h}\|\tau\|_{0,h}, \\ |\mathcal{A}(\tau,\tau)| &= |(A\tau,\tau)| \geqslant c\|\tau\|^2 \geqslant c\|\tau\|_{0,h}^2. \end{aligned}$$

Let $\tau \in \Sigma_h$, $v \in U_h$ and $\eta \in \Gamma_h$. Using the definition (3), property (12), and element-wise integration by parts, gives

$$\begin{aligned} \mathcal{B}(v,\eta;\tau) &= (\operatorname{div}\tau, v) + (\tau,\eta) = (\operatorname{div}\tau, v) + (\tau, \operatorname{grad}_h r_\eta) \\ &= \sum_{K\in\mathcal{T}_h} \left(\langle \tau\nu, v\rangle_{\partial K} - (\tau, \operatorname{grad}_h v)_K + \langle \tau\nu, r_\eta\rangle_{\partial K} + (\operatorname{div}\tau, r_\eta)_K \right). \end{aligned}$$

Since v is piecewise constant, $\operatorname{grad}_h v = 0$. By property (13) the last term also vanishes because $\operatorname{div}\tau$ is piecewise constant. Thus we get

$$\mathcal{B}(v,\eta;\tau) = \sum_{F\in\mathcal{F}} \langle \tau\nu, [\![v + r_\eta]\!]\rangle_F. \tag{18}$$

The $(\cdot,\cdot)_G$ denotes the L^2 inner product over $G \subset \Omega$ and $\langle\cdot,\cdot\rangle_{\partial G}$ denotes the L^2 inner product over ∂G. Suppose that $0 \neq (v,\eta) \in U_h \times \Gamma_h$ is given. Note that $[\![v + r_\eta]\!]|_F \in RM(F)$ because $v + r_\eta$ is a piecewise rigid body motion on each cube K and set

$$\tau\nu|_F = h_F^{-1} [\![v + r_\eta]\!]|_F, \quad \forall F \in \mathcal{F}. \tag{19}$$

Using the definition of norms (15)–(16) and the equality (18), we get

$$\begin{aligned} \|\tau\|_{0,h}^2 &= \sum_{F\in\mathcal{F}} h_F \|\tau\nu\|_F^2 = \sum_{F\in\mathcal{F}} h_F^{-1} \|[\![v + r_\eta]\!]\|_F^2 = \|(v,\eta)\|_h^2, \\ \mathcal{B}(v,\eta;\tau) &= \sum_{F\in\mathcal{F}} \langle \tau\nu, [\![v + r_\eta]\!]\rangle_F = \|(v,\eta)\|_h^2. \end{aligned}$$

□

Error analysis

Let $\Pi_h : H^1(\Omega;\mathbb{R}^{3\times 3}) \to \Sigma_h$ be the Raviart–Thomas interpolation operator defined by (10) and let $P_h : L^2(\Omega;\mathbb{R}^3) \to U_h$ and $Q_h : L^2(\Omega;\mathbb{R}^{3\times 3}_{\mathrm{skw}}) \to \Gamma_h$ denote the orthogonal L^2 projections. It holds that

$$\|\tau - \Pi_h\tau\| + \|v - P_h v\| + \|\eta - Q_h\eta\| \leqslant ch(\|\tau\|_1 + \|v\|_1 + \|\eta\|_1) \tag{20}$$

for $(\tau, v, \eta) \in H^1(\Omega;\mathbb{R}^{3\times 3}) \times H^1(\Omega;\mathbb{R}^3) \times H^1(\Omega;\mathbb{R}^{3\times 3}_{\mathrm{skw}})$.

Theorem 3. *Suppose (σ, u, γ) is the exact solution of (1)–(2) and $(\sigma_h, u_h, \gamma_h)$ is the corresponding finite element solution. Then there exists $c > 0$ independent of mesh sizes such that*

$$\|\Pi_h\sigma - \sigma_h\|_{0,h} + \|(P_h u - u_h, Q_h\gamma - \gamma_h)\|_h \leqslant ch(\|\sigma\|_1 + \|\gamma\|_1). \tag{21}$$

Theorem 4. *Suppose (σ, u, γ) is the exact solution of (1)–(2) and $(\sigma_h, u_h, \gamma_h)$ the corresponding finite element solution. Then the following error estimates hold:*

$$\|\sigma - \sigma_h\| + \|u - u_h\| + \|\gamma - \gamma_h\| \leqslant ch(\|\sigma\|_1 + \|\gamma\|_1). \tag{22}$$

Acknowledgment

The mesh-dependent norms were originally proposed by Prof. Rolf Stenberg in a private discussion and the authors would like to thank to him for his valuable help.

References

[1] G. Awanou, Rectangular mixed elements for elasticity with weakly imposed symmetry condition, *Adv. Comput. Math.* **38**:2 (2013) 351–367.

[2] S. C. Brenner, Korn's inequalities for piecewise H^1 vector fields, *Math. Comp.* **73**:247 (2004) 1067–1087.

[3] C. Lovadina and R. Stenberg, Energy norm a posteriori error estimates for mixed finite element methods, *Math. Comp.* **75**:256 (2006) 1659–1674.

[4] R. Stenberg, A family of mixed finite elements for the elasticity problem, *Numer. Math.* **53**:5 (1988) 513–538.

Proceedings of the 26th Nordic Seminar on Computational Mechanics
A. Logg, K.A. Mardal, A. Massing (Eds.)

Solving discrete multifield problems with the preconditioned GCR method in a subspace

Mika Malinen[1]

(1)CSC - IT Center for Science Ltd., P.O. Box 405, FI-02101 Espoo, Finland, mika.malinen@csc.fi

Summary. The development of solvers that enable the fully coupled iterative solution of linear algebraic equations arising from the discretization of multifield problems is a contemporary challenge in many fields of computational modelling. The classic block Gauss-Seidel iteration is still widely used in practice, since constructing the monolithic system matrix is not often seen to be a feasible approach. The block Gauss-Seidel scheme can nevertheless be adapted to be a preconditioner for the GCR method such that preconditioned iterations for the fully coupled system can be realized without assembling the monolithic system matrix in a literal manner and without a need to perform the full matrix-vector products corresponding to the monolithic discretization. We describe the key ideas which lead to such an implementation.

Key words: preconditioning, generalized conjugate residual method, subspace iteration, multiphysics

Introduction

By way of introduction, consider a generic two-field multiphysics problem, discretization and linearization (by a lagged value approximation of nonlinear terms, say) of which leads to solving a linear algebra problem

$$\begin{bmatrix} \mathbf{K} & \mathbf{D} \\ \mathbf{H} & \mathbf{A} \end{bmatrix} \begin{bmatrix} \mathbf{q} \\ \mathbf{v} \end{bmatrix} = \begin{bmatrix} \mathbf{f} \\ \mathbf{g} \end{bmatrix}, \tag{1}$$

where the vectors $\mathbf{q} \in \mathbf{E}^m$ and $\mathbf{v} \in \mathbf{E}^p$ describe the approximations of the unknown fields, with $\mathbf{E}^n$ the n-dimensional Euclidean space. Often sophisticated software for solving the constituent single-physics models associated with the coefficient matrices $\mathbf{K}$ and $\mathbf{A}$ may already be available, while software tools for constructing and handling the monolithic system (1) do not exist. Therefore, the coupling of the constituent models is customarily enabled by using segregated solution strategies where the solution is attempted by decoupling the equations and solving the resulting subproblems sequentially via an iteration. A common choice of this type is to apply the block Gauss-Seidel scheme.

Convergence problems may however limit the feasibility of the basic segregated solvers in cases where the physical coupling of the equations is strong. Robust solvers for the coupled problem (1) may in principle be devised by using the monolithic solution approach where all the discrete equations are assembled into the same system and then solved simultaneously by using the Krylov subspace methods such as the minimum residual methods GMRES or GCR. Despite this conceptual simplicity, a standard implementation of such strategy requires the ability to perform the matrix-vector product corresponding to the left-hand side of (1). This requires flexibility that may not be offered by the usual software, while enabling the functionality required would necessitate software modifications that may not be straightforward to implement. Due to these challenges and apparent constraints associated with reusing existing single-field solvers in the monolithic solution, the segregated solution strategies remain widely used in practical simulations.

Our aim here is to describe some ideas which enable applying a preconditioned version of the GCR method to the fully coupled problem (1) without assembling the monolithic system matrix in a literal manner and without a need to perform the full matrix-vector products corresponding to the monolithic discretization. We show that this is possible since in the case of the block Gauss-Seidel preconditioning the optimality criterion associated with the preconditioned GCR iteration can be expressed simply in terms of the matrix blocks $\mathbf{K}$ and $\mathbf{D}$. That is, the residuals generated in the iteration lie in an invariant subspace $\mathbf{V}$ of $\mathbf{E}^{m+p}$ which has the dimension m, provided that the residual corresponding to the initial guess also belongs to $\mathbf{V}$. It should be noted that related ideas have already been considered for example in [1, 2], but the use of the GCR method has not been considered in this context previously. We note that a relative merit of applying the GCR method in this connection is that the effect of the right-oriented preconditioning can be obtained without switching temporarily to a new variable vector. Thus, the fully coupled iteration for (1) can be implemented fairly easily when solvers for handling the discrete single-fields models in the primitive variables $\mathbf{q}$ and $\mathbf{v}$ are already available.

The optimality criterion and invariance

Let $(\mathbf{q}'_{k+1}, \mathbf{v}'_{k+1})$ denote the block Gauss-Seidel update which is obtained by using a previous estimate $\mathbf{v}_k$ of $\mathbf{v}$ as

$$\begin{aligned} \mathbf{K}\mathbf{q}'_{k+1} &= \mathbf{f} - \mathbf{D}\mathbf{v}_k, \\ \mathbf{A}\mathbf{v}'_{k+1} &= \mathbf{g} - \mathbf{H}\mathbf{q}'_{k+1}. \end{aligned} \tag{2}$$

The basic GCR method can easily be adapted such that the block Gauss-Seidel scheme (2) is utilized to generate search directions for the minimum residual iteration. Such preconditioned version of the GCR method thus produces a sequence of improving iterates such that the kth iterate lies in the space

$$\begin{bmatrix} \mathbf{q}_0 \\ \mathbf{v}_0 \end{bmatrix} + \mathcal{V}_k, \tag{3}$$

with

$$\mathcal{V}_k = \mathrm{span}\{ \begin{bmatrix} \mathbf{q}'_1 - \mathbf{q}_0 \\ \mathbf{v}'_1 - \mathbf{v}_0 \end{bmatrix}, \ldots, \begin{bmatrix} \mathbf{q}'_k - \mathbf{q}_{k-1} \\ \mathbf{v}'_k - \mathbf{v}_{k-1} \end{bmatrix} \}, \tag{4}$$

and makes the Euclidean norm of the corresponding residual minimal over all solution candidates from this space.

If we now define a subspace $\mathbf{V}$ of $\mathbf{E}^{m+p}$ as

$$\mathbf{V} = \{ \boldsymbol{\xi} \in \mathbf{E}^{m+p} \mid \boldsymbol{\xi} = \begin{bmatrix} \boldsymbol{\eta} \\ \mathbf{0} \end{bmatrix}, \ \boldsymbol{\eta} \in \mathbf{E}^m \ \}, \tag{5}$$

we find that the space $\mathbf{V}$ is invariant with respect to the preconditioned GCR method in the following sense.

Proposition. *Assume that the initial guess* $(\mathbf{q}_0, \mathbf{v}_0)$ *for solving (1) is chosen such that the associated residual belongs to* $\mathbf{V}$*, i.e. the system* $\mathbf{g} - \mathbf{H}\mathbf{q}_0 - \mathbf{A}\mathbf{v}_0 = \mathbf{0}$ *is satisfied. Then the residual associated with any solution candidate* $(\hat{\mathbf{q}}_k, \hat{\mathbf{v}}_k)$ *from (3) belongs to* $\mathbf{V}$*, i.e. all solution candidates satisfy*

$$\mathbf{g} - \mathbf{H}\hat{\mathbf{q}}_k - \mathbf{A}\hat{\mathbf{v}}_k = \mathbf{0} \tag{6}$$

for any $k \geq 1$*. In addition, the norm of the residual associated with the monolithic system (1) can be expressed as*

$$||\mathbf{f} - \mathbf{K}\hat{\mathbf{q}}_k - \mathbf{D}\hat{\mathbf{v}}_k||. \tag{7}$$

Although the standard implementation of the preconditioned GCR algorithm considered would depend on the ability to perform the matrix-vector product corresponding to the left side of (1), the above proposition implies that we can carry out the same iteration without implementing the full matrix-vector product. Indeed, by using the alternate (7) to express the optimality criterion associated with the method, the minimum residual iteration will basically depend only on routines for performing the matrix-vector products with the matrices $\mathbf{K}$ and $\mathbf{D}$. Therefore, the fully coupled solver can be implemented in such a way that it is essentially as modular as the basic block Gauss-Seidel method, supports independent discretizations in an analogous manner, and requires straightforward software modifications which can be localized into the independent single-field solvers.

Implementation aspects

In view of the proposition given in the preceding section, the optimality condition corresponding to the minimum residual GCR iteration based on the block Gauss-Seidel preconditioning is seen to reduce to finding iterates that satisfy the orthogonality condition

$$\langle \mathbf{f} - \mathbf{K}\mathbf{q}_k - \mathbf{D}\mathbf{v}_k, \mathbf{K}\mathbf{s}_q + \mathbf{D}\mathbf{s}_v \rangle = 0 \tag{8}$$

for all $(\mathbf{s}_q, \mathbf{s}_v) \in \mathcal{V}_k$. Here $\langle \cdot, \cdot \rangle$ denotes the Euclidean inner product, with $\| \cdot \|$ the corresponding norm. The equivalent orthogonality conditions and hence the same sequence of iterates as obtained with the standard implementation of the method can be achieved alternatively by simply implementing the modified Gram-Schmidt procedure that realizes the conditions (8). Importantly, this process requires only the matrix-vector products corresponding to the matrices $\mathbf{K}$ and $\mathbf{D}$ and hence enables the modular implementation with respect to the model corresponding to the matrix $\mathbf{A}$.

The GCR method generally requires that all basis vectors for spanning the search space and the associated residual space are saved. Significant savings in memory usage and also in computation may however be possible here, since in practice it suffices to save the entries which are relevant to computing the matrix-vector products in (8). Interesting scenarios arise especially when the size of $\mathbf{K}$ is considerably smaller than that of $\mathbf{A}$, or when the coupling matrix $\mathbf{D}$ is sparse such that $\mathbf{D}$ contains a large number of trivial rows (this happens, for example, when two PDE models are coupled via a surface coupling). In such cases the size of vectors that have to be saved in the computer memory may be reduced significantly. In addition, a rapid convergence of the iteration can then be expected, since the associated residuals lie in a subspace of small dimension.

To conclude, the block preconditioned GCR algorithm for solving the monolithic system (1) via the orthogonality requirement (8) to minimize the equivalent norm (7) can now be implemented as follows: Set $k = -1$ and let $\mathbf{v}_{-1}$ contain an approximation to $\mathbf{v}$. Then, perform the following steps:

1. Solve $\mathbf{q}'_{k+1}$ from the preconditioning system

$$\mathbf{K}\mathbf{q}'_{k+1} = \mathbf{f} - \mathbf{D}\mathbf{v}_k.$$

2. Solve $\mathbf{v}'_{k+1}$ from the preconditioning system

$$\mathbf{A}\mathbf{v}'_{k+1} = \mathbf{g} - \mathbf{H}\mathbf{q}'_{k+1}.$$

3. If $k = -1$, set $\mathbf{q}_0 = \mathbf{q}'_{k+1}$ and $\mathbf{v}_0 = \mathbf{v}'_{k+1}$, define the residual $\mathbf{r}_0 = \mathbf{f} - \mathbf{K}\mathbf{q}_0 - \mathbf{D}\mathbf{v}_0$, set $k = k + 1$ and go to Step 1. Otherwise compute the minimum residual update:

$$
\begin{aligned}
&\mathbf{s}_{k+1} = \begin{bmatrix} \mathbf{q}'_{k+1} - \mathbf{q}_k \\ \mathbf{v}'_{k+1} - \mathbf{v}_k \end{bmatrix} \\
&\mathbf{y}_{k+1} = \begin{bmatrix} \mathbf{K} & \mathbf{D} \end{bmatrix} \mathbf{s}_{k+1} \\
&\texttt{do } j = 1, k \\
&\quad \mathbf{y}_{k+1} = \mathbf{y}_{k+1} - \langle \mathbf{y}_{k+1}, \mathbf{y}_j \rangle \mathbf{y}_j \\
&\quad \mathbf{s}_{k+1} = \mathbf{s}_{k+1} - \langle \mathbf{y}_{k+1}, \mathbf{y}_j \rangle \mathbf{s}_j \\
&\texttt{end do} \\
&\mathbf{y}_{k+1} = \mathbf{y}_{k+1} / \|\mathbf{y}_{k+1}\| \\
&\mathbf{s}_{k+1} = \mathbf{s}_{k+1} / \|\mathbf{y}_{k+1}\| \\
&\mathbf{u}_{k+1} = \begin{bmatrix} \mathbf{q}_{k+1} \\ \mathbf{v}_{k+1} \end{bmatrix} = \begin{bmatrix} \mathbf{q}_k \\ \mathbf{v}_k \end{bmatrix} + \langle \mathbf{r}_k, \mathbf{y}_{k+1} \rangle \mathbf{s}_{k+1} \\
&\mathbf{r}_{k+1} = \mathbf{r}_k - \langle \mathbf{r}_k, \mathbf{y}_{k+1} \rangle \mathbf{y}_{k+1}
\end{aligned}
$$

4. If $\|\mathbf{r}_{k+1}\|/(\|\mathbf{K}\|\|\mathbf{u}_{k+1}\| + \|\mathbf{f}\|) < TOL$, where TOL is a given stopping tolerance, stop the iteration. Otherwise set $k = k + 1$ and go to Step 1.

It is noted that here the solver for the model associated with the coefficient matrix $\mathbf{A}$ may be utilized essentially in a black-box manner. In addition, the minimum residual iteration done in Step 3 can reuse the matrices which are assembled in Step 1 in order to solve the preconditioning problem.

Concluding remarks

The ideas which have been described here have many applications. We have applied the algorithm described in this paper to handle linear systems arising in acoustic fluid-structure interaction, approximation via domain decomposition and modelling dissipative wave propagation via the Navier–Stokes equations. These methods have been implemented into the finite element software Elmer [3], which is based on the use of modular design.

References

[1] Y. A. Kuznetsov. Matrix iterative methods in subspaces. In: *Proceedings of the International Congress of Mathematicians* (Warsaw, 1983), 1509–1521. North-Holland, Amsterdam, 1984.

[2] K. Ito and J. Toivanen. Preconditioned iterative methods on sparse subspaces. *Applied Mathematics Letters*, 19:1191–1197, 2006.

[3] Elmer finite element software homepage, http://www.csc.fi/elmer.

Proceedings of the 26th Nordic Seminar on Computational Mechanics
A. Logg, K.A. Mardal, A. Massing (Eds.)

Direct Fem-Simulation of turbulent bluff body flow

Johan Hoffman[1], Johan Jansson[1], Niclas Jansson[1], R. Vilela De Abreu[1], and Claes Johnson[1]

[(1)]Computer Science and Communication, KTH, SE-10044 Stockholm, Sweden, jhoffman@csc.kth.se, jjansson@csc.kth.se, njansson@csc.kth.se, rvda@kth.se, cgjoh@csc.kth.se

Summary. We simulate slightly viscous turbulent low Mach number 3d bluff body flow (including streamlined bodies) by computational solution of the incompressible Navier-Stokes equations with a slip boundary condition modeling observed small skin friction, by using a residual stabilized adaptive finite element method, referred to as Direct Fem-Simulation (DFS) since no turbulence model beyond automatic residual stabilization is used. We find by duality based a posteriori estimation that mean value quantities such as drag and lift are computable to accuracies comparable to experiments. As a key example, we show that the turbulent flow around a complete airplane is computable and inspecting solutions leads to a new theory of flight essentially different from the accepted theory by Kutta-Zhukovsky-Prandtl developed 100 years ago. We find that turbulent bluff body flow in general can be described as potential flow modified by rotational slip separation as a flow which is resolvable computationally using millions of mesh points, except in a far-field wake of little influence on lift and drag, and also is understandable through a mathematical stability analysis.

Key words: turbulence, bluff body, direct numerical simulation, aerodynamics

From Prandtl 1904 back to Euler 1757

Turbulent bluff body flow is considered as a main unsolved problem of classical mechanics beyond theoretical description and also beyond computational simulation, because of thin no-slip boundary layers dictated by Prandtl in 1904 [7] requiring impossible trillions of mesh points to be resolved. In recent work we have discovered that using a slip boundary condition as a model of the small skin friction of slightly viscous turbulent flow, allows predictive simulation of mean value quantities such as drag and lift of turbulent bluff body flow (including streamlined bodies), with instead millions of mesh points. Basic aspects of turbulent flow from an applications point of view thus show to be computable by stabilized finite element methods with automatic turbulence modeling from residual stabilization, referred to as Direct FEM-Simulation (DFS), which opens large areas for exploration.

As a key example, we show that the turbulent flow around a complete airplane is computable, in contradiction to state-of-the-art. From an idea that a computable phenomenon is also understandable mathematically, we are led to a new theory flight [2, 3] essentially different from the accepted theory by Kutta-Zhukovsky-Prandtl developed 100 years ago. With evidence from computation and basic stability analysis we have been led to the conclusion that turbulent bluff body flow, including the aerodynamics of flight, can be described mathematically as potential flow modified by a phenomenon of *rotational slip separation* as a both computable [4] and understandable flow, in accordance with Euler's original dream [1].

Neumann boundary conditions

The key to the break of the Prandtl spell, which has blocked development for 100 years, is the from a mathematical point of view obvious realization that the Navier-Stokes equations as an accurate model of fluid mechanics can be combined with either Dirichlet or Neumann

type boundary conditions or combinations thereof. For slighly viscous flow the skin friction is observed to be very small which allows accurate modeling by a slip boundary condition as a combined Dirichlet-Neumann condition. Using a slip condition eliminates no-slip boundary layers and thus circumvents the computational impossibility dictated by Prandtl and therefore opens to progress. Simulations show good agreement with observations for drag and lift (and more generally for pressure distributions), leading to the conclusion that Prandtl's conjecture of a main role of no-slip boundary layers is false.

Rotational Slip Separation

The key to understanding bluff body flow is its description as potential flow modified by rotational slip separation as a generic quasi-stable gross pattern flow resulting from a generic instablity of potential flow at separation [6]. The large eddy flow in the vicinity of the body thus shows to be resolvable computationally with millions of mesh points with quasi-stable features and total turbulent dissipation under mesh refinement. The turbulent dissipation occurs mainly in the far-field wake which increases in length under refinement, keeping total dissipation nearly constant, without changing the total pressure on the body. The flow field thus appears as a bride sweep which gets longer under refinement without changing drag or lift on the body.

References

[1] L. Euler, Principes generaux du mouvement des fluides, Memoires de l'academie des sciences de Berlin 11, 1757, pp. 274-315

[2] J. Hoffman, J. Janson and C. Johnson, New Theory of Flight, submitted to J. Math Fluid Mech.

[3] J. Hoffman and C. Johnson, Computational Turbulent Incompressible Flow, Springer 2008.

[4] N. Jansson, J. Hoffman, J. Jansson, Framework for Massively Parallel Adaptive Finite Element Computational Fluid Dynamics on Tetrahedral Meshes, SIAM J. Sci. Comput., Vol. 34(1), pp. C24-C41, 2012.

[5] J. Hoffman, J. Jansson and R. Vilela De Abreu, Adaptive modeling of turbulent flow with residual based turbulent kinetic energy dissipation, Computer Methods in Applied Mechanics and Engineering, Vol.200(37-40), pp.2758-2767, 2011.

[6] J. Hoffman and N. Jansson, A computational study of turbulent flow separation for a circular cylinder using skin friction boundary conditions, Quality in Large Eddy Simulation II, ERCOFTAC Series Vol.16, Springer, 2011.

[7] L. Prandtl, Motions of fluids with very little viscosity, NACA Technical Memorandum 452, 1904.

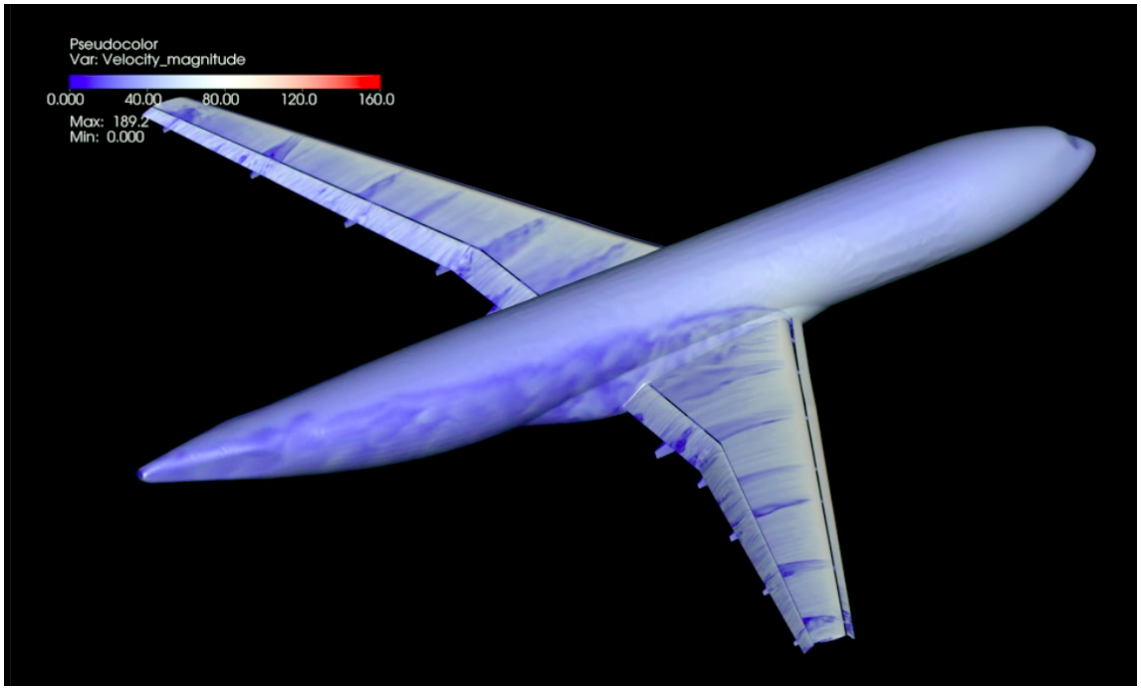

Figure 1. The velocity field of DFS with 3 million mesh points for an landing airplane at large angle of attack (20 degrees) and low subsonic speed.

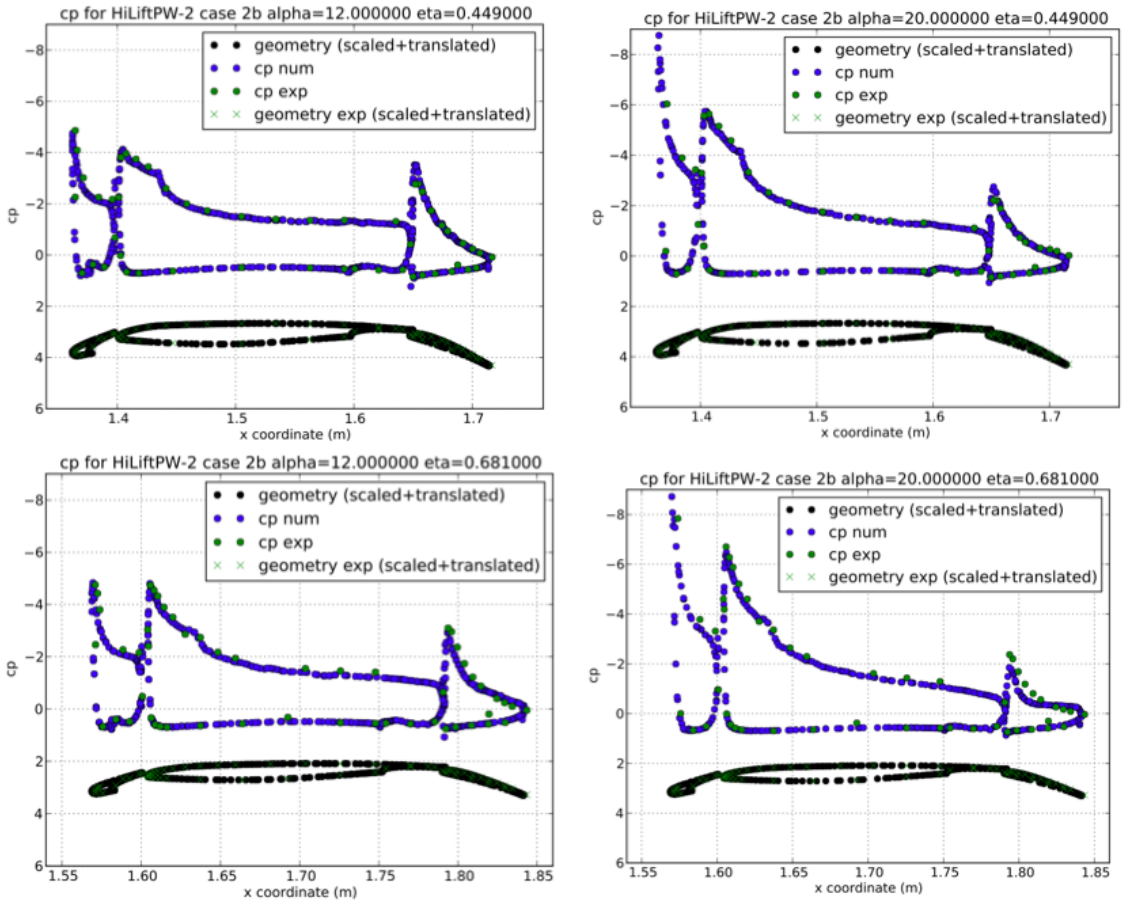

Figure 2. Comparison between simulation and experimental observation: pressure distribution around the above wing with flaps.

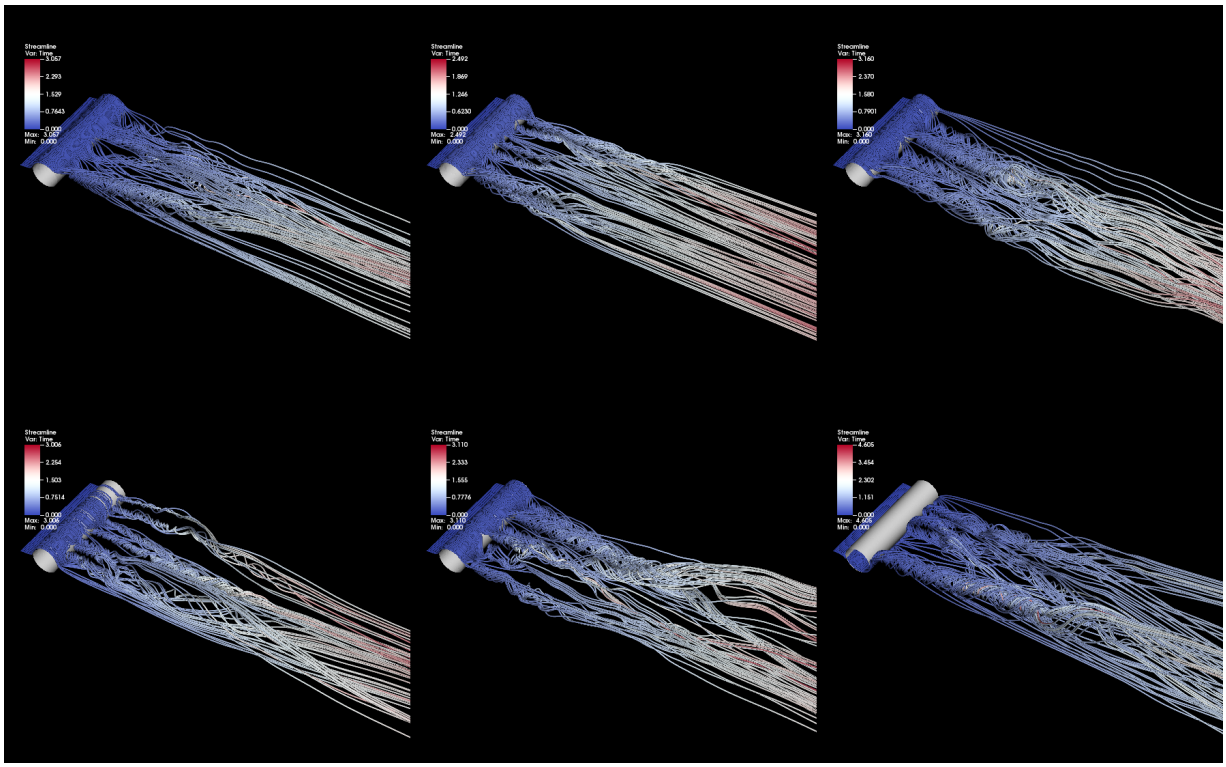

Figure 3. Quasi-stable rotational slip separation for slightly viscous incompressible flow around a circular cylinder with the length of the turbulent wake increasing under refinement keeping total dissipation constant.

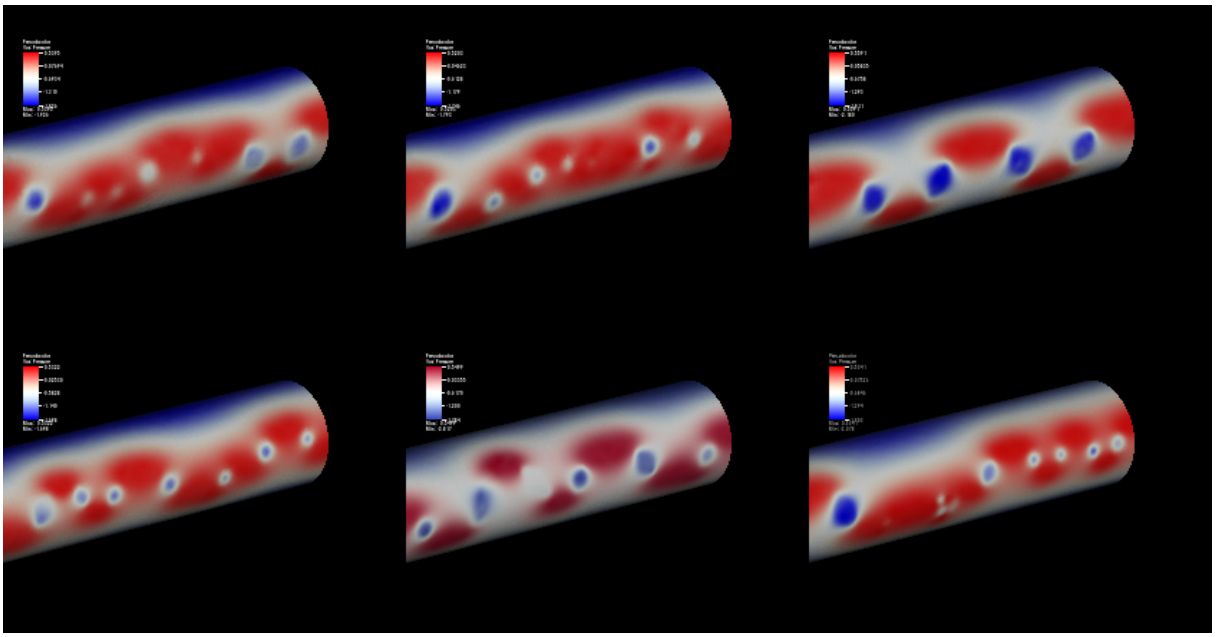

Figure 4. Corresponding surface pressure distribution showing stability of total pressure under mesh refinement.

Proceedings of the 26th Nordic Seminar on Computational Mechanics
A. Logg, K.A. Mardal, A. Massing (Eds.)

On capacity of grouted connections in wind turbine structures and jacket structures

Inge Lotsberg[1]

(1)Det Norske Veritas (DNV), Veritasveien 1, 1363 Høvik, Norway, Inge.Lotsberg@dnv.com

Summary. During the last years, offshore wind turbine structures were reported to settle on the monopile structure and the resulting force flow in the structures became different to that intended at the design stage. A joint industry project was therefore carried out by DNV to investigate the structural capacity of these connections from autumn 2009 to January 2011. It was found that the axial capacity of the grouted connections is a more sensitive function to the diameter and surface tolerances than that accounted for in existing design standards. Based on this experience a design procedure with conical shaped connections was developed. In January 2011 another joint industry project on capacity of cylindrical shaped grouted connections with shear keys was initiated. In this project analytical design equations were developed both for the Ultimate Limit State and the Fatigue Limit State. The recommended design methodology was supported by a number of laboratory tests. It was found that also the design documentation for grouted connections between piles and sleeves used in traditional jacket structures had to be improved. Some of the experience from these projects is presented in this paper.

Key words: Grouted connections, Piles, Wind turbines, Jackets, Failures

Introduction

During the last years, the offshore wind industry experienced that the design of the grouted connections between the transition piece and the monopile did not result in an acceptable safety level. A grouted connection is used to connect the transition piece to the monopile as indicated in Figure 1. A transition piece is installed on top of the monopile resting on temporary supports. The transition piece is then jacked up to the correct verticality before the grouting is carried out. After curing, the jacks are removed, leaving a gap between the temporary supports and the monopile. Most of the grouted connections between the transition piece and the monopile are grouted plain cylindrical connections made without using shear keys. Shear keys are normally used in grouted connections in jacket structures for transfer of load from the structure to the piles. By shear keys are understood use of circumferential weld beads around the piles and around the inside of the sleeves in the jacket structure such that sliding between steel and grout is restricted. The axial force due to the self-weight of the structure above the grouted connection in monopiles is in general relatively small. The moments have been assumed to be transferred mainly through contact forces (as force couples) and due to relevant friction between the steel and the grout surfaces [1]. The grouted connection is designed with a rather large diameter. Although the thicknesses of the transition piece and pile are large, the resulting diameter to thickness ratios is also large - and larger than those traditionally used in the design of jacket structures, where these connections have a long positive experience record.

The stresses in the monopile due to the bending moment from wind and wave loading can be more than one order of magnitude larger than those due to the axial load alone. Owing to the large diameter to thickness ratio, the grouted connections become rather flexible with respect to bending moment and a radial cracking of the grout may be expected. Some opening and sliding

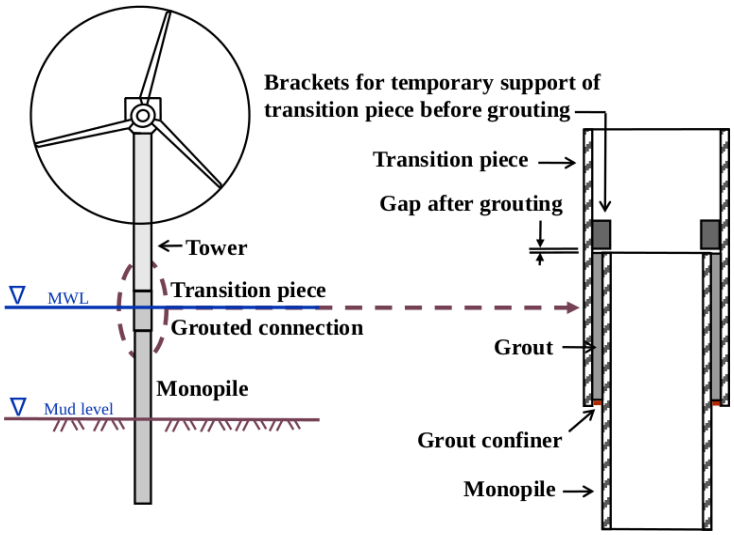

Figure 1. Principle of grouted connection in monopile structure.

between the steel and the grout may also be expected due to the flexibility of the connection when subjected to a large bending moment.

Joint industry projects on capacity of grouted connections in monopiles

During 2009 the axial capacity of large diameter plain grouted connections in monopile structures became questioned. Based on uncertainty related to capacity of these connections, a joint industry project was initiated regarding the capacity of large diameter grouted connections in offshore wind turbine structures (for plain connections without shear keys). This project was started in November 2009 and finished in January 2011. A design methodology based on grouted conical connections was established in this project [2, 3, 4]. This design methodology was included in the DNV standard in 2011 [1]. During early 2010 it was confirmed by inspection that a number of wind farms with plain grouted connections had settled such that the temporary supports were again resting on the top of the monopiles, ref. Figure 1, and the force flow through the structures was different from that assumed in design. The unintended force transfer through temporary supports has led to concern about fatigue cracking in these structures which has lead to costly repairs for the industry.

In January 2011 another joint industry project on capacity of cylindrical shaped grouted connections with shear keys was initiated. In this project analytical design equations were developed both for the Ultimate Limit State and the Fatigue Limit State for design of cylindrical shaped grouted connections with shear keys. Results from this project are presented in [5, 6]. The recommendations from this project are now being included in the DNV standard for wind turbine structures.

Testing of large diameter connections

Most of the laboratory fatigue tests on grouted connections with shear keys reported in the literature was performed with specimens with a diameter less than 400 mm. It has been questioned whether these specimens were representative for the structural behaviour of large diameter grouted monopile connections which are subjected to a static axial load and a significant dynamic bending moment. Therefore an effort was made to design test specimens with a representative radial stiffness similar to that of grouted connections of large diameter piles in the order of 5 meters or even larger.

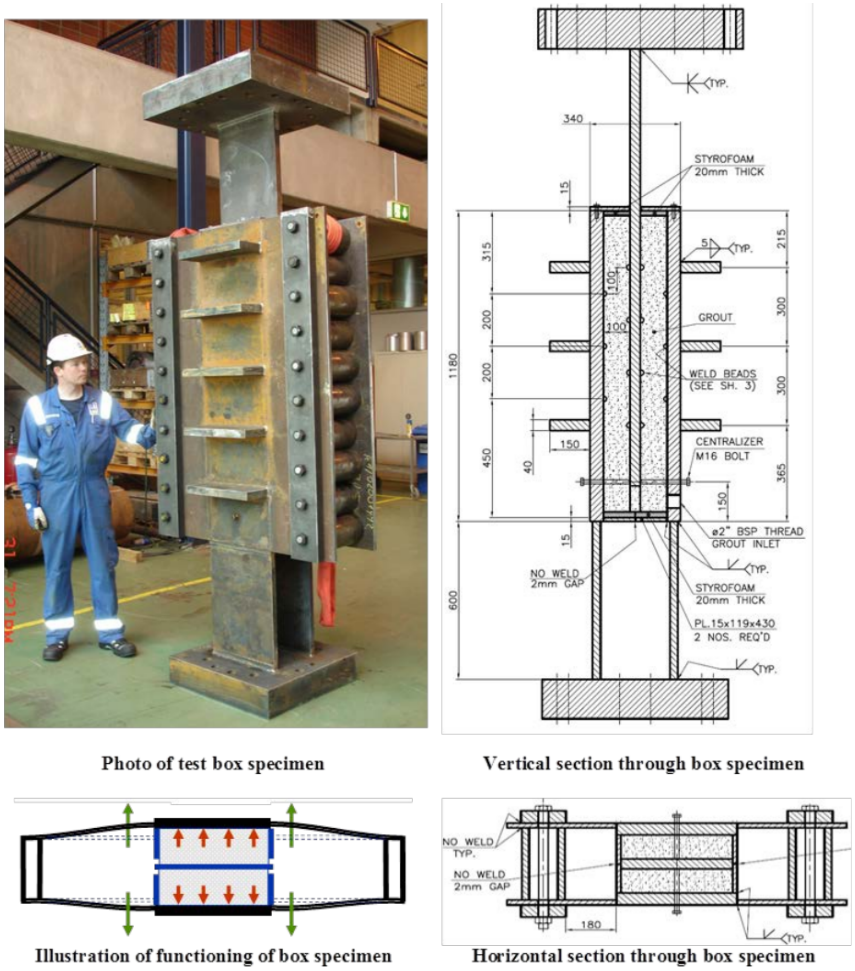

Figure 2. Box test specimen for simulation of large diameter connection.

From laboratory testing of grouted connections it has been observed that compression struts are developed in the grout between shear keys on the transition piece and the pile. These struts are rather stiff compared with the radial stiffness of the pile and the transition piece. Therefore the radial deflection is mainly governed by the thickness of the steel, the geometry of the connections in terms of radius, grout thickness; shear key geometry and Youngs modulus for the steel. From this information it was possible to design box specimens that could simulate the structural behaviour of large diameter connections. Reference is made to Figure 2 showing a photo of a box specimen. This figure also shows a vertical and a horizontal section through the grouted section. The box specimens were designed with a full size grout thickness of 100 mm, full size of shear keys (height = 12 mm) and a distance between the shear keys similar to that used in the full size structures. Because of the symmetry two volumes of grouted connections were tested as shown in Figure 2. The 180 mm wide plates shown in the horizontal section of Figure 2 were designed with a stiffness that gave a similar resistance against transverse pressure as that of radial resistance in large diameter connections. Four box specimens were designed, fabricated and tested under reversed cyclic loading in the joint industry project. The stiffness of the box tests corresponds to that of cylindrical diameters of approximately 800 mm, 2200 mm and 5000 mm.

Grouted connections in jacket structures

The design of the grouted connections in jacket structures has until recently been based on a control of capacity with respect to axial force in the pile while the effect of the bending moment

has been neglected, ref. ISO 19902 [7, 8]. In later design of grouted connections it is observed that the moments in the piles can contribute to more than two times larger stress in the pile than that due to axial load only. A significant moment can hardly be transferred from the pile to the sleeve without sliding of the steel against the grout. This sliding is considered to increase with increasing diameter of the pile. Therefore it is difficult to develop design criteria based on small scale testing. The contact pressure between grout and steel will lead to compressive and tensile stresses in the grout. This requires design criteria for compressive stress and tensile stress in the grout.

Based on a review of capacity of grouted connections the following revisions and additions were made in Norsok N-004 Annex K during 2013 [9, 10]:

- The capacity for axial load in connections without shear keys is revised as earlier capacity was non-conservative for assessment of contribution to capacity from plain pipes.
- A check is included for compressive stresses at the lower end of the grout due to bending moment and shear force in the pile.
- A check is included for fatigue assessment of grouted connection for alternating interface shear stress due to axial load and bending moment in the pile.
- A check on fatigue of the grout due to compression and shear stresses at the lower end of the grout due to shear load and bending moment in the pile is included.

References

[1] DNV-OS-J101. *Design of Offshore Wind Turbine Structures*. October 2007.

[2] I. Lotsberg, A. Serednicki, E. Cramer, H. Bertnes and P. Enggaard Haahr. *On Structural Capacity of Grouted Connections in Offshore Structures*. Presented at OMAE 2011-46169, 2011.

[3] I. Lotsberg, A. Serednicki, H. Bertnes and A. Lervik. *Design of Grouted Connections for Monopile Offshore Structures. Results from two Joint Industry Projects*. Stahlbau, Volume 81, Issue 9, pp. 695–704. 2012.

[4] I. Lotsberg, A. Serednicki, E. Cramer and H. Bertnes. *Behaviour of Grouted Connections of Monopile Structures at Ultimate and Cyclic Limit States*. The Structural Engineer, February, pp. 51–57. 2012.

[5] I. Lotsberg, A. Serednicki, R. Oerlemans, H. Bertnes and A. Lervik. *Capacity of Cylindrical Shaped Grouted Connections with Shear Keys in Offshore Structures reported from a Joint Industry Project*. The Structural Engineer, 91/1, pp. 42–48, 2012.

[6] I. Lotsberg. *Structural Mechanics for Design of Grouted Monopile Connections*. Marine Structures, Vol. 32, pp. 113–135, 2011.

[7] R. G. Harwood, C. J. Billington, J. Buitrago, A. Sele and J. V. Sharp. *Grouted Pile to Sleeve connections: Design Provisions for the New ISO Standard for Offshore Structures*. OMAE 1996.

[8] ISO 19902. *Design of steel structures*. 2007.

[9] I. Lotsberg and G. Solland. *Assessment of Capacity of Grouted Connections in Piled Jacket Structures*. OMAE 2013 – 10850, Nantes, France, 2013.

[10] Norsok N-004. *Design of Steel Structures*. Rev. 03, 2013.

Proceedings of the 26th Nordic Seminar on Computational Mechanics
A. Logg, K.A. Mardal, A. Massing (Eds.)

Isogeometric analysis of 3D finite deformation frictionless elastoplastic contact problems

Kjell Magne Mathisen[1], Knut Morten Okstad[2], Trond Kvamsdal[2], and Siv Bente Raknes[1]

[(1)]Norwegian University of Science and Technology, Department of Structural Engineering, Richard Birkelandsvei 1A, 7491 Trondheim, kjell.mathisen@ntnu.no, siv.bente.raknes@ntnu.no
[(2)]SINTEF Information and Communication Technology, Department of Applied Mathematics, P.O.Box 4760 Sluppen, 7465 Trondheim, knut.okstad@sintef.no, trond.kvamsdal@sintef.no

Summary. This paper focuses on the application of isogeometric analysis to model frictionless large deformation contact between deformable bodies and rigid surfaces that may be represented by analytical functions. The contact constraints are satisfied exactly with the augmented Lagrangian method, and treated with a mortar-based approach combined with a simplified integration method to avoid segmentation of the contact surfaces. The spatial discretization of the deformable body is performed with NURBS and C^0-continuous Lagrange polynomial elements. The numerical examples demonstrate that isogeometric surface discretization delivers more accurate and robust predictions of the response compared to Lagrange discretizations.

Key words: Isogeometric Analysis, NURBS, Contact Mechanics, Mortar Method, Elastoplasticity

Introduction

Large deformation contact problems in general involve geometrical, material and contact nonlinearities, which need to be solved simultaneously. Non-smooth C^0-continuous finite element discretization techniques still constitute the most widely used approach in solving computational contact problems. In order to improve the performance of contact algorithms, various smoothing techniques have been proposed based on, e.g., Hermite C^1, Bézier and NURBS discretization of the contact surface. Although surface smoothing improves the evolution of the contact pressure, these approaches in general do not preserve consistency between volume and surface discretization. Within the framework of isogeometric analysis, which was introduced by Hughes *et al.* [3], smooth surface discretization can be achieved by representing the contact geometry by a NURBS surface that is directly inherited from the NURBS discretization of the volume.

The robustness of contact computations also depends on an accurate and smooth description of not only the contact geometry but also the contact pressure. It is well-known that node-to-surface (NTS) contact formulations is affected by several pathologies, and has been shown not to satisfy the contact patch test, which implies that mesh refinement does not necessarily increase the accuracy of the contact pressure. Several improvements to the NTS (or knot-to-surface, KTS, for isogeometric analysis) have been proposed, but they either do not satisfy the contact patch test or cause LBB-instability. However, the more recent mortar-based approaches constitute a method for consistently treating the global and local contact interaction, satisfying both the patch test and LBB-stability, albeit at a higher computational cost [2].

The penalty (PL) method is the simplest and apparently the most widely used approach for solving contact problems. It leads to a pure displacement formulation where the constraints are enforced approximately. Furthermore, ill-conditioning may appear as the penalty parameter is

increased in order to improve the satisfaction of the contact constraints. To avoid the drawbacks of the PL method, the augmented Lagrangian (AL) method may be adopted. There are two solution schemes commonly used in the context of the AL method. The so-called Uzawa method, which combines the AL regularization with a first-order update of the Lagrange multipliers. Alternatively, a Newton-like solution scheme can be applied to solve the saddle-point problem for the displacements and Lagrange multipliers simultaneously as proposed by Alart and Curnier [1]. In view of the ascertained drawbacks of a non-mortar approach, we apply a mortar-based approach to satisfy the contact constraints combined with the latter version of the AL method, which is characterized by a remarkable degree of robustness and yields an asymptotic quadratic convergence rate in the Newton iterations. For comparison purposes, we have also implemented the PL method and C^0-continuous Lagrange polynomial elements. In this paper mortar-based isogeometric analysis as formulated by De Lorenzis *et al.* [4, 5] has been used to model finite deformation elastoplastic contact problems between deformable and rigid bodies.

Numerical results

A large deformation plain strain example is considered to demonstrate that isogeometric surface discretization delivers more accurate and robust predictions of the response compared to Lagrange discretization. A rigid cylinder is pressed vertically into a slab ($v = -0.075$) and then moved in the horizontal direction ($u = 2$). The problem has been assessed in the finite deformation regime with two different material models. First, the standard compressible neo-Hookean hyperelastic material behavior is assumed for the slab, with material parameters $E = 1$ and $\nu = 0.3$. Second, we consider a J_2-finite strain model expressed in principal stretch form, which represents a hyperelastic extension of J_2-flow theory with a standard neo-Hookean model for the elastic part, and nonlinear isotropic hardening with an associative flow rule based on von Mises yield criterion with isotropic hardening following a saturation law for the plastic part. The nonlinear isotropic hardening rule is defined in terms of the yield stress in uniaxial tension,

$$\sigma_y = \sigma_0 + (\sigma_\infty - \sigma_0)\left(1 - \exp(-\beta e_p)\right), \tag{1}$$

where $\sigma_0 = 79.66$ is the initial yield stress, $\sigma_\infty = 171.26$ is the residual yield stress, $\beta = 17.8$ is the saturation exponent and e_p is the equivalent plastic strain. The material parameters corresponds to an approximation of a two term extended Voce rule that was used to model aluminum alloy AA6060 typically used in bumper systems for cars.

The rectangular slab that is fixed at the bottom has width $W = 3.0$ and height $H = 1.0$, while the radius of the rigid cylinder is $R = 0.5$ (see Figure 1a). The slab is analyzed using NURBS and Lagrange basis functions of order $p = 2, 3, 4$, since for $p = 1$ NURBS and Lagrange approximations coincide. All NURBS and Lagrange discretizations include 49 basis functions in the horizontal and 25 in the vertical direction, respectively. We employ a standard Q_p pure displacement formulation for both the NURBS and Lagrange discretizations of the slab with $p+1$ Gauss-Legendre quadrature points in each direction within each knot span/Lagrange element.

A similar problem has also been studied by De Lorenzis *et al.* [4]. However, they consider the cylinder being elastic ($E = 1000$ and $\nu = 0.3$), account for friction ($\mu = 0.3$) and employed the PL method. Therefore, for the hyperelastic case, we cannot expect full compliance with the results obtained in [4].

Since for the hyperelastic case the Lagrange discretization fails due to divergence for $p = 4$, the solution in terms of strain energy versus horizontal displacement of the cylinder for NURBS and Lagrange discretizations presented in Figure 1b only shows results obtained for quadratic and cubic order. The plot of the strain energy demonstrates the remarkable smoothness obtained with the NURBS discretizations, while in contrast the Lagrange solutions are stiffer and experience oscillations. We observe that Lagrange discretizations exhibit oscillations that increase

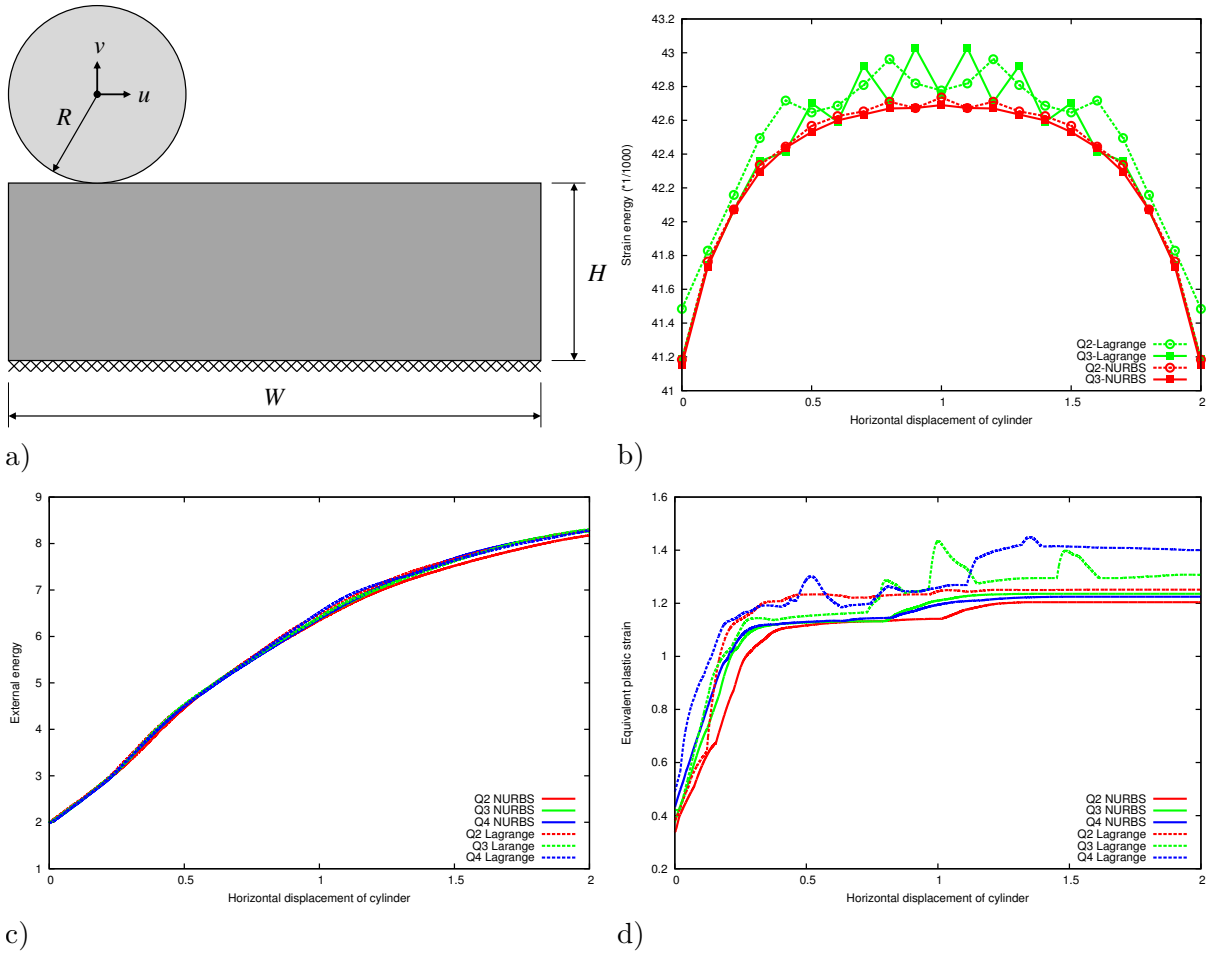

Figure 1. Ironing problem: a) Geometry and boundary conditions for the ironing problem. b) Strain energy for quadratic and cubic order NURBS and Lagrange discretizations for the elastic case. c) External energy for quadratic, cubic and quartic order NURBS and Lagrange discretizations for the elastoplastic case. d) Maximum equivalent plastic strain for quadratic, cubic and quartic order NURBS and Lagrange discretizations for the elastoplastic case.

with polynomial order of the basis functions, while in contrast for NURBS oscillations diminish with increased polynomial order. As a result Lagrange discretizations exhibit convergence problems in the Newton iterations while for NURBS the smoothness of the contact pressure increases monotonically with the order of the basis functions. The obtained results stem from the higher degree of smoothness which is achieved by representing the contact geometry by a NURBS surface that is directly inherited from the NURBS discretization of the volume.

Figure 1c shows the solution in terms of external energy versus horizontal displacement obtained for the elastoplastic material. In contrast to the elastic case the external energy is similar for all discretizations. Figure 1d shows the maximum equivalent plastic strain versus horizontal displacement obtained for the various discretizations.

Finally in Figure 2 the L_2-projected equivalent plastic strain is plotted on the deformed configurations for an imposed horizontal displacement of the cylinder $u = 0$, $u = 1$ and $u = 2$ for the quadratic order of NURBS and Lagrange discretizations, respectively. All results are shown with different scales adapted to the minimum and maximum values obtained in each case. For the Lagrange discretizations, we can clearly see oscillation patterns in the solution field for the equivalent plastic strain, while in contrast the NURBS solutions are smooth. Although we observe oscillations in the equivalent plastic strain, the global measure in terms of energy is almost coinciding between the various Lagrange and NURBS discretizations.

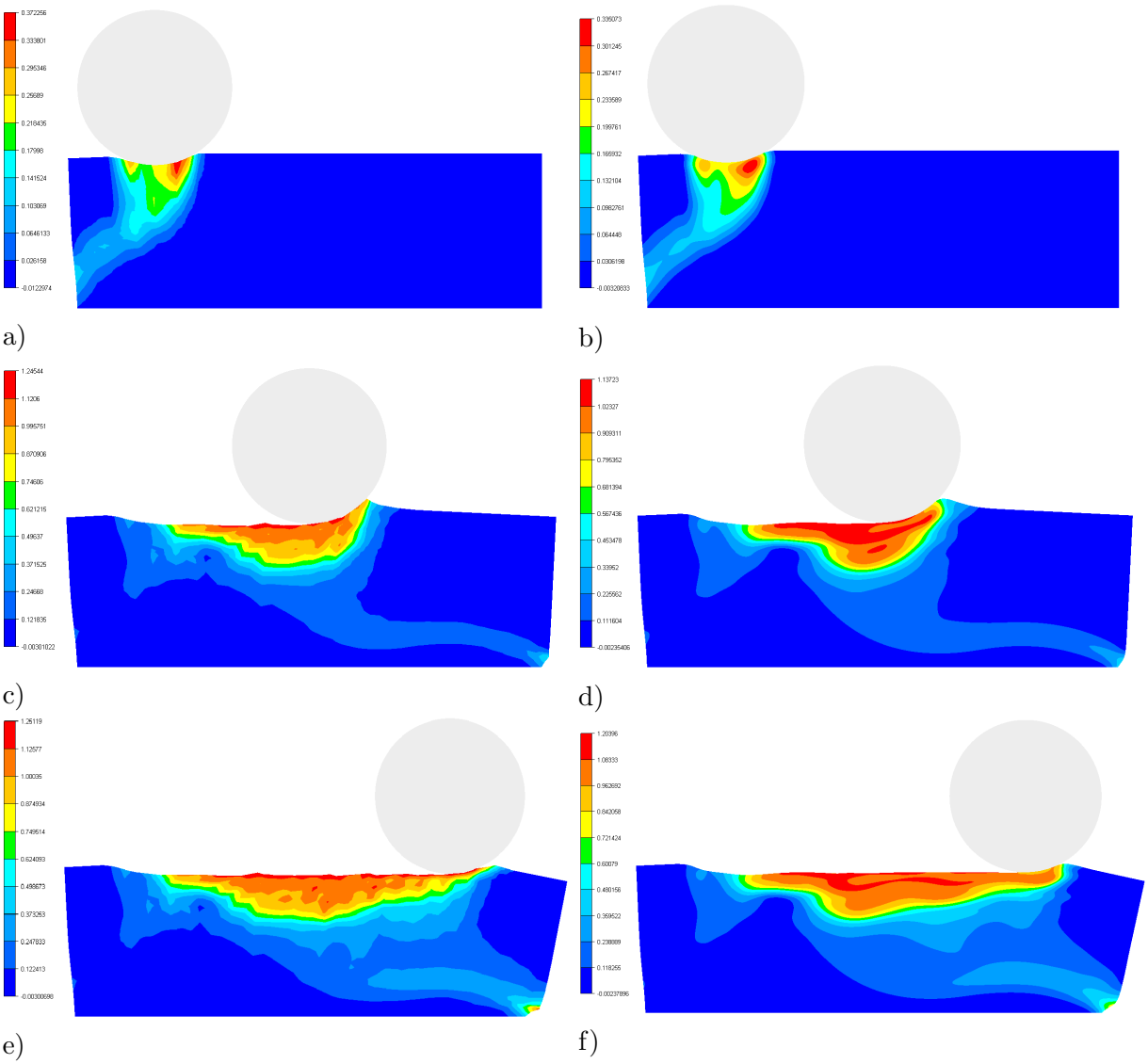

Figure 2. Ironing problem – Equivalent plastic strain: a) Q2 Lagrange, $u = 0$. b) Q2 NURBS, $u = 0$. c) Q2 Lagrange, $u = 1$. d) Q2 NURBS, $u = 1$. e) Q2 Lagrange, $u = 2$. f) Q2 NURBS, $u = 2$.

References

[1] Alart, P. and Curnier, A. A mixed formulation for frictional contact problems prone to Newton like solution methods. *Comput. Meth. Appl. Mech. Engrg.* (1999) **92**:353–375.

[2] Belgacem, F.B., Hild, P. and Laborde, P. The mortar finite element method for contact problems. *Math. Comp. Model.* (1998) **28**:263–271.

[3] Hughes, T.J.R., Cottrell, J.A. and Bazilevs, Y. Isogeometric Analysis: CAD, Finite Elements, NURBS, Exact Geometry and Mesh Refinement. *Comput. Meth. Appl. Mech. Engrg.* (2005) **194**:4135–4195.

[4] Lorenzis, L.De., Wriggers, P. and Zavarise, G.. A large deformation frictional contact formulation using NURBS-based isogeometric analysis. *Int. J. Numer. Meth. Engrg.* (2011) **87**:1278–1300.

[5] Lorenzis, L.De., Wriggers, P. and Zavarise, G. A mortar formulation for 3D large deformation contact using NURBS-based isogeometric analysis and the augmented Lagrangian method. *Comput. Mech.* (2012) **49**:1–20.

Proceedings of the 26th Nordic Seminar on Computational Mechanics
A. Logg, K.A. Mardal (Eds.)

Flexibility-based structural component mode synthesis: its history, promise, and future potential

K. C. Park(1), H. W. Park(2), D. Markovic(3), J. G. Kim(4), P. S. Lee(4)

(1)Center for Aerospace Structures, University of Colorado, Boulder, CO 80309
(2)Samsung Advanced Institute of Technology, Suwon, South Korea
(3)EDF R&D, Department of Analyses, Mecaniques et Acoustique, Clamart, France
(4)Division of Ocean Systems Engineering, KAIST, Daejeon 305-701, South Korea

Summary. A review of recent developments in flexibility-based component mode synthesis (F-CMS) methods is presented. It is shown that F-CMS methods rely on the partitioned solution methods (e.g., FETI-based algorithms) such that both the implementation overhead and solution methods are competitive with respect to the stiffness-based Craig-Bampton method. Accuracy of the F-CMS methods are shown to be superior to existing S-CMS methods, with an associated mode selection capability inherent with the F-CMS methods. To date, no such mode selection method is available for the Craig-Bampton method.

Key words: component mode synthesis, flexibility-based, mode selection criterion

Introduction

Historically, after the birth of the structural analysis software labeled as the NASA STRuctural ANalysis (NASTRAN) based on the stiffness method during the mid-1960s [1, 2], the classical force method began its steep decline [3]. During the 1990s a new computational paradigm for exploiting parallel computers gave birth to new solution methods now labeled as domain decomposition methods. Of a plethora of domain decomposition methods, the finite element tearing and interconnecting (FETI) method [4] and its subsequent refinements are perhaps one of the most popular parallel solution algorithms for structural analysis on parallel machines. From a viewpoint of the present work, the flexibility matrix that is employed to accelerate the solution process by a family of FETI methods spurred a reemergence of flexibility-based methods, labeled as dual formulation to the displacement-based method. We hold a view that flexibility-based methods should extend their applicabilities much beyond the parallel algorithms. While the potential of flexibility-based methods would extend far beyond the parallel algorithms, the present paper focuses on a specific extended application of flexibility-based methods, namely, flexibility-based component mode synthesis (F-CMS) construction of large-scale structural dynamic equations, which offers improved accuracy and robustness, and at the same time a mode selection criterion [5, 6, 7, 8]. Numerical performance indicates that the F-CMS method offers higher accuracy for low dominant modes as compared with the stiffness-based S-CMS [9].

Representative results

An example problem for the reduced-order model construction involving a hemispheric shell is shown in Figure 1, which is partitioned into 4 uneven substructures. The target accurate number of modes is set to be 20 and a reduced-order model consisting of 128 and 190 unknowns is used (out of 4000 degrees of freedom for the finite element model). As indicated in Figure 2, large

errors for modes 9 and 10 are observed without the use of the proposed mode selection criterion. Subsequent improvements by utilizing the proposed mode selection criterion are achieved as shown in the same figure. Formulation details and the use of mode selection guides will be presented at the seminar.

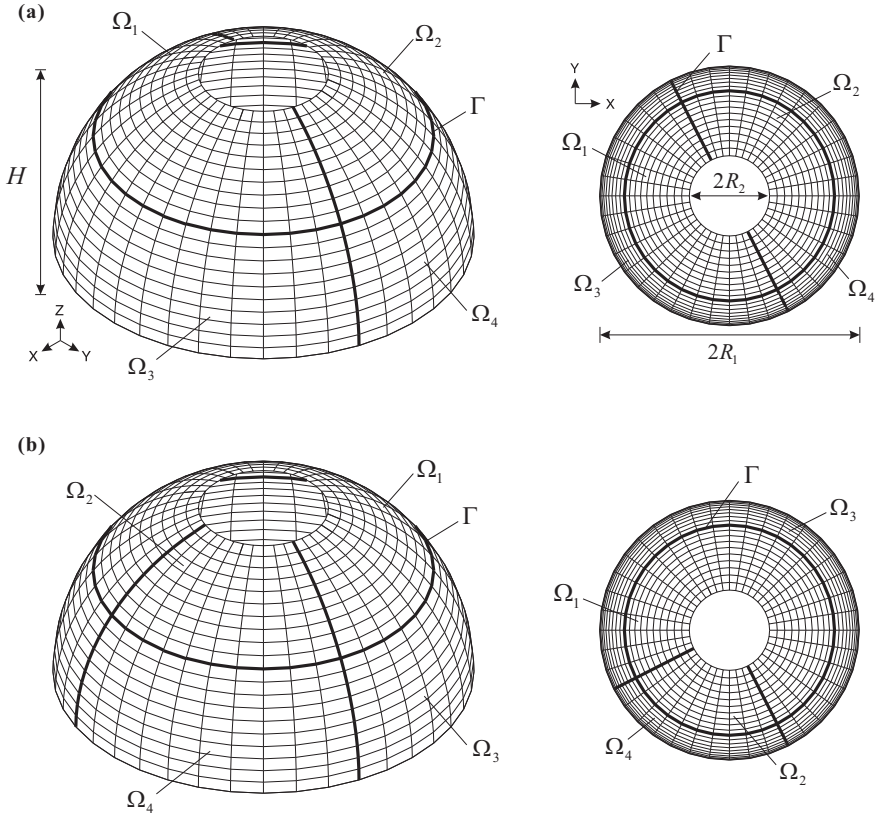

Figure 1. Hemisphere shell problem with two different partition types shown in (a) and (b) ($H = 3.804$m, $R_1 = 2$m, $R_2 = 0.618$m, $h = 0.05$m, $E = 69$GPa , $\nu = 0.35$, and $\rho_s = 2700$kg/m^3). Here, Ω_j and Γ denote the j^{th} substructures and the interface boundary, respectively.

References

[1] http://www.me.caltech.edu/centennial/history/nastran.htm

[2] R. H. MacNeal, The MacNeal Schwendler Corporation: The First Twenty Years, Gardner Litograph, Buena Park, CA, 1988.

[3] C. A. Felippa, "Will the force method come back?", *J. Appl. Mech.*, 54, 728–729, 1987.

[4] C. Farhart and F. X. Roux, "A method of finite element tearing and interconnecting and its parallel solution algorithm,Ó *Int. J. Numer. Method Eng.*, vol. 32, pp. 1205–1227, 1991.

[5] K. C. Park and Y.H. Park, "Partitioned component mode synthesis via a flexibility approach," *AIAA JOURNAL*, 42(6), 1236-1245, 2004.

[6] Markovic, D, Park, KC, Ibrahimbegovic, A., "Reduction of substructural interface degrees of freedom in flexibility-based component mode synthesis," *INTERNATIONAL JOURNAL FOR NUMERICAL METHODS IN ENGINEERING*, Volume: 69, Issue: 10, Pages: 2058-2074, 2007.

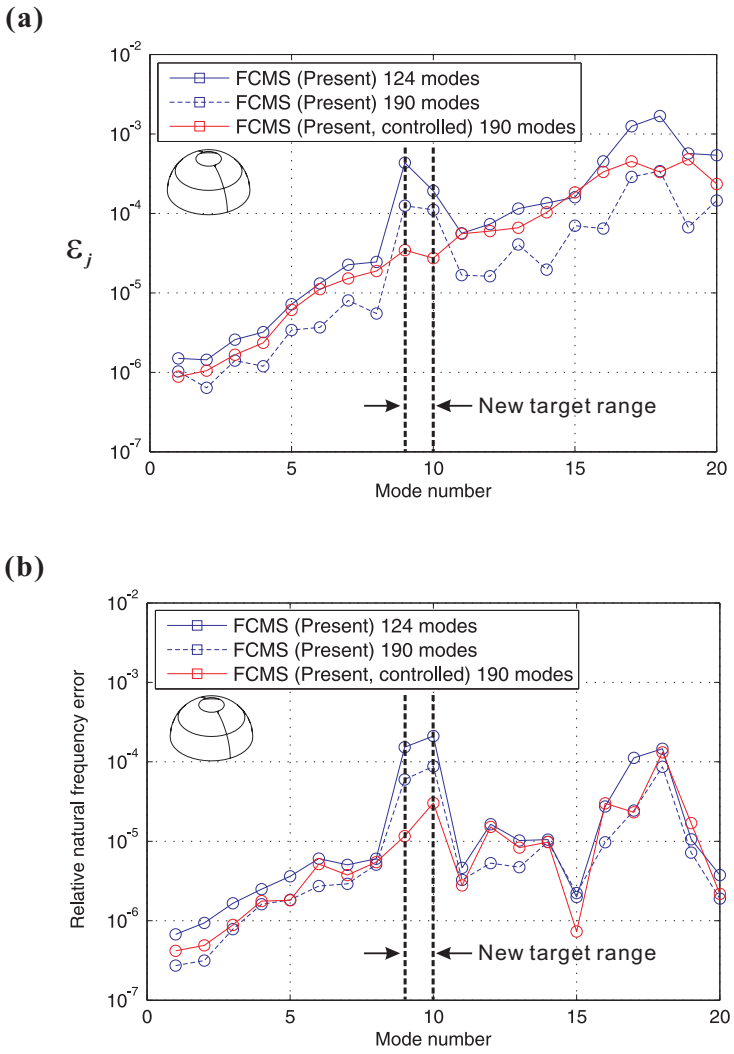

Figure 2. Error estimation and accuracy control in the hemisphere shell problem using the F-CMS method for the partition type in Figure 1(a). (a) Error estimation and (b) Accuracy control for the global modes 9 and 10

[7] Markovic, D., Ibrahimbegovic, A., Park, K.C., "Partitioning based reduced order modelling approach for transient analyses of large structures," ENGINEERING COMPUTATIONS, 26(1-2), 46-68, 2009.

[8] J. G. Kim, P. S. Lee, K. C. Park, "A Mode Selection Criterion Based on Flexibility Approach in Component Mode Synthesis: Performance Evaluation," Proc. SDM Conference, Honolulu, Hawaii, April 2011.

[9] Craig, Jr., R.R. and M.C.C. Bampton, "Coupling of Substructures for Dynamic Analysis," AIAA Journal, v. 6, 1313-1319 (1968).

Proceedings of the 26th Nordic Seminar on Computational Mechanics
A. Logg, K.A. Mardal, A. Massing (Eds.)

Oil exploration and flexible risers: Establishing carcass axial capacity using finite element analysis

Geir Skeie[1] and Gunnar Axelsson[2]

(1)DNV, Riser Technology, Høvik, Norway, geir.skeie@dnv.com
(2)4subsea, Hvalstad, Norway, gunnar.axelsson@4subsea.com

Summary. Recent incidents on the Norwegian shelf showed that the inner steel structure of a flexible riser, the carcass, can experience extensive axial loading. This resulted in carcass overload followed by a spin-out and eventually tear-off at the carcass end followed by shutdown of production. The carcass axial tension capacity has previously not been considered a critical design issue for flexible pipes. The incidents resulted in an extensive program, initiated by Statoil, to find the root cause of the problem. Both analytical and computational efforts validated through extensive testing of carcass axial capacity has been conducted. Advanced finite element analysis was used to establish both the carcass capacity and also the load level as a function of pitch length. The numerical results are compared and validated towards experimental data. The results form a basis to suggest operational policies to mitigate the risk of new failures.

Key words: flexible risers, carcass capacity, finite element analysis

Introduction

Between the years 2010-11 Statoil experienced a number of carcass failures in flexible risers at their facilities on the Norwegian shelf, Farnes et al.[1]. An inspection program for the remaining production risers was launched, using internal visual inspection, carcass pitch measurements tools etc. Inspections showed carcasses that had been torn off in or close to the end-fitting. The axial overloading resulted in un-spiraling along a substantial length of the carcass. To the authors' knowledge, the observed deficiency represents a new failure mode previously unknown to the industry. Although, comparable failures have been seen in flexible pipes blocked by e.g. hydrates and exposed to large differential pressures. However, the newly observed scenario has not been properly addressed in design, manufacturing, installation and operation of the risers. An extensive investigation was initiated by the operator Statoil to identify the failure mechanism and the load effects leading to carcass tear-off. The investigation has been performed as a joint effort by expertise from Statoil, 4Subsea, DNV and Sintef.

To evaluate the carcass axial load present in risers offshore and when investigating recovered pipes, it has been of great importance to establish measurable relations such as carcass pitch length as a function of axial loading. In the following sections, analysis covering a range of carcass dimensions and materials is discussed.

The current paper only addresses one part of the systematic failure mode investigations, namely the carcass axial capacity and pitch/strain indicators. A more complete picture and especially the load scenario that eventually leads to un-spiraling of the carcass is discussed in Farnes et al. [1]. The carcass axial tension capacity is also discussed in Skeie et al. [2].

Finite Element Analysis

Finite Element Analysis (FEA) complements testing in the way carcass tear-off is understood. Physical testing has been important for assessing the structural capacity of the carcass and the test results also forms the basis for validation of carcass capacity assessment using FEA. Further, the test results serve as assessment of the load acting on the carcass from pitch length measurements. The FEA allow for variation in parameters, alignment and tilting, that are hard to include in a physical test.

The carcass models were analyzed using two different solvers; DNV used Abaqus/Explicit from Dassault Systèmes (2011), while 4subsea used Marc (implicit), MSC Software (2012). The different carcass geometries listed in Table 1 were modeled based on cross-sectional as-built records or images taken from extracted samples of the carcass profiles, Figure 1. The two

Type of carcass	Inner diameter	Profile dimensions	Carcass material
A	6 inch	$23.4 \times 4.0 \times 0.8$	316L
B	6 inch	$29.1 \times 5.4 \times 0.9$	316L
C	8 inch	$27.1 \times 5.1 \times 1.0$	316L
D	8 inch	$27.1 \times 5.1 \times 1.0$	316L
E	9 inch	$27 \times 6.0 \times 1.2$	Duplex
F	9 inch	$34.9 \times 7.5 \times 1.5$	316L

Table 1. The carcass as-built properties.

solvers require different methods for setting up the analyses; however the general modeling is similar. Figures 1 and 2 shows the different FE models:

- The 2D carcass profile is *extruded* with a pitch to form the 3D carcass spiral.
- Both ends of the carcass profile are constrained using a rigid coupling through tying's or rigid surfaces.
- The model is meshed using linear hexahedral elements 2 and 5 elements through the thickness for Marc and Abaqus/Explicit, respectively. Further,
  - Abaqus/Explicit used elements with reduced integration and enhanced hour-glass control. The Marc solver used first order full integrated hex elements including an assumed strain formulation.
  - The mesh density was set to capture the physical behavior of the carcass during local to full plasticity of the carcass profile. Also to capture stress concentrations small radii have been modeled with a dense mesh.
- Contact including friction was modeled between all interacting faces.

The explicit method requires control of the dynamic effects in a quasi-static simulation. In Abaqus/Explict the time step and loading amplitude was adjusted to reduce the dynamic response in the system. Mass scaling was used to optimize the time increment size, but kept sufficiently low to avoid relative mass change exceeding 10%.

All of the modeled carcasses were made from 316L stainless steel, except one that was prepared in duplex stainless steel. Young's modulus was set to 210 GPa and Poisson's ratio 0.3. Plastic properties of 316L were taken from material tests on specimen extracted from the fabricated carcass. The yield strength of 316L was found to be 527 MPa, while for duplex it was found 790 MPa.

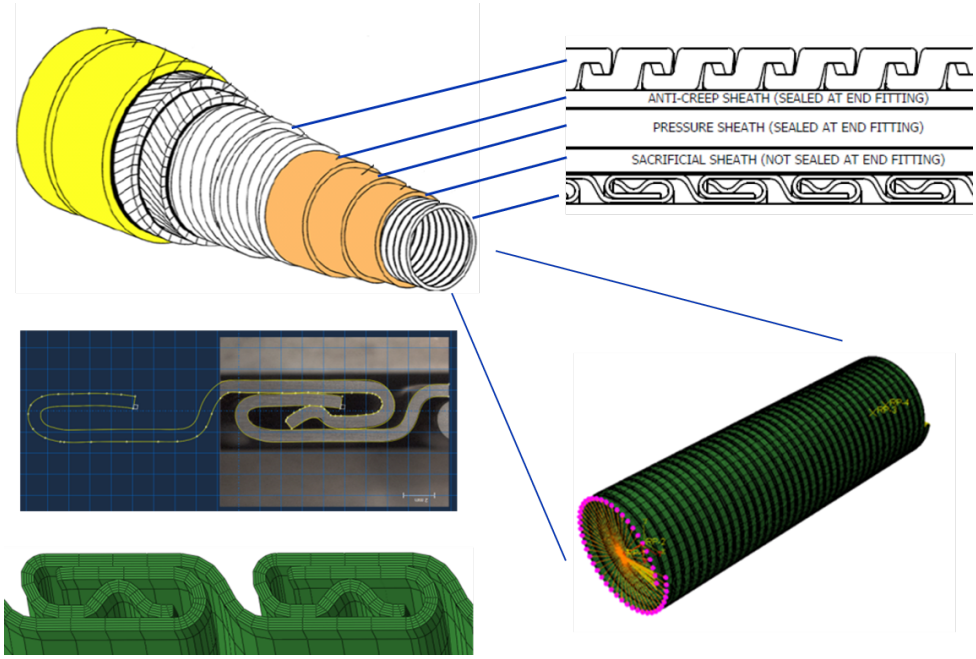

Figure 1. Modeling of the carcass geometry in Abaqus.

In the Abaqus analysis the same hardening curve was used for the whole mesh. In the Marc analysis the profile bends was given a work hardened higher yield strain, while the rest is modeled as in Abaqus.

Results from the tests and the FE analyses are summarized in Table 2 and show good agreement with the experimental tests, typically within ±10%. Figure 3 includes a comparison between the FE and test results. The FE results show good agreement to the test results, which shows that the axial failure of a thin plate structure with large plastic deformations may be analyzed by 3D finite elements with high accuracy. The accuracy depends upon access to as-built carcass profile geometry and relevant material data.

ID	Strip thickness	Material	Axial load capacity [kN]		
[“]	[mm]		Test	MSC Marc	Abaqus/Explicit
6	0.8	316L	54	57	55
6	0.9	316L	78	76	76
8	1.0	316L	86	89	84
9	1.5	316L	160	169	146
9	1.2	Duplex	155	165	Not Analyzed

Table 2. Summary of results from tests and FE analyses.

Observations

Finite element analysis has been performed on a number of carcass geometries and the results comply well with experimental results. Numerical analysis complements the experimental work and allows effective investigation of sensitivities related to geometric configurations and material parameters. The pitch versus load relation can be used to evaluate data from inspection that can be used to support further operation and thus to mitigate the risk of loss of containment

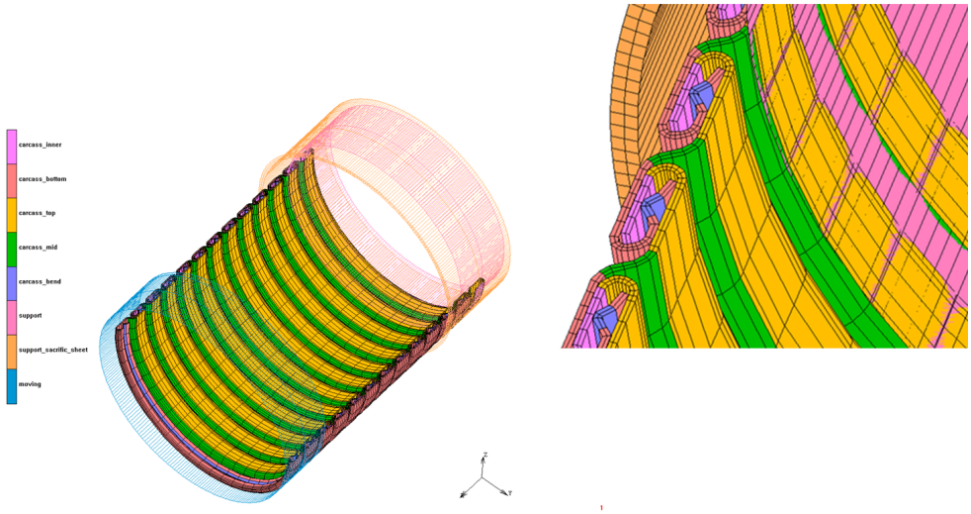

Figure 2. Modeling of the carcass geometry in Marc.

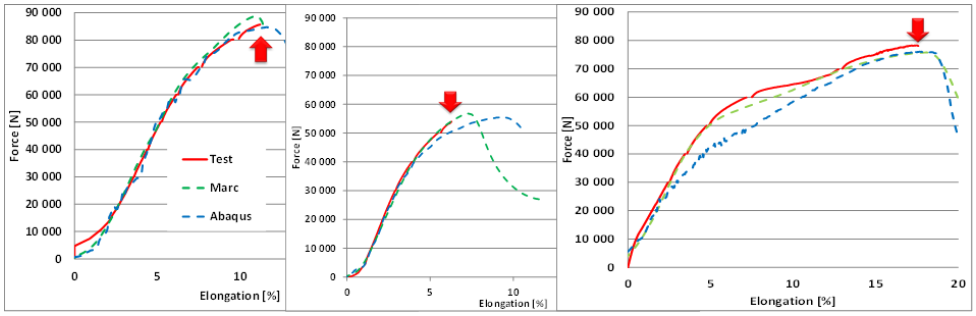

Figure 3. Carcass FEA results compared to tests, test capacity marked with red arrows.

from carcass tearing.

References

[1] Knut-Aril Farnes, Claus Kristensen, Steinar Kristoffersen, Jan Muren, and Nils Sødahl, *Carcass failures in multilayer PVDF risers*, OMAE 2013 (Nantes, France), June 9-14 2013.

[2] Geir Skeie, Håvard Skjerve, Sune Pettersen, Gunnar Axelsson, Bjørn Engh, and Stine Vethe, *Carcass axial capacity in flexible risers*, Proceeding of the Rio Pipeline Conference 2013, 2013.

Proceedings of the 26th Nordic Seminar on Computational Mechanics
A. Logg, K.A. Mardal, A. Massing (Eds.)

Integrated Computer Aided Design and Analysis (ICADA) – Vitality through locally refined splines and immersed boundary techniques

Trond Kvamsdal[1] and Knut Morten Okstad[2]

(1)Norwegian University of Science and Technology, Department of Mathematical Sciences, Alfred Getz vei 1, NO-7491 Trondheim, Norway, Trond.Kvamsdal@math.ntnu.no
(2)SINTEF ICT, Department of Applied Mathematics, Strindveien 4, NO-7465 Trondheim, Norway, Knut.Morten.Okstad@sintef.no

Summary. The new paradigm of Isogeometric Analysis, which was introduced by T. Hughes *et al.* [1], demonstrates that much is to be gained with respect to efficiency, quality and accuracy in analysis by replacing traditional finite elements by volumetric NURBS. Herein, we describe techniques that add vitality to the proposed Isogeometric Analysis concept by use of locally refined splines (LR B-splines) and immersed boundary techniques.

Key words: Isogeometry, adaptive FE analysis, immersed boundaries.

Introduction

Computer Aided Design (CAD) and Finite Element Analysis (FEA) are essential technologies in modern product development. However, the interoperability of these technologies is severely disturbed by inconsistencies in the mathematical approaches used. The main reason for inconsistencies is that the technologies evolved in different communities with the focus on improving disjoint stages in product development processes, and taking little heed on relations to other stages. Efficient feedback from analysis to CAD and refinement of the analysis model are essential for computer-based design optimization and virtual product development. The current lack of efficient interoperability of CAD and FEA makes refinement and adaptation of the analysis model cumbersome, slow and expensive.

The new paradigm of Isogeometric Analysis, which was introduced by T. Hughes *et al.* [1], demonstrates that much is to be gained with respect to efficiency, quality and accuracy in analysis by replacing traditional finite elements by volumetric NURBS[1] elements. However, NURBS are not flexible enough to be a common basis for future CAD and FEA due to the lack of local refinement. The recently proposed LR B-splines [2] have the potential to add versatility by facilitating adaptive refinement based on *a posteriori* error estimates [3]. Furthermore, the immersed boundary technique [4, 5] (see description related to the second example below) may free the analyst from time consuming work related to establishing a body fitted block mesh.

[1]NURBS – Non-Uniform Rational B-splines, the generic representation of free-form curves and sculptured surfaces in CAD-systems.

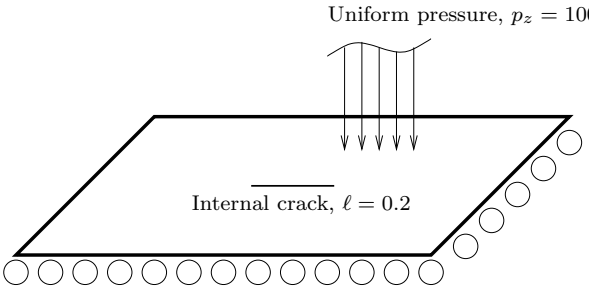

Geometry: Length and width: 1.0
Thickness: $t = 0.01$

Material: $E = 2.1 \times 10^{11}$
$\nu = 0.3$
$D = \frac{Et^3}{12(1-\nu)}$

Figure 1. Simply supported square plate with an internal crack and uniform pressure load.

Numerical examples

Square plate with internal crack

Figure 1 shows a simply supported square plate with an internal crack, subjected to a uniform pressure load. The crack is modelled by enforcing the multiplicity p of the LR B-spline mesh lines along the crack, such that the geometry (and solution) here becomes C^{-1} continuous. This introduces a singularity in the solution at each crack tip.

To catch these singularities in the FE solution, it is necessary to focus the degrees of freedom around the crack tip. This is most effectively done through some adaptive refinement scheme, where we refine the mesh based on a computed error estimate. Herein, we use the energy norm error $\|e_*\| = \sqrt{a(w_* - w_h, w_* - w_h)}$, where w_* represents an enhanced solution obtained by a global L_2-projection of the FE bending moments, $m_h^{\alpha\beta}$ onto the C^{p-1} continuous basis of the primary solution, w_h.

In Figure 2a) we plot the convergence of the energy norm error for four different simulations; two uniform refinements with quadratic and cubic basis functions, respectively, and two adaptive refinements with the same basis. We here clearly see that through adaptive refinement, the LR B-spline basis is able to reproduce the theoretical convergence rate governed by the polynomial order (illustrated by the two triangles in the plot), whereas the uniform refinement completely fails to do so. The refined mesh around the crack after 5 adaptive steps is shown in Figure 2b) for the case with quadratic basis functions.

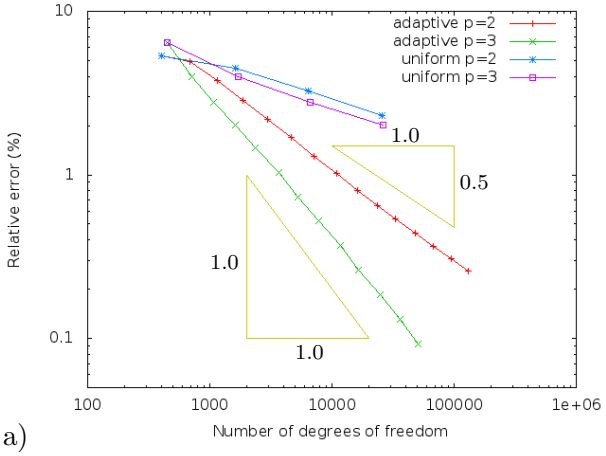

a)

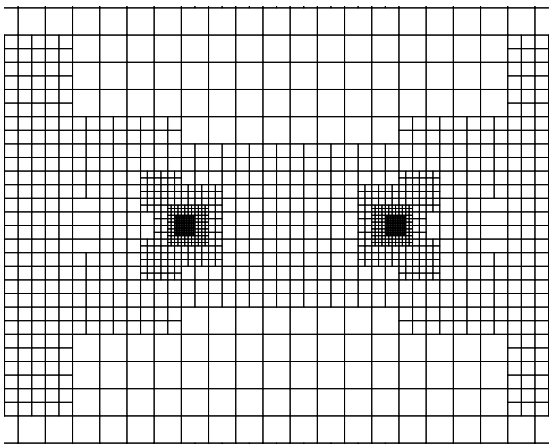

b)

Figure 2. Results for the cracked square plate: a) Convergence of the global relative error for two adaptive simulations and two uniform refinement simulations, using quadratic ($p = 2$) and cubic ($p = 3$) LR B-spline elements. b) 5th adaptively refined mesh around the crack for the quadratic ($p = 2$) case.

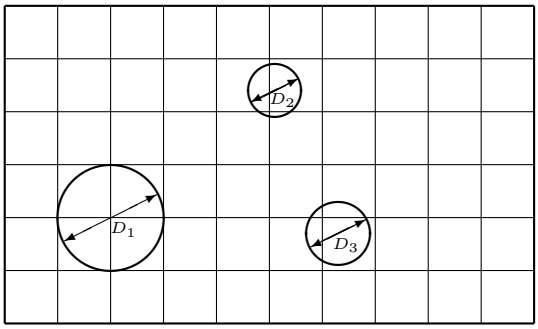

Geometry: Length: 10.0
Width: 6.0
Thickness: $t = 0.1$
Holes: $D_1 = 2.0$, $D_2 = 1.0$, $D_3 = 1.2$

Material: $E = 2.05 \times 10^{11}$
$\nu = 0.29$

Figure 3. Rectangular plate perforated by three circular holes (initial mesh). The three holes (D_1, D_2, D_3) are centered at the points $(2.0, 2.0)$, $(5.1, 4.4)$ and $(6.3, 1.7)$, respectively, w.r.t. the lower-left corner.

Perforated rectangular plate

In the next example we consider a simply supported rectangular plate perforated by three circular holes as illustrated in Figure 3, and subjected to a uniform pressure load.

The three holes are here not modelled physically in the grid, but are resolved using the *Immersed boundary* technique [4, 5]. The physical object is then immersed in a Cartesian regular grid. Each grid cell which is intersected by the physical boundary, is subdivided into 2^n sub-cells, in a quadtree/octree manner (n denoting the number of spatial dimensions). The subdivision is repeated a given number of levels (k) for those sub-cells that are still intersected by the boundary. A Gauss quadrature scheme is then imposed on the leaf sub-cells, whereas the FE basis is still according to the regular Cartesian grid.

Only the integration points that are inside the physical domain are included in the FE computations as indicated in Figure 4. Some basis functions may also have support entirely outside the physical domain. Those functions might be automatically detected, and the associated DOFs are eliminated as unknowns a priori. The same set of integration points as used for the stiffness matrix is used in the global L_2-projection, and subsequent error norm integration.

In the current analyses, we are using a maximum quad-tree depth equal to 5, and a 4×4 Gauss scheme on the finest sub-cells for both quadratic and cubic splines Uniform refinement is conducted on a series of grids ranging from 10×6 (as shown in Figure 3) to 160×96 knot-spans. This is compared with adaptive refinement using LR B-splines and 6 refinement steps. The 20% elements having the highest error are refined in each step. Results in terms of convergence of the energy norm error for the four different simulations and bending moment distribution on the 5th adaptively refined cubic mesh are shown in Figure 5.

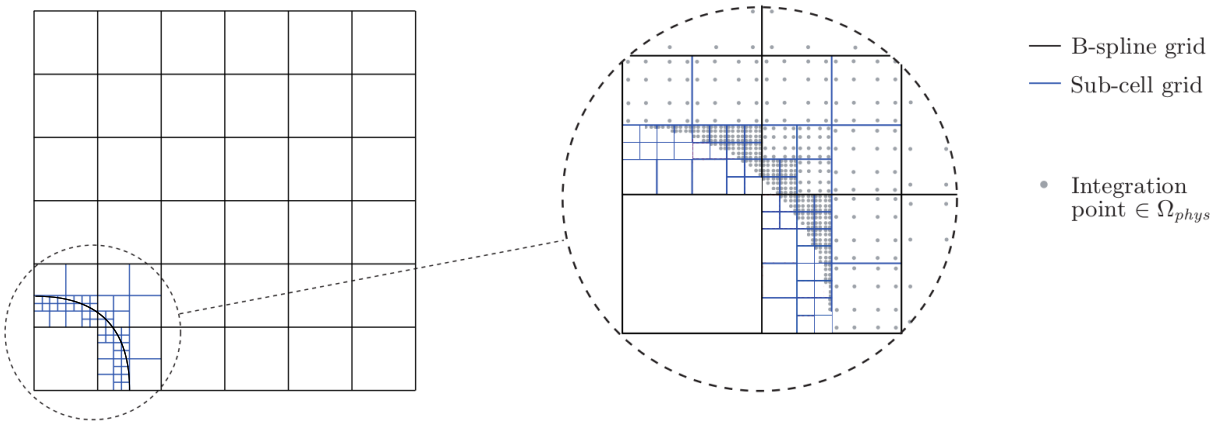

Figure 4. The immersed boundary concept. (Figure from [4].)

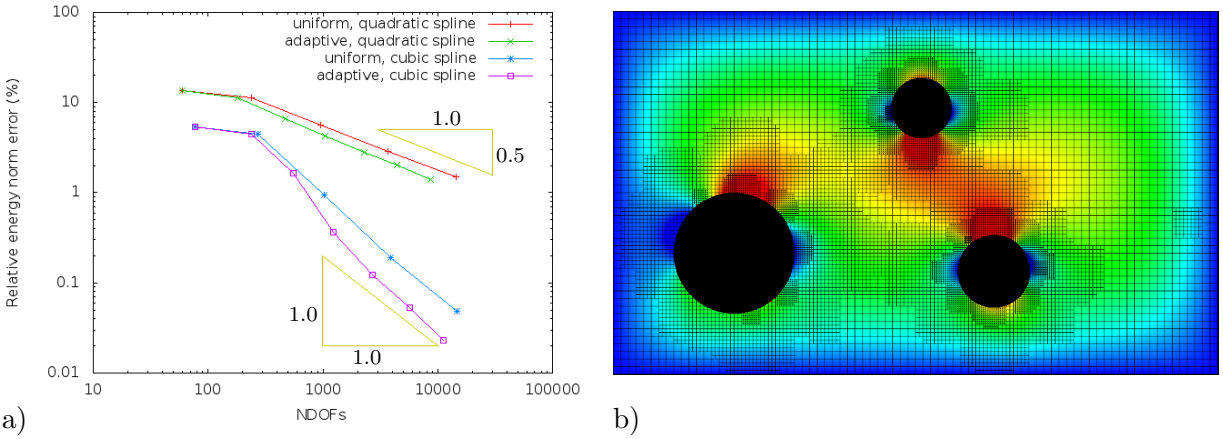

Figure 5. Results for the perforated rectangular plate: a) Convergence of the global relative error for two adaptive simulations and two uniform refinement simulations, using quadratic and cubic LR B-spline elements. b) The m_{xx} moment distribution on the 5th adaptively refined mesh for the cubic case. The fringe range is from -100.0 (blue) to 2400.0 (red).

Acknowledgement

The authors acknowledge the financial support from the Norwegian Research Council and the industrial partners of the ICADA-project; Ceetron, Det Norske Veritas and Statoil. They also acknowledge the support from the other co-workers in the ICADA-project, in particular, Kjetil Johannessen, Mukesh Kumar and Annette Stahl (NTNU, Department of Mathematical Sciences) and Arne Morten Kvarving (SINTEF ICT).

References

[1] T. J. R. Hughes, J. A. Cottrell, and Y. Bazilevs. Isogeometric Analysis: CAD, Finite Elements, NURBS, Exact Geometry and Mesh Refinement. *Computer Methods in Applied Mechanics and Engineering*, 194:4135–4195, 2005.

[2] T. Dokken, T. Lyche, , and K. F. Pettersen. Polynomial Splines over Locally Refined Box-partitions. *Computer Aided Geometric Design*, 30(3):331–356, March 2013.

[3] K. A. Johannessen, T. Kvamsdal, and T. Dokken. Isogeometric Analysis using LR B-splines. *Computer Methods in Applied Mechanics and Engineering*, (to appear 2013).

[4] D. Schillinger, L. Dedè, M. A. Scott, J. A. Evans, M. J. Borden, E. Rank, and T. J. R. Hughes. An Isogeometric Design-through-analysis Methodology based on Adaptive Hierarchical Refinement of NURBS, Immersed Boundary Methods, and T-spline CAD Surfaces. *Computer Methods in Applied Mechanics and Engineering*, 249–250:116–150, 2012.

[5] D. Schillinger, M. Ruess, N. Zander, Y. Bazilevs, A. Düster, and E. Rank. Small and Large Deformation Analysis with the *p*- and B-spline versions of the Finite Cell Method. *Computational Mechanics*, 50(4):445–478, 2012.

Proceedings of the 26th Nordic Seminar on Computational Mechanics
A. Logg, K.A. Mardal, A. Massing (Eds.)

An Effective Method to Compute Thermal Front Velocity in Geothermal Systems

Yapi Donatien Achou, master student in Applied mathematics, University of Oslo.

Computational geoscience group at Simula Research Laboratory, P.O.Box 134, Lysaker, Norway
yapi@simula.no

Summary. Injection of cold fluid into hot geothermal reservoirs can be formulated as conservation laws. The cold front velocity induced during injection has been computed in [6] from conservation of energy and the method of characteristics applied to an initial boundary value problem. This computed thermal front velocity is expressed as the ratio of two integrals. In this paper we present a new method for computing the thermal front velocity by solving a Riemann problem. We show that the unique solution of the Riemann problem moves at the speed equal to the thermal front velocity. Our result is computed from the Rankine-Hugoniot shock condition and is much easier to evaluate. It only depend on the flux function of the conservation laws, the injected fluid temperature and the reservoir temperature. A relative error of magnitude 10^{-3} was observed between the two results and the upper bound error of our result converges at least $133 \cdot 10^4$ times faster to zero then the one obtained in [6]. Convergence rate of about 2 was found when validating the numerical integration using the trapezoidal rule.

Key words: Thermal front velocity, entropy condition, conservation laws

Introduction

In geothermal energy extraction, reinjecting colder fluid into the hot reservoir is an integral part of resource management [1]. However due to cold injected fluid, cooling of the production wells can occur, as observed in Beowawe, Nevada and the Geysers Geothermal reservoir in the US [2], [3]. To mitigate this cooling effect, predicting the velocity of the cold water movement, is an essential part of reinjection scheme. Bodvarsson [4] derived the thermal front velocity for constant fluid and rock properties, using the characteristic method. This technique produces non physical solution when the rock and fluid properties are temperature dependent. By using the method of characteristics, Stopa and Wajnarowski solved an initial-boundary value problem for the conservation laws [6]. They derived the thermal front velocity using conservation of energy.

By formulating the injection problem as the well posed Riemann problem, we relied on the well established theory of hyperbolic conservation laws. Rather than using the method of characteristics, we used the unique solution for the Riemann problem given in [5]. This solution then propagates at the speed equal to the thermal front velocity.

Governing equation

A single phase(liquid) fluid flow in porous medium is given respectively by the conservation of mass and energy [7]:

$$\frac{\partial(\phi\rho_w(u))}{\partial t} + \frac{\partial}{\partial x}(\rho_w(u)u_w) = 0 \tag{1}$$

$$\frac{\partial}{\partial t}\left(\phi\rho_w(u)c_w(u)u + (1-\phi)\rho_r(u)c_r(u)u\right) + \frac{\partial}{\partial x}(\rho_w(u)c_w(u)u_w u) = \lambda\frac{\partial^2 u}{\partial x^2} \tag{2}$$

where u is the temperature, $c_w(u), c_r(u), \rho_w(u), \rho_r(u)$ are the heat capacity of water/rock and density of water/rock respectively and given in [6]. ϕ, u_w, λ are the porosity, the Darcy velocity of liquid phase and the heat conduction coefficient respectively. Assuming that the flow is convection dominated and neglecting conduction as second order effect [7], after rearranging equation (2) we get

$$\begin{aligned} c_w(u)u\left(\frac{\partial\phi\rho_w(u)}{\partial t} + \frac{\partial}{\partial x}(\rho_w(u)u_w)\right) + \frac{\partial}{\partial t}((1-\phi)\rho_r(u)c_r(u)u) \\ +\phi\rho_w(u)\frac{\partial}{\partial t}(c_w(u)u) + \rho_w(u)u_w\frac{\partial}{\partial x}(c_w(u)u) = 0. \end{aligned} \tag{3}$$

Using (1), the first expression in (3) vanishes:

$$\frac{\partial}{\partial t}((1-\phi)\rho_r(u)c_r(u)u) + \phi\rho_w(u)\frac{\partial}{\partial t}(c_w(u)u) + \rho_w(u)u_w\frac{\partial}{\partial x}(c_w(u)u) = 0. \tag{4}$$

Applying the chain rule on (4) and rearranging the terms we end up with

$$\frac{\partial u}{\partial t} + \frac{u_w}{\phi}F(u)\frac{\partial u}{\partial x} = \frac{\partial u}{\partial t} + \frac{\partial G}{\partial x} = 0 \tag{5}$$

where

$$F(u) = \frac{\phi\rho_w(u)\left(\frac{\partial(c_w(u)u)}{\partial u}\right)}{(1-\phi)\left(\frac{\partial(\rho_r(u)c_r(u)u)}{\partial u}\right) + \phi\rho_w(u)\left(\frac{\partial(c_w(u)u)}{\partial u}\right)} \tag{6}$$

Result from the theory of conservation laws

Injecting colder water into a hot geothermal reservoir can be formulated as a Riemann problem associated to (5) : Find the unique solution u of

$$\frac{\partial u}{\partial t} + \frac{\partial G}{\partial x} = 0, \quad u(x,0) = g(x) \tag{7}$$

$$g(x) = \begin{cases} u_l & \text{if } x \le 0 \\ u_r & \text{if } x \ge 0\ . \end{cases}$$

satisfying the Rankine-Hugoniot shock condition and the Kruzkov entropy condition [5]. From [5] we have following theorem:

Theorem 1 *The initial value problem (7) with flux function $G(u)$ such that $G_{\cup,\cap} \neq G$ on finitely many intervals alternating with interval where they coincide, has a unique weak solution given by:*

$$u(x,t) = \begin{cases} u_l & \text{if } x \le G'_\cup(u_l)t, \\ (G'_\cup)^{-1}(\frac{x}{t}) & \text{if } G'_\cup(u_l)t \le x \le G'_\cup(u_r)t \\ u_r & \text{if } x \ge G'_\cup(u_r)t \end{cases} \tag{8}$$

If $u_l < u_r$, and:

$$u(x,t) = \begin{cases} u_l & \text{if } x \le G'_\cap(u_l)t, \\ (G'_\cap)^{-1}(\frac{x}{t}) & \text{if } G'_\cap(u_l)t \le x \le G'_\cap(u_r)t \\ u_r & \text{if } x \ge G'_\cap(u_r)t \end{cases} \tag{9}$$

if $u_l > u_r$
where $G_\cup$ is the largest convex function on $[u_l, u_r]$ smaller than or equal to G and $G_\cap$ is the smallest convex function on $[u_l, u_r]$ greater than or equal to G.

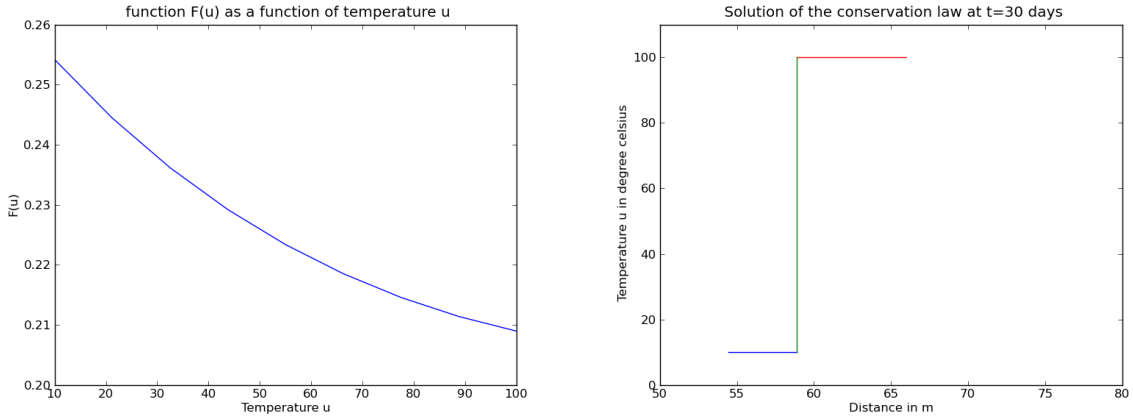

Figure 1. F (left) and unique entropy solution u of (7) at $t = 30$ days ($u_l = 10, u_r = 100$)

Thermal front velocity

From **Theorem 1**, the unique solution of (7) is given by Figure 1 at $t = 30$ days. This solution moves with speed s equal to the thermal front velocity V_{TF} given by the Rankine-Hugoniot shock condition [5]:

$$\begin{aligned} s = V_{TF} &= \frac{G(u_l) - G(u_r)}{u_l - u_r} \\ &= \frac{V_w}{(u_r - u_l)} \left(\int_{u_l}^{u_r} F(u) \mathrm{d}u \right), \quad V_w = \frac{u_w}{\phi}. \end{aligned} \tag{10}$$

where $F(u)$ is given as a function of temperature by (6) and Figure 1. The thermal front velocity v_{TF} was derived in [6] by using the characteristic method. Equation (7) was formulated as an initial-boundary value problem. The solution is non physical since there are points with multiple temperature values, see figure 2. A discontinuity was therefore inserted in the solution such that the position z of the discontinuity satisfies conservation of energy [6]:

$$t v_w \int_{u_l}^{u_r} U(u) F(u) \mathrm{d}u = z \int_{u_l}^{u_r} U(u) \mathrm{d}u \tag{11}$$

setting $v_{TF} = \frac{z}{t}$ we get

$$v_{TF} = v_w \left(\frac{\int_{u_l}^{u_r} U(u) F(u) \mathrm{d}u}{\int_{u_l}^{u_r} U(u) \mathrm{d}u} \right) \tag{12}$$

with

$$U(u) = (1 - \phi) \rho_r(u) c_r(u) + \phi \rho_w(u) c_w(u). \tag{13}$$

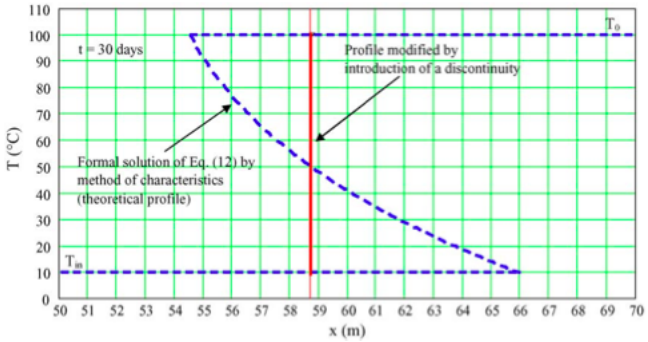

Figure 2. Non physical solution from the method of characteristics. Graph obtained from [6]

u_l	u_r	$V_{TF}(10^{-5}m/s)$ from (10)	$v_{TF}(10^{-5}m/s)$ from (12)	$V_{TF} - v_{TF}$
10	100	2.261	2.257	$4 * 10^{-8}$
55	100	2.15	2.15	0.0
10	55	2.370	2.369	10^{-8}
30	70	2.264	2.263	10^{-8}

Table 1. approximated values for evaluating (10) and (12) using the trapezoidal rule

n	E_1 (10^{-6})	E_2	E_3	convergence rate	$E_2/E_1(10^6)$	$E_3/E_1(10^6)$
4	351	663.35	469.2	(E_1): $[1.99, 2.01, 1.98]$	2.1	1.34
5	225	425.5	300.31	(E_2): $[2.00, 1.99, 2.02]$	1.9	1.33
6	156	294.8	208.5	(E_3): $[1.99, 2.00, 1.99]$	1.9	1.34
7	115	216	153.2		1.88	1.33

Table 2. Convergence test using the trapezoidal rule

Table 1 shows the values of the thermal front velocity for different range of temperatures. In Table 2, E_1 represent the upper bound error in evaluating (10) while E_2 and E_3 represent the upper bound error in evaluating the upper and the lower integral in (12). E_1 converge very rapidly to zero than E_2 and E_3 as given by the ratio E_2/E_1 and E_3/E_1. E_1, E_2 and E_3 where evaluated using a C code implementation of (10) and (12). The convergence rate is about 2, which is the order of the error of the trapezoidal rule.

Conclusion

For temperature dependent fluid and rock properties, injecting cold water into a hot geothermal reservoir can be formulated as a Riemann problem . The thermal front velocity coincide with the velocity of the discontinuity solution. Our result was compared with the result obtained in [6]. The error in evaluating the thermal front velocity from our result goes rapidly to zero compared with the error in evaluating the thermal front velocity obtained in [6].

References

[1] G. Axelsson. *Importance of Geothermal Reinjection.* Workshop for decision makers on direct heating use of Geothermal resources in Asia, 2008.

[2] J.J. Beall and M.C. Adams. *Tracing of Injection in The Geysers.* Geothermal resources Council, 18: 1551-159, 1994.

[3] W.R. Benoit and D. Stock. *Injection at the Beowawe Nevada Geothermal Reservoir.* Geothermal resources council, 17: 473-480, 1993

[4] G. Bodvarsson. *Thermal problem in siting of reinjection wells.* Geothermics 1(2): 63-66 , 1972.

[5] H. Holden and N. H. Risebro. *Front Tracking for Hyperbolic conservation laws.* New York: Springer, 2007

[6] J. Stopa and P. Wajnarowski. *Analytical model of cold water front movement in a geothermal reservoir* . Geothermics, 35: 59-69 2006.

[7] A.W. Woods and S.D. Fitzgerald. *Vaporisation of a liquid front moving through a hot porous rock*. J. Fluid Mech, 251: 563-579, 1993.

Proceedings of the 26th Nordic Seminar on Computational Mechanics
A. Logg, K.A. Mardal, A. Massing (Eds.)

Mathematical model of single crystal growth

Jan Blechta[1]

[(1)]Mathematical Institute of Charles University, Sokolovská 83, 186 75 Prague 8,
blechta@karlin.mff.cuni.cz

Summary. Mathematical model of a specific crystal growth problem is proposed. It incorporates heat transfer due to conduction, convection and a latent heat release and accounts for a jump in density due to phase change. Numerical algorithm using finite-element (FE) method and some implementational issues in FEniCS are presented.

Key words: solidification, heat transfer, FEniCS

Introduction

Vertical Bridgman method serves for a production of high-quality single crystals. Melted material is slowly pulled through temperature gradient such that material crystallizes. In work [1] we developed a model for a description of crystal growth in a particular Bridgman growth apparatus shown in figure 1. Heating and cooling conditions and pulling rate need to be specifically chosen to avoid homogeneous nucleation in a melt and to maintain phase interface being convex w.r.t. solid phase (as shown in figure 1). Hence the aim of the model is to predict temperature field in the system, position and shape of the phase interface.

Mathematical model

In figure 2 we present computational domains representing the system. On the domains occupied by some fluid – i.e. Ω, Λ and Δ – we solve for heat transfer due to conduction and natural convection, while in solid regions Φ, Ψ we solve merely heat conduction. Difference in a densities of solid and liquid $PbCl_2$ at melting point $\theta_\mathrm{m} = 774$ K is about 15%. As a result, the surface $\partial\Omega \cap \partial\Lambda$ changes its position within ampoule significantly during the whole process. This surface is material, hence Boussinsq-like mass balance $\operatorname{div} \mathbf{u} = 0$ would not be compatible with velocity boundary/interfacial conditions on $\partial\Omega$ and $\partial\Lambda$. We therefore use pseudo-incompressibility constraint instead so that we have balance equations

$$\operatorname{div}(\rho\mathbf{u}) = \alpha \qquad \text{in } \Omega, \Lambda, \Delta, \tag{1}$$

$$\rho\dot{\mathbf{u}} = -\nabla p + \operatorname{div}\mu\left(\nabla\mathbf{u} + \nabla\mathbf{u}^\top\right) - S\mathbf{u} + \rho\mathbf{g} \qquad \text{in } \left(\overline{\Omega}\cup\overline{\Lambda}\right)^\circ, \Delta, \tag{2}$$

$$\rho c_p^{\mathrm{eff}}\dot{\theta} = \operatorname{div}(\kappa\nabla\theta) \qquad \text{in } \left(\overline{\Omega}\cup\overline{\Lambda}\cup\overline{\Delta}\cup\overline{\Phi}\cup\overline{\Psi}\right)^\circ. \tag{3}$$

Quantity α approximates $-\rho'$ by a spatial constant in Ω and Λ separately and is taken as zero in Δ. In fact, we choose its value explicitly every time step to enforce mass conservation of $PbCl_2$ in Ω.

All the coefficients ρ, μ, S, c_p^{eff} and κ are continuous functions of temperature, different in all of the subdomains Ω, Λ, Δ, Φ, Ψ where applicable. Outside Ω, the coefficient S is zero and effective heat capacity c_p^{eff} is merely heat capacity at constant pressure c_p.

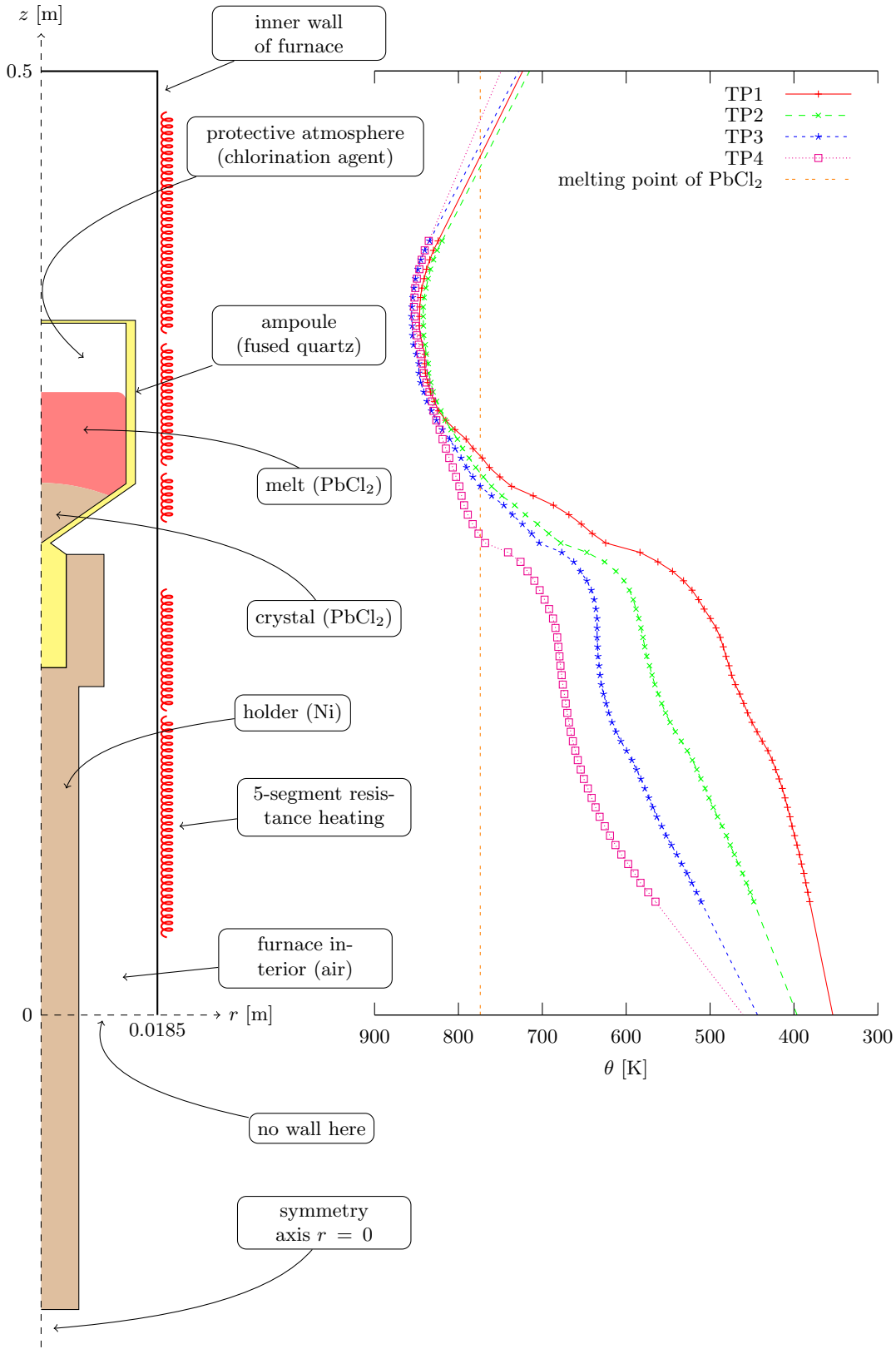

Figure 1. Scaled layout of used Bridgman apparatus. Aspect ratio is not preserved. Only half-section is shown – axial symmetry applies. On the right, four temperature profiles at the inner wall of furnace are shown. The points are measured values and the lines are linearly extrapolated from two outer values.

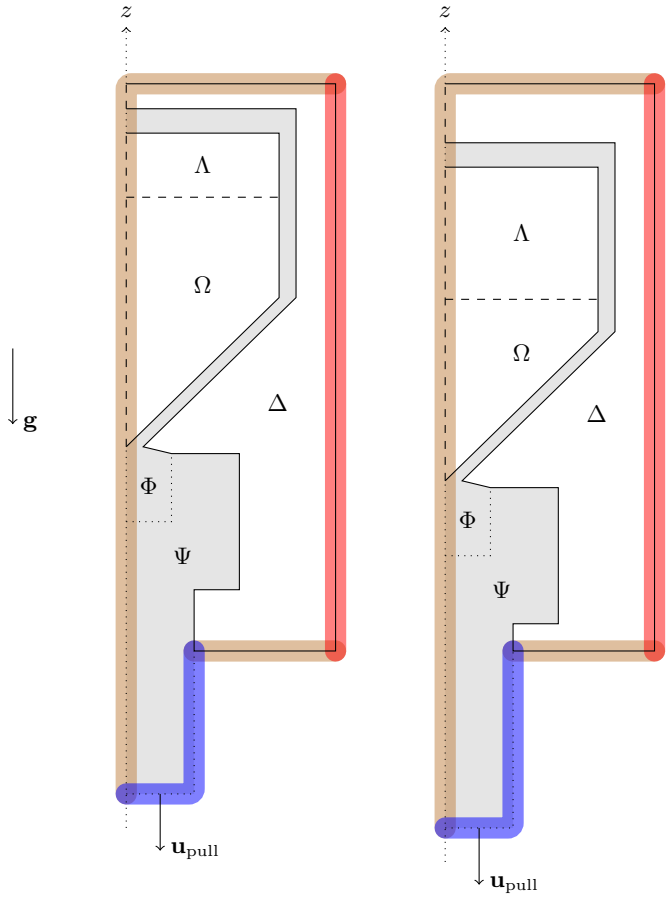

Figure 2. Schematic layout of computational domains in subsequent times: Ω – crystal and melt, Λ – protective atmosphere, Δ – air in furnace, Φ – ampoule, Ψ – holder; velocity boundary conditions: —— no-slip, - - - - free-slip, ····· not applicable; temperature boundary conditions: Dirichlet cooling $\theta = 350$ K, Dirichlet heating - see Figure 1, thermal insulation (zero Neumann condition). Note that domains $\overline{\Omega} \cup \overline{\Lambda}$, Φ and Ψ are rigid and they are moving downwards with constant velocity $\mathbf{u}_{\text{pull}}$ so that Δ is being deformed such that $\partial\Delta \backslash (\overline{\Phi} \cup \overline{\Psi})$ stays at rest.

There are both solid and liquid phase in domain Ω. We simply choose small numerical parameter ϵ of temperature dimension and let concentration of liquid phase be the approximate $\mathcal{C}^0$ Heaviside function

$$c(\theta) = \begin{cases} 0 & \theta \leq \theta_{\text{m}} - \epsilon \\ \left(\frac{\theta - \theta_{\text{m}}}{\epsilon} + 1\right)/2 & \theta_{\text{m}} - \epsilon < \theta < \theta_{\text{m}} + \epsilon \\ 1 & \theta \geq \theta_{\text{m}} + \epsilon \end{cases} . \tag{4}$$

Then we linearly interpolate material coefficients of solid and liquid $PbCl_2$ using $c(\theta)$ to get temperature dependence of ρ, c_p and κ. We add a multiple of the approximate $\mathcal{C}^0$ Dirac-δ to capacity c_p so that we obtain effective capacity c_p^{eff} incorporating latent heat of crystallization. No flow condition in solid phase $c = 0$ is enforced by Darcy-like forcing with S taking large values for $c = 0$ and being zero for $c = 1$. Viscosity of liquid $\mu = \mu(\theta)$ can simply be extended to a solid phase.

Similar enthalpy formulation with smeared latent heat has been suggesed by Gartling [2] and Morgan [3]. Darcy-like forcing approach has been proposed by Voller and Prakash [4]. Pseudo-incompressibility constraint is being typically used in Earth sciences.

Numerical algorithm

Problem (1)–(3) is transformed into a weak formulation using cylindrical coordinates thus exploiting axial symmetry of the growth system and making the problem two-dimensional. Deparis [5] gives a technical treatment on the Stokes/Navier-Stokes problem of axially-symmetrical flow and its FE discretization. We employ P2/P1/P1 spatial discretization.

The described model enables us to use a mesh not fitted to the phase interface. However, there are moving parts in the system and a mesh needs to be deformed every time-step. We use the Triangle library [6] to generate constrained Delaunay triangulation fitted to all the interfaces between Ω, Λ, Δ, Φ, Ψ and deform it in subsequent time-steps – (i) to meet the external constraint given by pull rate, (ii) to enforce a mass conservation of $PbCl_2$ by moving the melt surface $\partial\Omega \cap \partial\Lambda$, (iii) smoothing unconstrained vertices harmonically. When a mesh becomes poor-quality, a new one is generated and the fields are projected to respective function spaces. As a result, a projection error needs to be attenuated well, hence we employ backward Euler temporal discretization. Also reference frame velocities need to be considered on a moving mesh in a fashion of the ALE method.

The whole solution procedure is presented as algorithm 1. The algorithm was implemented using the FEniCS library [7]. Support of coupled calculations on multiple subdomains is currently under active development in FEniCS. Nevertheless, there is an usual workaround we used – (i) define unknown FE functions on a whole domain, (ii) eliminate redundant DOFs using the (algebraic) Dirichlet constraint. This is not optimal as it wastes computational resources. Due to this deficiency we also had to choose a possibly unrealistic interfacial condition – a continuity of a tangential velocity on surface $\partial\Omega \cap \partial\Lambda$.

We have tried to develop a parallel implementation. As the FEniCS lacks a support for evaluation of a FE function on non-matching meshes (needed in a projection step while remeshing) in parallel so far, we developed a workaround – `serial-meshes` branch of the DOLFIN library.[1] It enables building serial DOLFIN objects out of parallel ones and vice versa. The projection step is then performed by initializing a serial copy of a parallel function, performing supported serial projection and finally reconstructing a parallel function. Hence this step does not scale with available CPUs at all. Moreover, it requires that process performing a serial projection has memory to accommodate a whole function and both whole meshes thus canceling the opportunity to solve problems limited by memory demands using distributed memory. Next drawback is that data transfer between parallel and serial parts of the procedure is performed using a file system. All these properties are making this an inefficient, non-scalable hack.

Unfortunately, we did not succeed getting the parallel computation working reliably. We

[1] Available at `https://bitbucket.org/blechta/dolfin`.

```
prepare initial mesh;
compute initial condition;
while some liquid PbCl2 remains do // time-stepping
    if mesh quality is poor then
        create new mesh and project fields onto it;
    end
    pull rigid domains Ω ∪ Λ, Φ, Ψ downwards;
    smooth mesh harmonically in Δ;
    set reference frame velocity and no-slip condition in Δ;
    move vertices on ∂Ω ∩ ∂Λ so that mass in Ω is conserved;
    set reference frame velocity, no-slip condition and α in Ω, Λ;
    solve field equations;
end
```

Algorithm 1: Algorithm of entire calculation.

suspect an outdated OpenMPI library known to causing problems operating on the Karlín cluster[2] although we cannot exclude possible bug in the our code, the FEniCS, `serial-meshes` or a stack of other used libraries.

Resulting discrete nonlinear system was solved using FEniCS built-in Newton method with an automatic differentiation and LU method for a solution of linear algebraic systems.

Results

Experimental measurements of temperature were performed by Král [8] on the system of interest. Obtained numerical results were in a qualitative agreement with expected behaviour but quite large discrepancies were observed in a comparison to the experimental results. We proposed two sorts of possible explanations – (i) unrealistic boundary conditions for temperature on $\partial\Psi$ were used for our computations, (ii) the experimental arrangement influences two much the measured system. To confirm or disprove suggestion (ii), numerical simulations using this experimental arrangement could be run and compared to the performed simulations of the original growth system. However, this would require additional development of an efficient preconditioning algorithm, a transition to Krylov solver and other implementational tweaks – most notably mesh generation and marking facilities – to handle 3D computations because the aforementioned experimental arrangement does not preserve axial symmetry.

References

[1] J. Blechta. *Mathematical modeling of crystal growth*. Master thesis, Charles University in Prague, 2013. Available online at `http://artax.karlin.mff.cuni.cz/~blecj6am/thesis/`.

[2] D. K. Gartling. Finite element analysis of convective heat transfer problems with change of phase. *Computer Methods in Fluids*. (Eds. K. Morgan et al.), Pentech, London, 1980, pp. 257–284.

[3] K. Morgan. A numerical analysis of freezing and melting with convection. *Computer Methods in Applied Mechanics and Engineering*, 28(3):275–284,1981.

[4] V. R. Voller and C. Prakash. A fixed grid numerical modelling methodology for convection-diffusion mushy region phase-change problems. *International Journal of Heat and Mass Transfer*, 30(8):1709–1719,1987.

[5] S. Deparis. *Numerical Analysis of Axisymmetric Flows and Methods for Fluid-Structure Interaction Arising in Blood Flow Simulation*. PhD thesis, École polytechnique fédérale de Lausanne, 2004.

[6] J. R. Shewchuk. Triangle: Engineering a 2D Quality Mesh Generator and Delaunay Triangulator. *Applied Computational Geometry: Towards Geometric Engineering*. (Eds. M. C. Lin, D. Manocha), Springer, Berlin, 1996, pp. 203–222.

[7] A. Logg, K.-E. Mardal, G. N. Wells (Eds.) *Automated Solution of Differential Equations by the Finite Element Method*. Springer, Heidelberg, 2012. ISBN 978-3-642-23098-1.

[8] R. Král. Study on influence of growth conditions on position and shape of crystal/melt interface of alkali lead halide crystals at Bridgman growth. *Journal of Crystal Growth*, 360:162–166,2012.

[2] `http://cluster.karlin.mff.cuni.cz`

Proceedings of the 26th Nordic Seminar on Computational Mechanics
A. Logg, K.A. Mardal, A. Massing (Eds.)

Thrombosis modeling in stented cerebral aneurysms with Lattice Boltzmann method

Kartik Jain[1,*], Simon Zimny[1,2], Harald Klimach[1] and Sabine Roller[1]

(1) University of Siegen, Simulation Techniques and Scientific Computing, Siegen, Germany
(2) German Research School for Simulation Sciences and RWTH Aachen University, Aachen, Germany

Summary. This contribution presents the results of numerical simulations of thrombosis in a patient specific cerebral aneurysm, deployed with stents of different porosity. The thrombosis models are based on low wall shear stress constraint and high residence time of fluid. Simulations have been performed with a massively parallel Lattice Boltzmann solver on 8192 cores of Intel Sandy Bridge processors. Our studies show that the treatment of a cerebral aneurysm with a flow diverter stent induces thrombosis in the aneurysm bulge, which is even more intense with a less porous stent, due to enhanced flow diversion.

Key words: cerebral aneurysm, stent, thrombosis, Lattice Boltzmann method

Introduction

A cerebral aneurysm is a weak balloon like bulging of the wall of a brain artery. Rupture of an aneurysmal sac, termed subarachnoid hemorrhage (SAH) is a lethal condition and endovascular treatments have proved to be a good alternative over surgical options for their cure. Deployment of a flow diverter stent is one such treatment, the goal of which is to trigger the process of thrombosis inside the aneurysm by changing the local flow properties. Configuration and porosity of the stent plays a significant role on the aneurysmal fluid dynamics and consequently on thrombosis. Thrombosis modeling is a multiscale problem and its application in a patient specific case requires the use of efficient numerical techniques together with high performance computing resources [1]. We employ the Lattice Boltzmann method (LBM) with thrombosis models based on flow properties to qualitatively observe the changes in clotting inside an aneurysm bulge after the deployment of a stent.

Numerical Method

The Lattice Boltzmann Method

The Lattice Boltzmann method, which is based on the mesoscopic representation of fictional particle movements, is a numerical technique to simulate incompressible flows. The particles collide and stream on a fixed grid and in fixed directions, each of which have discrete velocities, to relax towards a thermodynamic equilibrium. Evolution of these particles over time is described by the Lattice Boltzmann equation with the BGK collision operator:

$$f_i(\mathbf{r} + \mathbf{c}_i \Delta t, t + \Delta t) = f_i(\mathbf{r}, t) + \Omega \left(f_i^e(\mathbf{r}, t) - f_i(\mathbf{r}, t) \right) \tag{1}$$

where f_i denotes the probability of finding a particle with discrete velocity $\mathbf{c}_i$ at a position $\mathbf{r}$ at time t. The indices which run from $i = 1 \ldots Q$ denote the links per element i.e. the discrete

*Corresponding Author. Tel: +49-(0)271-74-03882; E-mail address: kartik.jain@uni-siegen.de

directions, depending on the chosen stencil (D3Q19 in our case). The BGK collision operator Ω implies a single relaxation time at which distributions f_i relax towards the equilibrium f_i^e:

$$f_i^e = w_i \rho \left(1 + \frac{\mathbf{c}_i \cdot \mathbf{u}}{c_s^2} - \frac{\mathbf{u}^2}{2c_s^2} + \frac{1}{2} \frac{(\mathbf{c}_i \cdot \mathbf{u})^2}{c_s^4} \right) \tag{2}$$

where w_i are the weights for each discrete link, c_s is the speed of sound in vacuum and $\mathbf{u}$ is the fluid velocity.

Flekkøy model for convection-diffusion in LBM

The Flekkøy model for passive scalar transport [2] is analogous to the transport of distributions within the LBM and is used in our thrombosis models to trace the age of the fluid. The transport counterparts of eqns. 1 & 2 for the Flekkøy model read:

$$\Delta_i(\mathbf{r} + c_i \Delta t, t + \Delta t) = \Delta_i(\mathbf{r}, t) + \Omega_D(\Delta_i^e(\mathbf{r}, t) - \Delta_i(\mathbf{r}, t)) \tag{3}$$

$$\Delta_i^e = w_i \rho \left(1 + \frac{\mathbf{c}_i \cdot \mathbf{u}}{c_s^2} \right) \tag{4}$$

where Δ_i represents the probability distributions for the species, $\mathbf{u}$ is taken from the underlying fluid and the relaxation parameter Ω_D is now dependent on the diffusion coefficient. For the species, a reduced D3Q6 stencil is used. Since the convection-diffusion equation itself does not contain any quadratic $\mathbf{u}$ terms, they are allowed to vanish in the equilibrium distribution Δ_i^e as well. The kinematic viscosity and the diffusion coefficient are determined by:

$$\nu = \frac{1}{6} \left(\frac{2}{\Omega} - 1 \right) \qquad D = \frac{1}{6} \left(\frac{2}{\Omega_D} - 1 \right) \tag{5}$$

Thrombosis models based on flow properties

The thrombosis models used in this study are based on local flow properties namely *Wall shear stress* and *Residence time* of fluid. An additional *proximity condition* is imposed on both these models, which allows only those fluid elements to turn into solid which are already attached to wall or previously formed clot. This condition ensures that no isolated clots appear in the center of the domain or near the in/outlets.

Wall shear stress constraint

Thrombosis is believed to occur in areas of low wall shear stress (WSS) and being locally driven by the blood shear rate near the vessel walls, which is controlled by a threshold [3]. This threshold level is influenced by factors like platelets, tissue, physiology etc. [3]. The occurrence of thrombosis in areas of low WSS is further supported by the fact that high shear can nevertheless wash away the onset of thrombosis. Numerically, WSS is computed for each element in the vessel to allow the decision for solidification together with the proximity condition.

Residence time model

Medical literature illustrates the coagulation of blood as a time dependent process [4]. The reason is that the activated platelets and procoagulants which are present in the blood need sufficient time to aggregate and form clots. This inspires the use of a residence time model as an additional constraint to the WSS for thrombosis modeling [5]. The residence time is computed by injecting a passive scalar, convection of which traces the age of the underlying fluid. The decision for solidification of elements in this model thus depends on the residence time and WSS thresholds along with the proximity condition.

Simulation Parameters

The patient specific aneurysm and the stent geometry were provided as surface meshes in STL format. Simulations were performed with our fully parallel Multiphysics framework *Apes* [6]. The mesh generation tool *Seeder* [7] created a voxelized mesh that was used by the LBM solver *Musubi* [8] for computations, and finally visualized by the post-processing tool *Harvester*.

The stented aneurysm geometry is shown in fig. 1(a). For a reasonable resolution of the stent, the mesh was discretized with cubical elements of $\delta x = 65\mu$m which resulted in nearly 45 million fluid elements. Stent pores which are located towards aneurysmal sac are $\sim 585\mu m \times 295\mu m$ which gave us roughly 55 fluid elements between the pores, whereas the struts were resolved with nearly 1 element. The parent artery diameter was $D_{artery} \sim 3.96mm$. The simulation time step was $\delta t = 28.9\mu$s and inlet velocity $u_{in} = 9.435 \times 10^{-2}$m/s. Density and kinematic viscosity of the blood were respectively set to $\rho = 1025$kg/m^3 and $\nu = 3.8 \times 10^{-6}$m^2/s. The parent artery Reynolds number was 50 based on D_{artery}, $u_{mean} = u_{in}/2$ and the prescribed blood properties. The simulations were performed using 8192 cores of the *SuperMUC* x86 cluster, at LRZ Munich.

Simulation Results

Thrombosis with wall shear stress constraint

Figure 1(b) shows the onset of thrombosis in the stented aneurysm with an upper WSS threshold of $1.037 \times 10^{-2} Pa$. The clotting was initiated after the simulation achieved a steady state and the clots continued to grow up to nearly 8000 iterations after that.

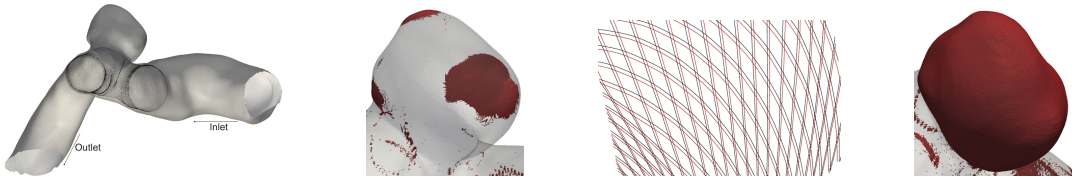

(a) Stented aneurysm (b) Thrombosis with 1 stent (c) Cross section of 2 telescoped stents (d) Thrombosis with 2 stents

Figure 1: Thrombosis with a wall shear stress threshold of WSS $\leq 1.037 \times 10^{-2} Pa$.

Telescoping stents

A common treatment for wide neck aneurysms is multiple stent-in-stent deployments which are surgically carried out in a telescoping fashion [9]. Fig. 1(c) shows such an overlay of stents which decreased the porosity of the original stent by $\sim 1.5\times$, and consequently increased the clotting in the bulge dramatically for the same shear threshold (fig. 1(d)).

Thrombosis with residence time model

Figure 2 shows thrombosis growth in the aneurysm, post deployment of a single stent with thresholds of $t_{thr} \geq 3.88s$ & WSS $\leq 1.037 \times 10^{-1} Pa$. Unlike the WSS model, the clots cultivated

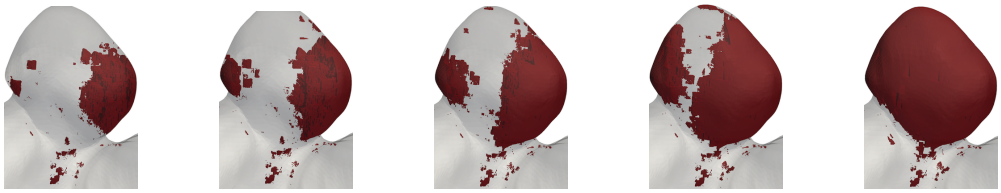

Figure 2: Thrombosis progression with residence time model: 10^5, $2 \cdot 10^5$, $3 \cdot 10^5$ and $4 \cdot 10^5$, $6.6 \cdot 10^5$ time steps after clotting initiation. Thresholds are $t_{thr} \geq 3.88s$ & WSS $\leq 1.037 \times 10^{-1} Pa$. Complete bulge obliterated after $1.3 \cdot 10^6$ time steps.

in layers with this model to eventually obliterate the complete aneurysm bulge. *Telescoping* of stents with this model showed similar results, but the complete occlusion was ~ 1.4 times faster

as the less porous stent did not only decrease the shear stress, but it also increased the residence time of fluid inside the bulge markedly.

Conclusions

These results qualitatively show that stent deployment sparks the onset of thrombosis in a side wall aneurysm and the technique of telescoping stents looks promising for treatment of such aneurysms. The use of LBM seems very suitable for such simulations due to its ease in handling complex boundary conditions and resolving a stent. The residence time model puts an additional constraint to shear stress and mimics biology more meticulously as the clots grow in layers over time. It is however too early to quantify the performance of different stents with the use of time independent flow and assuming blood as a Newtonian fluid. Our future work will cover investigations with pulsating flow due to cardiac cycle and non-Newtonian models on different classes of aneurysms like those with bifurcation, with physiologically realistic parameters.

Acknowledgements

The geometries used for these studies were provided by the *THROMBUS* project, funded by the EU in the FP7 in the area of VPH (ICT-2009.5.3, PR 269966). Computer resources for this project were provided by the Leibniz Supercomputing Center under grant *pr45du*.

References

[1] S. Zimny, B. Chopard, O. Malaspinas, E. Lorenz, K. Jain, S. Roller, and J. Bernsdorf. A multiscale approach for the coupled simulation of blood flow and thrombus formation in intracranial aneurysms. In *ICCS 2013*, Barcelona, Spain, 2013.

[2] E.G. Flekkoy. Lattice BGK models for miscible fluids. *Physical Review*, 47(6):4247–4257.

[3] R. Ouared, B. Chopard, B. Stahl, D. A. Rüfenacht, H. Yilmaz, and G. Courbebaisse. Thrombosis modeling in intracranial aneurysms: a lattice Boltzmann numerical algorithm. *Computer Physics Communications*, 179(1):128–131, 2008.

[4] R. I. Lee and P. D. White. A clinical study of the coagulation time of blood. *The Americal Journal of The Medical Sciences*, 145(4):495–503, 1913.

[5] J. Bernsdorf, S E Harrison, S. M. Smith, P V Lawford, and D R Hose. Concurrent numerical simulation of flow and blood clotting using the lattice boltzmann technique. In *ICPADS'05*, volume II, pages 336–340. IEEE, July 2005.

[6] S. Roller, J. Bernsdorf, H. Klimach, M. Hasert, D. Harlacher, M. Cakircali, S. Zimny, K. Masilamani, L. Didinger, and J. Zudrop. An adaptable simulation framework based on a linearized octree. In *High Performance Computing on Vector Systems 2011*, pages 93–105. Springer Berlin Heidelberg, 2012.

[7] D. F. Harlacher, M. Hasert, H. Klimach, S. Zimny, and S. Roller. Tree based voxelization of stl Data. In *HPC on Vector Systems 2011*, pages 81–92. Springer Berlin Heidelberg, 2012.

[8] M. Hasert, S. Zimny, K. Masilamani, J. Qi, H. Klimach, J. Bernsdorf, and S. Roller. The parallel octree-based lattice boltzmann simulation framework musubi. `https://bitbucket.org/apesteam/musubi`, 2013.

[9] B. N. Roszelle, L. F. Gonzalez, M. H. Babiker, J. Ryan, F. C. Albuquerque, and D. H. Frakes. Flow diverter effect on cerebral aneurysm hemodynamics: an in vitro comparison of telescoping stents and the pipeline. *Neuroradiology*, 55(6):751–758, 2013.

Proceedings of the 26th Nordic Seminar on Computational Mechanics
A. Logg, K.A. Mardal, A. Massing (Eds.)

Investigation of Patch Coatings Influence on the Stress Intensity Factor for Surface Cracks

Soren Heide Lambertsen[1], Michael S. Jepsen, Lars Damkilde,

(1)Division of Structures and Materials, Aalborg University Esbjerg Denmark, shl@civil.aau.dk

Summary. In this paper, it is investigated how a surface layer of epoxy glue will affect the crack propagation of a surface crack. The intension is to reduce or even stop the crack propagation by means of patch layer coating. When adding a patch layer to the surface with small cracks, the layer will attempt to clamp the free end of the crack, which will reduce the stress intensity factor and subsequently reduce the crack growth. The considered patch consists of a surface layer of 0.2 mm two component adhesive Epoxy, 3M DP 460. The models described in this work contains five different crack sizes with a patch layer on the surface. The stress intensity factor is computed by means of the J-integral and the FE-model is setup with a nonlinear material model to establish the upper boundary for the patch stress capacity. A reduction of the stress intensity factor of approximately 2 % and a reduction of the crack growth of 5.4-6.1 % for crack sizes of 0.5, 1 and 2 mm is achieved by applying the patch layer. In the analysis, cracks of 3 mm and 5 mm are rejected due to plastic strain in the patch layer, consequently the effect of the patch layer is insignificant.

Key words: Patch repairing, Fatigue life, Stress intensity factor.

Introduction

Repairing of cracks with reinforced patches is applicable for several types of structures. In the industry the reinforced patch repairing technique is often used where replacement of damaged components is not possible. This is frequently the case in the aircraft industry where the patch repairing method is used to repair cracks. Cracks, which are repaired with this technique will normally be fully developed, i.e. these cracks are about 1 mm, and in the case of a surface crack they will be visible to the naked eye. The patch repairing technique is able to stop or slow down the crack propagation in a damaged component. The major advantage of the method compared to the hole-drilling method is that no additional stress concentration field is established. Consequently the patch repairing technique is straightforward to implement.

The patch is usually a composite of epoxy and carbon fibers, where the epoxy connects the carbon fibers to the steel or aluminum structure [1]. Further, the epoxy connects the fibers together, and the fibers add stiffness and strength to the patch. Consequently, the addition of fibers will unload the crack front significantly, by redistributing the stresses in the cracked area. Thus, the crack propagation stops or slow down.

The succeeding study investigates how a surface layer of epoxy affects the stress intensity factor. A patch layer at the surface can reduce the stress intensity factor because the layer will attempt to maintain the crack surface together. Consequently, the implementation of a patch layer before finishing with the original painting will slow down the rate of crack propagation [2]. It is the modulus of elasticity of the patch, which controls the reduction of the stress intensity factor [3]. A limited reduction in stress intensity factor can change the crack growth significantly.

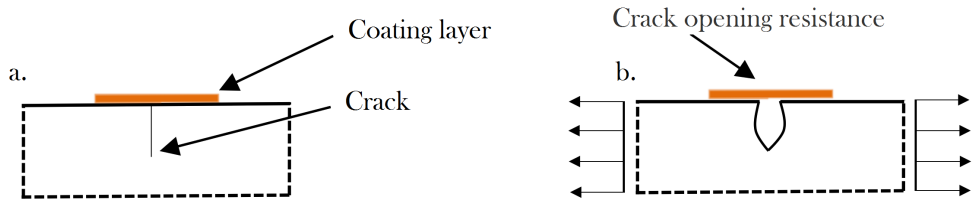

Figure 1. a. Shows a non-loaded surface crack with a layer of coating, b. Illustrates a loaded crack with coating.

Figure 1 a) shows a unloaded coated defect and Figure 1 b) shows the mechanical behavier after loading. Normally the coatings modulus of elasticity is much lower than the component material. Consequently, the coating will elongate and the crack surfaces will separate as shown in figure 1 b).

As mentioned the modulus of elasticity controls the separation of the crack surfaces. The modulus of elasticity of ordinary water-based coating is low compared to the epoxy-based coatings. Further the epoxy-based coatings also has higher strength. Thus, it will be more beneficial to use epoxy-based coating to take advantage of the higher modulus of elasticity [4]. The modulus of elasticity can be further increased by intermixing the patch matrix by adding glass or carbon fibers. If the modulus of elasticity is infinite, no separation occur and the stress intensity factor is comparable with a center crack. A upper bound for the stress intensity factor of a coated crack is then a edge crack and the lower bound of the stress intensity factor is a center crack. Identification of the ratio of the patch effect on the stress intensity factor, is achieved by dividing the stress intensity factor for a center crack and an edge crack, cf. Eq.1.

$$\frac{K_{ICenter}}{K_{IEdge}} = \frac{\sqrt{1/2}\sigma\sqrt{a\pi}}{1.12\sigma\sqrt{a\pi}} = 0.63 \tag{1}$$

The effect of the coating patch is then calculated to a ratio of 0.63, cf. Eq.1. However, the patch is not able to obstruct separation of the free end of the crack. In the succeeding FE-analysis and the J-integral is used to study the stress intensity factor in a case where the free end of the crack is coated.

Fatigue Damage Calculation

In this case, the crack propagation is the main parameter for the fatigue damage, as the variation in stress intensity factor govern the crack propagation. The stress intensity factor K is a function of the far field stress and the crack size and is given in Eq. 2.

$$\Delta K = \Delta\sigma\sqrt{\pi a}\alpha \tag{2}$$

In the analytical expression the influence of the surface layer adjust the α value and thereby the stress intensity factor. However, in the case of the FE-analysis the stress intensity factor is calculated by the J-Integral and thereby α can be calculated.

In the estimation of the surface layers influence on the crack propagation, a 5 % crack propagation is used. The number of cycles before a specific crack length propagates is calculated with Eq. 3.

$$N_f = \frac{2}{(n-2)A(\Delta\sigma)^n(\pi)^{3/2}\alpha^n}\left[\frac{1}{a_i^{(n-2)/2}} - \frac{1}{a_f^{(n-2)/2}}\right] \tag{3}$$

Where a_i and a_f is the start and stop crack length and $\Delta\sigma$ is the stress variation. The material parameters used in the calculation are $A = 6.9 \cdot 10^{-12} m/cycle$ and $n = 3$.

The Finite Element Model

The study is carried out in Ansys Workbench 14.5 and computes the stress intensity factor for the coated cracks. A 2D model is used to determine the coatings influence on the stress intensity factor, see figure 2. The number of elements for the 1 mm cracked body is 12060 and 384 elements for the coating layer. The element type used in the analysis is PLANE183 higher order 2-D elements. Computing of the stress intensity factor for five crack sizes are present. The crack sizes are 0.5, 1, 2, 3 and 5 mm. The patch layer is added when the crack is closed. No separation or slip are assumed to occur in the bonding between the crack surfaces and the coating. In this study, the patch coating material 3M DP460 has limited strength, about 27.6 MPa. To include the limited strength of the patch layer in the FE analysis, a nonlinear material model is applied. A bilinear material behavior is used in the FE-model, with a Youngs modulus

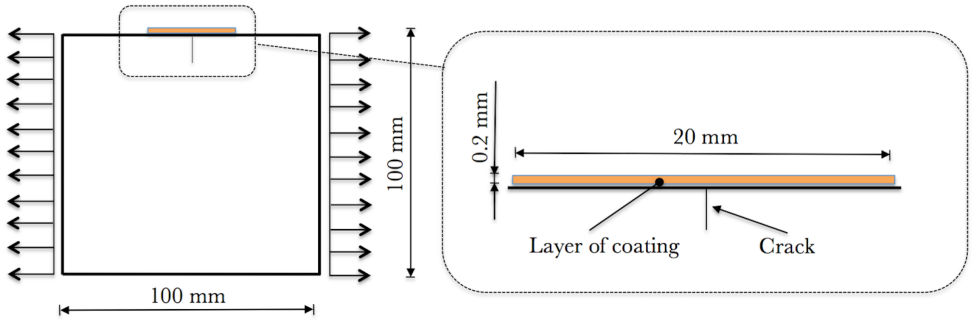

Figure 2. The crack model used for the FE analysis in Ansys Workbench.

of 2.7 GPa to the yield limit of 27.6 MPa. Beyond yielding the tangent modulus is set to 0 MPa. Further the coating has a thickness at 0.2 mm and is 30 mm wide see figure 2. The far field stress level is a tension stress state at 100 MPa. The plastic behavior is studied in 11 load cycles. The crack part is a isotropic elastic material with a young modulus of 200 GPa. The mesh is shown in figure 3. The mesh of the patch layer contains four elements in thickness and the crack have six rings of elements surrounding the crack tip.

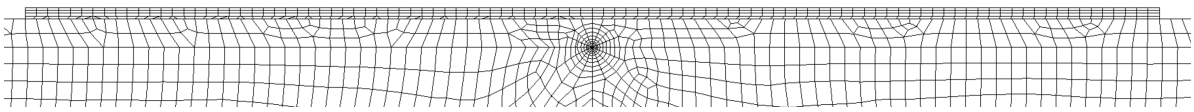

Figure 3. The mesh for the 1 mm crack with a coating layer at the surface.

Results

Results of the FE solution are shown in table 1. The stress intensity factor has constant amplitudes in cases of a crack size 0.5, 1 and 2 mm.

In the calculations with crack sizes of 3 mm and 5 mm, the stress intensity factor changes for every load cycle, especially in the first three load cycles the changes are significant. The strain level in the layer exceeds the elastic limit at 27.6 MPa. Then irreversible strains occur in the layer and looses its effect on the stress intensity factor. Consequently the calculations of the 3mm and 5mm cracks are not considered relevant. The results of crack sizes 0.5, 1 and 2 mm shows a reduction in stress intensity factor of 1.7-2.0 %. The number of cycles to propagate the cracks 5% is calculated, and the result is shown in table 2. In the case of a 1 mm crack, the number of cycles is increased by 22464 cycles or 6.1%. The α value changes from 1.12 to

Table 1. Results of the stress intensity factor with and without layer of coating on the surface.

Crack Size / Coating Method	0.5 mm	1 mm	2 mm	3 mm	5 mm
Coated	137.7	194.9	276.8	340.8-341	446.3-446.5
Non-coated	140.2	198.8	281.7	346.1	450.0
% changes stress intensity	1.8	2.0	1.7	1.5	0.8

about 1.1 in the cases where the patch layer is applied. However it is clear that the patch layer changes the stress intensity factors and thereby the α parameter.

Table 2. Result of changes in the number of cycles with and without a layer of coating on the surface.

Crack Size	0.5mm	1mm	2mm
α coated	1.0985	1.0996	1.1041
α non-coated	1.1184	1.1217	1.1237
Life coated	777614	387641	191460
Life non-coated	736840	365177	181615
% changes life	5.5	6.1	5.4

Conclusion

The investigation shows that the potential of the patch layer is insignificant due to the low elastic strength and low modulus of elasticity of the patch layer. It is computed that the patch layer changes the stress intensity factor by 1.7-2 % for cracks < 2 mm. The changes for a crack to propagate 5% of the original length are also calculated. This shows that the patch layer changes the number of cycles for the crack to grow by 5.4-6.1 %. It can be concluded that the use of pure epoxy as patch repairing method is not beneficial. It is noted that the patch layer will have an improved impact, if the modulus of elasticity and the elastic strength of the patch layer is increased.

References

[1] Woo-Yong Leea, Jung-Ju Leeb, Successive 3D FE analysis technique for characterization of fatigue crack growth behavior in composite-repaired aluminum plate,

[2] Dae-Cheol Seo, Jung-Ju Lee. Fatigue crack growth behavior of cracked aluminum plate repaired with composite patch, *Composite Structures*, Volume 57 Issues 1-4 July 2002 Pages 323-330.

[3] S. Naboulsi, S. Mall Characterization of fatigue crack growth in aluminium panels with a bonded composite patch, *Composite Structures*, Volume 37 Issues 3-4 March-April 1997 Pages 321-334

[4] Yaowen Yang, Bahador Sabet Divsholi, Lihua Tang, and Lei Zhang, Strain Transfer Models for Macrofiber-Composite Strain Actuators, *Materials and Manufacturing Processes*, Volume 25, 237-242, 2010

Proceedings of the 26th Nordic Seminar on Computational Mechanics
A. Logg, K.A. Mardal, A. Massing (Eds.)

Preliminary study of the impact of spinal cord nerve roots and denticulate ligaments on drug movement in the cervical spinal subarachnoid space

Mikael Mortensen[1,2], Kent A. Mardal[2], Soroush H. Pahlavian[3] and Bryn A. Martin[3]

(1)Dept. of Mathematics, University of Oslo, Moltke Moe's vei 35, 0851 Oslo, mikaem@math.uio.no
(2)Simula Research Laboratory, Martin Linge's vei 17, 1325 Lysaker, Norway
(3)Conquer Chiari Research Center, Dept. of Mechanical Engineering, University of Akron, Akron, OH, U.S.A.

Summary. Transport of drugs that are infused in the cerebrospinal fluid (CSF) within the cervical spinal subarachnoid space (SSS) for chronic neurological conditions is poorly understood. For example, the impact of fine anatomy on drug movement is not known. The lack of understanding is largely due to the difficult measurement access to the cervical SSS.

In this work we utilize computational fluid dynamic (CFD) simulations of CSF to provide detailed information about the impact that nerve roots and denticulate ligaments (NRDL) have on drug movement in the SSS. We do this by simulating two separate cases of the SSS, one with and the other without the internal NRDL. We find that the inclusion of NRDL leads to a higher pressure drop throughout the SSS. Inclusion of NRDL is also found to disturb the flow by setting up a more complex flow pattern with strong and persistent vortical structures that, even though not turbulent, greatly enhances mixing and movement of drugs along the SSS.

This work could help the development of new tools to place spinal catheters in the most optimal location on a subject specific basis and help design improved spinal drug delivery catheters.

Key words: Cerebrospinal fluid, Computational Fluid Dynamics, drug diffusion, nerve roots, denticulate ligaments, cervical spinal subarachnoid space

Subject specific computational mesh

A three dimensional geometry of cervical SSS is shown in Figure 1. The anatomical model was constructed based on manual segmentation of T2-weighted magnetic resonance (MR) image sequences of a healthy volunteer using freely available software ITK-Snap (Version 2.2, University of Pennsylvania). Idealized NRDL were separately constructed and added to the model using Autodesk Maya (Autodesk Inc., Cleveland, OH). Nonuniform unstructured computational meshes were generated using ANSYS ICEM CFD (ANSYS Inc., Canonsburg, PA). An example of the surface elements of the computational mesh is shown in Figure 1 (c). The complete geometry [Figure 1 (a)] is 18 cm from top to bottom and the two end planes are both placed in the xz-plane.

CFD simulations

Simulations have been performed using the open source Navier-Stokes solver *Oasis* [2] - a high-level/high-performance solver utilizing the Python interface to FEniCS [1]. We solve the incompressible Navier-Stokes equations for the fluid flow and a scalar advection equation for the injected drug. The drug is injected at the same temperature and density as the spinal fluid and we assume that the total amount of drugs is negligible compared to the total volume of fluid.

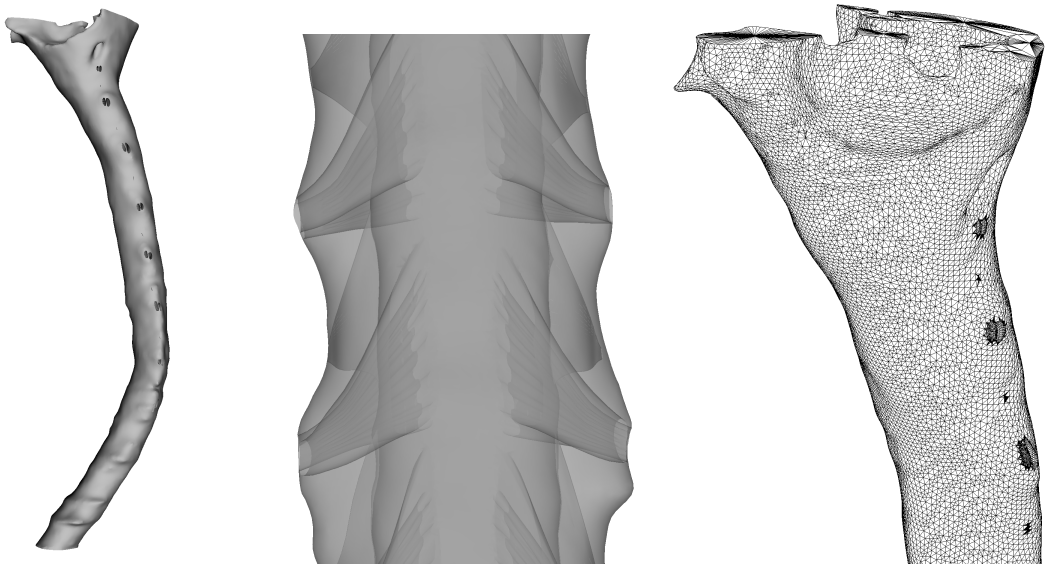

(a) (b) (c)

Figure 1: SSS geometry and computational surface mesh. (a) Complete surface model. (b) Transparent model showing nerve roots and denticulate ligaments. (c) Surface elements of the final computational mesh.

Hence there is no feedback to the Navier-Stokes equations from the drug and the injection does not disturb the flow.

Oasis is set to use regular linear (P1-P1) Lagrange finite elements (higher order can easily be chosen), collocated for both velocity, pressure and drug. The velocity and pressure are solved for in a segregated manner, utilizing a second order accurate in time fractional step method (incremental pressure correction). The discretized system of equations being solved (before constructing the finite element weak forms) is:

$$\frac{\boldsymbol{u}^I - \boldsymbol{u}^{n-1}}{\triangle \mathrm{t}} + (\overline{\boldsymbol{u}} \cdot \nabla)\tilde{\boldsymbol{u}} = \nu \nabla^2 \tilde{\boldsymbol{u}} - \nabla p^{n-3/2}, \tag{1}$$

$$\nabla^2 p^{n-1/2} = \nabla^2 p^{n-3/2} - \frac{1}{\triangle \mathrm{t}} \nabla \cdot \boldsymbol{u}^I, \tag{2}$$

$$\boldsymbol{u}^n = \boldsymbol{u}^I - \triangle \mathrm{t} \nabla (p^{n-1/2} - p^{n-3/2}), \tag{3}$$

$$\frac{c_\alpha^n - c_\alpha^{n-1}}{\triangle \mathrm{t}} + \overline{\boldsymbol{u}} \cdot \nabla \tilde{c}_\alpha = D_\alpha \nabla^2 \tilde{c}_\alpha + f_\alpha, \tag{4}$$

where $\boldsymbol{u}$, ν (10^{-6} $\mathrm{m^2 s^{-1}}$), p, c_α and D_α (10^{-7} $\mathrm{m^2 s^{-1}}$) are, respectively, the velocity vector, kinematic viscosity, pressure, drug concentration and drug diffusivity. The superscript n denotes timestep and superscript I is used for an intermediate velocity. The Adams-Bashforth projected velocity $\overline{\boldsymbol{u}} = 1.5\boldsymbol{u}^{n-1} - 0.5\boldsymbol{u}^{n-2}$ and the Crank-Nicolson interpolated velocity $\tilde{\boldsymbol{u}} = 0.5(\boldsymbol{u}^I + \boldsymbol{u}^{n-1})$ are both second order accurate in time. The fractional step method can be used both non-iteratively or with iterations over the pressure velocity system [Eqs. (1) and (2)], but in this work we have only used it non-iteratively. The drug is computed using Crank-Nicolson interpolation $\tilde{c}_\alpha = 0.5(c_\alpha^n + c_\alpha^{n-1})$. There is no added stabilization since we in this work have used a rather large mass diffusivity to speed up and stabilize calculations. The Schmidt number (ratio of momentum diffusivity and mass diffusivity) of the drug is as such set to 10. For future reference, stabilization will be required for more realistic diffusivities with Schmidt number in the order of 1000.

Table 1: Flow rate, [ml/s] through bottom of geometry. One cycle takes 0.78 sec.

time [s]	[ml/s]	time [s]	[ml/s]	time [s]	[ml/s]	time [s]	[ml/s]
0.00	1.74	0.20	-3.43	0.39	-0.75	0.59	0.56
0.07	1.05	0.26	-2.84	0.45	0.16	0.65	0.92
0.13	-1.61	0.33	-2.05	0.52	0.28	0.72	1.41

The flow through the spine is oscillating up and down and the velocity is fixed in the bottom inlet of the geometry using Dirichlet boundary conditions. The magnitude of the velocity is taken from 4D MRI measurements that are reproduced in Table 1. The pressure is fixed at zero in the top outlet of the geometry.

The drug is introduced through the source term f_α using a constant spherical source located in the lower part of the spine centred at $y = 6$ cm. The source is held fixed for the first two cycles of flow and is then set to zero. The flow is run for a total of 70 cycles and thus for the last 68 cycles the drug is simply transported throughout the spine due to the flow. The concentration of the drug is reported as a fraction of the total average concentration of injected drug after two cycles. The total average concentration of drugs remains constant after 2 cycles until the drug starts to leave the geometry through the lower outlet.

Results and future work

The spine is simulated with and without the NRDL that are visible in Figure 1 (b). The mesh that includes the NRDL consists of 15 million tetrahedrons, whereas the mesh without the nerves consists of 1.5 million tetrahedrons. The mesh is refined close to all solid walls, which partly explains the need for a denser mesh in the case with NRDL. All simulations are run with 500 timesteps per computed cycle since the flow is assumed to be laminar. Some preliminary tests with much shorter timesteps have not revealed any significant evidence of transition to turbulence. Oasis is run on the Abel supercomputer at the University of Oslo using MPI for parallel performance and 96 CPU compute cores for the large mesh and 16 CPUs for the smaller mesh. Each timestep takes about 2.5 seconds real time for the large and 0.8 seconds for the smaller mesh and as such the largest simulation is run for a total of 20 hours whereas the smallest is run for 8 hours.

The evolution of the average concentration of the drug in two cross-sectional planes relative to

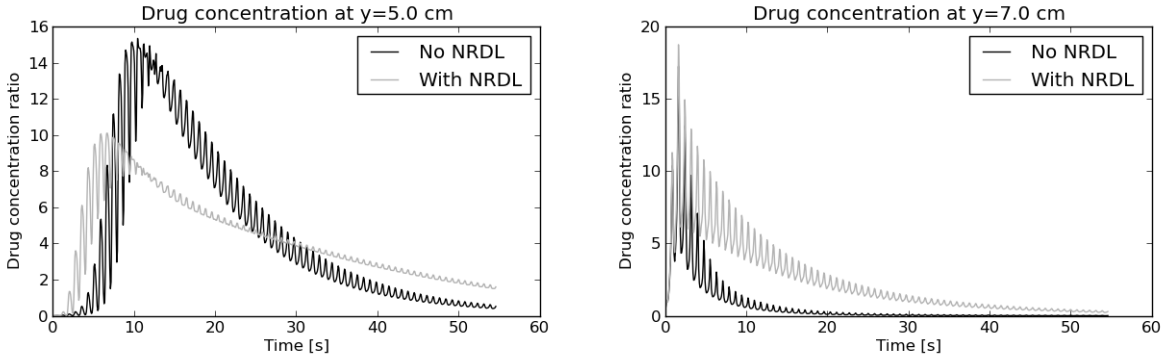

(a) (b)

Figure 2: Average drug concentration in plane located at (a) $y = 5$ cm and (b) $y = 7$ cm from the bottom.

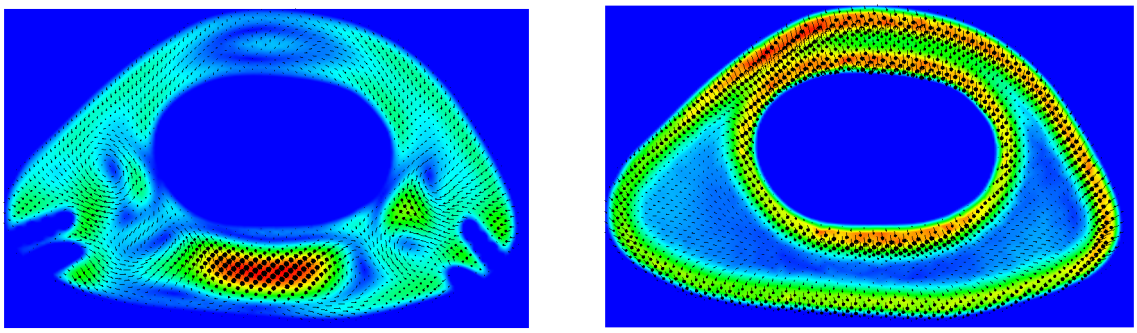

(a) (b)

Figure 3: Velocity vectors in a plane located 5 cm from the bottom of the computational mesh at $t = 0.6\tau$, where $\tau(= 0.78)$ is the time required for one cycle. Colour represents velocity magnitude.

the total average concentration after two cycles is shown in Figure 2. The two planes are located at 1 cm above (b) and 1 cm below (a) the injection center. Evidently, the drug is transported much faster in the y-direction with the inclusion of the NRDL. There are several reasons for this. First, the NRDL increases the total internal wall surface area, which increases the drag and requires a larger applied forcing (pressure gradient in y-direction) to uphold the same flow rate through the spine. The somewhat lower internal volume of the SSS with NRDL also reduces the cross sectional area, which speeds up the flow slightly simply due to mass conservation. A less obvious factor is the effect the NRDL have on the nature of the flow. Snapshots of the flow fields in both cases at $t = 0.6\tau$, where $\tau = 0.78$ is the time for one cycle, are illustrated in Figure 3. Here it is evident that the NRDL sets up a much more complex flow field with strong and persistent vortical structures aligned with the centre axis along the length of the SSS. The vortices lead to enhanced stretching, rotation, strain and tilting of the fluid elements, much like observed in a turbulent flow, resulting in greatly enhanced effective mixing rates.

Due to numerical stability issues the molecular drug diffusivity used in this work has been the order of 100 times larger than realistic. However, even with this unrealistic diffusivity, the mixing is still dominated by the convective transport of the fluid and it is therefore unlikely that this parameter would have any significant impact on the results shown in Figure 2. Furthermore, these results are averages over cross-sectional planes, representing only the level of macromixing (large scale mixing) in the SSS. Macromixing is largely controlled by convective transport and reveals nothing about the degree of mixing on the fines molecular scale, where drugs react. Mixing on the molecular level (micromixing) is controlled by molecular diffusion and thus mathematically by the diffusivity. Future work will assess the significance of diffusion using more realistic values for the diffusivity and a streamline upwind Petrov-Galerkin method for stabilization without the addition of artificial diffusion.

References

[1] http://fenicsproject.org.

[2] https://github.com/mikaem/oasis.

Proceedings of the 26th Nordic Seminar on Computational Mechanics
A. Logg, K.A. Mardal, A. Massing (Eds.)

A novel view of computations of steady flows of Bingham and Herschel-Bulkley fluids using implicit constitutive relations

J. Hron[1], J. Málek[1], J. Stebel[2], K. Touška[1]

(1)Charles University in Prague, Faculty of Mathematics and Physics, Mathematical Institute, Sokolovská 83, 186 75 Prague, Czech Republic {hron,malek}@karlin.mff.cuni.cz
(2)Institute of Mathematics AS CR, Žitná 25, 110 00 Prague, Czech Republic, stebel@math.cas.cz

Key words: incompressible fluid, non-Newtonian fluid, implicit constitutive relation, Bingham fluids

Introduction

There are many flows of various fluids, such as polymeric liquids, powders, food materials, etc., that exhibit the formation of "dead-zones" - these are subdomains in which the fluid is merely rotating and translating, and in fact no real flow takes place inside such parts of the flow container. Such behavior of materials is usually described by the following dichotomy. If the shear stress is below certain (given) critical value then the corresponding part of the fluid behaves as a rigid body. On the other hand, if the shear stress exceeds this critical value, the fluid behaves as a Navier-Stokes fluid or a power-law fluid, depending on the response characterized by a specific constitutive relation. The critical shear stress whose value plays a key role in the total response of the material is called the yield stress. Since such response differs from the behavior of a Navier-Stokes (Newtonian) fluid, the presence of yield stress belongs among (significant) non-Newtonian phenomena.

The above described fluid behavior is usually written as follows:

$$\begin{aligned} &|\mathbf{S}| \leq \tau_* \Leftrightarrow \mathbf{D} = \mathbf{0}, \\ &|\mathbf{S}| > \tau_* \Leftrightarrow \mathbf{T} = -p\mathbf{I} + \mathbf{S} = -p\mathbf{I} + \tau_* \frac{\mathbf{D}}{|\mathbf{D}|} + 2\nu(|\mathbf{D}|^2)\mathbf{D}. \end{aligned} \tag{1}$$

Here, $\tau_* > 0$ is the yield stress (the critical value in which the activation takes place), $\mathbf{T}$ is the Cauchy stress and $\mathbf{S}$ is its deviatoric (traceless) part, p is the mean normal stress, i.e., $p := -\frac{1}{3}\operatorname{tr}\mathbf{T}$, and $\mathbf{D}$ is the symmetric part of the velocity gradient $\nabla\vec{v}$, $\vec{v}$ being the velocity. Finally, the specific form of the generalized viscosity $\nu := \mathbb{R}_0^+ \mapsto \mathbb{R}_0^+$ distinguishes between the fluid of a Bingham or a Herschel-Bulkley type. If ν is constant then the response described by (1) is associated with a Bingham fluid. If ν depends on $\operatorname{tr}\mathbf{D}^2 = |\mathbf{D}|^2$ polynomially, one talks about a Herschel-Bulkley fluid. More complex forms for the generalized viscosity can be however considered.

It can be observed (see [2], [1]) that the response (1) can be equivalently described by implicit relation

$$2\nu(|\mathbf{D}|^2)\left(\tau_* + (|\mathbf{S}| - \tau_*)^+\right)\mathbf{D} = (|\mathbf{S}| - \tau_*)^+\mathbf{S}\,, \tag{2}$$

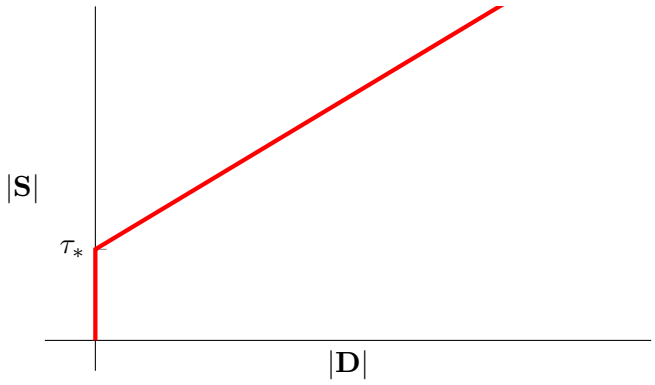

Figure 1. Bingham fluid response with yield stress τ_*.

where $z^+ := \max\{z, 0\}$ for $z \in \mathbb{R}$. One can observe that the Bingham and Herschel-Bulkley fluids are special cases of incompressible fluids described through a general implicit constitutive equation of the form

$$\mathbf{G}(\mathbf{S}, \mathbf{D}) = \mathbf{0}. \tag{3}$$

Bingham fluid

We first consider a steady state, slow flow of an Bingham fluid resulting in a Stokes-like system of the following form:

$$\begin{aligned} \operatorname{div} \vec{v} &= 0, \\ -\nabla p + \operatorname{div} \mathbf{S} &= \vec{f}, \\ \mathbf{G}(\mathbf{S}, \mathbf{D}) &= 0, \end{aligned} \tag{4}$$

where the implicit constitutive relation $\mathbf{G}(\mathbf{S}, \mathbf{D})$ can be one of two following variants

$$\mathbf{G}(\mathbf{S}, \mathbf{D}) = 2\nu\tau_*\mathbf{D} + (|\mathbf{S}| - \tau_*)^+(2\nu\mathbf{D} - \mathbf{S}), \tag{5}$$

$$\mathbf{G}(\mathbf{S}, \mathbf{D}) = 2\nu\tau_*\mathbf{D} + (2\nu|\mathbf{D}|)^+(2\nu\mathbf{D} - \mathbf{S}). \tag{6}$$

We investigate several variants of the mixed finite element discretizations of the system (4) with respect to its advantages in numerical solution. It leads to a twofold saddle point systems (see [4]). This can be compared to classical approaches using regularization in [7, 3] or with [6] where an augmented Lagrangian method is used.

Driven cavity problem

The tests are done on the classical problem of lid driven cavity flow. The domain is the unit square $\Omega = (0, 1) \times (0, 1)$. At the top wall of the domain the velocity is prescribed to be $\vec{v}_D = (16x^2(1 - x)^2, 0)$ and noslip boundary condition is prescribed on the remaining parts of the boundary. In figure 2 the resulting rigid zones of such flow are shown for several yield stress values.

References

[1] K. R. Rajagopal. On implicit constitutive theories for fluids. *J. Fluid Mech.*, 550:243–249, 2006. ISSN 0022-1120.

[2] K. Rajagopal and A. Srinivasa. On the thermodynamics of fluids defined by implicit constitutive relations. *Zeitschrift für Angewandte Mathematik und Physik*, 59(4):715–729, 2008.

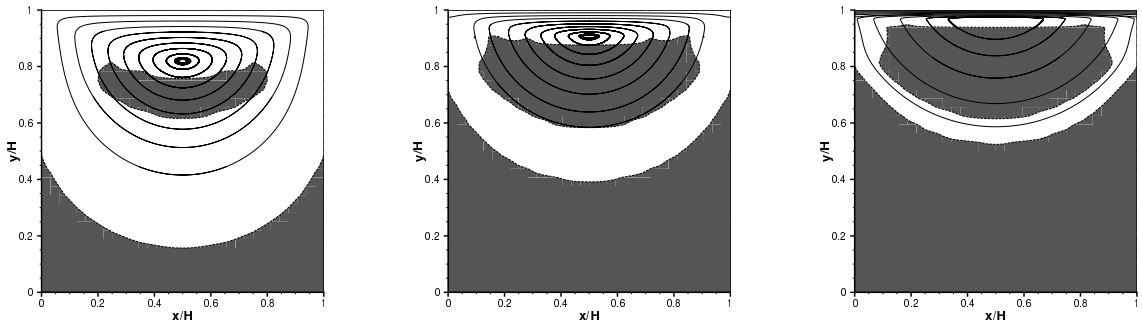

$\tau^* = 5$ $\tau^* = 50$ $\tau^* = 500$

Figure 2. Rigid zones for the Bingham fluid flow in a lid driven cavity problem.

[3] E. A. Muravleva and M. A. Olshanskii. Two finite-difference schemes for calculation of Bingham fluid flows in a cavity. *Russian Journal of Numerical Analysis and Mathematical Modelling*, 23(6):615–634, 2008.

[4] J. Howell and N. Walkington. Inf–sup conditions for twofold saddle point problems. *Numerische Mathematik*, 118(4):663–693, 2011.

[5] L. Diening, C. Kreuzer, and E. Süli. Finite element approximation of steady flows of incompressible fluids with implicit power-law rheology. *SIAM J. Numer. Anal.*, 51(2):984–1015, 2012.

[6] E. Dean, R. Glowinski, and G. Guidoboni. On the numerical simulation of Bingham viscoplastic flow: Old and new results. *Journal of Non Newtonian Fluid Mechanics*, 142(1-3): 36–62, Mar. 2007.

[7] J. C. De los Reyes and S. G. Andrade. Numerical simulation of two-dimensional Bingham fluid flow by semismooth Newton methods. *Journal of Computational and Applied Mathematics*, 235(1):11–32, Nov. 2010.

Proceedings of the 26th Nordic Seminar on Computational Mechanics
A. Logg, K.A. Mardal, A. Massing (Eds.)

Analysing the strength of wrinkle defects in glass-epoxy laminates

E. T. Christensen[1], J. Glud[1], E. Lindgaard[1], and B. L. V. Bak[1]

(1)Department of Mechanical and Manufacturing Engineering, Aalborg University, Fibigerstraede 16, 9220 Aalborg Oest, Denmark, esben@m-tech.aau.dk

Summary. In this paper a new method for predicting the failure load for glass-epoxy laminated sandwich structures containing wrinkle defects is proposed. In previous work the pointwise evaluated, stress based NU criterion has been used to predict the occurrence of delamination in such defects. The NU criterion only provided information regarding delamination initiation in non-critical parts of the structure, and thus underpredicted the load carrying capability. In this work cohesive zone modelling is used in the finite element method together with a modified max stress criterion for failure prediction. This method provides a greater insight into the failure process.

Key words: composite structures, glass-epoxy, wrinkle defect, cohesive zone modelling, composite materials, fracture mechanics.

Introduction

This work is conducted at Aalborg University in collaboration with Siemens Wind Power A/S as a part of a master thesis [1]. Siemens Wind Power A/S is one of the leading manufacturers in the wind turbine industry. The blades for their turbines are manufactured as glass-epoxy laminated sandwich structures using balsa wood as core material. In the infusion process of large glass-epoxy composite structures, such as a wind turbine blades, several types of manufacturing defects can arise. One of these defects is an out-of-plane misalignment of the glass fibers, also termed a "wrinkle" defect. The occurrence of wrinkle defects presents a great expense in the production of the blades since they are, in most cases, repaired due to lack of reliable methods of estimating the reduction in load carrying capability [2].

The main failure mode of a glass-epoxy laminated structure containing a wrinkle defect is layerwise delamination in the defect. This has been found in previous work in which, besides a phenomenological study of the failure mode, the pointwise evaluated, stress based NU-criterion has been used for predicting the onset of this delamination [2]. In the present work Cohesive Zone Modeling (CZM) has been used in the framework of the Finite Element (FE) method. The use of CZM facilitates the simulation of the fracture process and can thus provide more information regarding the failure process than the NU-criterion.

Methodology

The study has been performed using an advanced parametrised FE model, created in the ANSYS Parametric Design Language (APDL). Material data, geometry and normalization of results has been chosen so that comparison to the experimental results obtained in [2] is possible. In Figure 1a one of the wrinkle defects, that has been examined in [2], is shown. These specimens will henceforth be referred to as the test specimens.

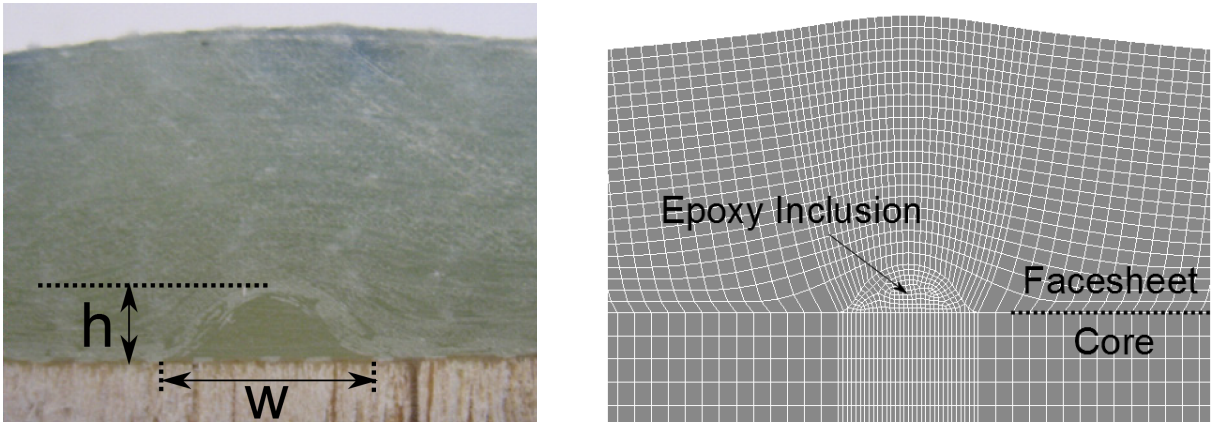

(a) (b)

Figure 1: (a) Photograph of test specimen with wrinkle defect used in [2]. (b) Illustration of the meshed model.

ANSYS 14.0, which has been used for the present work, features a basic 3D 8-node isoparametric CZM element called INTER205 [4]. This element does not have the required possibilities for this study, so a new implementation was created and used as a User Programmable Feature (UPF) [5]. The UPF was implemented as a 3D 8-node isoparametric interface element using a bilinear constitutive model, the Benzeggagh-Kenane mode interaction criterion [7] and a 1st order Newton-Cotes integration scheme. For details on the mentioned models and the element kinematics see [6]. The work carried out concerning the development, implementation and verification of the UPF is presented in [3].

The FE model was created with one quarter the width of the test specimens for the sake of reducing the solution time, and this was found not to have any significant influence on the results. The bulk material was meshed with the SOLID185, a 3D 8-node solid element, using the enhanced strain formulation [4]. In Figure 1b an example of the meshed model is shown. Note that the mesh presented in the figure is coarser than the one used for actual computation. Two types of interfaces were meshed with the UPF: The interface between the balsa core and the facesheet (C/F-interface), and between individual plies in the facesheet (P-interface).

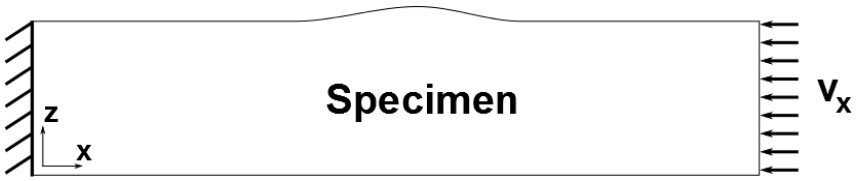

Figure 2: Boundary conditions for the model.

The model was clamped in one end and a displacement BC was imposed on the other as shown in Figure 2. The physical specimens were tested under load control. A displacement BC was chosen in order to avoid unstable behaviour when solving the nonlinear problem. By doing this the standard Newton-Raphson solver, which provided faster solving than e.g. the arc-length method, could be used.

Results

In the work of [2] it was found that at $70-90\%$ of the specimen failure load, a crack developed in the C/F-interface. This behaviour was reproduced in the FE simulation by manually fitting the fracture mechanical properties of the CZM constitutive model in this interface. The found properties indicated a very low interface strength which might be attributed to residual stresses

in the resin inclusion. In Figures 3a and 3b the transverse shear strain field, γ_{xz}, as obtained from the FE model and DIC measurements, respectively, can be seen. Note that the strains are normalized w.r.t. the far field normal strain, ϵ_x, according to [2]. In these figures, CZM elements have only been used in the C/F-interface. It is seen that the strain fields match well, apart from a few localized peaks in the DIC measurements which can be attributed to measurement error/inaccuracy. It was found that the presence of a crack in the C/F-interface increased the normalised local strain concentrations in the slanted bands seen in Figure 3 compared to those seen in an uncracked model. Thus the capability of the model to show the crack development in the C/F-interface increases the predictive capabilities of the simulation.

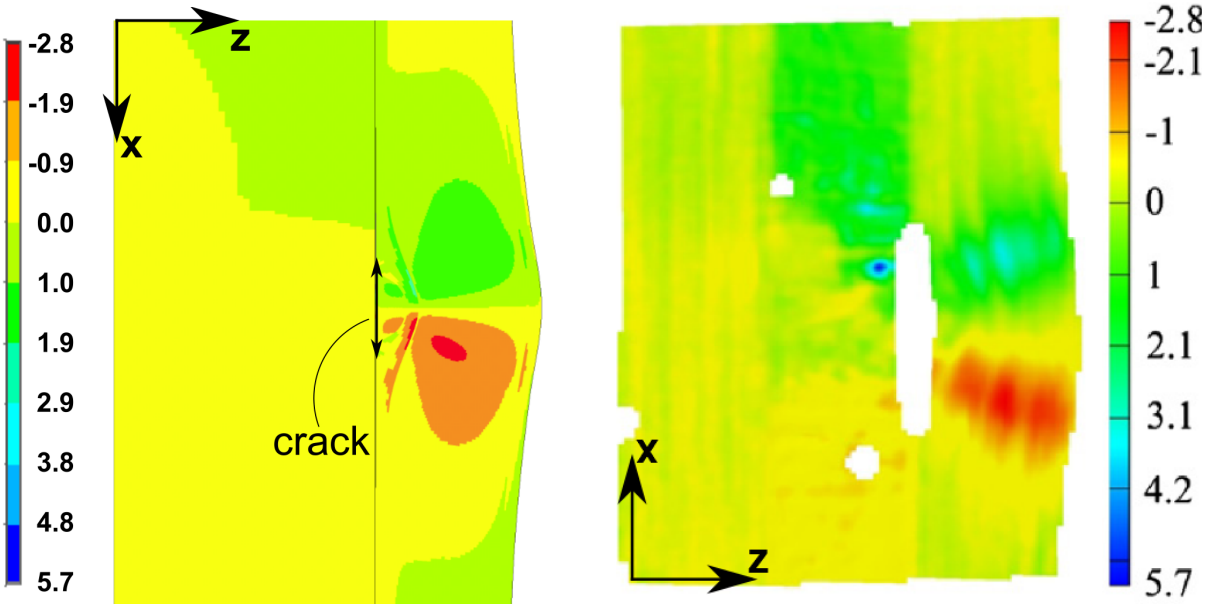

(a) (b)

Figure 3: The normalised γ_{xz} field as obtained from (a) the FE model and (b) using DIC [2].

Complete failure of the specimens occurs when the P-interfaces delaminate. This behaviour was not possible to reproduce since the required onset tractions of the CZM constitutive model would require a model with an impractically fine mesh (>2M nodes as compared to the ∼90k nodes of the present model). When using CZM in predicting crack propagation, the onset traction is less important than the energy release rate, and can thus in many applications be lowered without compromising the overall behaviour of the model [3]. However, the failure process in the examined specimens is very sudden and delamination occurs in all the P-interfaces simultaneously [2]. This behaviour indicates that crack initiation and complete delamination occurs at the same load, and the result is that even the smallest crack in the P-interfaces will be unstable at this load. Therefore the correct onset of crack initiation is important in order to obtain good predictions from the model. The need for a high onset traction was also evident in that, with a reduced onset traction, a physically unreasonable compliance in the P-interfaces of the model was observed at loads much lower than the failure load.

It was found that the delamination in the P-interfaces is governed by the transverse shear stress. This was both indicated by the stress distribution in the model and by the fact, that CZM elements in the P-interfaces showed mode II crack development only. Since it was not possible to simulate the delamination in these interfaces with the proper onset traction, the Max Stress Criterion was used to predict the onset of crack initiation. For this purpose the transverse shear strength of the plies was replaced with the maximum transverse shear stress that was observed in the model at the failure load for one of the specimens. In this way, the model is specifically adjusted to exactly predict the failure load for the selected specimen.

Using the described method for failure load prediction, a parametric study has been carried out, where the height and width of the wrinkle defect (h and w respectively in Figure 1a) are varied independently. In Figure 4 the results from this study are compared to the experimental results from [2].

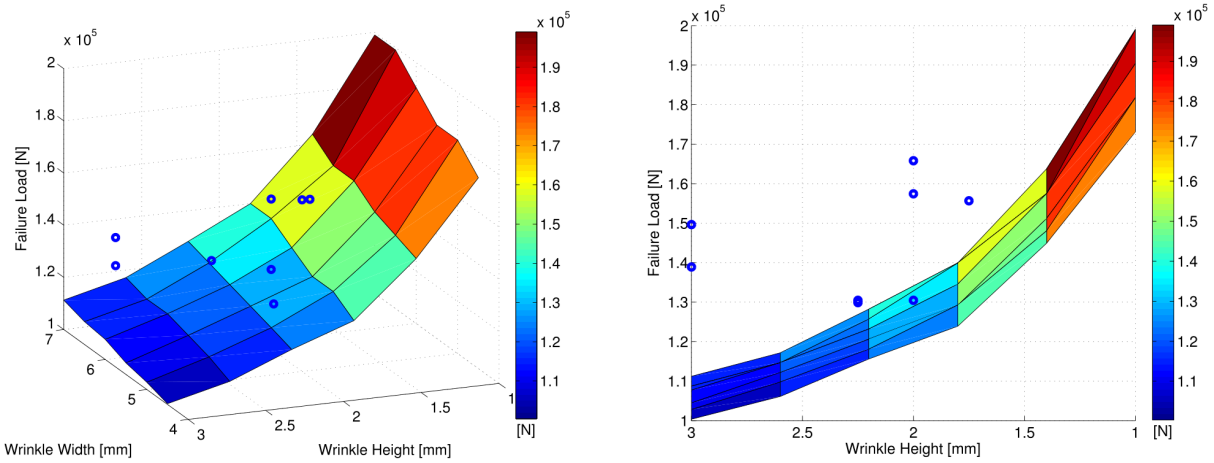

Figure 4: The predicted compressive failure load (surface) and experimental results (points).

From Figure 4 a tendency agreement is apparent although more experimental data would be required to properly verify this. For the chosen shear delamination strength the model provides conservative estimates. It should also be noted that increasing the wrinkle width or decreasing the wrinkle height increases the failure load of the specimen. This conforms well with the observation, that the transverse shear stress governs the failure process.

References

[1] E. T. Christensen, J. Glud and J. Sjølund. *Formulation of Cohesive Finite Element for Analysing Strength of Wrinkles in Glass-Epoxy Laminates*. Master Thesis, Department of Mechanical and Manufacturing Engineering, Aalborg University, Denmark, 2013.

[2] M. Leong. *The Influence of Defects on the Failure of Wind Turbine Blades*. Ph.D. Thesis, Department of Mechanical and Manufacturing Engineering, Aalborg University, Denmark, 2012. ISBN: 87-91464-44-7.

[3] J. Glud, E. T. Christensen, E. Lindgaard, and B. L. V. Bak. *Implementation of a State-of-the-art Cohesive Zone Element for ANSYS Mechanical*. Proceedings of the 26th Nordic Seminar on Computational Mechanics, Eds. A. Logg, K.A. Mardal, Oslo, Norway, October 23-25, 2013.

[4] ANSYS, Inc. *ANSYS Mechanical APDL Element Reference*. Release 14.0, 2011.

[5] ANSYS, Inc. *ANSYS Mechanical APDL Programmer's Manual*. Release 14.0, 2011.

[6] A. Turon, P. P. Camanho, J. Costa, and C. G. Dávila. *A Damage Model for the Simulation of Delamination in Advanced Composites under Variable-Mode Loading*. Mechanics of Materials, 38(11):1072-1089, 2006.

[7] M. L. Benzeggagh and M. Kenane. *Measurement of Mixed-Mode Delamination Fracture Toughness of Unidirectional Glass/Epoxy Composites with Mixed-Mode Bending Apparatus*. Composites Science and Technology, 49:439-449, 1996.

Proceedings of the 26th Nordic Seminar on Computational Mechanics
A. Logg, K.A. Mardal, A. Massing (Eds.)

Estimating Gear Teeth Stiffness

Niels Leergaard Pedersen

Dept. of Mechanical Engineering, Solid Mechanics, Technical University of Denmark
Nils Koppels Allé, Building 404, DK-2800 Kgs. Lyngby, Denmark
email: nlp@mek.dtu.dk

Summary. The estimation of gear stiffness is important for determining the load distribution between the gear teeth when two sets of teeth are in contact. Two factors have a major influence on the stiffness; firstly the boundary condition through the gear rim size included in the stiffness calculation and secondly the size of the contact. In the FE calculation the true gear tooth root profile is applied. The meshing stiffness's of gears are highly non-linear, it is however found that the stiffness of an individual tooth can be expressed in a linear form assuming that the contact length is constant.

Key words: Gears, Stiffness, Spur, FE

Single gear stiffness

The computations are performed with the same spur gear set as used in [1], the data used are (z number of teeth, M module, b tooth width)

$$z_1 = 21, \qquad z_2 = 49, \qquad M = 4\text{mm}, \qquad b = 20\text{mm}$$

i.e. no profile shift is used. The tooth width is not involved in the FE calculations but used for the specific stiffness values shown. In Figure 1 the pinion gear single tooth of the pinion ($z_1 = 21$) and the wheel ($z_2 = 49$) are shown, the difference in shape is clear.

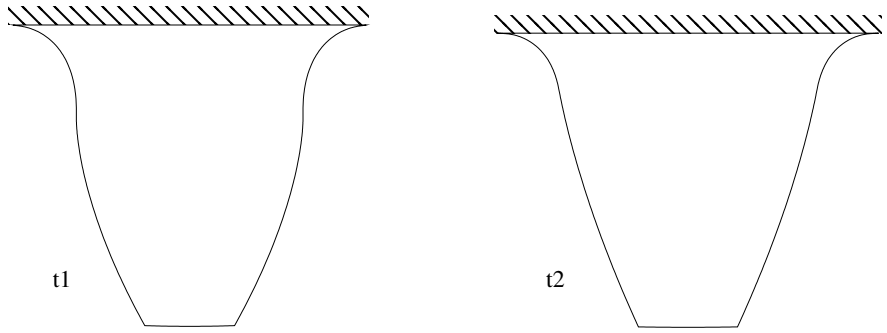

Figure 1. Single tooth clamped at the root for two different size gears ($M = 4$mm). a) 21 teeth gear. b) 49 teeth gear.

In the present paper two factors are shown to have a major influence on the gear teeth stiffness, these are:

- The contact zone size.
- The gear rim size included in the stiffness calculation

The stiffness, K_g, of a structure related to a given load is usually in the linear case defined as the load F_c (in this paper a contact load) divided by the corresponding load displacement d_c.

$$K_g = \frac{F_c}{d_c} \tag{1}$$

The main problem with this definition is that in many cases the displacement does not have a clear and unique definition. To avoid this we will define the stiffness from the total elastic energy U (sum of strain energy U_ϵ and stress energy U_σ). Often the stress energy is referred to as the complementary elastic energy. For the linear case we have that $U_\epsilon = U_\sigma = U/2$. Assuming that we only have one set of loads, that scales proportional to the total load F_c the corresponding stiffness is given by

$$U = F_c d_c = F_c \frac{F_c}{K_g} \Rightarrow K_g = \frac{F_c^2}{U} \tag{2}$$

In the present paper 2D FE analysis is used for finding the elastic energy. The FE calculation is performed using the COMSOL program ([2]). Assuming linearity we can apply a unit load and the stiffness is then directly given as the inverse of the total elastic energy. In the FE calculation of the elastic energy plane stress is assumed.

It is a valid assumption that the contact stress acts as a Hertzian stress, and we know the radii of curvature; these are s_1 and s_2, see Figure 2. Idealized, the contact point of two gears

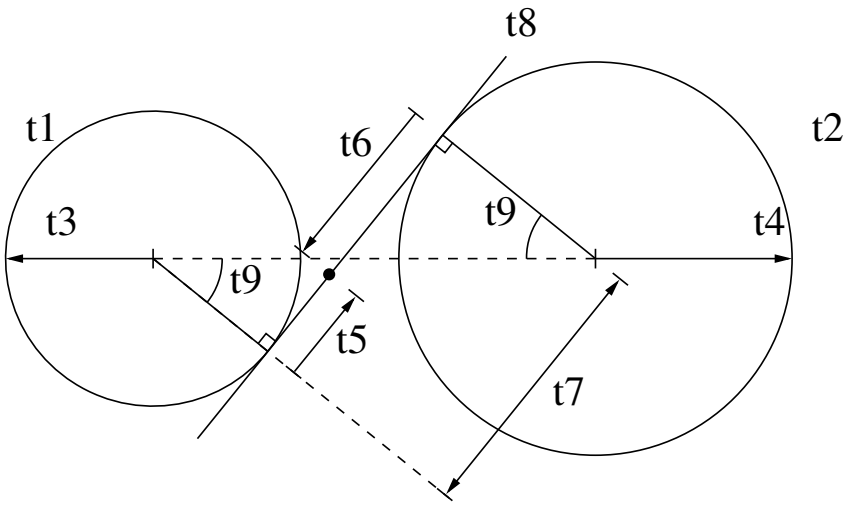

Figure 2. Basic gear geometry, the dot indicates a contact point.

follows the straight line of action. The line of action is the tangent to both base circles. The sum of the two arc length parameters s_1 and s_2 is therefore a constant s_c, see Figure 2.

Influence from contact zone size

Assuming the load distribution to be Hertzian and applying it at the pitch point of the tooth the stiffness variation found is as seen in Figure 3. Although it is clear that the stiffness depends on the contact zone length in a non-negligible way the remaining part of the paper use $a = 74.5\mu$m.

Influence from boundary conditions

The second problem of defining a unique stiffness function for a tooth is the boundary condition applied. In the previous shown cases we clamped the tooth at the root which is a common

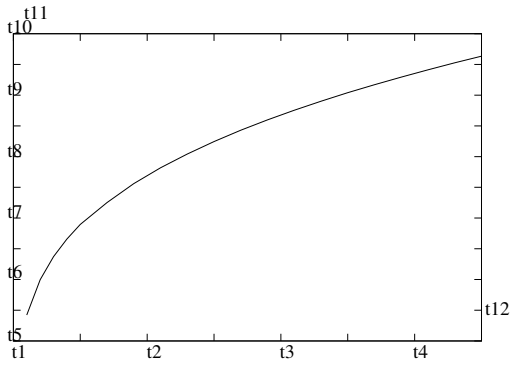

Figure 3. Stiffness of single tooth (Figure 1a) as a function of half the contact length. The load center is at the pitch point (assuming no profile shift).

assumption applied in the literature. The stiffness is not only controlled by the tooth shape itself also the rim (or ring) thickness has a non-negligible influence. In the present paper we estimate the influence from the rim thickness by using a model where the teeth are attached to a rim with thickness r_t. In Figure 4 part of a one tooth and a three teeth model are shown. In the figure the full rings that are used in the FE calculation are not shown. In the FE calculations results presented in Figure 5 the inside of the rim is clamped and the load is applied at the pitch point as done previously.

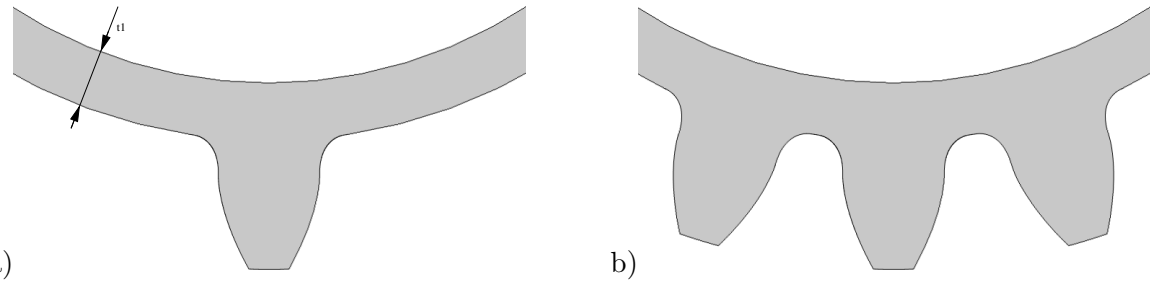

Figure 4. Part of geometry model here with a rim thickness $r_t = M$. 1) One tooth model. b) Three teeth model.

By varying the rim thickness the stiffness presented in Figure 5 is found, where the rim thickness is normalized by the tooth module. From the results it is clear that a one tooth model is sufficient for the stiffness estimation. The fact that the rim can not be neglected from the calculation is also evident. In figure 6 a strain energy density colour and contour plot is given.

Stiffness as a function of contact position

The stuffiness's are presented in Figure 7 as a function of s^2. For the problem at hand with pinion (21 teeth) and wheel (49 teeth) we select to use input shaft diameter 50mm and output shaft diameter 65mm

In the figures linear curve-fits of the stiffness variation are also given. These linear curve-fits in the squared s_1 and s_2 parameters are

$$K_1(s_1) = (-8.844 \cdot 10^2 \cdot (s_1/\text{mm})^2 + 7.776 \cdot 10^5)\text{N/mm} \quad (3)$$

$$K_2(s_2) = (-2.574 \cdot 10^2 \cdot (s_2/\text{mm})^2 + 7.589 \cdot 10^5)\text{N/mm} \quad (4)$$

These two simple curve-fits can directly be used for estimating mesh stuffiness's.

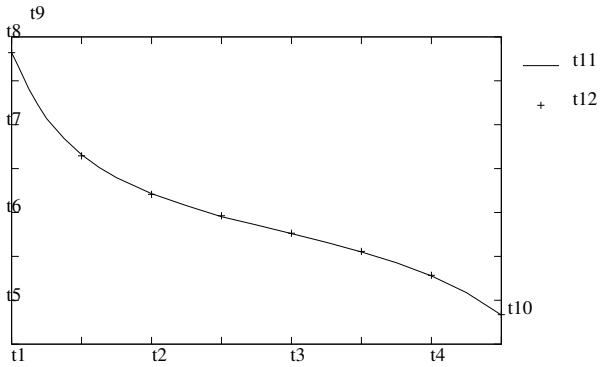

Figure 5. Stiffness of single tooth (Figure 1a) as a function of rim thickness using either 1 tooth model (Figure 4a) or 3 teeth model (Figure 4b). The load center is at the pitch point (assuming no profile shift).

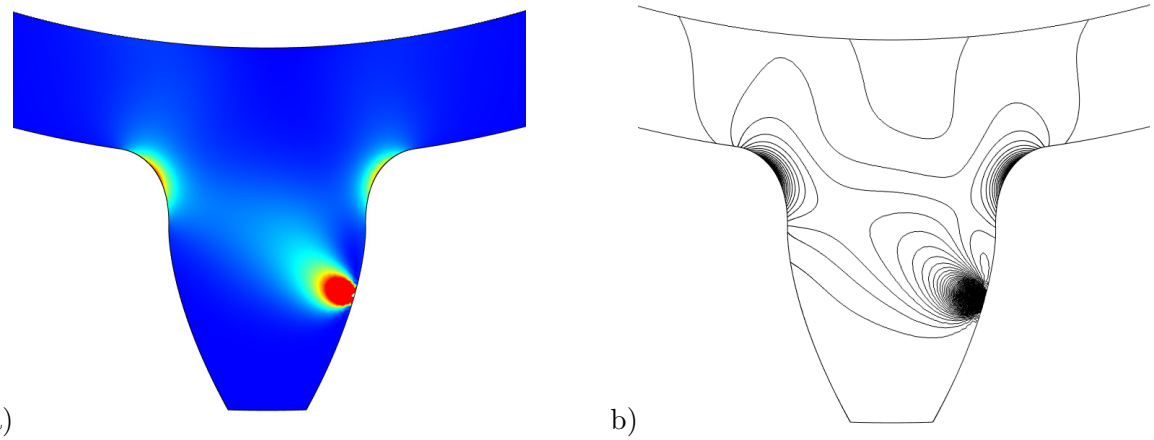

Figure 6. Illustration of the distribution of strain energy density. a) Colour plot. b) Contour plot.

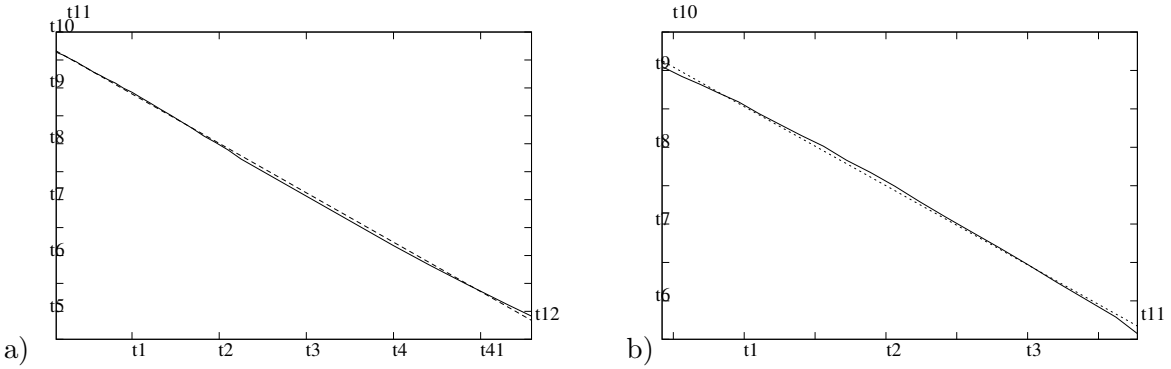

Figure 7. Stiffness of single tooth shown by the full lines given as a function of squared contact point position. Linear curve-fits are shown in dashed lines. a) 21 teeth b) 49 teeth.

References

[1] J. I. Pedrero, M. Pleguezuelos, M. Artés, and J. A. Antona. Load distribution model along the line of contact for involute external gears. *Mechanism and Machine Theory*, 45(5):780–794, 2010.

[2] COMSOL AB. Stockholm, www.comsol.se, 1998-2009.

Proceedings of the 26th Nordic Seminar on Computational Mechanics
A. Logg, K.A. Mardal, A. Massing (Eds.)

Soft body impact on insulated glass structures

Kent Persson[1] and Maria Fröling[1]

(1)Div. of Structural Mech., Lund University, Box 118, 221 00, Lund, Sweden,
kent.persson@construction.lth.se

Summary. Modelling strategies were developed to determine the stresses for glass structures subjected to soft body impact loads. A reduced finite element model for determining the stresses of glass panes subjected to dynamic impact loads was developed and compared to a full dynamic finite element model. The reduced model is based on the Rayleigh-Ritz method. The Ritz vectors are determined by simple static load-cases. The model is applicable to centric and eccentric applied impact and to glass of various support conditions. Structure-acoustic analysis is also used to analyse impact loads on insulated glass structures with fluid-filled cavities. It is demonstrated that the modelling framework well captures the features of a test example with four-sided supported glass.

Key words: glass, impact, model reduction, fluid-structure interaction

Introduction

When performing strength design of glass structures, dynamic impact load is one of the load cases that often need to be included in the analysis. Since glass is a brittle material, it is sensitive to impact load and it is necessary to accurately determine the stress distribution in the glass due to this load case. Most often strength design of glass structures subjected to dynamic impact load is performed by means of experimental tests. The European standard EN-12600, [7], is available to classify glass for impact strength but also describes a soft body impactor that can be used for testing of various glass structures. The experimental test method used for classifying glass for impact strength is shown in Figure 1(a). The arrangement consists of a glass pane held within a steel frame and an impactor consisting of a weight encased in two tires. Between the steel frame and the glass there are rubber strips. During the test, the tire is swung in a pendulum motion into the glass pane. The dimensions of the frame are standardized to 1.95 x 0.887 m2 and the weight of the impactor is 50 kg. The test is considered as a soft impact with a long pulse time, Figure 1(b).The process of experimental testing is, however, time consuming when considering parameter variation in strength design.

An alternative to experimental tests is to use finite element simulations. Several authors have demonstrated the applicability of full transient finite element simulations in order to simulate the application of impact load to glass structures. However, finite element modeling of transient impact load is advanced, time consuming and may require access to advanced commercial finite element programs.

To make the model more computationally efficient the size of the finite element model can be reduced by means of model reduction techniques. Several methods that are variants of the Rayleigh-Ritz procedure are available. The methods can be subdivided into the following main categories: generalised coordinate methods, condensation methods and component mode synthesis. When generalised coordinates are introduced, the system is described using only a few deflection shapes of the original system where for example eigenvectors, Lanczos vectors and Ritz vectors may be utilized. Condensation methods involves removing the degrees of freedom

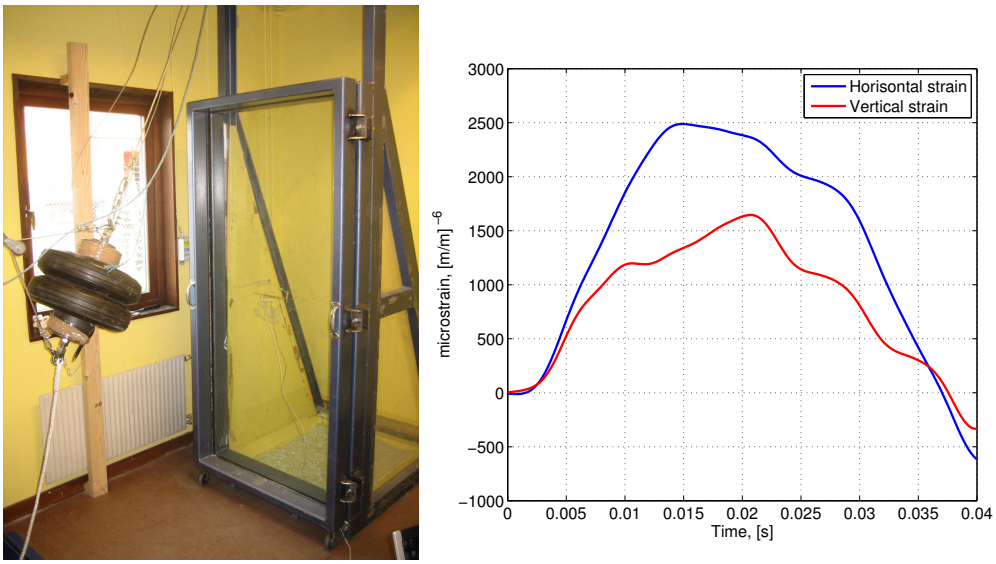

Figure 1. Test arrangement for pendulum impact test (a) and example of result (b).

that are not necessary in order to describe the dynamic behavior of the system. This can be accomplished using for example static (Guyan) condensation, [4] or dynamic condensation, see for instance [5]. In component mode synthesis the domain of the problem is divided into subdomains and each subdomain is described by a different set of basis vectors.

Reduced Model for Soft Body Impact on Glass Structures

In the reduced dynamic modeling of the glass pane, including the supports, the Rayleigh-Ritz method, [3], was adopted. Consequently, the displacements, $\mathbf{u}(t)$, were expressed as a linear combination of shape (Ritz) vectors ψ_j:

$$\mathbf{u}(t) = \sum_{j=1}^{J} z_j(t)\psi_j = \Psi \mathbf{z}(t), \tag{1}$$

where $z_j(t)$ are the generalized coordinates.
The glass pane together with the supports can be represented as a multi-degree-of-freedom system with one degree of freedom for each Ritz vector. The equations of motion for an undamped multi-degree-of-freedom system in free vibration are given as, [3],

$$\mathbf{m}\ddot{\mathbf{u}} + \mathbf{k}\mathbf{u} = \mathbf{0}, \tag{2}$$

where $\mathbf{m}$ is the mass matrix and $\mathbf{k}$ is the stiffness matrix. Substituting (1) into (2) yields

$$\mathbf{m}\Psi\ddot{\mathbf{z}} + \mathbf{k}\Psi\mathbf{z} = \mathbf{0}. \tag{3}$$

Premultiplying each term in (3) by Ψ^T yields

$$\tilde{\mathbf{m}}\ddot{\mathbf{z}} + \tilde{\mathbf{k}}\mathbf{z} = \mathbf{0}, \tag{4}$$

where $\tilde{\mathbf{m}} = \Psi^T\mathbf{m}\Psi$ and $\tilde{\mathbf{k}} = \Psi^T\mathbf{k}\Psi$. $\tilde{\mathbf{m}}$ and $\tilde{\mathbf{k}}$ are the generalized mass and stiffness matrices. The impactor is suggested to be represented by a single-degree-of-freedom system with the displacement degree of freedom u_i, and m_i and k_i are the mass and stiffness of the impactor.
In this work, two Ritz-vectors were selected to represent the glass structure and with the impactor modelled as a single spring-mass system connected to z_1 a three-degree-of-freedom system is

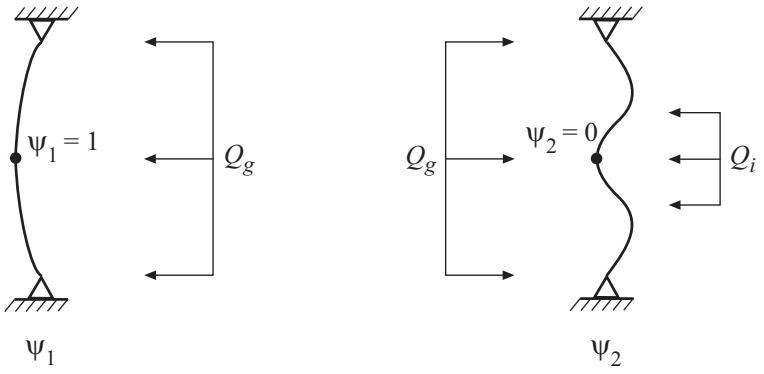

Figure 2. Load cases applied for determining the two Ritz vectors.

obtained. The two Ritz vectors were determined by solving a static finite element model for two load cases as shown in Figure 2. When adding additional Ritz vectors there is a trade-off between increasing the accuracy and decreasing the computational efficiency. The obtained deformation modes from the two load cases were used as the two Ritz vectors after being scaled to be one and zero at the location of the impactor, respectively.

A simple contact condition is assumed where the solution is valid only until the contact force between the glass and the impactor change signs. When the contact force becomes negative, the impactor is disassembled from the model.

The system is solved using the Newmark procedure, ([2], [3]), as implemented in [1] by means of MATLAB. Initial values for $\bar{\mathbf{z}}$ and $\dot{\bar{\mathbf{z}}}$ are required. In Figure 3 a comparison is shown of the reduced model with one and two Ritz vectors as well as a full FE-model with linear and nonlinear geometry. Setting up and solving the reduced model is made within a few seconds since it only involves solving a static FE-model for two load cases and then performing the time-stepping for the reduced three-DOF system. The full model, however, involves a transient solution of a large model with contact conditions which normally takes hours of computer time.

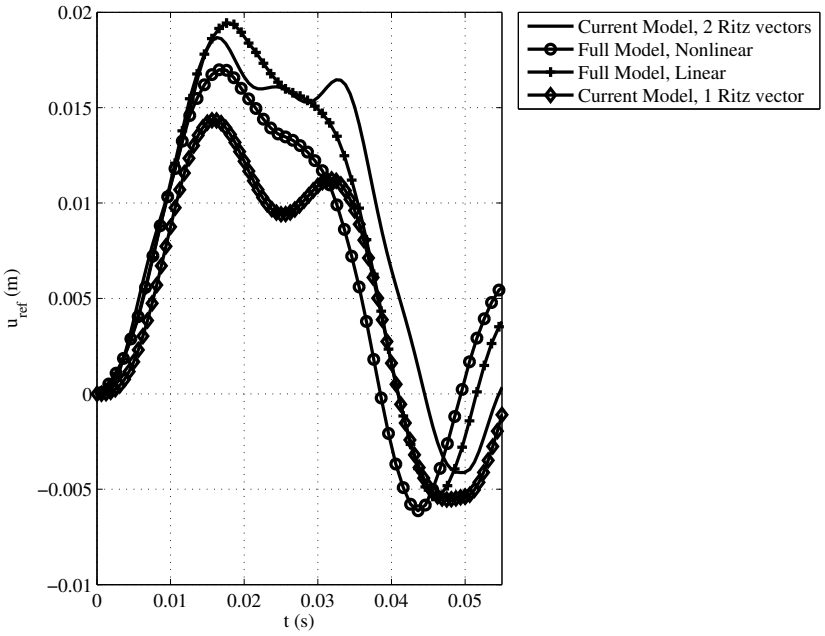

Figure 3. Lateral displacement of the midpoint of the glass versus time for a glass whith the in-plane dimensions according to [7] and 10mm in thickness.

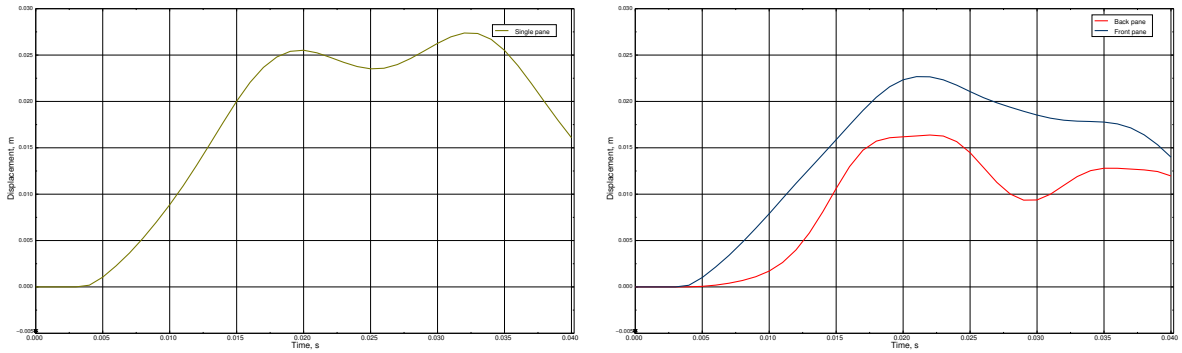

Figure 4. Lateral displacement of the midpoint of the glass versus time for a 1.2x1.2 m^2 window for a single glass (*left*) and insulated two-glass structure (*right*).

Soft Body Impact on Insulated Glass Structures

Insulating glass consists of two or more glass panes with gas filled cavities in between. Insulating glass units are favorable for use in buildings due to for instance the thermal insulating properties that the insulating glass possesses.

In this work, structure-acoustic analysis, [6], is used in the finite element modeling of insulated glass subjected to dynamic impact load. In this approach, the gas filled space is modeled by means of the acoustic wave equation and the interaction between the glass and the gas filled space is taken into account. A numerical example is made that simulates the pendulum impact test, [7]. ABAQUS is used for the simulations.
In Figure 4 an example of a result is shown where it is shown that the inner glass plate carries the greatest part of the load during the impact. In general there is only a small decrease in the maximum stress when a two-glass structure is used instead of a single glass.

References

[1] P.E. Austrell et al. CALFEM-A Finite Element Toolbox, Version 3.4. KFS, Lund, Sweden, 2004.

[2] K.-J. Bathe. Finite Element Procedures. Prentice Hall, (2006).

[3] A.K. Chopra. Dynamics of Structures-Theory and Applications to Earthquake Engineering. Pearson Prentice Hall, Upper Saddle River, New Jersey, (2007).

[4] R. Guyan. Reduction of Stiffness and Mass Matrices. AIAA, 3, 380, (1965).

[5] A.Y.T. Leung. An Accurate Method of Dynamic Condensation in Structural Analysis. International Journal for Numerical Methods in Engineering, 12, 1705-1715, (1978).

[6] G. Sandberg, P.A. Wernberg and P. Davidsson. Fundamentals of Fluid-Structure Interaction. Computational Aspects of Structural Acoustics and Vibration, CISM Courses and Lectures, G. Sandberg and R. Ohayon (eds), vol. 505. Springer, Wien, Austria, (2008).

[7] SS-EN-12600. Glass in building-Pendulum test-Impact test method and Classification for flat glass. Swedish Standards Institute, 2003.

Proceedings of the 26th Nordic Seminar on Computational Mechanics
A. Logg, K.A. Mardal, A. Massing (Eds.)

Isogeometric analysis of non-linear 3D Euler-Bernoulli beams

S.B. Raknes[1], K.M. Mathisen[1], B. Haugen[2], T. Kvamsdal[3], Y. Bazilevs[4], X. Deng[4]

[(1)]Norwegian University of Science and Technology, Department of Structural Engineering, Richard Birkelandsvei 1A, 7491 Trondheim, siv.bente.raknes@ntnu.no, kjell.mathisen@ntnu.no
[(2)]Norwegian University of Science and Technology, Department of Engineering Design and Materials, Richard Birkelands vei 2, 7491 Trondheim, bjorn.haugen@ntnu.no
[(3)]Norwegian University of Science and Technology, Department of Mathematical Sciences, Alfred Getz' vei 1, 7034 Trondheim, trond.kvamsdal@math.ntnu.no
[(4)]University of California San Diego, Department of Structural Engineering, 9500 Gilman Drive, La Jolla, CA 92093-0085, yuri@ucsd.edu, x8deng@eng.ucsd.edu

Summary. An isogeometric beam formulation is derived from a 3D continuum, where large-deformation kinematics and the St. Venant–Kirchhoff constitutive law are assumed. It is also assumed that the beam cross-sections are symmetric and planar, and that the director stays normal to the beam cross-section during the deformation. The beam geometry representation reduces to a curve in 3D space. Four degrees of freedom are employed in the modeling, three displacement and one rotational, enabling the formulation to account for membrane, bending and torsional effects.

Key words: Isogeometric analysis, NURBS, Euler-Bernoulli beams, large displacements, non-linear.

Large-deformation beam formulation

Local curvilinear coordinate system

A local curvilinear coordinate system is chosen where ξ_1 is the parametric variable used to define the beam's middle curve. The functions $\mathbf{X}(\xi_1)$ and $\mathbf{x}(\xi_1)$ denote the coordinates of the beam's middle curve in the reference and deformed configuration, respectively. The initial configuration may be curved and twisted an angle ϕ_0 about the middle curve. The displacement of the

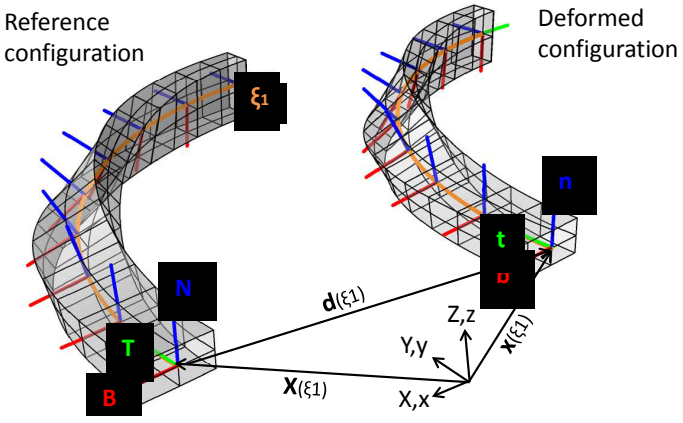

Figure 1. Sketch of the 3D beam in both the undeformed reference configuration and the deformed current configuration, showing the beam's middle curve and the local coordinate system consisting of the tangent $(\mathbf{T}, \mathbf{t})$, binormal $(\mathbf{B}, \mathbf{b})$ and normal $(\mathbf{N}, \mathbf{n})$ vectors.

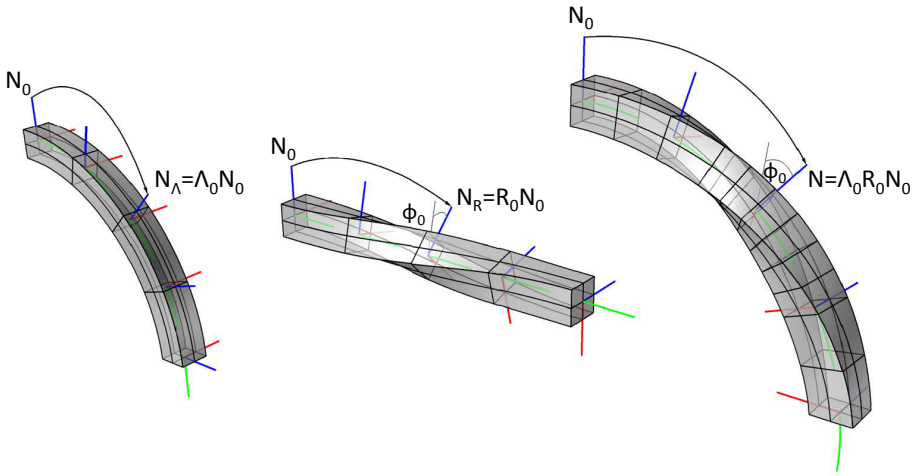

Figure 2. Rotation of the local curvilinear coordinate system from the triad $\{\mathbf{T}_0, \mathbf{B}_0, \mathbf{N}_0\}$ to $\{\mathbf{T}, \mathbf{B}, \mathbf{N}\}$ by applying the rotation operators $\mathbf{\Lambda}_0$ and $\mathbf{R}_0$.

beam's middle curve is given by $\mathbf{d}(\xi_1) = \mathbf{x}(\xi_1) - \mathbf{X}(\xi_1)$. The local curvilinear coordinate system consisting of the tangent $(\mathbf{T}, \mathbf{t})$, binormal $(\mathbf{B}, \mathbf{b})$ and normal $(\mathbf{N}, \mathbf{n})$ vectors is illustrated in Figure 1. Note that $\{\mathbf{T} \perp \mathbf{B} \perp \mathbf{N}\}$ and $\{\mathbf{t} \perp \mathbf{b} \perp \mathbf{n}\}$.

The unit tangent vectors to the middle curve are calculated directly from the beam's geometry, and are given by

$$\mathbf{T}(\xi_1) = \frac{\mathbf{X}_{,\xi_1}}{||\mathbf{X}_{,\xi_1}||}, \quad \mathbf{t}(\xi_1) = \frac{\mathbf{x}_{,\xi_1}}{||\mathbf{x}_{,\xi_1}||}, \tag{1}$$

in the reference and current configuration, respectively. Comma denotes differentiation.

The reference configuration normal vectors are calculated by applying two rotation operators, $\mathbf{\Lambda}_0$ and $\mathbf{R}_0$, to the fixed triad $\{\mathbf{T}_0, \mathbf{B}_0, \mathbf{N}_0\}$ in $\xi_1 = 0$, as shown in Figure 2. $\mathbf{\Lambda}_0$ gives the geometrical rotation due to bending and $\mathbf{R}_0$ the initial rolling twist around the middle curve. The normal vectors in the reference and current configuration are given by

$$\mathbf{N}(\xi_1, \phi_0(\xi_1)) = \mathbf{\Lambda}_0(\mathbf{T}_0, \mathbf{T}(\xi_1))\mathbf{R}_0(\phi_0(\xi_1), \mathbf{T}_0)\mathbf{N}_0 = \mathbf{Q}_0\mathbf{N}_0, \tag{2}$$

$$\mathbf{n}(\xi_1, \phi(\xi_1)) = \mathbf{\Lambda}(\mathbf{T}(\xi_1), \mathbf{t}(\xi_1))\mathbf{R}(\phi(\xi_1), \mathbf{T}(\xi_1))\mathbf{N} = \mathbf{Q}\mathbf{N}, \tag{3}$$

where ϕ is the current twist angle. Similarly for the binormal vectors; $\mathbf{B} = \mathbf{Q}_0\mathbf{B}_0$ and $\mathbf{b} = \mathbf{Q}\mathbf{B}$. By Rodriguez formula, with $\mathbf{I}$ being the identity matrix, $\mathbf{\Lambda}$ and $\mathbf{R}$ are given by

$$\mathbf{\Lambda}(\mathbf{T}, \mathbf{t}) = (\mathbf{T} \cdot \mathbf{t})\mathbf{I} + (\mathbf{T} \times \mathbf{t}) \times \mathbf{I} + \frac{1}{1 + \mathbf{T} \cdot \mathbf{t}}(\mathbf{T} \times \mathbf{t}) \otimes (\mathbf{T} \times \mathbf{t}), \tag{4}$$

$$\mathbf{R}(\phi, \mathbf{T}) = \mathbf{I} + sin(\phi)(\mathbf{T}) \times \mathbf{I} + (1 - cos(\phi))(\mathbf{T} \otimes \mathbf{T} - \mathbf{I}). \tag{5}$$

Similar derivations for the linear case are found in [1].

Beam geometry description in 3D space

The 3D beam geometry is parametrically defined as

$$\mathbf{x}^{3D}(\xi_1, \xi_2, \xi_3) = \mathbf{x}(\xi_1) + \xi_2\mathbf{b}(\xi_1) + \xi_3\mathbf{n}(\xi_1), \tag{6}$$

in the current configuration, and

$$\mathbf{X}^{3D}(\xi_1, \xi_2, \xi_3) = \mathbf{X}(\xi_1) + \xi_2\mathbf{B}(\xi_1) + \xi_3\mathbf{N}(\xi_1) \tag{7}$$

in the reference configuration. ξ_2 and ξ_3 represent the cross-section parameterization. With the kinematics given by Eq. (6), the beam cross-sections remain planar and normal to the middle curve in the deformed configuration, the main assumption of the Euler–Bernoulli beam theory. The authors showed a similar beam formulation without torsion in [2].

Strain measure

We use the Green-Lagrange strain tensor given by

$$\mathbf{E} = \frac{1}{2}(\mathbf{F}^T\mathbf{F} - \mathbf{I}) = E_{\alpha\beta}\mathbf{G}^\alpha \otimes \mathbf{G}^\beta, \tag{8}$$

$$E_{\alpha\beta} = \frac{1}{2}(\mathbf{g}_\alpha \cdot \mathbf{g}_\beta - \mathbf{G}_\alpha \cdot \mathbf{G}_\beta) = \frac{1}{2}(\mathbf{x}^{3D}_{,\xi_\alpha} \cdot \mathbf{x}^{3D}_{,\xi_\beta} - \mathbf{X}^{3D}_{,\xi_\alpha} \cdot \mathbf{X}^{3D}_{,\xi_\beta}), \tag{9}$$

where $\alpha, \beta = \{1, 2, 3\}$, summation is applied on repeated indices, $\mathbf{G}^\alpha$ and $\mathbf{g}^\alpha$ are the contravariant basis vectors in the reference and current configuration, respectively, and $\mathbf{G}_\alpha$ and $\mathbf{g}_\alpha$ are the covariant basis vectors. $\mathbf{G}^\alpha = \mathbf{G}_\alpha/\|\mathbf{G}_\alpha\|^2$. The strains may be expressed as

$$E_{11} = \epsilon + \xi_2\kappa_b - \xi_3\kappa_n, \quad E_{12} = \frac{1}{2}\xi_3\kappa_t, \quad E_{13} = -\frac{1}{2}\xi_2\kappa_t, \tag{10}$$

where ϵ is the strain due to membrane action, κ_b and κ_n the curvature due to bending about the binormal and the normal, and κ_t the curvature due to rotation around the tangent vector.

Constitutive equation

We use the second Piola-Kirchhoff stress tensor, $\mathbf{S}$, and introduce a linear constitutive law on the dimensionless ($\bar{E}_{\alpha\beta} = E_{\alpha\beta}\|\mathbf{G}^\alpha\|\|\mathbf{G}^\beta\|$ and $\bar{S}^{\alpha\beta} = S^{\alpha\beta}/(\|\mathbf{G}^\alpha\|\|\mathbf{G}^\beta\|)$) stress-strain relation;

$$\begin{bmatrix} \overline{S}^{11} \\ \overline{S}^{12} \\ \overline{S}^{13} \end{bmatrix} = \begin{bmatrix} E_c & 0 & 0 \\ 0 & G_c & 0 \\ 0 & 0 & G_c \end{bmatrix} \begin{bmatrix} \overline{E}_{11} \\ 2\overline{E}_{12} \\ 2\overline{E}_{13} \end{bmatrix}, \tag{11}$$

where E_c is Young's modulus and G_c is the shear modulus.

Variational equations of equilibrium

The equilibrium of virtual work, $\delta W = \delta W^{ext} + \delta W^{\text{int}} = 0$, is given by

$$\delta W^{\text{ext}} = -\int_{S_0} \delta\mathbf{x} \cdot A_0\rho_0\mathbf{f}_b \, dS - \int_{S_0} \delta\mathbf{x} \cdot \mathbf{h} \, dS - \delta\mathbf{x} \cdot \mathbf{F}_p - \delta\phi \cdot \mathbf{F}_t, \tag{12}$$

$$\begin{aligned} \delta W^{\text{int}} &= \int_{V_0} \mathbf{S} : \delta\mathbf{E} dV = \int_{S_0} \delta\epsilon A_0 E_c \epsilon \|\mathbf{G}^1\|^4 \, dS + \int_{S_0} \delta\kappa_n I_0^n E_c \kappa_n \|\mathbf{G}^1\|^4 \, dS \\ &+ \int_{S_0} \delta\kappa_b I_0^b E_c \kappa_b \|\mathbf{G}^1\|^4 \, dS + \int_{S_0} \delta\kappa_t J_0 G_c \kappa_t \|\mathbf{G}^1\|^2 \, dS, \end{aligned} \tag{13}$$

where V_0 is the beam volume, A_0 the cross-sectional area, S_0 is the beam's middle curve, I_0^n and I_0^b the beam's second moments of area and J_0 the polar moment, all in the undeformed configuration. $\mathbf{f}_b$ are the body forces per unit masss, ρ_0 is the beam's density, $\mathbf{h}$ is the applied traction that has dimensions of force per unit length, $\mathbf{F}_p$ are point forces and $\mathbf{F}_t$ are torsional moments. $\delta\epsilon$, $\delta\kappa_n$, $\delta\kappa_b$ and $\delta\kappa_t$ are the first variations of the membrane strain and the three curvatures. We find the tangent stiffness matrix by calculating the second variation of the external and internal virtual work, $\Delta\delta W^{\text{ext}}$ and $\Delta\delta W^{\text{int}}$. As second derivatives with respect to ξ_1 will be present in the formulation, we use NURBS of order $p \geq 2$ as basis functions, resulting in C^1 or greater continuity across element boundaries.

Numerical example

Clamped semicircular arch with a point load at the tip

We consider a semicircular arch clamped at one end and forced by a point load with magnitude F_p at the opposite end, see Figure 3a. The load F_p is normalized as $\widetilde{F}_p = F_pR^2/E_cI_0 = 1.0$, where

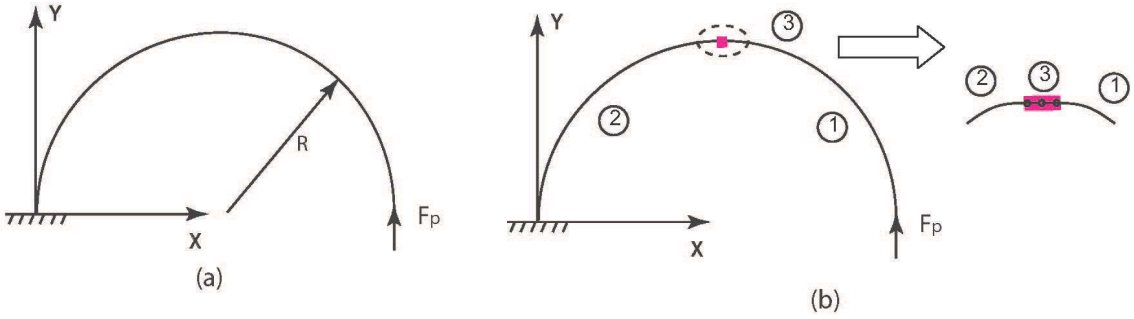

Figure 3. Clamped semicircular arch with a point load at the tip. (a) Problem setup without the bending strip. (b) Problem setup with the bending strip.

$R = 1$ is the arch radius. We let $t = \sqrt{E_c I_0 / E_c A_0}$ denote the length scale of the cross-section and investigate $R/t = 100.0$, i.e., a thin arch. For this, we let $E_c I_0 = 1.0$, and $E_c A_0 = 10^4$. We use cubic NURBS with exact representation of the arch geometry. The tip deflection in the x- and y-direction as a function of the number of elements is plotted in Figure 4. The results are compared to a benchmark solution obtained using Kirchhoff–Love shell formulation with zero Poisson's ratio and appropriate boundary conditions to reproduce the beam-like response [3]. We consider a single-curve C^1-continuous discretization of a 180° arc and a two-curve discretization, 90° each, joined with a bending strip [3], see Figure 3b. The bending-strip thickness is set to $E_c^b = 100 E_c$. Rapid convergence to the benchmark solution is obtained for both discretizations. The converged values of the x- and y-deflections at the tip are 2.000 and 4.713.

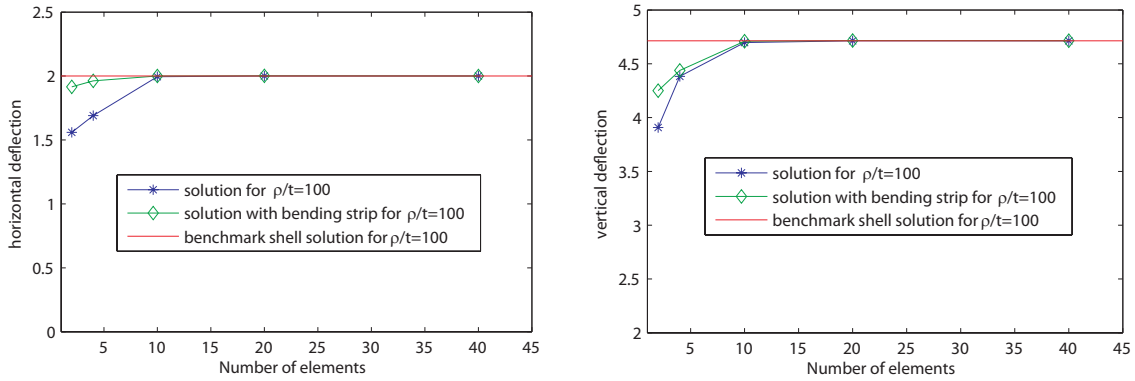

Figure 4. Clamped semicircular arch with a point load at the tip. Tip displacement convergence.

References

[1] L. Greco and M. Cuomo. B-Spline interpolation of Kirchhoff-Love space rods. *Computer Methods in Applied Mechanics and Engineering*, 256:251–269, 2013.

[2] S.B. Raknes, X. Deng, Y. Bazilevs, D.J. Benson, K.M. Mathisen and T. Kvamsdal. Isogeometric rotation-free bending-stabilized cables: Statics, dynamics, bending strips and coupling with shells. *Computer Methods in Applied Mechanics and Engineering* , 263:127–143, 2013.

[3] J. Kiendl, Y. Bazilevs, M.-C. Hsu, R. Wüchner and K.-U. Bletzinger. The bending strip method for isogeometric analysis of Kirchhoff–Love shell structures comprised of multiple patches. *Computer Methods in Applied Mechanics and Engineering* , 199:2403–2416, 2010.

Proceedings of the 26th Nordic Seminar on Computational Mechanics
A. Logg, K.A. Mardal, A. Massing (Eds.)

Effective analysis of thin-walled cross-sections by a two-dimensional cubic-linear isoparametric element

Jan Høgsberg and Steen Krenk

Department of Mechanical Engineering
Technical University of Denmark, DK-2800 Lyngby, Denmark
jhg@mek.dtu.dk , sk@mek.dtu.dk

Summary. The analysis of moderately thin-walled beam cross-sections is based on the representation of extension, bending, shear and torsion as individual load cases. The weak form equations for the warping associated with shear and torsion are solved numerical by introducing a cubic-linear isoparametric element that is able to (a) represent quadratic shear stress variations in the cross-section flanges and (b) describe fairly curved cross-section geometries. The efficiency is demonstrated by numerical examples.

Key words: Thin-walled beam, cross-section analysis, finite element method, isoparametric element

Introduction

Accurate analysis of beam structures requires a detailed determination of the cross-section properties, which in technical beam theory are derived from a kinematic formulation that contains cross-section translations, rotations and warping displacements. In the current approach the six equilibrium states associated with homogeneous tension, bending, shear and torsion are treated as individual load cases [1]. This enables the formulation of the governing weak form equations for the out-of-plane warping functions from pure shear and torsion, and the subsequent determination of the resulting cross-section stiffness parameters, the location of the elastic center and the shear center, and the warping functions and shear stresses associated with shear and torsion loading. The weak form equations are solved numerically by the finite element method, introducing a cubic-linear two-dimensional isoparametric element, suitable for cross-sections with moderate wall thickness. Because of the cubic displacement interpolation this particular element accurately represents a quadratic shear stress variation along the wall of the cross-section, and thus moderately thin-walled cross-sections can be effectively discretized using only a small number of these cubic-linear elements, see [2]. The ability of the cubic-linear element to represent curved cross-section geometries, to accurately determine cross-section parameters and to provide shear stress distributions is demonstrated by numerical examples, where the present finite element implementation is used to analyze a tubular and a wind turbine blade cross-section.

Load cases and governing equations

The six homogeneous load cases associated with technical beam theory are shown in Fig. 1, where the tension force N and the bending moments M_α act at the elastic center (c_1, c_2), while uncoupling of the shear forces Q_α and the torsion moment M identify the shear center (a_1, a_2). Greek subscripts represent the cross-section dimensions x_1 and x_2, while z is the axial coordinate. The transverse displacements are described by the translations ξ_α and the angle of twist φ as

$$u_\alpha(\mathbf{x}, z) \;=\; \xi_\alpha(z) - e_{\alpha\beta}\big(x_\beta - a_\beta\big)\varphi(z) \tag{1}$$

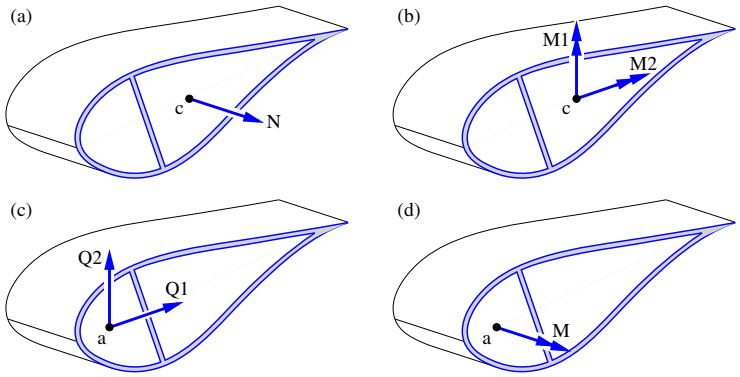

Figure 1. Section forces: (a) tension, (b) bending, (c) shear and (d) torsion.

where $e_{\alpha\beta}$ is the permutation tensor. The axial displacement is described in terms of the axial translation ζ and the cross-section inclinations η_β as

$$w(\mathbf{x},z) \;=\; \zeta(z) - \big(x_\beta - c_\beta\big)\eta_\beta(z) + \psi_\beta(\mathbf{x})\big(\xi'_\beta(z) - \eta_\beta(z)\big) - \omega(\mathbf{x})\varphi'(z) \tag{2}$$

where $\psi_\beta(\mathbf{x})$ and $\omega(\mathbf{x})$ are the out-of-plane warping functions from shear and torsion, respectively, and the prime denotes differentiation with respect to the longitudinal coordinate z. The contribution from warping is neglected in the expression for the corresponding normal strain, whereby the kinematic formulation becomes energetically conjugate to the load cases in Fig. 1.

Cross-section parameters

In the extension-bending problem the normal force and the bending moments in Fig. 1a,b are $N = F\zeta$ and $M_\alpha = I_{\alpha\beta}\eta'_\beta$, where the axial stiffness and bending stiffness are defined as

$$F \;=\; \int_A E(\mathbf{x})\,dA \qquad , \qquad I_{\alpha\beta} \;=\; \int_A \big(x_\alpha - c_\alpha\big)\big(x_\beta - c_\beta\big)\,E(\mathbf{x})\,dA \tag{3}$$

The elastic center coordinates c_α are found in terms of the static moments S_α as

$$c_\alpha \;=\; \frac{S_\alpha}{F} \qquad , \qquad S_\alpha \;=\; \int_A x_\alpha\,E(\mathbf{x})\,dA \tag{4}$$

In the pure shear load case a modified warping function $\chi_\alpha(\mathbf{x})$ is introduced so that the contribution to the axial displacement becomes proportional to the generalized shear strain $\xi'_\beta + \eta_\beta$,

$$\chi_\alpha(\mathbf{x})\,Q_\alpha \;=\; \big[\,\big(x_\beta - c_\beta\big) + \psi_\beta(\mathbf{x})\,\big]\big(\xi'_\beta + \eta_\beta\big) \tag{5}$$

The axial stress equilibrium equation is $\tau_{\alpha,\alpha} + \sigma' = 0$. Substitution of the constitutive relations for the shear stress and the axial stress leads to the differential equation for the warping functions $\chi_\alpha(\mathbf{x})$. By multiplication with a virtual warping function this can be written in weak form as

$$\int_A \delta\chi_{,\alpha}(\mathbf{x})G(\mathbf{x})\,\chi_{\gamma,\alpha}(\mathbf{x})\,dA \;=\; \int_A \delta\chi(\mathbf{x})E(\mathbf{x})I^{-1}_{\gamma\beta}\big(x_\beta - c_\beta\big)\,dA\;, \qquad \gamma = 1,2 \tag{6}$$

This weak form equation is effectively solved in terms of the finite element method, as demonstrated in [3] and in the following section. The shear flexibility components $D_{\alpha\beta}$ are subsequently determined by establishing the elastic energy associated with pure shear. This leads to

$$D_{\alpha\beta} \;=\; \int_A \chi_{\gamma,\alpha}(\mathbf{x})G(\mathbf{x})\chi_{\gamma,\beta}(\mathbf{x})\,dA \tag{7}$$

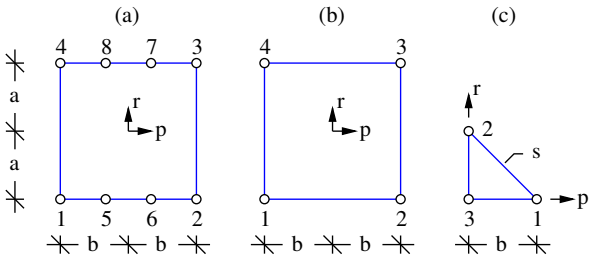

Figure 2. (a) 8-node cubic-linear, (b) 4-node bilinear elements and (c) 3-node linear triangular element.

In the torsion problem the axial stress vanishes and the stress equilibrium reduces to $\tau_{\alpha,\alpha} = 0$. Thus, the corresponding weak form governing equation for the torsion warping function ω has a similar left side as in (6), while the loading term on the right side is different,

$$\int_A \delta\omega_{,\alpha}(\mathbf{x}) G(\mathbf{x})\, \omega_{,\alpha}(\mathbf{x})\, dA \;=\; -\int_A \delta\omega_{,\alpha}(\mathbf{x}) G(\mathbf{x})\, e_{\alpha\beta}\big(x_\beta - a_\beta\big)\, dA \tag{8}$$

The torsion stiffness is found by forming the elastic energy associated with homogeneous torsion,

$$K \;=\; \int_A G(\mathbf{x})\big(x_\alpha - a_\alpha\big)\big(x_\alpha - a_\alpha\big)\, dA \;-\; \int_A G(\mathbf{x})\, \omega_{,\alpha}(\mathbf{x})\, \omega_{,\alpha}(\mathbf{x})\, dA \tag{9}$$

where the second term reduces the torsion stiffness relative to that of a cylindrical cross-section.

Numerical solutions

The weak form of the governing equations in (6) and (8) is effectively solved numerically in terms of finite elements. Furthermore, cross-sections with moderate wall thickness are considered, which means that the shear stress distribution in the main direction of the flanges is of parabolic order. This leads to the introduction of the two-dimensional 8-node isoparametric element shown in Fig. 2a, with cubic interpolation of the displacements by four nodes along the sides in the flange direction and linear interpolation by two nodes in the thickness direction. Junctions and corners are handled by the 4-node bilinear element and the 3-node triangular element shown in Fig. 2. The introduction of isoparametric elements enables the use of standard shape functions and integration rules. Furthermore, quite complicated and curved geometries can be represented by the 8-node element because of the cubic order interpolation. This is demonstrated for a thin-walled tubular cross-section in Fig. 3a, where only four 8-node cubic-linear elements are required for the discretization. Both a closed and an open tubular section are analyzed, where the open section has a thin cut in the cross-section, as indicated in the figure. For pure torsion Figs. 3b,c show the warping function for the open section and the shear stress distribution for the closed section, respectively. It is seen that the numerical results practically reproduce the analytical results. The cross-section parameters found by the numerical procedure are given in Table 1.

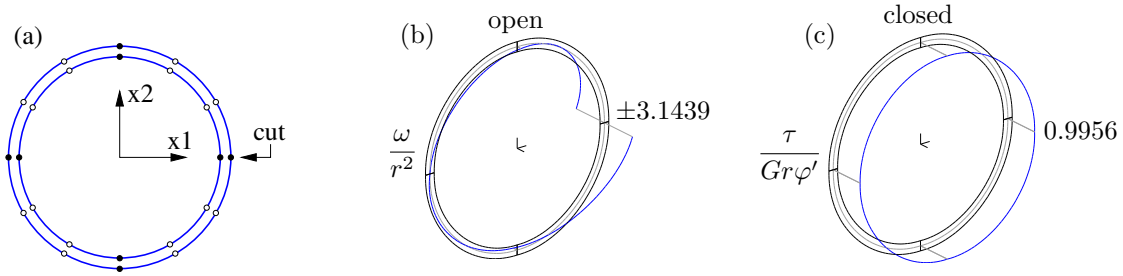

Figure 3. Tubular cross-section with radius r and wall thickness $t = r/10$: (a) discretization by four cubic elements, (b) torsion warping for open section and (c) torsion shear stress for closed section.

Table 1. Parameters for open and closed tubular sections with $t/r = 0.1$.

$\frac{F}{Ert}$	$\frac{I_\alpha}{Er^3t}$	$\frac{c_\alpha}{r}$	$\frac{a_\alpha}{r}$	$\frac{GA_\alpha}{2\pi Grt}$	$\frac{K}{Gr^3t}$	$\frac{I_\omega}{Er^5t}$
Closed section (24 dofs)						
6.2931	3.1594	$O(10^{-15})$	$O(10^{-14})$	0.5029 0.5029	6.3187	$1.7228 \cdot 10^{-7}$
Open section (26 dofs)						
—	—	—	−1.9959 0.0000	0.5029 0.1677	0.0210	8.1476

Figure 4a shows the discretization of a typical wind turbine blade cross-section. The numerical model for this cross-section contains only 66 degrees of freedom because the 8-node cubic-linear elements are able to effective represent large parts of the curved aerodynamic profile of the cross-section. It is seen that the 4-node bilinear elements are used at junctions and where the outer profile changes thickness, while two 3-node triangular elements represent the tail of the section. Figure 4b shows the shear stress distribution from torsion, which shows that in particular the leading and trailing parts of the blade section carry the load. The shear stress distributions from the two separate load cases associated with flexure are shown in Figs. 4c,d. It is seen that while the trailing part is significantly loaded in edgewise flexure, the internal web and the leading part of the section mainly provide the shear stiffness in the flapwise direction.

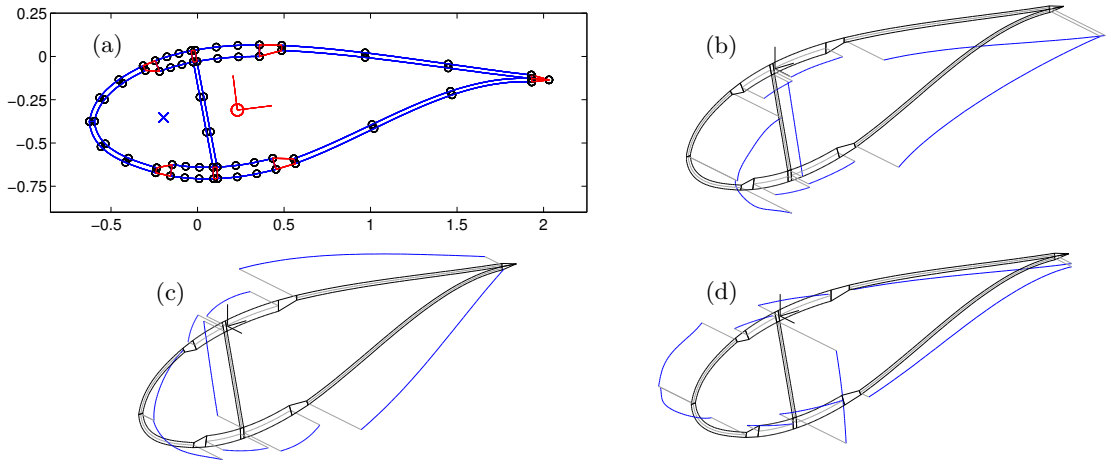

Figure 4. Discretization of wind turbine blade section and shear stress distributions.

References

[1] S. Krenk and B. Jeppesen. Finite elements for beam cross-sections of moderate wall thickness. *Computers and Structures*, 32:1035-1043, 1989.

[2] J. Høgsberg and S. Krenk. Analysis of moderately thin-walled beam cross-sections by cubic isoparametric elements. *Submitted for publication*, 2013.

[3] V. Giavotto, M. Borri, Ghiringhelli, V. Carmaschi, G.C. Maffioli and F. Mussi. Anisotropic beam theory and applications. *Computers and Structures*, 16:403-413, 1989.

Proceedings of the 26th Nordic Seminar on Computational Mechanics
A. Logg, K.A. Mardal, A. Massing (Eds.)

Design of Stroke Amplifying Brace Concepts for Damping of Wind Turbine Tower Vibrations

Mark Laier Brodersen and Jan Høgsberg

Department of Mechanical Engineering
Technical University of Denmark, DK-2800 Lyngby, Denmark
mlai@mek.dtu.dk, jhg@mek.dtu.dk

Summary. Three stroke amplifying brace concepts are introduced for damping of tower vibrations of monopile supported offshore wind turbines. Damper stroke and attainable damping are key aspects that are studied for the three brace concepts. The optimum location of the damper system is at the bottom of the tower, where it is found that a brace height 4 m results in a damper stroke of 2-5 mm and attainable damping ratio of 0.013 critical damping.

Key words: Offshore wind turbine, monopile, toggle-brace, attainable damping, damper stroke

Introduction

Design of monopile support structures for offshore wind turbines is often driven by fatigue. For pronounced wind-wave misalignment tower vibrations lateral to the rotor direction will cause a large amount of fatigue damage, due to the relatively low inherent damping of the side-side vibrations [1]. Future offshore wind turbines will be significantly larger and operate at larger water depths. Thereby the critical tower frequency of the turbines will be lowered and approach the typical excitation frequencies of large ocean waves. This causes fatigue damage from wave loading to increase significantly, and under these conditions the monopile support structure may reach its limit of structural feasibility. A way to extend this limit is to reduce the dynamic response of the turbine by installing dampers inside the wind turbine to act on the relative motion of the tower. Critical aspects for the effective implementation of the dampers are the sufficient damper stroke and the attainable damping. Sufficient damper stroke is achieved by the use of stroke amplifying braces, while attainable damping is associated with the ability of the damper system to alter the natural frequency of the structure. In the present paper three stroke amplifying brace concepts are presented. The damper stroke and the attainable damping level are studied for these concepts using a realistic benchmark off-shore wind turbine model [2] implemented in the nonlinear aeroelastic code HAWC2 (www.HAWC2.dk).

Stroke amplifying braces

For the side-side vibration form bending of the tower is the primary deformation mode. The lower toggle brace in figure 1(a), the upper toggle brace in figure 1(b) and the curvature toggle brace in figure 1(c) have been designed to maximize the damper stroke when the tower is vibrating in the side-side vibration form. For all three toggle-braces the two brace members are of equal length, and the damper is fixed to the two other brace members in the direction normal to the diagonal, in order to exploit the toggle mechanism in the best possible way. In this way the angle ψ is determined by the height of the brace and the geometry of the tower. The angle

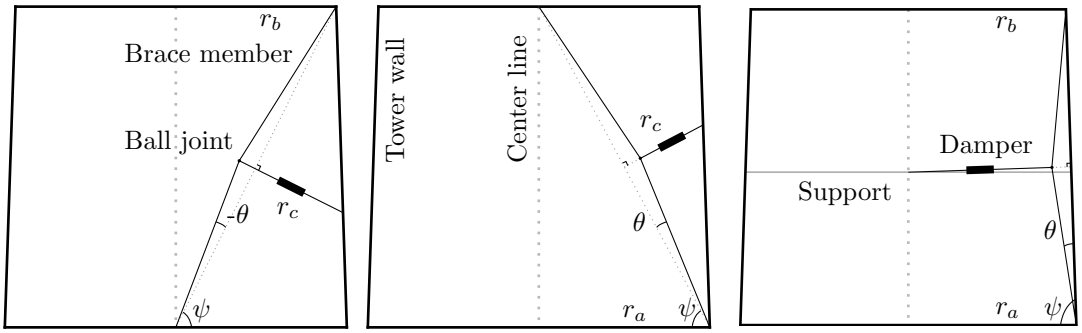

(a) (b) (c)

Figure 1: lower toggle brace (a), upper toggle brace (b) and curvature toggle brace (c).

θ should be as small as possible in order to increase the damper stroke as much as possible, while large enough to avoid snap-through of the toggle joint. In all the following computations $\theta = 5^o$, whereby snap-through is avoided for typical vibration amplitudes of the turbine.

Influence vector

The influence of mounting a local damper in the wind turbine tower is described by its influence vector $\mathbf{w}$ and the magnitude of the damper force f_d. The load vector is then given as

$$\mathbf{f}(t) = -\mathbf{w} f_d(t) \tag{1}$$

The vector $\mathbf{w}$ describes the connection of the damper to the tower structure through the stroke amplifying braces. Considering equilibrium in the undeformed state, consistent with small deformation theory, leads to a linear asymptotic expression for $\mathbf{w}$ given in terms of the angles ψ and θ and the radii r_a,r_b,r_c at the points of connection with the tower, see figure 1. Influence vector for the lower toggle brace, upper toggle brace and curvature toggle brace is respectively

$$\mathbf{w}_i^l = \begin{bmatrix} \frac{1}{2}\frac{\cos\psi}{\sin\theta} - \frac{1}{2}\sin\psi \\ 0 \\ -\frac{1}{2}\frac{\cos\psi}{\sin\theta} - \frac{1}{2}\sin\psi \\ -\frac{1}{2} r_b \frac{\sin\psi}{\sin\theta} + \frac{1}{2} r_b \cos\psi \\ \sin(\psi) \\ -r_c\cos(\psi) \end{bmatrix} \quad \mathbf{w}_i^u = \begin{bmatrix} \frac{1}{2}\frac{\cos\psi}{\sin\theta} - \frac{1}{2}\sin\psi \\ -\frac{1}{2} r_a \frac{\sin\psi}{\sin\theta} - \frac{1}{2} r_a \cos\psi \\ -\frac{1}{2}\frac{\cos\psi}{\sin\theta} - \frac{1}{2}\sin\psi \\ 0 \\ \sin(\psi) \\ r_c\cos(\psi) \end{bmatrix} \quad \mathbf{w}_i^c = \begin{bmatrix} \frac{1}{2}\frac{\cos\psi}{\sin\theta} + \frac{1}{2}\sin\psi \\ -\frac{1}{2} r_a \frac{\sin\psi}{\sin\theta} + \frac{1}{2} r_a \cos\psi \\ -\frac{1}{2}\frac{\cos\psi}{\sin\theta} + \frac{1}{2}\sin\psi \\ \frac{1}{2} r_b \frac{\sin\psi}{\sin\theta} + \frac{1}{2} r_b \cos\psi \\ -\sin(\psi) \\ 0 \end{bmatrix}$$

As the brace is assumed linear and collocated, the damper displacement u_d is found by

$$u_d(t) = \mathbf{w}^T \mathbf{u}(t) \tag{2}$$

where $\mathbf{u}(t)$ is the displacement vector of the wind turbine. Whereby, if the damper is assumed viscous with viscosity c, the load vector is given in terms of the velocity vector $\dot{\mathbf{u}}(t)$ as

$$\mathbf{f}(t) = -c\mathbf{w}\mathbf{w}^T \dot{\mathbf{u}}(t) \tag{3}$$

Numerical modeling using HAWC2

In order to study the performance of the three braces, the braces have been implemented into a HAWC2 model of the OC3 reference wind turbine provided by DTU Wind Energy [4], and HAWC2 has been used for computing the side-side mode $\mathbf{s}$ and side-side eigenfrequency ω by solving the eigenvalue problem for the OC3 turbine at standstill

$$\left(\mathbf{K} - \omega^2\mathbf{M} + i\omega c\mathbf{w}\mathbf{w}^T\right)\mathbf{s} = 0 \tag{4}$$

The mass matrix $\mathbf{M}$ and stiffness matrix $\mathbf{K}$ are determined by HAWC2 based on the inherent multi body formulation, while the brace and damper has been included as an external system as described for a gear box in [3].

Damper stroke

Damper stroke of the three braces is determined by assuming that the tower is vibrating in the undamped side-side mode $\mathbf{s}$. The mode shape is computed using HAWC2, where after the damper stroke is computed using (2). The amplitude of the mode shape is fixed so that the top amplitude of the tower is approximately 0.5 m. The damper stroke is computed for different positions in the tower for a brace height of 4 m, see figure 2(a), and for different heights of a brace installed in the bottom of the tower, see figure 2(b). As seen from figure 2(a) the largest damper stroke is achieved when the brace is positioned in the lower half of the tower, although the difference to a position in the upper half of the tower is not significant. The curvature toggle brace performs much better than the lower and upper toggle braces, providing a damper stroke almost twice as large. When the height is varied the damper stroke is increased as seen in figure 2(b). There is an almost linear relation between height and damper stroke, and again the curvature toggle brace performs better than the upper and lower toggle braces. Between 2-5 mm damper stroke can be expected when the brace is installed in the lower half of the tower with a brace height of 4 m. This may be a small stroke for conventional passive dampers, while it is sufficient for active damper systems using e.g. hydraulics.

Attainable damping

Attainable damping is associated with the ability of the dampers to lock the wind turbine in a new modified mode shape. When the change in mode shape is small attainable damping can be directly related to the frequency change $\Delta\omega = \omega_\infty - \omega_0$ between the frequency of the undamped wind turbine ω_0 (c = 0) and the turbine where the damper has been locked ω_∞ (c = ∞) via the two-component representation in [5]. The analytical estimate of the modal damping ratio can be written

$$\zeta_{max} = \frac{\Delta\omega}{2\omega_0} \tag{5}$$

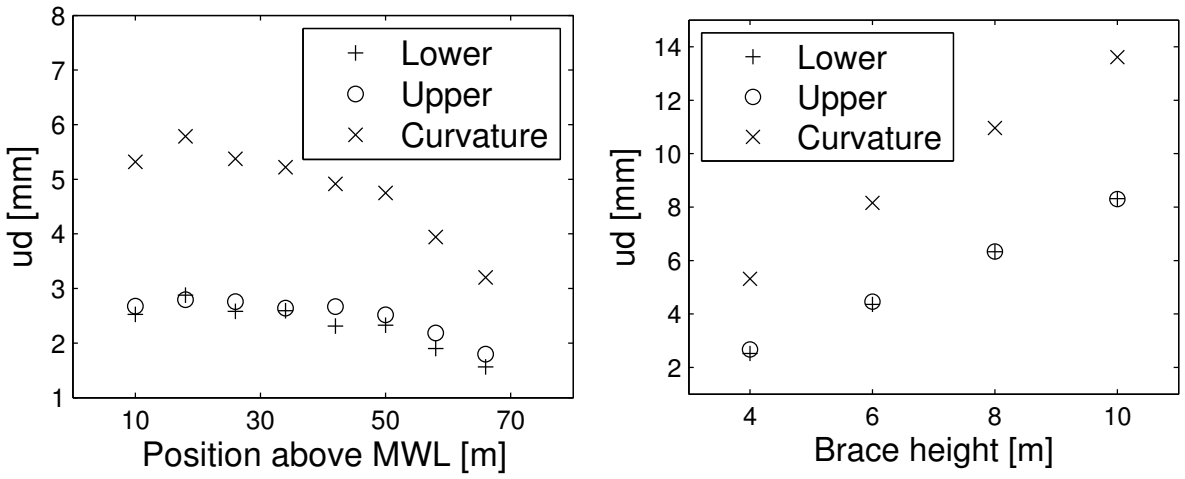

(a) (b)

Figure 2: Damper stroke for a varying position of the brace (a) and varying brace height (b).

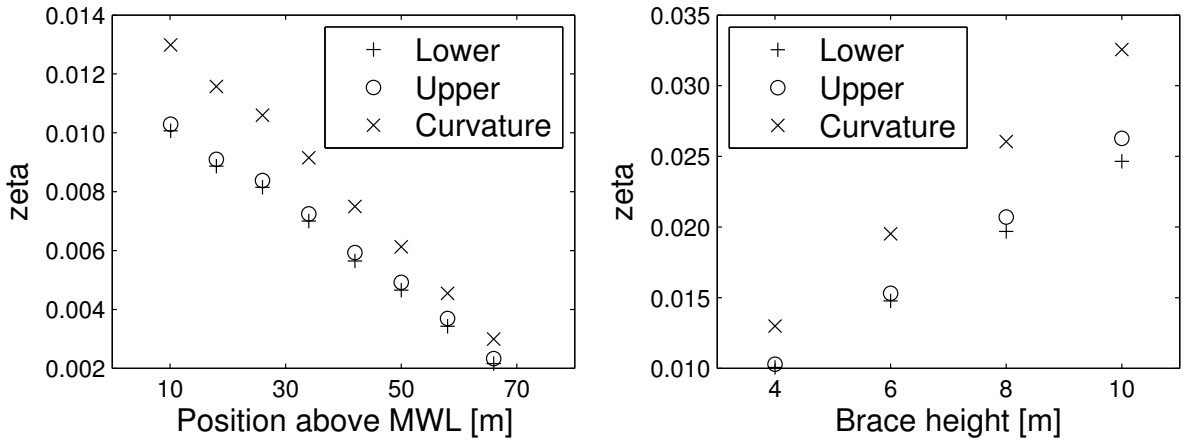

(a) (b)

Figure 3: Attainable damping for a varying position of the brace (a) and varying height of the brace (b).

Using the HAWC2 model of the OC3 turbine eigenfrequency for the side-side mode when the damper is locked is computed, and from (5) attainable damping is determined. Attainable damping is computed for different brace locations inside the tower for a brace height of 4 m, see figure 3(a), and for different heights of the brace, when the brace is installed at the bottom of the tower, see figure 3(b). As seen from figure 3(a) all three braces perform best when installed at the bottom of the tower, with an almost linear reduction relative to the location of the brace. The curvature brace performs better than the lower and the upper toggle braces. The largest attainable damping is therefore achieved using a curvature brace at the bottom of the tower. For a brace height of 4 m attainable damping is approximately $\zeta_{max} = 0.013$, which could be increased to $\zeta_{max} = 0.025$ with two brace system of height 4 m located on top of each other at the bottom of the tower. Initial estimates performed by the wind energy community indicate that an increase in damping ratio of about $\zeta = 0.02$ is required to sufficiently reduce the amplitude level of the side-side vibration mode. As seen from figure 3(b) attainable damping increases with increasing height of the brace, and again the correlation seems to be almost linear. Therefore, it appears reasonable to maximize the height of the brace as well.

References

[1] Tarp-Johansen, Niels Jacob and Lars Andersen and Christensen, Erik Damgaard and Christian Mørch and Sten Frandsen and Bjarne Kallesøe. Comparing Sources of Damping of Cross-Wind Motion. *Proceedings of the European Wind Energy Conference & Exhibition*, Stockholm,2009.

[2] Jonkman, J and Musial, W. Offshore Code Comparison Collaboration (OC3) for IEA Task 23 Offshore Wind Technology and Deployment. *NREL/TP-500-48191*, National Renewable Energy Laboratory, 2010.

[3] A. M Hansen and T. J. Larsen. Gear Dynamics. *Research in Aeroelasticity EFP-2007-II*, 134-142, Risoe-R-1698(EN), Risoe National Lab., 2009.

[4] Yde, Anders. Phase 2 - Extended Monopile. *http://www.hawc2.dk/HAWC2%20Download/HAWC2%20model/Phase%20II%20-%20Extented%20Monopile.aspx*, Accessed September 1, 2013.

[5] Main, JA and Krenk, S. Efficiency and tuning of viscous dampers on discrete systems. *Journal of Sound and Vibration*, 286(1-2):97–122,2005.